EJA

European Journal of Anatomy

Volume 28 - Number 2 March 2024

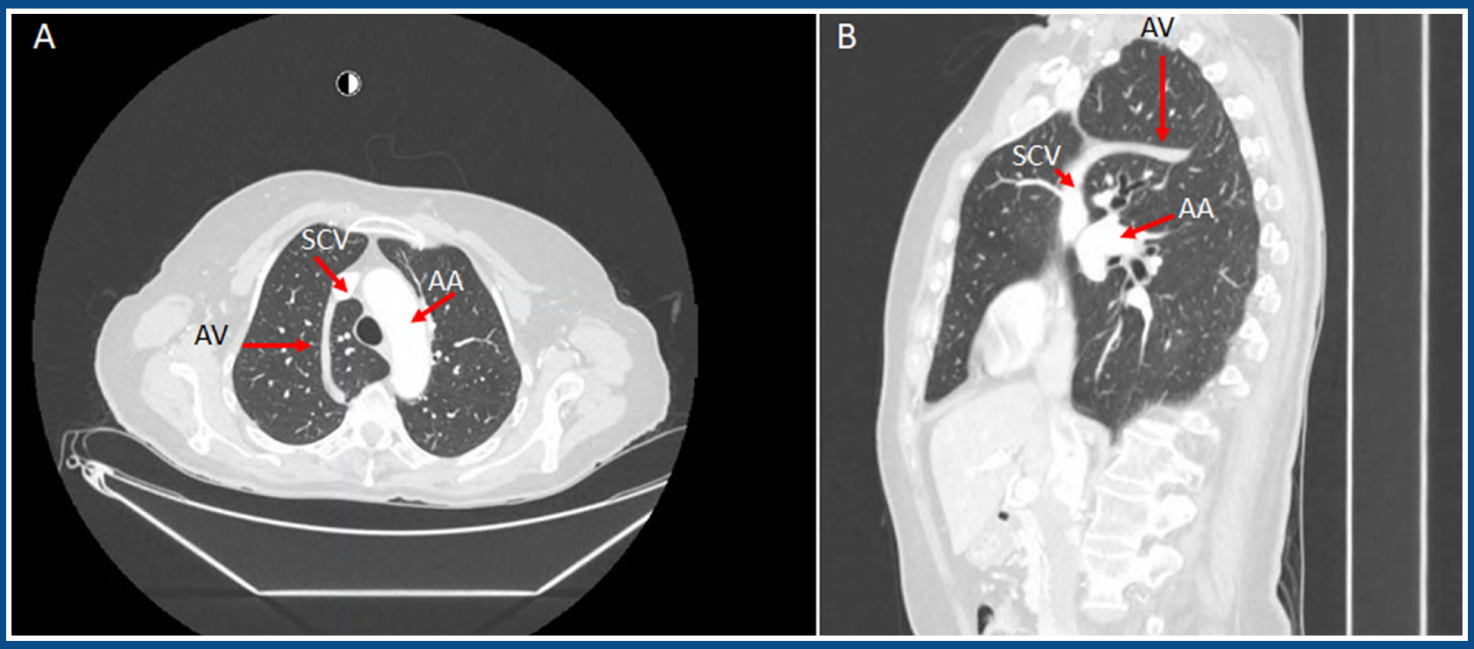

Indexed in:

CLARIVATE
- JCR:2020
- Q4 (21/23)
- I.F. J.C.I.: 0.19

DIALNET

EMBASE / Excerpta Medica

SCOPUS
- SJCR: 2020
- Q4 (31/39)
- I.F.: 0.162

Emerging Sources Citation Index

LATINDEX. Catálogo v1.0 (2002-2017)

Official Journal of the Spanish Society of Anatomy

Published by: **LOKI & DIMAS**

www.eurjanat.com

EJA
European Journal of Anatomy

Volume 28 - Number 2 March 2024

ORIGINAL ARTICLES

CASE REPORTS

Spleen anatomic variations in the context of morphology

Sani Baimai, Panicha Chaiwichayanant, Sirinush Sricharoenvej, Chayanit Manoonpol

Department of Anatomy, Faculty of Medicine Siriraj Hospital, Mahidol University, Bangkok 10700, Thailand

SUMMARY

The immune and hematopoietic systems in the human body depend on the spleen. The understanding of anatomical and morphological variations of the spleen and its arterial vascular segments (AVS) is crucial for performing whole or partial splenectomy in the treatment of splenomegaly and splenic rupture. The aim of this study was to compare the anatomical differences in the spleen and its AVS in Thai cadavers of both sexes. This cadaveric study was performed on 77 cadaveric spleens (males = 38 and females = 39) from the Gross Anatomy Laboratory at the Department of Anatomy, Faculty of Medicine Siriraj Hospital, Mahidol University. The average morphological measures of the observed spleens were 9.11±1.40 cm in length, 6.57±1.46 cm in width, 3.11±0.67 cm in thickness in male cadavers, and 8.77±1.87 cm in length, 5.91±1.35 cm in width, and 2.90±0.78 cm in thickness in female cadavers. The variations in spleen form were 7.79% oval, 16.88% tetrahedral, 28.57% triangular, and 46.75% wedge. The mean splenic hilum length was 5.14±1.10 cm in males and 5.12±1.22 cm in females. The mean lobar branch to hilum distance was 2.26±0.98 cm in males and 2.29±1.05 cm in females. Females were more likely than males to have two lobar arteries. Three lobar arteries, however, were more prevalent in males. The occurrence of accessory spleens was 2.63% for males and 7.50% for females. According to the data, there were significant differences in the number of lobar arteries and spleen size between male and female Thai cadavers.

Key words: Spleen – Anatomical Variation – Cadaver – Morphology

INTRODUCTION

The spleen is the largest organ in the lymphatic system. A soft dark purple in color, the spleen varies in shape and size and is located in the left upper quadrant of the abdomen. The mean average length, width, and thickness are 12, 7, and 3 centimeters, respectively, and spleens weigh approximately 150 grams. It has anterior and posterior extremities, as well as anterior and inferior borders and visceral and diaphragmatic surfaces (Cesta, 2006). The development of the spleen occurs during the fifth week of gestation by the aggregation of mesenchymal cells (Coetzee, 1982). Failure of splenic nodule fusion can lead to the development of the accessory spleen and the appearance of one or more notches on the border of the spleen. The spleen plays a crucial role in both the immune and hematopoietic systems, including filtration and regulation of erythrocytes,

Corresponding author:
Sani Baimai, M.D., Ph.D. Department of Anatomy, Faculty of Medicine Siriraj Hospital, Mahidol University, Bangkok 10700, Thailand. Phone: (+66) 82-210-6507. E-mail: Sani.bai@mahidol.ac.th / sanibaimai@gmail.com

Submitted: June 2, 2023. **Accepted:** September 19, 2023

https://doi.org/10.52083/IXWW6102

production of lymphocytes, and prevention of infection from pathogens (Kapila et al., 2021). The blood supply of the spleen is from the splenic artery, where its terminal branch divides into lobar, segmental, and trabecular arteries. Due to the lack of anastomoses between the lobar arteries, the number of lobar arteries plays an important role in indicating the number of splenic segments (Sahni et al., 2003).

The major splenic disorders are splenomegaly, hypersplenism (hyperfunction), and splenic rupture. Splenomegaly, or spleen enlargement, is brought on by several potential causes, such as hematologic cancers, liver diseases, venous thrombosis, and infections from bacteria, parasites, and viruses. The spleen can be replaced by cancer cells, or it can be hyperactive. Hypersplenism is caused by an overactive spleen, which filters and destroys an excessive number of both healthy and damaged blood cells, resulting in anemia. The emergency condition known as splenic rupture is typically brought on by trauma or injury that results in severe internal bleeding in the upper left portion of the abdomen (Bowdler, 2002).

The spleen is the organ that is well-known for its variation in morphology and AVS which can potentially lead to complications. Therefore, the knowledge of the splenic variations is important for physicians, surgeons, and radiologists for precise diagnosis and potential preoperative planning for various upper abdominal surgeries and arterial intervention practices. In the case of severe splenic diseases, the spleen can be removed as a treatment option. Splenectomy can be divided into total splenectomy and partial splenectomy (Yi and Buicko, 2022). Both surgical procedures necessitate an understanding of anatomical variations and the arterial vascular segments (AVS), particularly to perform partial splenic removal effectively as an alternative treatment for some diseases. The aim of this study was to identify the anatomical variations of the spleen and AVS in the Thai population and compare the differences between males and females.

MATERIALS AND METHODS

During the academic year 2021-2022, the anatomical variation of spleens and the AVS was evaluated at the Department of Anatomy, Faculty of Medicine Siriraj Hospital, Mahidol University, Bangkok, Thailand. The experiment was approved by the Siriraj Institutional Review Board, Mahidol University, Thailand (694/exemption). Exclusion criteria were splenic diseases such as splenomegaly of Thalassemia or tumor of the spleen.

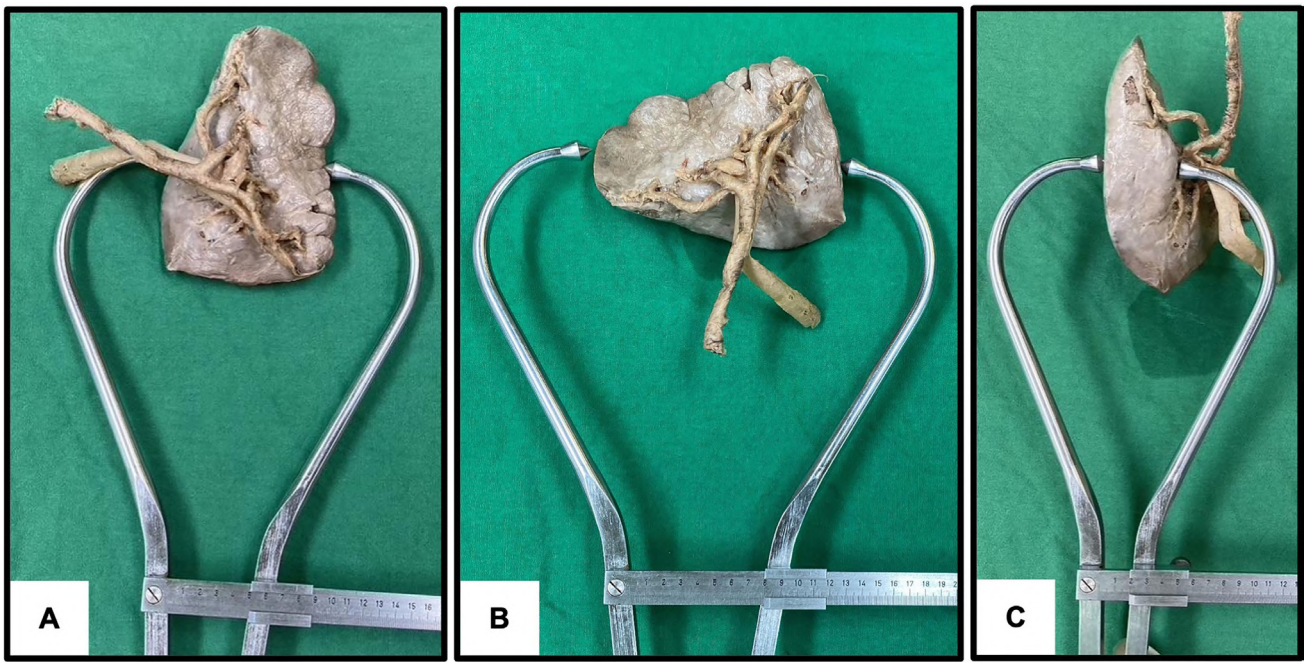

Fig. 1.- Measurement of the splenic size (width, length, and thickness) using the Vernier caliper. A: width; B: length; C: thickness.

The cadavers were all Thai and fixed in a 10% solution of formaldehyde. 77 cadaveric spleens (38 males and 39 females) were excised and photographed. The spleens were examined for morphological characteristics, including shape and number of notches on all borders as well as accessory spleen. Variations in spleen shape were classified into four main shapes: wedge, triangular, tetrahedral, and oval. The size (length, width, and thickness) of the spleen was measured using the Vernier caliper (Fig. 1). The length was measured by the maximum distance between the posterior extremity and the anterior extremity. The width was measured by the maximum distance between the superior border and the inferior border. The thickness was measured at the midpoint between the visceral and the diaphragmatic surfaces. Furthermore, the splenic hilum area and the splenic vessels were cleaned for the investigation of the area. The length of the hilum was measured (Fig. 2.). The number of lobar arteries that branched from the splenic artery was identified and counted. Next, the distance from the beginning point of the lobar branches from the splenic artery to the point of the hilum was measured with the Vernier caliper (Fig. 2.). In cases where the lobar artery branched after the splenic hilum, the distance value was presented as negative. Last, the presence or absence of an accessory spleen within the hilum of the spleen was observed. The mean and standard deviation of the data were determined (SD). Using the independent t-test, differences between independent groups were examined (SPSS version 20.0 software, Inc., Chicago, IL, USA). A *p*-value of 0.05 was used to determine if the differences were significant.

RESULTS

According to the demographic characteristics of the cadavers, the total number of cadavers was 77 cadavers with 77 spleens, separating into 38 males and 39 females. All the cadavers were Thai, with an age range of 40-99 years old at the time of death, with a mean age of 74.49 years.

Shapes and dimensions of the spleen, including length, width, and thickness

There were four different shape variations of the spleen, including a wedge shape, a triangular shape, a tetrahedral shape, and an oval shape. Out of the 77 spleens studied, 36 (46.75%) had a wedge shape, followed by triangular, tetrahedral, and oval shapes, at 28.57%, 16.88%, and 7.79%, respectively (Fig. 3).

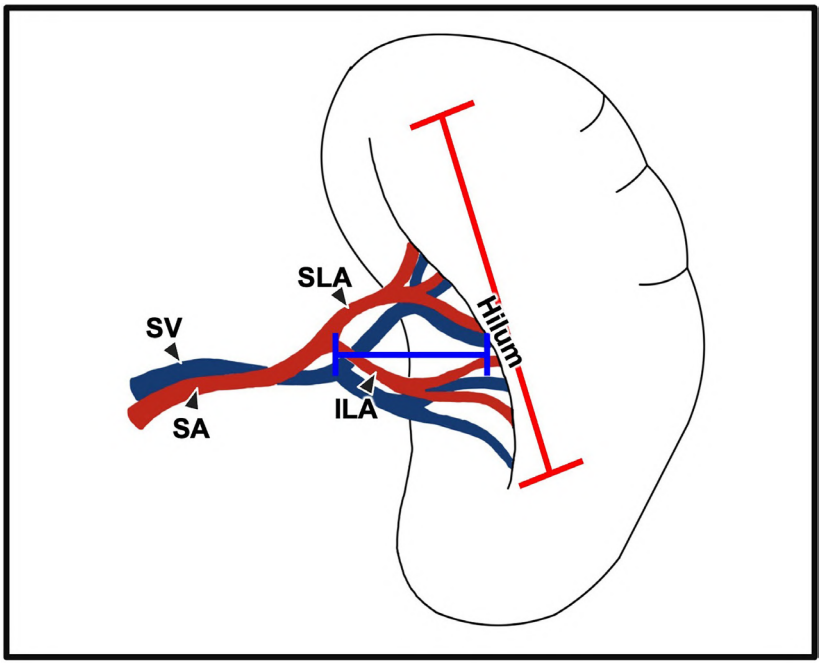

Fig. 2.- Schematic of spleen with blood vessels at the hilum. The length of the splenic hilum (red line); The distance from the beginning point of the lobar branches to the splenic hilum (blue line); Splenic artery (SA); Splenic vein (SV); Superior lobar artery (SLA); Inferior lobar artery (ILA).

Fig. 3.- The shape variations of the spleen. **A**: Wedge shape; **B**: Triangular shape; **C**: Tetrahedral shape; **D**: Oval shape.

In this study, male spleen lengths ranged from 6.90 cm to 13.90 cm, with an average of 9.11±1.40 cm, and female spleen lengths ranged from 4.80 cm to 13.50 cm, with an average of 8.77±1.87 cm. Male spleen widths ranged from 4.20 cm to 9.55 cm, with an average of 6.57±1.46 cm, and female spleen widths ranged from 3.20 cm to 9.30 cm, with an average of 5.91±1.35 cm. The thickness of the spleens ranged from 1.90 cm to 4.90 cm in males with an average of 3.11±0.67 cm and 1.70 cm to 5.20 cm in females with an average of 2.90±0.78 cm.

The notches of the splenic borders

The presence of notches on either border was also observed. Forty-four spleens (57.14%) presented with notches on the superior border only; 6 spleens (7.79%) had notches on the inferior border only; 21 spleens (27.27%) showed notches on both borders; and 6 spleens (7.79%) were found with the no notches on either border. The *p*-value was 0.001 for the location of notches between the superior and inferior borders.

The length of the splenic hilum

The length of the splenic hilum was measured. In male cadavers, the length of the hilum ranged from 3.25 cm to 9.10 cm, with a mean value of 5.14±1.10 cm. In female cadavers, the length of the hilum ranged from 2.70 cm to 9.10 cm, with a mean value of 5.12±1.22 cm. There was no statistically significant difference (p = 0.95) in the length of the splenic hilum between the sexes.

The distance from the beginning point of the lobar branch to the hilum

The distance from the beginning point of the lobar branch to the hilum varied from -0.20 cm to 4.10 cm in males and 0.70 cm to 5.40 cm in females (Table 1). There was no statistically significant difference (p = 0.91) between the sexes in the distance from the beginning point of the lobar branch to the hilum. There is 1.30% of a single branch of the splenic artery that directly terminates into the spleen without branching. However, the lobar arteries are presented after entering the hilum which results in a negative value by measuring from the hilum level the beginning point of the lobar branch.

Table 1. Distance from the beginning point of lobar branches to the splenic hilum.

Parameters	Minimum (cm)	Maximum (cm)	Mean ± SD (cm)
Males (n = 38)	-0.20	4.10	2.26 ± 0.98
Females (n = 39)	0.70	5.40	2.30 ± 1.05

*p<0.05; compared the distance from the beginning point of lobar branches to the splenic hilum between both sexes

The number and percentage of lobar artery branching types

The number of lobar arteries was found to be between two and three branches in this study, including the superior lobar artery, the middle lobar artery, and the inferior lobar artery (Fig. 4). There was a statistically significant difference (p = 0.048) in the number of lobar arteries between both sexes. Two lobar arteries were more common in females than in males. In contrast, three lobar arteries were more common in males, as exhibited in Table 2. However, in both sexes, there were more two-lobar arteries than three-lobar arteries.

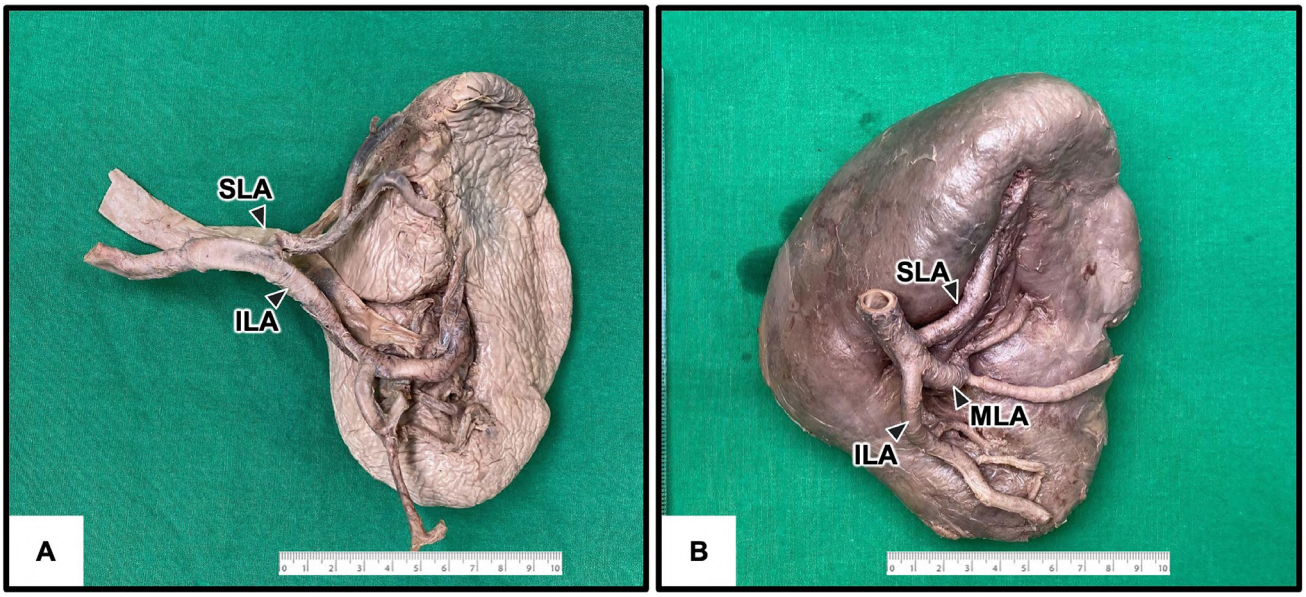

Fig. 4.- The medial view of the branches of the lobar arteries (**A-B**). Superior lobar artery (SLA); Inferior lobar artery (ILA); Middle lobar artery (MLA).

Table 2. Presence of number and percentage (%) of lobar artery branching types of the splenic arteries.

Parameters	Number and percentage (%) of lobar artery branching types	
Males (n = 38)	2 branches (superior and inferior)	3 branches (superior, middle, and inferior)
	Mean ± SD = 2.16 ± 0.37 br.	
	n = 32 (84.21%)	n = 6* (15.79%)*
Females (n = 39)	2 branches (superior and inferior)	3 branches (superior, middle, and inferior)
	Mean ± SD = 2.03 ± 0.16 br.	
	n = 38* (97.44%)*	n = 1 (2.56%)

*p<0.05; compared the number and percentage of lobar artery branching types between both sexes

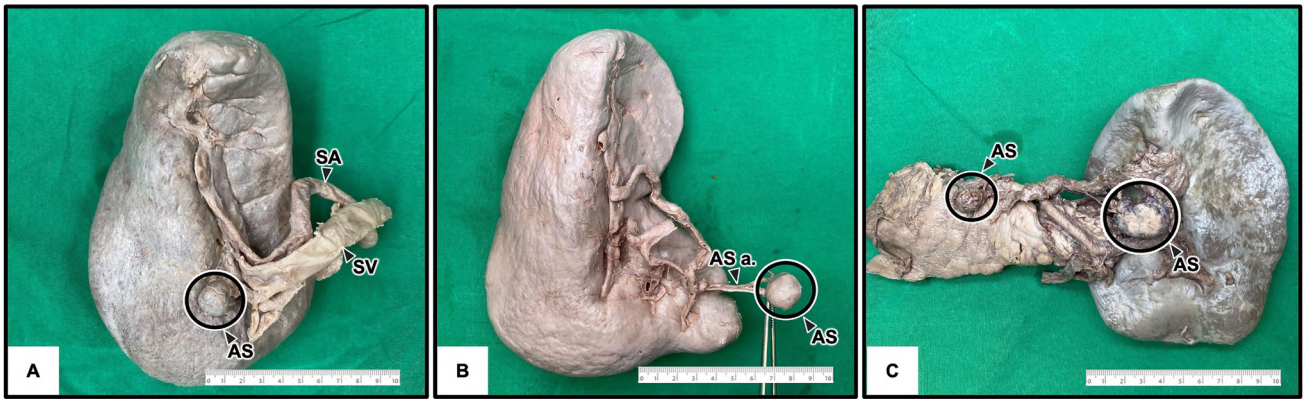

Fig. 5.- Variation of locations of accessory spleen. **A**: Accessory spleen at the splenic hilum. **B**: Accessory spleen at the splenic hilum with its arterial supply. **C**: Accessory spleens at the tail of pancreas and splenic hilum. Accessory spleen (AS); Splenic artery (SA); Splenic vein (SV); artery of accessory spleen (AS a.).

Table 3. The number and percentage of absence and presence of accessory spleens.

Parameters	**Accessory spleen (Number and percentage (%))**	
Males (n= 38)	**Absence**	**Presence**
	n = 37	n = 1
	97.37 %	2.63 %
Females (n = 39)	**Absence**	**Presence**
	n = 36	n = 3
	92.31 %	7.69 %

*p<0.05; compared the number and percentage of absence and presence of accessory spleens between both sexes

The number and percentage of accessory spleens and their locations

The presence of an accessory spleen was found in four cases in this study: one spleen (2.63%) in males and three spleens (7.69%) in females (Table 3).

The accessory spleen was found in various locations, including at the splenic hilum and at the tail of the pancreas. Some accessory spleens had their own artery, which independently supplied the accessory spleen body directly (Fig. 5).

DISCUSSION

In the present study, the anatomical variations of the spleen and its AVS were observed in 77 spleens, with an average dimension of 9.11 cm in length, 6.57 cm in width, and 3.11 cm in thickness in male cadavers and 8.77 cm in length, 5.91 cm in width, and 2.90 cm in thickness in female cadavers. The average length, width, and thickness in the previous studies by Mohammadi et al. (2016) report the male average as 11.50 cm, 8.20 cm, and 2.06 cm, respectively and the female average as 10.67 cm, 7.51 cm, 1.86 cm, respectively. The findings on the size of the spleen were closely consistent in both studies. Moreover, the comparison of the spleen dimension in both genders indicates a larger spleen size among males than in females. Therefore, the spleen size is significantly correlated with gender which can potentially apply as a reference for spleen-related surgeries.

The shape variations of the spleen appeared in this study. The most prevalent splenic shape was a wedge shape, followed by a triangular shape, a tetrahedral shape, and finally an oval shape with the same order in both genders. When compared with the previous studies, all the reported results appeared to align with the present study in terms of variations in splenic shape. Setty and Katikireddi (2013) reported the percentage of each shape of the spleen as 40% wedge, 32% triangular, 20% tetrahedral, and 8% oval. Chidambaram et al. (2015) reported 73.33%, 13.33%, 6.67%, and 6.67%, respectively. The findings showed a strong

variation of splenic shapes in the overall population without notable differences in shape variations between sexes.

Splenic notches are caused by the improper lobulation of splenic nodules during the embryonic stage (Gandhi et al., 2013). It was observed mostly on the superior border (57.14%) and only 7.79% on the inferior border. The greater proportion of notches on the superior versus inferior border (p = 0.001) found in the present study also correlated with previous studies, as 63.33% versus 10.00% were noted by Chidambaram et al. (2015) and 70% versus 14% were noted by Setty and Katikireddi (2013). Therefore, this supports the statistically higher chance of finding notches on the superior border compared to the inferior border. In some cases, abnormal deep fissures might be present which could lead to the misinterpretation of splenic hematoma by radiologists (Nayak et al., 2014; Smidt, 1967). However, the appearance of splenic fissures was absent in the present study. The presence of notches is essential for physicians as a clinical landmark for distinguishing splenomegaly and differentiating it from the tumor of the left kidney since splenic notches are more exaggerated and palpable (Gandhi et al., 2013; Nayak et al., 2011; Coetzee, 1982).

The *p-value* for the length of the splenic hilum was 0.95, indicating that no statistically significant difference existed between the sexes. The distance between the starting point of lobar branches and the splenic hilum had a *p-value* of 0.91. Therefore, there was no statistically significant difference in the distance from the beginning of lobar branches to the hilum between both sexes. To perform partial splenectomy, investigation of the distance between the splenic AVS and the length of the splenic hilum is crucial in terms of surgical planning since the terminal branches of the splenic artery need to be differentiated and incised to separate the segments of the spleen body. There is no significant variation between the sexes in the length of the splenic hilum and the distance of the terminal branches of the splenic arteries, so these measurements might not essentially affect the performance of a partial splenectomy.

The number of lobar branches of the splenic artery was found to be significantly different between sexes at a *p-value* of 0.048. According to Table 2, the presence of three lobar arteries was more common in males (15.79%) than in females (2.56%). Therefore, it could possibly be said that there is a significantly higher chance of finding three lobar arteries in males than in females. In the present study, 89.74% of the cases had two branches, while 8.97% had three branches of lobar arteries. In comparison, Gupta et al. (1967) reported 84% with two branches and 16% with three branches. Likewise, Katritsis et al. (1982) found 85.7% with two branches and 14.3% with three branches. Moreover, Alim et al. (2014) stated that 70% of the cases had two lobar arteries, 23% had three lobar arteries, and they even found 7% with four branches of lobar arteries. The number of lobar arteries varies from two to more than four, which would indicate the number of AVS (superior, middle, and inferior segments) of the splenic body. This also directly has a significant association with the performance of partial splenectomy due to the diversity of a number of AVS in different patients (Sahni et al., 2003).

The presence of a small nodule formed by splenic tissue located outside of the main spleen is known as the accessory spleen. The accessory spleen is a benign mesenchymal remnant from the embryonic period. In cases where an accessory splenic artery was present, similar physiology was seen in the accessory spleen as the normal spleen body (Bajwa and Kasi, 2018; Kumar et al., 2014). This study also discovered the presence of accessory spleens in various locations. A slightly higher number of accessory spleens was observed in females (7.69%) versus male cadavers (2.63%). The location of the accessory spleen varies from the splenic hilum to any area in the abdominal cavity which sometimes causes complications of misdiagnosis due to the mimicry of the accessory spleen to tumors or lymphadenopathy for the radiologists (Nivargi et al., 2014). Therefore, the possibility of an accessory spleen is important to consider when reviewing a CT scan before performing abdominal surgeries. Since the accessory spleen can function as a normal spleen, the removal of the accessory spleen is also necessary while performing the splenectomy to treat vascular disorders such as hypersplenism to entirely recover. (Bajwa and Kasi, 2018).

The overall findings suggest that there is prevalent variation in the spleen main body and its AVS. The investigation obtained a statistically significant value for the presence of the lobar artery. The variation of the aforementioned findings including the information on the length of the hilum and the distance between the hilum beginning of lobar arteries are significantly correlated with the performance of splenic arterial interventions to treat traumatic injuries and other complications. The knowledge is also important for physicians and radiologists in order to apply to other interventional radiology practices (Madoff et al., 2005). The data pool of the present studies confirmed the anatomical variations of the spleen that would be associated with the performance of upper abdominal surgeries, especially partial splenectomy. Due to possible complications and the diminished hematologic and immunologic function of the spleen from total splenectomy, partial removal might be more suitable for some cases. To preserve the spleen function, the variation of splenic terminal branches and AVS advocates partial splenectomy as an alternative to treat splenomegaly, hypersplenism, or splenic rupture. Therefore, physicians must acknowledge and understand the variation of the spleen and its artery including any potential rare conditions such as accessory spleen for accurate diagnosis and successful treatments.

CONCLUSION

The characteristics of splenic architectures and their AVS were found because of the high recognition of morphological variations. The prevalence of the lobar artery and the number of notches between both borders in the cadavers under study varies statistically significantly between males and females. Moreover, the findings of the length of the hilum and the distance between the beginning of the splenic branch of the hilum indicate significant clinical implications for physicians. Regarding anatomical variances, the study can be utilized as a guide for diagnosis and surgeries including a whole splenectomy and particularly a partial splenectomy.

ACKNOWLEDGEMENTS

This research was supported by Chalermphrakiat Grant, Faculty of Medicine Siriraj Hospital, Mahidol University, Thailand. The authors express their sincere gratitude to those who donated their bodies to science so that anatomical research and teaching could be performed. Results from such research can potentially increase scientific knowledge and enhance patient care. Therefore, these donors and their families deserve our highest respect.

REFERENCES

ALIM A, NURUNNABI ASM, MAHBUB S, AHMED R, ARA S (2014) Cadaver study on the branching pattern of the splenic artery in a Bangladeshi population. *Medicine Today*, 26(1): 15-17.

BAJWA SA, KASI A (2018) Anatomy, abdomen and pelvis, accessory spleen. StatPearls Publishing, Treasure Island, Florida.

BOWDLER AJ, editor (2002) The complete spleen: structure, function, and clinical disorders, 2nd ed. Humana Press, Totowa, New Jersey.

CESTA MF (2006) Normal structure, function, and histology of the spleen. *Toxicol Pathol*, 34(5): 455-465.

CHIDAMBARAM RS, SRIDHAR S (2015) Morphological variations of spleen: A cadaveric study. *J Evid Based Med Healthcare*, 2(29): 4248-4254.

COETZEE T (1982) Clinical anatomy and physiology of the spleen. *S Afr Med J*, 61(20): 737-746.

GANDHI KR, CHAVAN SK, OOMMEN SA (2013) Spleen with multiple notches: A rare anatomical variant with its clinical significance. *Int J Students' Res*, 3(1): 24.

GUPTA CD, GUPTA SC, ARORA AK, SINGH PJ (1976) Vascular segments in the human spleen. *J Anat*, 121(3): 613.

KAPILA V, WEHRLE CJ, TUMA F (2021) Physiology, Spleen. StatPearls Publishing, Treasure Island, Florida.

KATRITSIS E, PARASHOS A, PAPADOPOULOS N (1982) Arterial segmentation of the human spleen by post-mortem angiograms and corrosion-casts. *Angiology*, 33(11): 720-727.

KUMAR N, PATIL J, SWAMY RS, GURU A, NAYAK SB (2014) Atypical arterial supply to the spleen by polar branches of splenic artery and accessory splenic artery - a case report. *J Clin Diagn Res*, 8(8): AD03-4.

MADOFF DC, DENYS A, WALLANCE MJ, MURTHY R, GUPTA S, PILLSBURY EP, AHRAR K, BESSOUD B, HICKS ME (2005) Splenic arterial interventions: anatomy, indications, technical considerations, and potential complications. *Radiographics*, 25: 191-211.

MOHAMMADI S, HEDJAZI A, SAJJADIAN M, KEBRIAEI SMM, NASER GN, YAGHMAEI A, MOGHADAM MD, MOHAMMADI M (2016) Morphometric study of spleen in Iranian cadavers from Razavi-Khorasan province. *Bangladesh Med Res Counc Bull*, 42: 61-66.

NAYAK BS, SHETTY P, SIRASANAGANDLA SR, SHETTY DS (2014) A lobulated spleen with multiple fissures and hila. *J Clin Diagn Res*, 8(9): AD01-2.

NAYAK BS, SOMAYAJI SN, SOUMTA KV (2011) A study on the variations of size, shape and external features of the spleen in South Indian population. *Int J Morphol*, 29(3): 675-677.

NIVARGI S, KIRANKUMAR R, KULKARNI U, HUKKERI VB (2014) Accessory spleen - In clinical perspective. *National J Clin Anat*, 3(4): 229.

SMIDT PS (1977) Splenic scintigraphy: a large congenital fissure mimicking splenic hematoma. *Radiology*, 122(1): 169.

SAHNI AD, JIT BI, GUPTA CNM, GUPTA DM, HARJEET E (2003) Branches of the splenic artery and splenic arterial segments. *Clin Anat*, 16(5): 371-377.

SETTY SRS, KATIKIREDDI RS (2013) Morphometric study of human spleen. *Int J Biol Med Res*, 4(3): 3464-3468.

YI SL, BUICKO JL (2022) Splenectomy. StatPearls Publishing, Treasure Island, Florida

Nephroprotective effect of bone marrow mesenchymal stem cells on cisplatin induced kidney injury in albino rats

Mohamed Elsheikh[1], Heba A. Mubarak[2], Sayed Anwar Sayed[3]

[1] Department of Human Anatomy and Embryology, Faculty of Medicine, Aswan University, Aswan, Egypt
[2] Department of Histology and Cell Biology, Faculty of Medicine, Assiut University, Assiut, Egypt
[3] Department of Human Anatomy and Embryology, Faculty of Medicine, Assiut University, Assiut, Egypt

SUMMARY

Cisplatin is a chemotherapeutic drug used in the treatment of a variety of cancers, with a known side effect of nephrotoxicity. Using stem cell therapy represents a distinctive and encouraging approach to remediate damaged organs. The administration of bone marrow mesenchymal stem cells (BMMSCs) has the potential to mitigate the adverse effects of cisplatin nephrotoxicity, thus helping with both functional and histological recuperation. Twenty-four mature male albino rats were divided into four groups. 1 ml of normal saline was injected intraperitoneally (I.P.) into the control group. Cisplatin was injected once (6 mg/kg I.P.) into the cisplatin group. 0.5 ml of culture media with 5 x 106 BMMSCs was injected i.p. with 6 mg/kg I.P. cisplatin in the BMMSC group. The withdrawal group received no treatment after cisplatin injections. At different times, groups were sacrificed. Kidney specimens were made for histology and immunohistochemistry. Morphometric and statistical studies were done. Blood urea and serum creatinine were evaluated before sacrifice. There were statistically significant differences between the studied groups regarding markers of incidence of acute tubular necrosis and recovery, suggesting that cisplatin therapy caused acute tubular necrosis, whereas BMMSCs improved renal function markers, including blood urea and serum creatinine levels and tissue restoration. Stem cell rats also showed cluster of differentiation 44 (CD44) in cells near tubules, helping injured kidneys regenerate tubular cells. The use of bone-marrow-derived mesenchymal stem cells (BMMSCs) mitigated the nephrotoxic effects of cisplatin, thus showing a restorative effect on both functional and histological parts.

Key words: Cisplatin – Kidney – MSCs – CD44 – PCNA

INTRODUCTION

The symptoms of acute kidney injury (AKI) include an abrupt drop in glomerular filtration rate, the kidney's failure to eliminate wastes such as nitrogenous wastes, and disruption of the homeostasis of fluids and electrolytes. Drug-induced nephrotoxicity, in which the proximal convoluted tubules of the nephron are the major site of dam-

Corresponding author:
Mohamed Elsheikh, MD. Anatomy department, Faculty of Medicine, Aswan University, Aswan, 81528 Egypt. Phone: 00201008048586. E-mail: Melsheikh4047@gmail.com

Submitted: June 2, 2023. **Accepted:** September 22, 2023

https://doi.org/10.52083/UFPK9237

age, is one of the renal or intrinsic AKI causes (Makris and Spanou, 2016). Treatments for uraemic symptoms, electrolyte imbalance correction and pH issues, and fluid management are all part of the therapy for AKI; however, these treatments do not reverse the progressive irreversible decline in renal function (Fall and Szerlip, 2010). To find a permanent cure for kidney damage, it is imperative to investigate novel, non-traditional treatments for nephropathic patients. Cisplatin, also known as Cis-diamminedichloroplatinum (II), (CDDP), is an antineoplastic medication used to treat a variety of malignancies (Miller et al., 2010). There have been several hypothesized theories on how cisplatin causes nephrotoxicity, such as direct toxicity to renal tubular epithelial cells (McSweeney et al., 2021). A novel and promising therapeutic strategy for organ repair is stem-cell-based treatment (Aly, 2020). Bone marrow contains multipotent cells called MSCs that can develop into adipocytes, chondrocytes, and osteocytes (Ullah et al., 2015). MSCs are known to secrete soluble substances that aid damaged renal cells in healing (Du et al., 2013). According to certain studies, markers of renal cell activation and proliferation, such as immunostaining for PCNA in renal tissue, may be helpful in the diagnosis and/or prognosis of renal disorders (Pramanik et al., 2019). The advancement of renal disease may be linked to the rise in proliferating cell nuclear antigen (PCNA) expressions by renal cells (Pramanik et al., 2019). Moreover, PCNA participates in DNA repair, and its expression promotes the recovery of injured cells as well as mitogenesis and the replacement of depleted epithelial cells that results from it (Choe and Moldovan, 2017). Caspases (cysteine proteases) play a crucial role in the regulation and execution of apoptotic cell death and act upstream of DNA fragmentation (Yuan et al., 2016). A transmembrane adhesion glycoprotein called Cluster of Differentiation 44 (CD44) is essential for cell adhesion, motility, and inflammation (Senbanjo and Chellaiah et al., 2017). For the potential stem cells that may migrate inside the glomerular parietal epithelial cells of the adult kidney, CD44 has been recommended as a marker (Herrera et al., 2007). This study's objective was to determine if bone-marrow-derived stem cells can diminish the acute kidney injury (AKI) that cisplatin causes in Albino rats.

MATERIALS AND METHODS

Animals

Experimental group size: The sample size was calculated using G*Power program with α. Error = 0.05 and power 80% then the calculated sample size was 24 rats.

Rats were purchased from animal house. The experiment was done according to the guidelines of laboratory animals' care. Rats were divided into six in each cage, and were kept under a controlled housing condition with temperature $22^0C \pm 1^0C$, humidity 60 % ± 10 in an adequately ventilated room under a regular 12 h light/12h dark cycle. Free access to food and water ad libitum for 14 days before and during the experiment was provided. Rats weighing 180 to 220 grams were used in the present study.

Grouping: Rats were divided into four groups:

- Group I: the control group, which included 6 rats, received a single injection of 1 ml of normal saline intraperitoneal (I.P).
- Group II: the cisplatin-treated group, which included 6 rats, received a single injection of the drug (6 mg/kg I.P) dissolved in 1 ml of saline.
- Group III (n=6): this group included 6 rats, and received an intraperitoneal injection of 0.5 ml of culture media containing 5 x 106 BMMSCs and a single injection of Cisplatin (6 mg/kg I.P) dissolved in 1 ml of saline.
- Group IV: known as the withdrawal group, it included 6 rats that were not given any further therapy after receiving a cisplatin injection.

Rat sacrifice: The rats were anesthetized with a combination of xylazine (10 mg/kg, CEVA Santé Animale, Naaldwijk, the Netherlands) and ketamine (10 mg/kg, Ketaset®, Eurovet Animal Health, Bladel, the Netherlands) administered via intraperitoneal (i.p.) injections. Blood and bone marrow samples were then obtained.

Sample analysis: Eight days following injection, the control (group I) and cisplatin (group II) rats were sacrificed. One month later, the rats from both the cisplatin and bone-marrow stem-cell

treatment group (group III) and the withdrawal group (group IV) were slaughtered. There were visible kidneys, and following a mid-dorsal plane cut, the kidneys were removed and immediately fixed in 10% neutral formalin. Tap water was used to wash the tissue. In observance of Charmi et al. (2009), the paraffin sections were produced and stained with hematoxylin and eosin stain, and Masson trichrome stain for histological analysis.

Immunohistochemical technique

Paraffin sections of 5-6 µm thickness were de-paraffinized with xylene. Rehydration was performed by placing sections in two changes of 100% alcohol for 10 minutes each, followed by descending grades of alcohol (two changes of 95% alcohol 10 minutes each). For complete rehydration, sections were washed in two changes of distilled water for five minutes each. Tissue specimens were kept in 3% hydrogen peroxide for 10 minutes to block the activity of endogenous peroxidase. Tissue slides were then placed inside the microwave for 10 minutes in 0.01 M citrate buffer (pH 6.0) solution at the temperature of 65°C. Following the microwave, specimens were cooled down at room temperature and then rinsed three times with phosphate-buffered saline (PBS) for 5 minutes. Sections were incubated for 10 minutes with protein block to prevent non-specific reactions. The used primary antibodies were rabbit polyclonal anti-PCNA antibody (cross-reacts with rat) (abx013174, Abbexa, United Kingdom at a dilution of 1:100), a marker of cell proliferation, rabbit polyclonal anti-caspase-3 antibody, (cross-reacts with rat) (A11319, ABclonal, USA at a dilution of 1:100), a marker of cell apoptosis and the monoclonal mouse anti-human antibody, (M7082, Dako, Singapore at a dilution of 1:50) for CD44 which was used to confirm MSCs. These antibodies were kept at 4°C overnight. PCNA, Caspase 3, and CD44 were performed on a DakoCytomation AutoStainer. Following washing three times by PBS for 5 minutes, the slides were incubated with biotinylated secondary antibody for 30 minutes at room temperature. Sections were washed four times in the buffer for five minutes each. Two to three drops of HRP-conjugated streptavidin enzyme label were placed on each slide. The slides were incubated for 45 minutes at room temperature in the humidity chamber. Sections were washed four times in the buffer for five minutes each. Following that, slides were incubated with DAB (Diaminobenzidine) for 3 minutes. Later counterstaining was performed using Harry's hematoxylin. Results were interpreted using a light microscope.

Preparation of Bone-Marrow-Derived MSCs

Bone-marrow-derived MSCs were created by flushing the tibiae and femurs of 6-week-old male white albino rats with Dulbecco's changed Eagle's medium enhanced with 10% fetal bovine serum. The bone marrow was extracted. Nucleated cells were separated, aided by a density gradient, and re-suspended in a full culture medium with 1% penicillin-streptomycin. As a primary culture or after the development of substantial colonies, cells were incubated for 7 days at 37 °C in 5% humidified CO2. After two PBS washes, cultures were trypsinized with 0.25% trypsin in 1 mM EDTA for five minutes at 37 °C once sizable colonies had formed (80–90% confluence). Centrifugation was followed by resuspension of the cells in media containing serum and incubation in 50- cm^2 culture flasks (Falcon). First-passage cultures was the term given to the resulting cultures. Additionally, we identified CD90 and CD34 as MSC surface markers using flow cytometry.

Ethical Approval

The study's goals were reviewed by the staff in charge. The Ethics Committee of the Faculty of Medicine Aswan University revised and approved this work. The protocols for animal experimentation and handling of animals followed the ethical standards laid down in The Helsinki Declaration, the Animal Welfare Act, and the Guide for the Care and the Use of Laboratory Animals.

Image analysis

Aided by a computer, digital picture analysis (Digital morphometric study)/ Slide digitization and imaging:

With a 0.5X photo adaptor attached to an Olympus microscope and a 40X objective, slides were

photographed and saved as TIFF files. Using VideoTest Morphology® software (Russia), which has a dedicated built-in routine for area measurement, cell counting, and stain measurement, the results photos were examined on an Intel® Core I7® based computer.

Five random fields from each of the two slides created for each scenario were examined.

Statistical analysis

Statistical Package for social science (SPSS) version 26.0 was used to tabulate, code, and analyze data to provide descriptive data. Data were expressed as Mean ±SD One way ANOVA (Analysis of variance) was used to compare between over two different groups of numerical (parametric) data followed by post-hoc Tukey. P value <0.05 was considered statistically significant.

RESULTS

Haematoxylin and eosin staining

Haematoxylin and eosin staining of the control group revealed the presence of well-defined cut sections of proximal convoluted tubules lined by cubical cells with basal rounded nuclei and a striated border on their lumen (many microvilli). As for distal convoluted tubules, there were well-defined cut sections lined by low cubical cells. Visceral and parietal layers of Bowman's space were well visualized with patent Bowman's space. All examined glomeruli were normal (Fig. 1A). The cisplatin-treated group (group II) had a dilated tubular system with thinned lining cells of proximal and distal convoluted tubules, cloudy swelling of the tubular system, narrow lumens of proximal convoluted tubules, some darkly stained nuclei, and marked cytoplasmic vacuolation in the cytoplasm of collecting ducts, as well as presence of inflammatory cells in the interstitium (Fig. 1B). When cisplatin and bone marrow stem cells were co- administered (group III), hematoxylin and eosin staining revealed well-defined cut sections of proximal and distal convoluted tubules lined by cubical cells with basal rounded nuclei, their lumen showed striated border (many microvilli), visceral and parietal layers of Bowman's space were well visualized, and all glomeruli had normal appearance (Fig. 1C). After one month of cisplatin administration without further intervention (group IV), hematoxylin and eosin staining showed dilated tubular system with thinned lining cells. Bowman's space was significantly dilated and the interstitium was noticeably infiltrated with inflammatory cells (Fig. 1D).

Masson trichrome staining

In the control group (group I), Masson trichrome staining revealed well-defined cut sections of the tubular system, patent Bowman's space with normal width. All glomeruli had normal configuration, and a small amount of collagen was seen. Within 8 days of cisplatin injection (group II), Masson trichrome staining revealed significantly increased amount of collagen in the interstitium (Fig. 2A). When the rats were co-treated with cisplatin and bone marrow stem cells (group III), the interstitium showed little amount of collagen compared to cisplatin only- injected rats (Fig. 2B). After one month of cisplatin injection with no further administrations (group IV), staining with Masson trichrome showed significantly increased collagen levels in the interstitium (Fig. 2C). There were statistically significant differences between the studied groups in the percent of Masson area with the highest mean values in the cisplatin group and lowest mean values in the control group with in-between significant differences, as the stem cell group showed significantly lower mean values than the cisplatin group but higher than the control group. After 30 days of cisplatin injection, the percentage of Masson area was lower than in the cisplatin group but higher than in the control group or stem cell group, with statistically significant differences (Table 1).

Immunohistochemistry

The lining tubular epithelial cells for the group that received cisplatin on the eighth day showed some positive PCNA immunoreactive nuclei (Fig. 3A), in contrast to the immunodetection of PCNA in the control group, which showed typical renal parenchyma with focal positive PCNA cells. Thirty days after cisplatin administration (withdrawal group), the lining tubular epithelial cells' PCNA staining indicated many positive PCNA im-

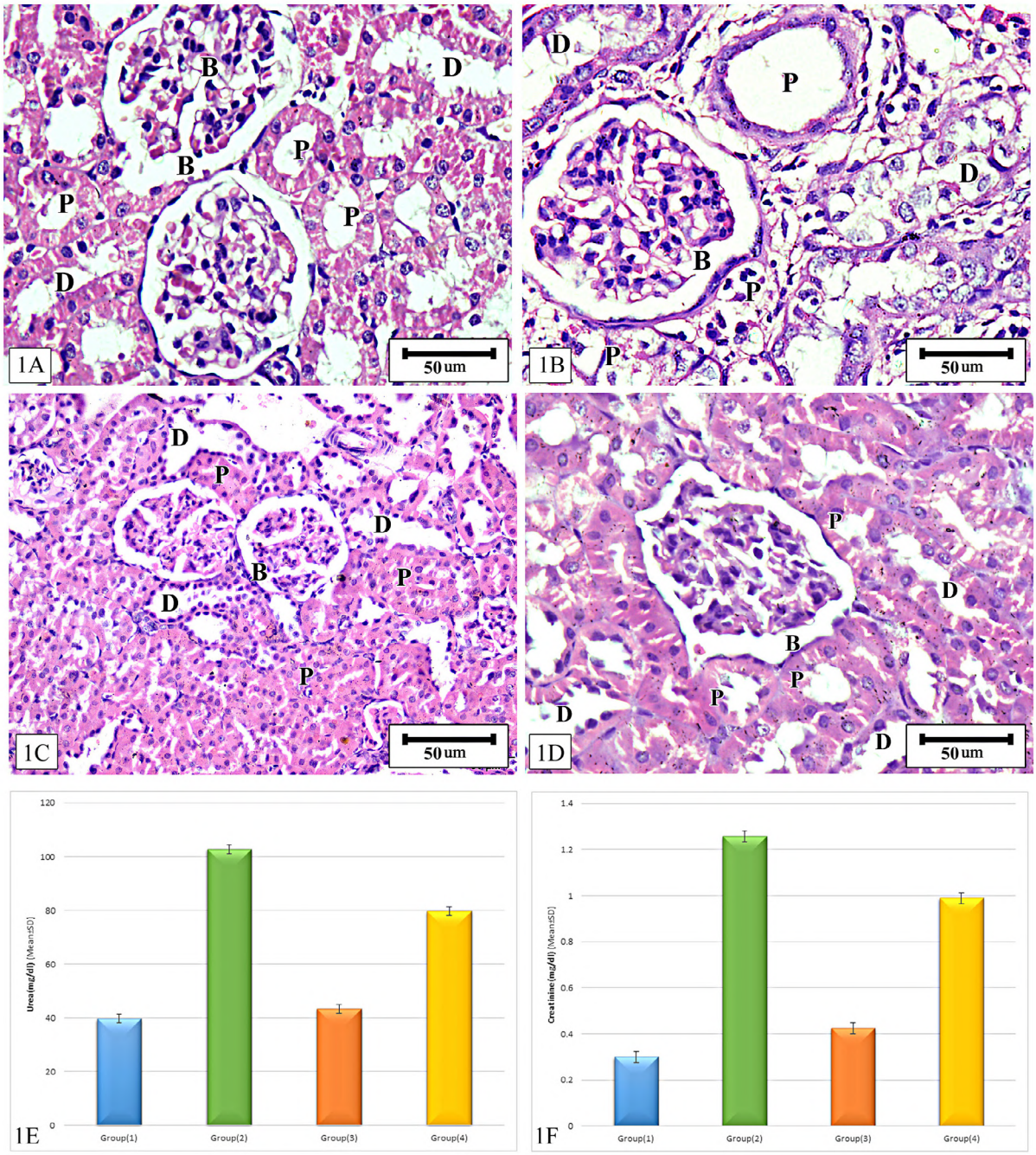

Fig. 1.- Histopathological analysis. The kidney sections were stained with hematoxylin and eosin, and representative images are shown. **(A)** The control group showed normal renal parenchyma. **(B)** The cisplatin-treated group exhibited dilated tubular system with thinning of lining cells of proximal and distal convoluted tubules, cloudy swelling of tubules, a narrow lumen of proximal convoluted tubules, some nuclei are darkly stained, the cytoplasm of collecting ducts showed marked cytoplasmic vacuolation, inflammatory cells in the interstitium. **(C)** The MSC group showed tubules less dilated, well-defined cut sections of proximal and distal convoluted tubules lined by cubical cells with basal rounded nuclei, their lumen shows striated border (many microvilli), well-visualized visceral and parietal layers of Bowman's space. **(D)** The withdrawal group revealed a less dilated tubular system with thinning of lining cells, the interstitium is infiltrated with inflammatory cells. **(E)** Mean±SD of blood urea (mg/dl) levels between the studied groups. **(F)** Mean±SD of serum creatinine (mg/dl) levels between the studied groups. Proximal convoluted tubules (P), Distal convoluted tubules (D), Bowman's space (B). Scale bars (A-D): 50 µm.

munoreactive nuclei (Fig. 3C), suggesting that a self-repair system may be triggered in the injured kidneys. Comparing the stem cell group to other groups, positive PCNA immunoreactive nuclei seemed more common (Fig. 3B). There were statistically significant differences in the number of nuclei stained by PCNA among the studied groups, with the highest mean values among the stem cells group and the lowest mean values among the control group, and with in-between statistical-

ly significant differences as the withdrawal group had higher mean values of nuclei stained by PCNA than cisplatin group (Table 1).

Caspase 3

The kidneys of rats in control groups showed normal renal parenchyma with focal positive cytoplasmic Caspase-3 protease activity by immunodetection of caspase 3. The Caspase-3 protease activity in cisplatin-rat kidneys (group II) increased gradually over time relative to the controls at all periods (Fig. 4A), becoming statistically significant by day 30 (withdrawal group) (Fig. 4C). We discovered, however, that administration of MSCs during cisplatin-induced AKI dramatically reduced kidney caspase-3 levels (Fig. 4B). There were statistically significant differences between the studied groups in the intensity of Caspase-3, with the highest mean values among rats in the withdrawal group and the lowest mean values in the control group, and with in-between statistically significant differences as Caspase-3 intensity was higher among the cisplatin group than stem cell group (Table 1).

Cluster of differentiation (CD44)

Our findings showed that CD44 was found in stem cells of rats near the tubules (Fig. 5C), confirming the localization of the BMMSCs in the tubules in the cortex, and repairing the tubular cells of injured kidneys. Immunodetection of CD44 for the control group revealed some positive CD44 (Fig. 5A). Statistically significant differences were reported between the studied groups regarding the number of CD44 cells, with the highest mean values in the stem cell group (group III) and lowest mean values in the control group, and with significantly higher mean values in the withdrawal group than in the cisplatin-treated group (Table 1).

Table 1. Comparison of Masson trichrome stain surface area, PCNA (No. of nuclei/H.P.F.), Caspase 3 (Intensity), CD44 (No. of stem cells/H.P.F.), Urea (mg/dl) and s. creatinine (mg/dl) between the studied groups.

	Group (I)	Group (II)	Group (III)	Group (IV)	P value
Masson % area	3.07±0.94	15.98±2.25	8.92±1.44	12.45±1.74	<0.001*
Post-hoc		P1=<0.001*	P1=<0.001* P2=<0.001*	P1=<0.001* P2=<0.001* P3=<0.001*	
PCNA (No. of nuclei/HPF)	8.55±2.46	35.97±8.68	162.70±16.86	95.10±11.84	<0.001*
Post-hoc		P1=<0.001*	P1=<0.001* P2=<0.001*	P1=<0.001* P2=<0.001* P3=<0.001*	
Caspase 3 (Intensity)	419.0±56.25	1800.0±240.80	947.40±88.14	2683.0±32.04	<0.001*
Post-hoc		P1=<0.001*	P1=<0.001* P2=<0.001*	P1=<0.001* P2=<0.001* P3=<0.001*	
CD44 (No. of S C/HPF)	6.98±2.18	12.13±3.63	44.70±12.18	30.42±9.48	<0.001*
Post-hoc		P1=0.006*	P1=<0.001* P2=<0.001*	P1=<0.001* P2=<0.001* P3=<0.001*	
Urea(mg/dl)	39.66±1.63	102.80±4.19	43.39±3.65	79.84±5.73	<0.001*
Post-hoc		P1=<0.001*	P1=0.4 P2=<0.001*	P1=<0.001* P2=<0.001* P3=<0.001*	
S.creatinine (mg/dl)	0.300±0.024	1.257±0.080	0.425±0.039	0.990±0.119	<0.001*
Post-hoc		P1=<0.001*	P1=0.04* P2=<0.001*	P1=<0.001* P2=<0.001* P3=<0.001*	

Data expressed as Mean ± SD
SD: standard deviation
P: Probability *:significance <0.05
Test used: One way ANOVA followed by post-hoc Tukey
P1: significance vs Group (1), P2: significance vs Group (2), P3: significance vs Group (3).

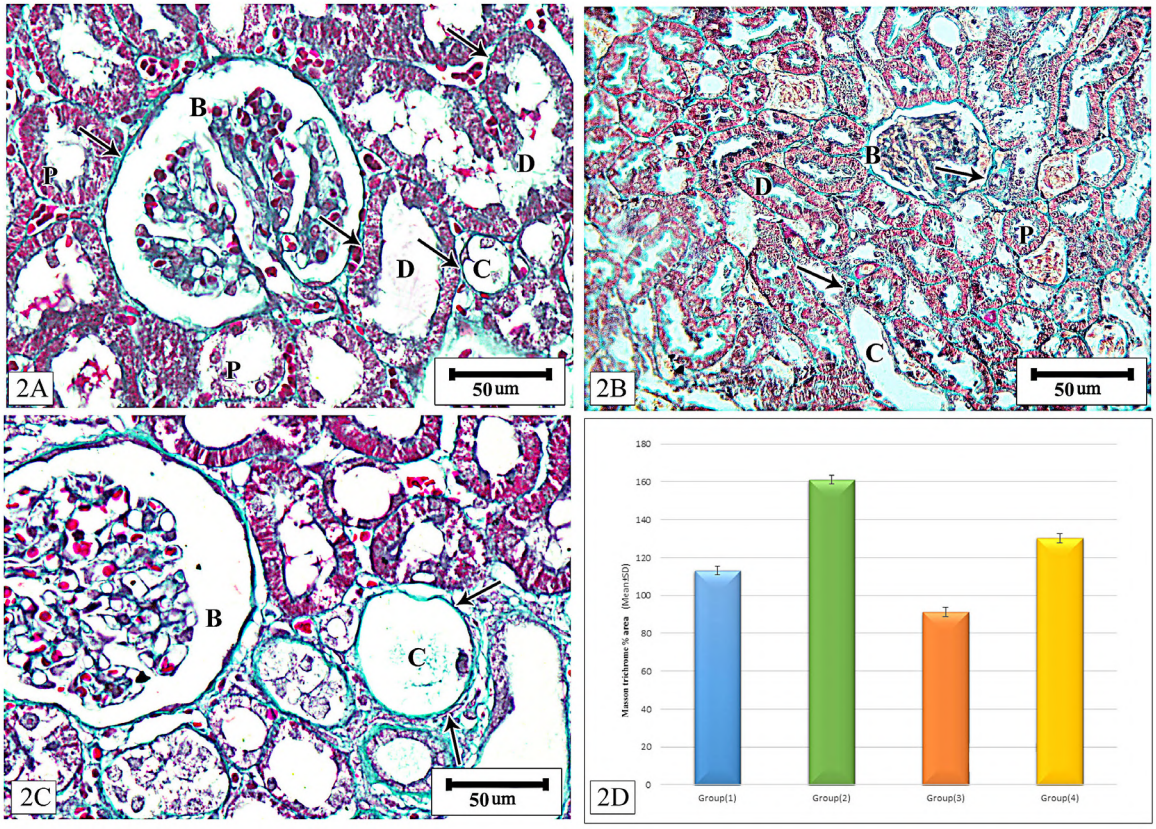

Fig. 2.- (A) The cisplatin-treated group (group II), Masson trichrome staining revealed an increase in the amount of collagen in the interstitium (arrows). **(B)** The cisplatin and bone marrow stem cells had little collagen in the interstitium. (arrows). **(C)** Staining with Masson trichrome for the withdrawal group (group IV) increased collagen levels in the interstitium (arrows). **(D)** Mean±SD of Masson trichrome % area between the studied groups. Proximal convoluted tubules (P), Distal convoluted tubules (D), Bowman's space (B). Collecting tubules (C). Scale bars (A-C): 50 µm.

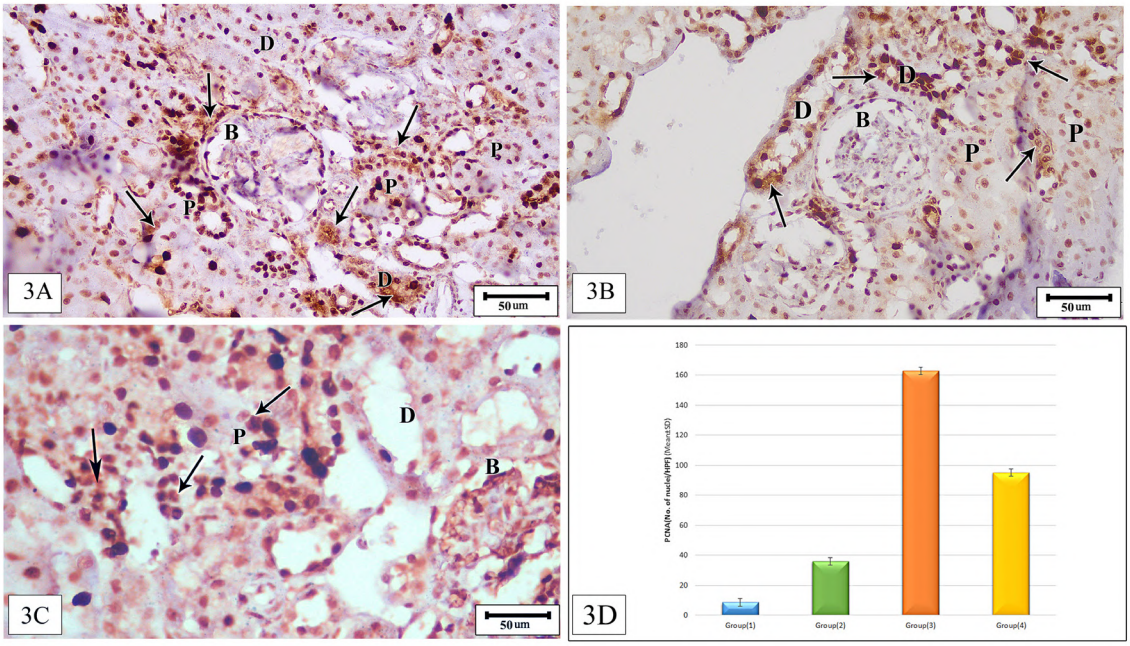

Fig. 3.- Immunodetection of PCNA: **(A)** PCNA staining for the cisplatin-treated group at day eight revealed some PCNA immuno-reactive nuclei in the lining tubular epithelial cells (arrows). **(B)** PCNA staining for the cisplatin and bone marrow stem cells group revealed an apparent increase in positive PCNA immunoreactive nuclei in contrast to other groups (arrows). **(C)** The lining tubular epithelial cells for the withdrawal group displayed many positive PCNA immunoreactive nuclei (arrows). **(D)** Mean ± SD deviation of PCNA (No. of nuclei/HPF) between the groups under study. Proximal convoluted tubules (P), Distal convoluted tubules (D), Bowman's space (B). Scale bars (A-C): 50 µm.

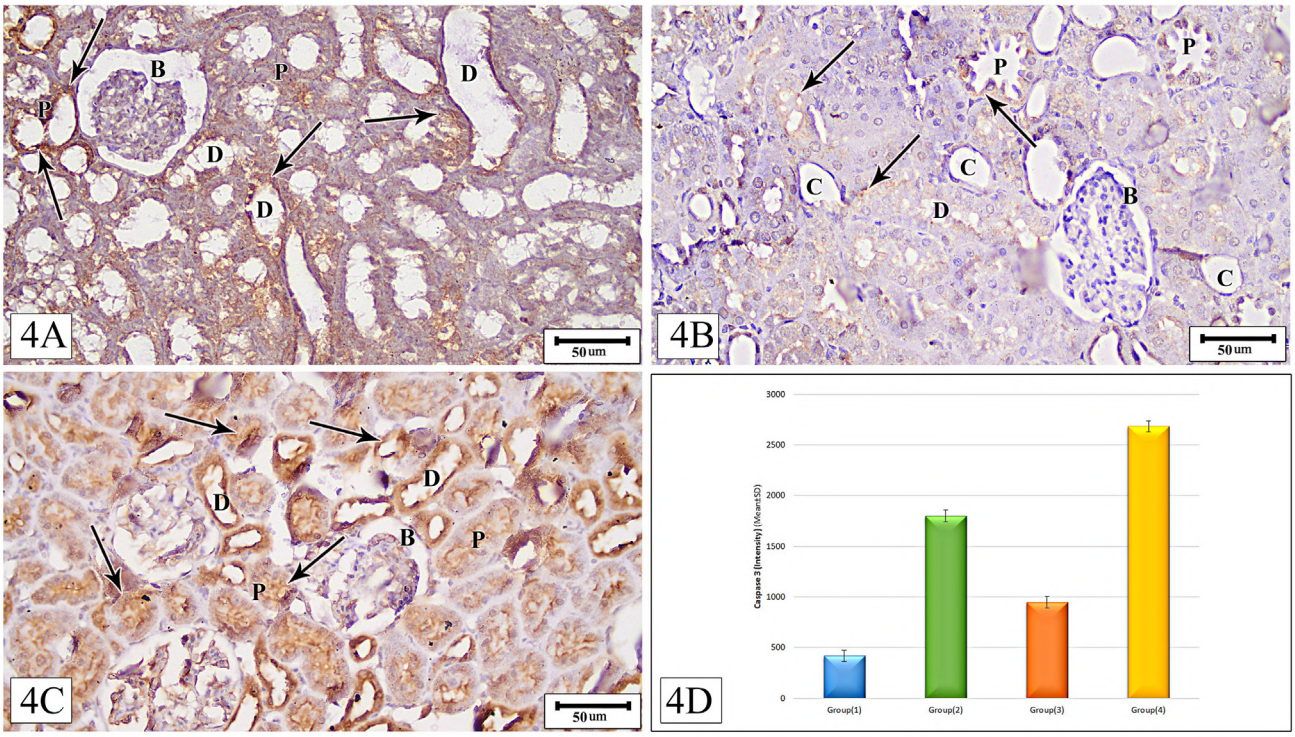

Fig. 4.- Immunodetection of caspase 3: **(A)** a cisplatin-treated rat (group II) showing positive expression of caspase-3 protease activity (arrows). **(B)** cisplatin and bone marrow stem cells group showed decreased expression of caspase-3 protease activity (arrows). **(C)** withdrawal group showed increased expression of caspase-3 protease activity (arrows). **(D)** Mean ± SD of Caspase 3 (Intensity) between the studied groups. Proximal convoluted tubules (P), Distal convoluted tubules (D), Bowman's space (B), Collecting tubules (C). Scale bars (A-C): 50 µm.

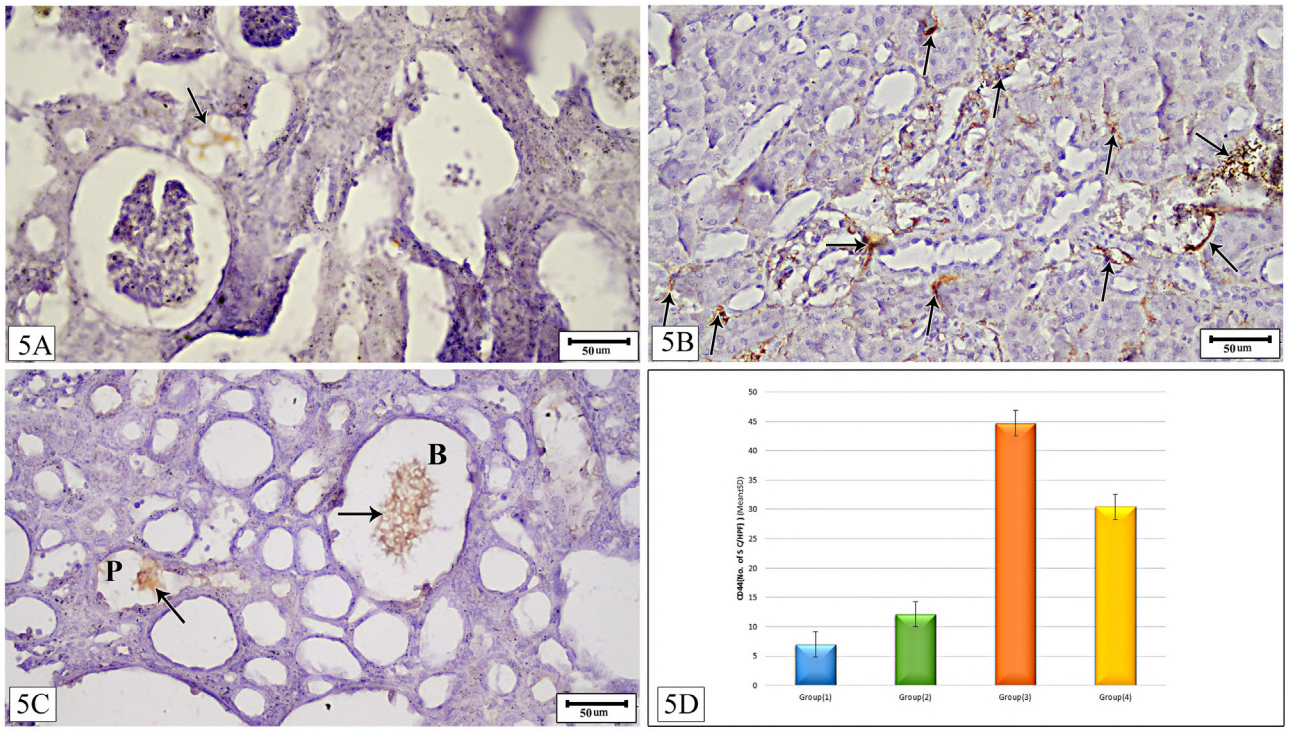

Fig. 5.- Immunodetection of CD44: **(A)** a control rat showing expression of CD44 (arrow). **(B)** cisplatin-treated group showed expression of CD44 (arrows). **(C)** MSCs group showed increased expression of CD44 (arrows). **(D)** Mean±SD of CD44 (Number of stem cells/H.P.F.) between the studied groups. Proximal convoluted tubules (P), Bowman's space (B). Scale bars (A-C): 50 µm.

Biochemical reaction: Our results demonstrated a statistically significant difference in blood urea and serum creatinine levels between the studied groups, with rats receiving cisplatin having the highest mean values and rats in the control group having the lowest mean values, with similar outcomes between the stem cells group and control group (Table 1).

DISCUSSION

Acute kidney injury (AKI) is characterized by an abrupt drop in glomerular filtration rate, the kidney's inability to eliminate waste products such as nitrogen wastes, and disruptions in the homeostasis of fluids and electrolytes. Drug-induced nephrotoxicity, when the predominant site of the lesion is the proximal convoluted tubules of the nephron, is one of the renal or intrinsic causes of AKI (Makris and Spanou, 2016). Recent advances in cell therapy have shown positive therapeutic outcomes for kidney damage (KI). However, more research on the effects of genetic and biomolecular factors is required before contemplating the use of this therapy as a medical alternative. BMSCs and in-vitro-grown mesenchymal stem cells were the main subjects of the majority of these investigations (Zhou et al., 2020). Our findings showed that a statistically significant difference existed between the test groups regarding blood urea and serum creatinine levels as rats received cisplatin had the highest mean values, while rats in the control group had the lowest mean values with comparable results between stem cells group and the control group, demonstrating a striking increase in creatinine in cisplatin-treated group. At day 30 post-AKI, however, a decrement was observed in withdrawal and stem cell groups. Even though there was no statistically significant difference between the control and stem cell groups, this could be explained by the initial restoration of renal function. Similarly to this, Takai et al. (2015) reported that mice given CDDP (30 mg/kg) had blood creatinine concentrations of (1.72 ± 0.37 mg/dl) 24 hours later. According to histopathological examination, CDDP causes acute tubular necrosis (ATN), per the World Health Organization's categorization of tubulointerstitial disorders, which takes into account the etiology, clinical, and histological characteristics.

In our study, inflammatory infiltration and tubular dilatation, both histological features associated with toxic ATN were seen in the cisplatin-treated group. These outcomes are in agreement with Takai et al. (2015), who studied mice kidneys obtained 72 hours after CDDP injection and reported tubular necrosis, dilatation, and hyaline casts. Our findings in the cisplatin-treated and withdrawal groups at days 8 and 30 post-AKI were in line with (Fogo and Kashgarian, 2017), who found a dilated tubular system and inflammatory infiltration.

Our findings corroborated those of Liu et al. (2016), who administered 20 mg/kg of CDDP in mice intraperitoneally and reported severe pathological changes characterized by distortion of the overall kidney morphology, particularly dilation of renal tubules. Mata-Miranda et al. (2019), administered 15 mg/kg of CDDP intraperitoneally in mice and reported similar results 4 days after AKI.

In the MSCs group, the tubules were less dilated and the microarchitecture was better retained. The proximal tubular cells also contained cytoplasmic vacuoles. It is known that cells with reversible lesions can be identified under a microscope by the presence of hazy swelling or hydropic degeneration, which is brought on by ions and fluid homeostasis, and results in an increase of intracellular water. These findings imply that the degenerative process of nephrotoxicity was prevented in the early stages in the treated mice, encouraging a regeneration process that is consistent with Elseweidy et al. (2017), Begum et al. (2019) and Mata-Miranda et al. (2019). It has been demonstrated in several studies using mice models of acute renal failure (ARF) that MSCs can localize in injured kidneys, promoting both morphological and functional recovery (Herrera et al., 2007; Mata-Miranda et al., 2019). It is interesting to note that PCNA participates in DNA repair and its expression promotes the recovery of injured cells as well as mitogenesis and the replacement of damaged epithelial cells (Choe and Moldovan, 2017). Proliferating cell nuclear antigen (PCNA) expression levels rising in renal cells may be related to the progression of renal disease, and markers of renal cell activation and proliferation, such as immunostaining of renal tissue for PCNA. This

may be helpful in the diagnosis and/or prognosis of renal diseases (Pramanik et al., 2019). According to our findings, the tubular epithelial cells on the eighth day after cisplatin therapy revealed a few positive PCNA immunoreactive nuclei. In the tubular epithelial cells (withdrawal group), PCNA staining revealed several positive PCNA immunoreactive nuclei, indicating that a self-repair system may be triggered in the injured kidneys. Comparing the stem cell group to other groups, there was an apparent increase in PCNA immunoreactive nuclei that were positive. These findings showed that MSCs might restore AKI-damaged kidneys by preventing apoptosis and encouraging tubular cell growth. MSCs support regeneration and inhibit apoptosis in cisplatin-induced nephrotoxicity. Caspases (cysteine proteases) function upstream of DNA fragmentation and are crucial for both the execution of apoptotic cell death and its modulation (Yuan et al., 2016). Our findings demonstrated that the Caspase-3 protease activity in treated rat kidneys increased gradually over time relative to the controls at all periods, becoming statistically significant by day 30 (withdrawal group). However, we discovered that the administration of MSCs during cisplatin-induced AKI dramatically reduced kidney Caspase-3 levels. Our findings revealed that the nephroprotective impact of MSCs during cisplatin-associated AKI was partially mediated by Caspase-3 activation. These outcomes are supported by Ying et al. (2020). These results imply that cisplatin nephrotoxicity may be prevented and treated effectively by inhibiting apoptosis as a therapeutic approach. According to our findings, MSCs prevent kidney apoptosis in AKI as seen by decreased Caspase-3 expression. Glomerular parietal epithelial cells in the adult kidney that are CD44-positive have recently been found to be the potential stem cells that might move within the glomerular tuft and tubules and differentiate into new cells (Herrera et al., 2007; Roeder et al., 2018). Glomerular parietal epithelial cells (GPECs), a group of cells lining the interior of Bowman's capsule, have been linked to CD44 expression (Hamatani et al., 2020). It has been demonstrated that GPECs move into the glomerular tuft and develop into mature podocytes (Miesen et al., 2017). Additionally, a subgroup of GEPCs in the adult human kidney's Bowman's capsule exhibit characteristics of multipotent progenitor cells and take part in renal healing (Huang et al., 2021). CD44 may help promote renal regeneration by attracting exogenous MSC to damaged renal tissue (Herrera et al., 2007; Liesveld et al., 2020). Studies suggest that stimulation of the receptor by its ligand stromal-derived factor may play a significant role in the migration of transplanted MSC to areas of injury in the ovary (Ling et al., 2022). Although CXCR4 appears to be expressed at a low level on the surface of MSCs, studies suggest that this receptor may be stimulated by its ligand (Wynn et al., 2004). Our results showed that CD44 was detected in many cells around the tubules in stem cell of rats, which verify the localization of the BMMSCs in the tubules in the cortex, repairing the tubular cells of injured kidneys. These results came in agreement with Herrera et al. (2007), who demonstrated that the localization of exogenous MSC to damaged renal tissue is influenced by the expression of cell surface CD44. Early MSC migration to the kidney, the functional and morphological healing of the injured kidney was hastened by the recruitment of MSCs (Herrera et al., 2007). However, Abd El Zaher et al. (2017), discovered that only a small proportion of bone-marrow-derived cells were integrated into the damaged tubules as epithelial cells. The degree of renal damage following an ischemia/reperfusion event determines whether bone-marrow-derived stem cells engraft into the tubules and take on an epithelial phenotype (Ornellas et al., 2017).

In conclusion, based on our preliminary research, it appeared that MSC reduces CDDP nephrotoxic damage, resulting in functional and histological repair. To suggest new preventative measures in nephrotoxic therapies and increase the possibilities for regenerative medicine, it is vital to research the protective processes and actions of the MSCs.

CONCLUSION

The MSC implant reduces the nephrotoxicity caused by cisplatin, which is reflected in functional and histological recovery. In conclusion, our early research revealed that MSCs reduce the nephrotoxic damage caused by cisplatin, resulting in functional and histological repair.

Recommendation: To suggest novel preventative measures in nephrotoxic therapies and increase the possibilities for regenerative medicine, it is vital to research the protective processes and actions of MSCs.

Data availability statement

This study was carried out in the Histology and Anatomy Departments, Faculty of Medicine, Assiut University. All data generated or analyzed during this study are included in this article, further inquiries can be directed to the corresponding author.

Authorship contribution: Author (A) collected the data and wrote the manuscript; Author (B) did histopathology; All work was under supervision of author (C). All authors contributed equally.

REFERENCES

ABD EL ZAHER F, EL SHAWARBY A, HAMMOUDA G, BAHAA N (2017) Role of mesenchymal stem cells versus their conditioned medium on cisplatin-induced acute kidney injury in albino rat. A histological and immunohistochemical study. *Egypt J Histol*, 40(1): 37-51.

ALY RM (2020) Current state of stem cell-based therapies: an overview. *Stem Cell Invest*, 7: 8.

BEGUM S, AHMED N, MUBARAK M, MATEEN SM, KHALID N, RIZVI SAH (2019) Modulation of renal parenchyma in response to allogeneic adipose-derived mesenchymal stem cells transplantation in acute kidney injury. *Int J Stem Cells*, 12(1): 125-138.

CHARMI A, BAHMANI M, SAJJADI M, KAZEMI R (2009) Morpho-histological study of kidney in farmed juvenile beluga, Huso huso (*Linnaeus*, 1758). *Pakistan J Biol Sci*, 12(1): 11-18.

CHOE KN, MOLDOVAN G-L (2017) Forging ahead through darkness: PCNA, still the principal conductor at the replication fork. *Mol Cell*, 65(3): 380-392.

DU T, ZOU X, CHENG J, WU S, ZHONG L, JU G, ZHU J, LIU G, ZHU Y, XIA S (2013) Human Wharton's jelly-derived mesenchymal stromal cells reduce renal fibrosis through induction of native and foreign hepatocyte growth factor synthesis in injured tubular epithelial cells. *Stem Cell Res Ther*, 4(3): 1-13.

ELSEWEIDY M, ASKAR M, ELSWEFY S, SHAWKY M (2018) Nephrotoxicity induced by cisplatin intake in experimental rats and therapeutic approach of using mesenchymal stem cells and spironolactone. *Appl Biochem Biotechnol*, 184(4): 1390-1403.

FALL P, SZERLIP HM (2010) Continuous renal replacement therapy: cause and treatment of electrolyte complications. *Seminars in dialysis*, 23(6): 581-585.

FOGO AB, KASHGARIAN M (2017) Diagnostic Atlas of Renal Pathology. 3rd ed. Philadelphia, Elsevier.

HAMATANI H, ENG DG, HIROMURA K, PIPPIN JW, SHANKLAND SJ (2020) CD44 impacts glomerular parietal epithelial cell changes in the aged mouse kidney. *Physiol Rep*, 8(12): e14487.

HERRERA M, BUSSOLATI B, BRUNO S, MORANDO L, MAURIELLO-ROMANAZZI G, SANAVIO F, STAMENKOVIC I, BIANCONE L, CAMUSSI G (2007) Exogenous mesenchymal stem cells localize to the kidney by means of CD44 following acute tubular injury. *Kidney Int*, 72(4): 430-441.

HUANG J, KONG Y, XIE C, ZHOU L (2021) Stem/progenitor cell in kidney: characteristics, homing, coordination, and maintenance. *Stem Cell Res Ther*, 12(1): 1-18.

LIESVELD JL, SHARMA N, ALJITAWI OS (2020) Stem cell homing: From physiology to therapeutics. *Stem Cells*, 38(10): 1241-1253.

LING L, HOU J, LIU D, TANG D, ZHANG Y, ZENG Q, PAN H, FAN L (2022) Important role of the SDF-1/CXCR4 axis in the homing of systemically transplanted human amnion-derived mesenchymal stem cells (hAD-MSCs) to ovaries in rats with chemotherapy-induced premature ovarian insufficiency (POI). *Stem Cell Res Ther*, 13(1): 1-19.

LIU M, JIA Z, SUN Y, ZHANG A, YANG T (2016) A H2S donor GYY4137 exacerbates cisplatin-induced nephrotoxicity in mice. *Mediators Inflamm*, 2016: 8145785.

MAKRIS K, SPANOU L (2016) Acute kidney injury: definition, pathophysiology and clinical phenotypes. *Clin Biochem Rev*, 37(2): 85-98.

MATA-MIRANDA MM, BERNAL-BARQUERO CE, MARTINEZ-CUAZITL A, GUERRERO-ROBLES CI, SANCHEZ-MONROY V, ROJAS-LOPEZ M, VAZQUEZ-ZAPIEN GJ (2019) Nephroprotective effect of embryonic stem cells reducing lipid peroxidation in kidney injury induced by cisplatin. *Oxid Med Cell Longev*, 2019: 5420624.

MCSWEENEY KR, GADANEC LK, QARADAKHI T, ALI BA, ZULLI A, APOSTOLOPOULOS V (2021) Mechanisms of cisplatin-induced acute kidney injury: Pathological mechanisms, pharmacological interventions, and genetic mitigations. *Cancers (Basel)*, 13(7): 1572.

MIESEN L, STEENBERGEN E, SMEETS B (2017) Parietal cells - new perspectives in glomerular disease. *Cell Tissue Res*, 369(1): 237-244.

MILLER RP, TADAGAVADI RK, RAMESH G, REEVES W (2010) Mechanisms of cisplatin nephrotoxicity. *Toxins*, 2(11): 2490-2518.

ORNELLASA FM, ORNELLASA DS, MARTINIA SV, CASTIGLIONE RC, VENTURA GM, ROCCO PR, GUTFILEN B, DE SOUZA SA, TAKIYA CM, MORALES MM (2017) Bone marrow–derived mononuclear cell therapy accelerates renal ischemia-reperfusion injury recovery by apoptotic related molecules. *Cell Physiol Biochem*, 41(5): 1736-1752.

PRAMANIK S, SUR S, BANKURA B, PANDA CK, PAL D (2019) Expression of proliferating cell nuclear antigen and Ki-67 in renal cell carcinoma in eastern Indian patients. *Int Surg J*, 6(10): 3687-3693.

ROEDER SS, BARNES TJ, LEE JS, KATO I, ENG DG, KAVERINA NV, SUNSERI MW, DANIEL C, AMANN K, PIPPIN JW, SHANKLAND SJ (2017) Activated ERK1/2 increases CD44 in glomerular parietal epithelial cells leading to matrix expansion. *Kidney Int*, 91(4): 896-913.

SENBANJO LT, CHELLAIAH MA (2017) CD44: A multifunctional cell surface adhesion receptor is a regulator of progression and metastasis of cancer cells. *Front Cell Dev Biol*, (5): 18.

TAKAI N, ABE K, TONOMURA M, IMAMOTO N, FUKUMOTO K, ITO M, MOMOSAKI S, FUJISAWA K, MORIMOTO K, TAKASU N, INOUE O (2015) Imaging of reactive oxygen species using [3H] hydromethidine in mice with cisplatin-induced nephrotoxicity. *EJNMMI Research*, 5(1): 1-8.

ULLAH I, SUBBARAO RB, RHO GJ (2015) Human mesenchymal stem cells-current trends and future prospective. *Biosci Rep*, 35(2): e00191.

WYNN RF, HART CA, CORRADI-PERINI C, EVANS CA, WRAITH JE, FAIRBAIRN LJ, BELLANTUONO I (2004) A small proportion of mesenchymal stem cells strongly expresses functionally active CXCR4 receptor capable of promoting migration to bone marrow. *Blood*, 104(9): 2643-2645.

YING J, WU J, ZHANG Y, QIAN X, YANG Q, CHEN Y, ZHU H (2020) Ligustrazine suppresses renal NMDAR1 and caspase-3 expressions in a mouse model of sepsis-associated acute kidney injury. *Mol Cell Biochem*, 464(1): 73-81.

YUAN J, NAJAFOV A, PY BF (2016) Roles of caspases in necrotic cell death. *Cell*, 167(7): 1693-1704.

ZHOU S, QIAO YM, LIU YG, LIU D, HU JM, LIAO J, LI M, GUO Y, FAN LP, LI LY, ZHAO M (2020) Bone marrow derived mesenchymal stem cells pretreated with erythropoietin accelerate the repair of acute kidney injury. *Cell Biosci*, 10(1): 130.

Gross morpho-biometry, histometry and immunohistochemical investigations of pituitary gland in the juvenile and adult male African giant rats (*Cricetomys gambianus*)

Taidinda T. Gilbert[1], Funmilayo E. Olopade[2], Olanrewaju I. Fatola[1], Rachael O. Folarin[3], Adedunsola A. Obasa[1], James O. Olopade[1]

[1] Department of Veterinary Anatomy, Faculty of Veterinary Medicine, University of Ibadan, Ibadan, Nigeria

[2] Department of Anatomy, College of Medicine, University of Ibadan, Ibadan, Nigeria

[3] Department of Biomedical Laboratory Science, College of Medicine, University of Ibadan, Nigeria

SUMMARY

This work was designed to investigate the morphometry and immunohistochemical features of pituitary glands in the African Giant Rats (AGR). Adult and juvenile AGR were sacrificed and their brains harvested, and the pituitary glands were carefully dissected. The weight, length and width of brains and pituitary glands were subsequently measured. Sections were prepared and stained using Haematoxylin and Eosin (H&E), Cresyl-violet and periodic-acid-Schiff (PAS) for histological analysis. Immunohistochemical analysis was carried out with Glial-Fibrillary-Acidic-Protein (GFAP) and Ionized-Calcium-Binding-Adapter-Molecule 1 (Iba1). Grossly, the AGR pituitary gland is a somehow laterally extended, saddle-shaped organ that is dorso-ventrally flattened. The gray-coloured adenohypophysis (anterior-pituitary lobe) was bigger in size than the whitish neurohypophysis (posterior-pituitary lobe) on physical examination. Histometrically, the adenohypophyseal length was noticeably greater than that of neurohypophysis in both juvenile and adult. Similarly, the adenohypophyseal and neurohypophyseal width in adult were found to be more than that of juvenile. Also, the histological staining of the neurohypophysis and adenohypophysis were distinct. In the neurohypophysis, fibrous and protoplasmic pituicytes were observed among fibres and Herring-bodies. Chromophils and chromophobes were identified in the adenohypophysis and melanotrophs in the intermediate lobe. Immunohistochemistry showed pituicytes in the neurohypophysis, which was positive with GFAP-antibody. With Iba1-antibody, the neurohypophysis expressed a stronger positive immunolabelling to microglia as compared to macrophages in the adenohypophysis. In conclusion, the gross and microscopic characteristics of pituitary glands of the AGR are found to be similar to other rodents and mammals. We recommend further study to compare morphometrical parameters between male and females of this model.

Corresponding author:
Taidinda Tashara Gilbert. Department of Veterinary Anatomy, Faculty of Veterinary Medicine, University of Ibadan, Nigeria. Phone: +2347068459438. E-mail: gilberttashara@gmail.com

Submitted: July 13, 2023. **Accepted:** September 25, 2023

https://doi.org/10.52083/YCQN8605

Key words: African giant rat – Pituitary gland – Gross morpho-biometry – Histometry – Immunohistochemistry

INTRODUCTION

The African Giant Rats (AGRs) (Cricetomys gambianus) are nocturnal rodents, feeding omnivorously both on vegetation and invertebrates. They inhabit a variety of habitats ranging from arid to temperate regions, but need some form of shelter to survive (Ajayi, 1974; Nzalak et al., 2005). The size of AGR makes them suitable for broader range of experiments and studies and they can live longer in captivity, thereby providing an extended time window for longitudinal studies. The most significant and interesting attribute of AGR in research is their exceptional sense of smell. They have a highly developed olfactory system, which enables them to detect and distinguish a wide range of scents (Olude et al., 2014; Freeman et al., 2020). This advantage has been utilized in detecting landmines and tuberculosis in field studies. The AGR has been proposed as an adaptable native research model due to its unique neuro-behavioural attributes, and thus the need to establish baseline information on its nervous system (Mustapha et al., 2019).

The pituitary gland is a hypothalamic structure of the brain and serves as a master gland that controls almost all the activities of other glands in the body. The pituitary gland is divided into adenohypophysis (anterior-pituitary lobe) and neurohypophysis (posterior-pituitary lobe); it is situated within the hypophyseal fossa of the sphenoid bone called sella turcica, and it is covered by diaphragma sellae. Studies have claimed the variation in size of the pituitary gland associated with age, gender and pathological conditions (Lamichhane et al., 2015). Alteration in the shape and size of the pituitary gland can result in abnormal nervous processes and hormonal behaviours (Emerald, 2016). There are many reported anatomical investigations on the pituitary glands of mammals, including the greater cane rat (Gilbert et al., 2020), the rabbit (Vionna et al., 2020), the guinea pig (Amat, 1970; Luay, 2016), the rat (Mixner and Turner, 1942; Montemurro, 1964; Popoola and Sakpa, 2018), the mink (Weman and Nobin, 1973; Weman, 1974; Cardin et al., 2000), the hedgehog (Treier et al., 2001; Botermann et al., 2021) and the viscacha (Acosta and Mohamed, 2009); however, the pituitary gland of AGRs has been rarely investigated in detail, especially anatomical investigation. AGR being an indigenous rodent, it will be then interesting to look at the pituitary gland and generate baseline anatomical data, since there is an increasing demand for indigenous animal models for scientific research. The measurements of selected parameters of the brain excluding pituitary gland of the AGR have been documented by Olude et al. (2016) and Nzalak et al. (2005). The present work, therefore, was designed to investigate the gross biometric and histometric features in both adult and juvenile male AGR, and to determine the basic cellular architecture and immunohistochemical expression of the pituitary glands in the AGR in order to provide basic research data, which will add to the understanding of the biology in this unique African rodent.

MATERIALS AND METHODS

Ethics

The animal experiment was approved by Animal Care Committee of National Veterinary Research Institute, Vom (NVRI/AEC/03/11622).

Animals

A total of 15 male AGRs were used for this study. The rats were divided based on age gap into two groups of nine (9) adults and six (6) juveniles. Age groups were estimated in accordance to Ajayi (1974) (Juveniles: >70g but <500g; Adult: >500g). They were sourced from Oranyan Market and University of Ibadan in Ibadan metropolis, Oyo State, Nigeria. They were transported live in cages to the experimental animal house, Neuroscience Unit, Department of Veterinary Anatomy, Faculty of Veterinary Medicine, University of Ibadan, Ibadan, Nigeria. The rats were allowed to acclimatize for a few hours prior to sacrifice. At the time of sacrifice, the body weight of each rodent was obtained with a digital electronic balance (Zhongshan Camry Electronic Co. Ltd, China).

Extraction of Brain and Pituitary Gland

The rats were sacrificed after the protocol described by Olopade et al. (2011). They were deeply anesthetized intraperitoneally (ketamine 100 mg/kg body weight and xylazine 10 mg/kg body weight) and perfused transcardially with normal saline followed by 10% neutral buffered formalin (NBF). The brains were subsequently harvested from the skull, and the pituitary glands were carefully dissected. Both the brains and pituitary glands were examined *in situ* to rule out any pathology before removal for gross morphological investigation. Gross biometry of the pituitary gland was measured and described according to the method of Ju et al. (2010) and Rahman et al. (2011). The pituitary glands were trimmed of meninges, and their weight was measured using Electronic Balance FA2004B (Shanghai York Instrument Co. Ltd., China). The length (rostro-caudal distance) and width (distance between the lateral edges) of the glands were obtained using stainless steel Electronic Digital Caliper K-319 (Kales Tool Industry & Trade Co., Ltd., China), as indicated in Fig. 1. The recorded measurements were used to calculate Organo-somatic Index (OSI) of the brain and pituitary gland, by dividing organ weight with body weight multiplied by 100 (weight of organ (g)/ weight of body (kg) x 100), as described by Radhiah and Azhar (2020).

Tissue Processing for Light Microscopic Study

The pituitary gland tissues were processed for routine paraffin embedding. Five microns-thick sections were cut from the paraffinized tissue blocks unto glass slides, using a microtome (Microm GmbH, D-6900 Heidelberg, West Germany). The sections were deparaffinized and stained with Haematoxylin and Eosin (H&E) and Cresyl violet for general histological examination (Gilbert et al., 2022). Tissue sections were subsequently stained with Periodic acid-Schiff (PAS) special stain, as described by Kondoh et al. (2017). The stained tissue sections were visualized using a light microscope (Leica Microsystems, Wetzlar, Germany) equipped with a CEFC Industrial digital camera. Histometry was carried out using the Motic® Images Plus 2.0 ML software (Motic Asia, Kowloon, Hong Kong).

Table 1. The mean body, brain and pituitary gland weights.

Parameters / Group	Number of animals	Mean Body Weight (g) Mean ± SEM	Mean Absolute Brain Weight (g) Mean ± SEM	Mean Absolute Pituitary Weight (g) Mean ± SEM
Adult	9	984.8 ± 34.09	5.6 ± 0.18	0.019 ± 0.0021
Juvenile	6	493.7 ± 23.41	4.42 ± 0.11	0.012 ± 0.0054

SEM = standard error of mean; g = grams; Normality test (Shapiro-Wilk test) = body (adult: P<value 0.356; juvenile P<value 0.093), brain (adult: P<value 0.612; juvenile P<value 0.540), pituitary gland (adult: P<value 0.149; juvenile P<value 0.082)

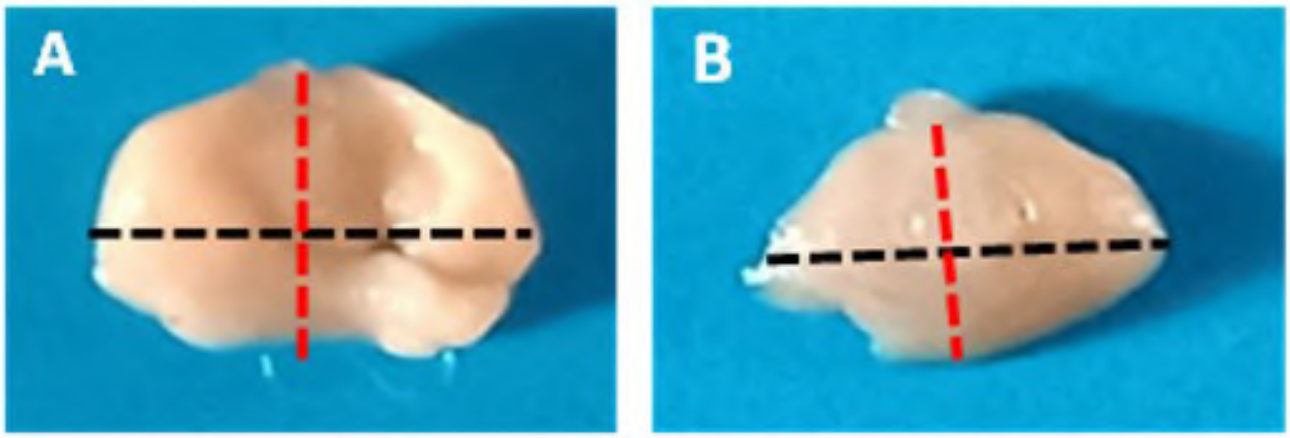

Fig. 1.- The pituitary gland of AGR. **A:** Showing the rostro-caudal (red dot-lines) and transverse distance (black dot-lines) from the dorsal view in adult AGR. **B:** Showing the rostro-caudal (red dot- lines) and transverse distance (black dot-lines) from the dorsal view in juvenile AGR.

Immunohistochemistry

The tissues were prepared for immunohistochemical examination based on the protocol described by Gilbert et al. (2020). Briefly, tissue sections of 5 µm thick paraffinized pituitary tissues were mounted on well-labelled charged glass slides and baked in an oven (60°C) for 90 minutes in order to melt the wax. The paraffinized tissue sections were subsequently deparaffinized in two changes of xylene, and then hydrated in descending concentration of alcohol to water. Retrieval of antigen was done with 10 mM citrate buffer (pH of 6.0) in order to unmask the hidden antigenic site. Tissue sections were treated with 30% H_2O_2/methanol so as to stop endogenous peroxidase activities and prevent non-specific binding by antibody. 2% PBS milk was used for blocking via incubation for 60 minutes and tissue sections were subsequently immune-labelled with these antibodies: rabbit anti-Iba1 antibody (dilution 1:1000, Wako Pure Chemical Industries Ltd., Japan) for microglial cells and rabbit anti-GFAP antibody (1:1000; Dako, Denmark), to visualize pituicytes or astrocytic-like cells. The primary antibodies were diluted in 1% PBS milk and 0.1% Triton X detergent and incubated overnight at 4°C. Secondary antibodies (dilution 1:200, Abcam Inc, USA) were subsequently added and the end product of entire reaction was improved with a chromogen, 3,3'-diaminobenzidine (DAB) (1:25 dilution, Vector Laboratories, USA) for 5 minutes. After dehydration of tissue sections in graded solutions of alcohol concentration, double changes of xylene were further used for 5 minutes each to remove the alcohol. Lastly, the tissue sections were mounted wet in permount, cover slipped and allowed to dry before microscopy (Leica Microsystems, Wetzlar, Germany).

Statistical analysis

Data are expressed as Means ± SEM and the differences among groups were considered significant at p-value < 0.05. Data were analysed using Excel software. Normal distribution of the data was confirmed with normality test (Shapiro-Wilk test), then unpaired t-tests and descriptive statistics were carried out using GraphPad Prism version 9.0.0 (GraphPad Software, San Diego).

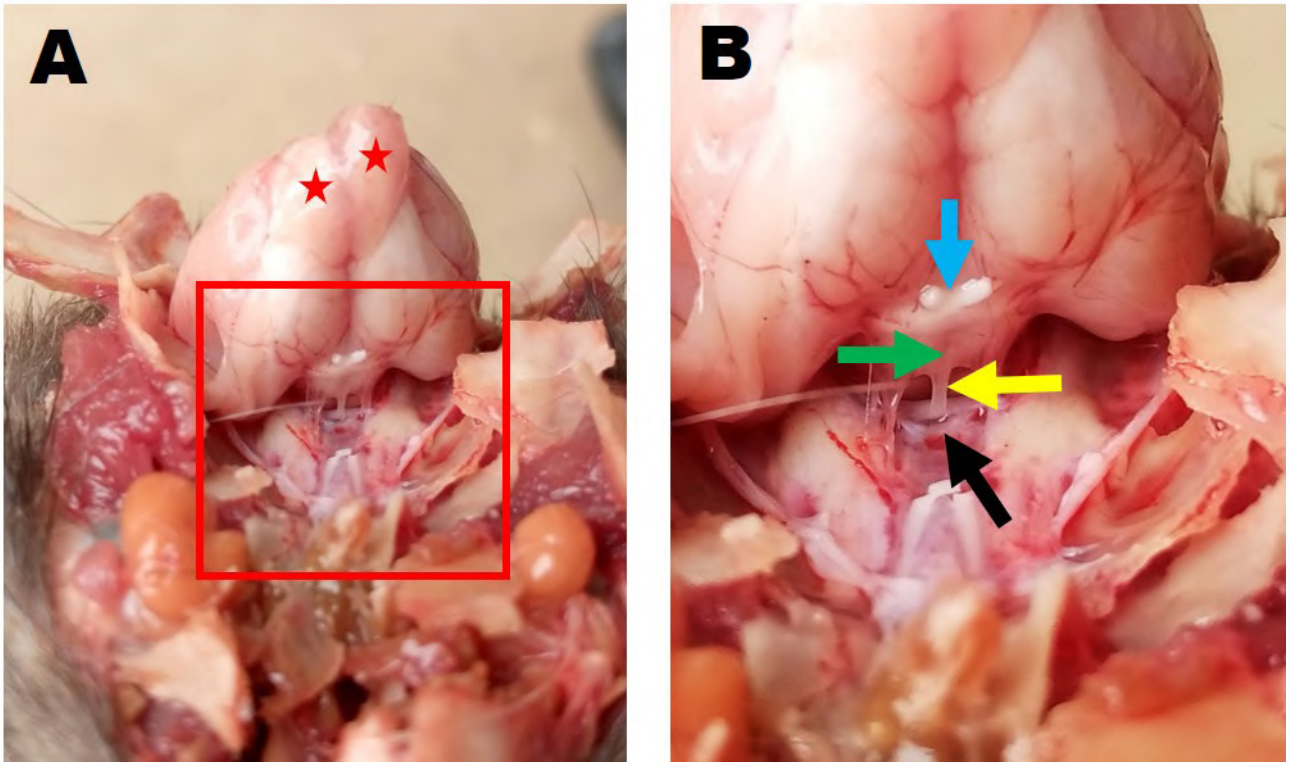

Fig. 2.- Photograph of head of the AGR showing the connection of pituitary gland to the base of brain. Lower (**A**) and higher (**B**) magnification of the head showing the pituitary gland (black arrow) still connected to the median eminence (green arrow) through the pituitary stalk (yellow arrow). Blue arrow = optic chiasma, red stars = olfactory bulb.

RESULTS

Gross morphological examination of pituitary gland

In the AGR, the pituitary stalk or infundibulum attaches dorsally to the median eminence (*tuber cinereum*) and ventrally to the pituitary gland (Fig. 2). The pituitary gland of the AGR was also observed to be located in the hypophyseal fossa called *sella turcica* (Fig. 3A and 3B), which appeared as a very shallow depression on the sphenoid bone of the skull (Fig. 3C and 3D).

The pituitary gland in the AGR was somehow laterally extended with saddle-shaped and dorso-ventrally flattened (Fig. 4), and was enclosed with meninges which were serving as its capsule. The meninges were attached to it except at the upper part, where the pituitary stalk comes out and connects to the brain through median eminence of the hypothalamus (Fig. 2). The anterior pituitary (adenohypophysis) and posterior pituitary (neurohypophysis) lobes were distinguishable on physical examination (Fig. 4).

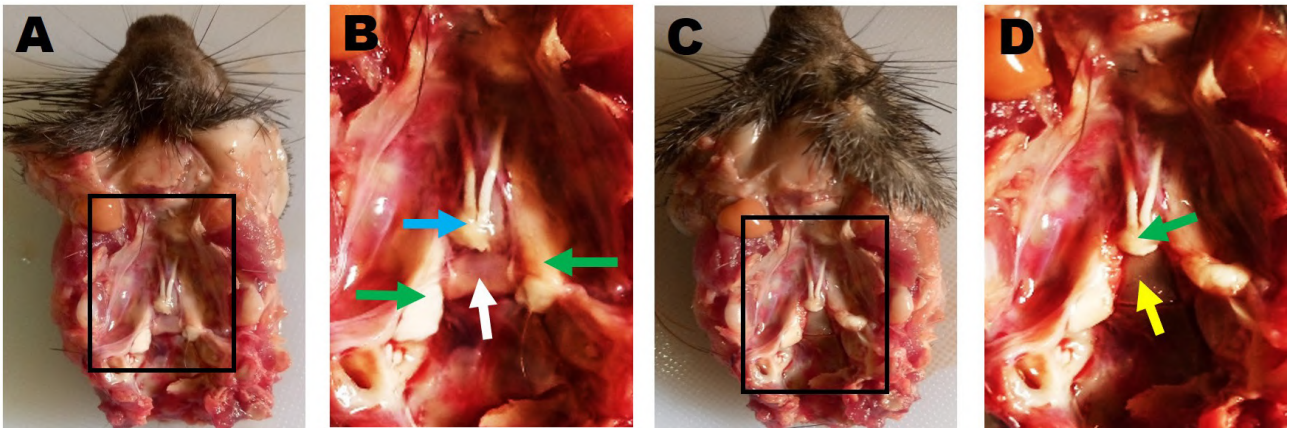

Fig. 3.- Photograph of head of AGR showing pituitary gland and other related structures after careful removal of the brain. **A, B:** The pituitary gland (white arrow) lying in the *sella turcica* on the basisphenoid bone. The optic nerve with small remnant of optic chiasm (blue arrow) is seen located rostral to the pituitary gland while the trigeminal nerve roots (green arrows) located at the lateral boundaries. **C, D:** The basisphenoid bone showing the *sella turcica* (yellow arrow) after the pituitary gland was removed.

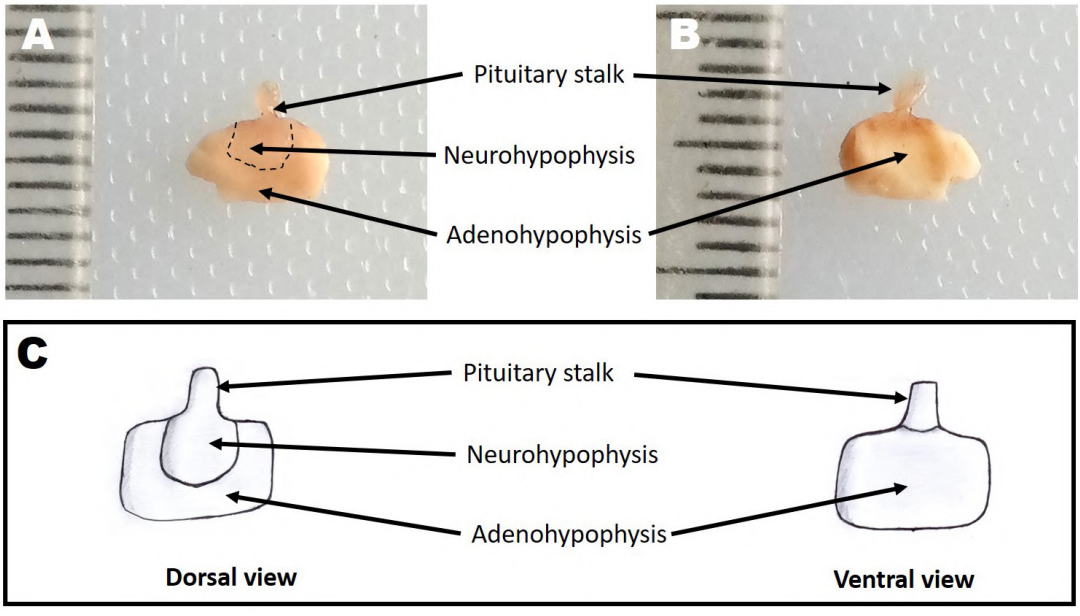

Fig. 4.- The photographs of AGR pituitary glands showing the infundibular stalk, adenohypophysis and neurohypophysis. **A:** Dorsal view of AGR pituitary gland. **B:** Ventral view of AGR pituitary gland. **C:** Schematic showing both the dorsal and ventral view of the AGR pituitary gland.

Grossly, the adenohypophysis was observed to be gray in colour and was greater in size than the neurohypophysis (Fig. 5), while the neurohypophysis was seen to be whitish in colour. There were no obvious differences on gross examination between the adult and juvenile groups.

The body, brain and pituitary gland weights

The mean weights of the body, brain and pituitary gland of the adult group in AGRs were 984.8 ± 34.09 g, 5.6 ± 0.18 g and 0.019 ± 0.0021 g respectively. In the juvenile, the mean weights of the body, brain and pituitary glands were 493.7 ± 23.41 g, 4.42 ± 0.11 g and 0.012 ± 0.0054 g respectively. The body weights were significantly ($P > 0.05$) higher in adult AGR (984.8 ± 34.09 g) when compared to juvenile (493.7 ± 23.41 g). The weights of brain were significantly ($P > 0.05$) higher in adult AGR (5.6 ± 0.18 g) when compared to juvenile (4.42 ± 0.11 g). The weights of pituitary glands were also significantly ($P > 0.05$) higher in adult AGR (0.019 ± 0.0021 g) when compared to juvenile (0.012 ± 0.0054 g).

The mean relative weight of the pituitary gland in adult AGR (0.0019 ± 0.0016 g) and young AGR (0.0023 ± 0.0022 g) is indistinguishable.

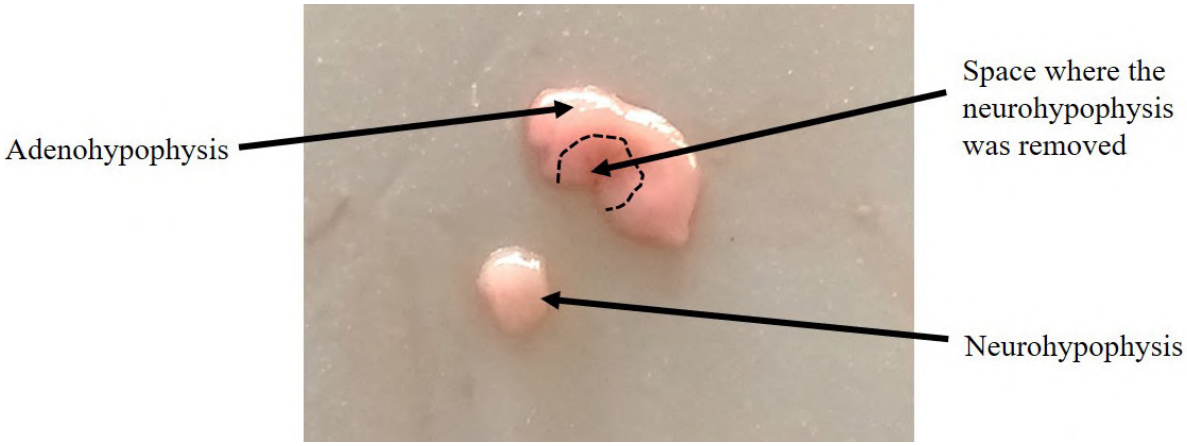

Fig. 5.- A photograph showing the adenohypophysis and neurohypophysis of the pituitary gland on physical examination.

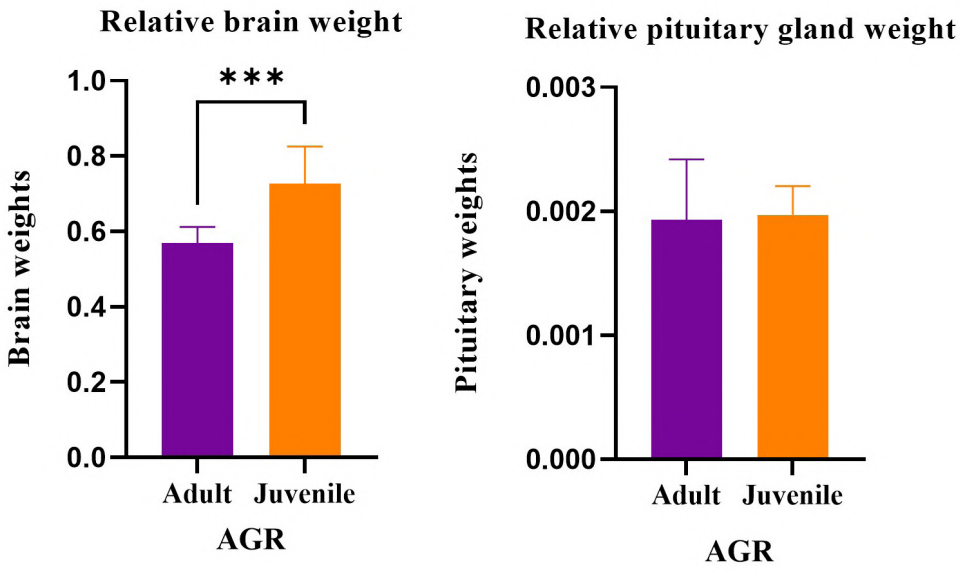

Fig. 6.- Bar diagrams showing the relative brain weight (A) and relative pituitary weight (B) of juvenile and adult African giant rat (AGR). Plots are mean ± SEM of relative organ weight. Student's t-test, ***$P < 0.001$. Statistical significance is indicated for adult and juvenile AGR brain weight data. No statistical difference for relative pituitary weight ($P<0.05$). Normality test (Shapiro-Wilk test) = relative brain weight (adult: P<value 0.903; juvenile P<value 0.171), relative pituitary weight (adult: P<value 0.317; juvenile P<value 0.899).

Table 2. Measurements of the length and width of the pituitary gland in AGR.

Parameters Group	Number of animals	Mean Pituitary Length (mm) Mean ± SEM	Mean Pituitary Width (mm) Mean ± SEM
Adult	9	4.105 ± 0.005	5.910 ± 0.006
Juvenile	6	3.515 ± 0.005	4.815 ± 0.005

SEM = standard error of mean; mm = millimeters; Normality test (Shapiro-Wilk test) = adult (length: P<value 0.954; width P<value 0.496), juvenile (length: P<value 0.0.6708; width P<value 0.067).

With increasing body weight, there was contemporaneous increase in the weight of the pituitary gland. The mean relative weight of the brain in the adult AGR (0.57 ± 0.014 g) was significantly lower than the mean relative brain weight in young AGR (0.73 ± 0.040 g). This implies that, as the body size is increasing, there is exponential increase in brain weight of young AGR. On the other hand, it appears that in the adult AGR the brain weight did not increase at the same rate as the body size was increasing. This was observed when the mean relative brain weight of adult AGR was compared to that of young AGR (Fig. 6). The normal distribution of the data was confirmed by employing normality test (Shapiro-Wilk test).

The length and width of the pituitary gland

The pituitary glands were generally wider (distance from their lateral edges) than they were longer (rostro-caudal distance). Grossly, the mean length of pituitary glands showed statistically significant (P > 0.05) variation between both the adult (4.105 ± 0.005 mm) and juvenile (3.515 ± 0.005 mm) groups. The length is higher in the adult when compared to juvenile. The width of the pituitary gland was also significantly (P < 0.05) higher in the adult (5.910 ± 0.006 mm) when compared to the juvenile group (4.815 ± 0.005 mm) (Table 2).

Histological examinations of the pituitary gland

The pituitary gland of the AGR consists of anterior lobe or adenohypophysis (*pars tuberalis, pars distalis*) and posterior lobe or neurohypophysis (*pars nervosa*), which are separated by the intermediate lobe (*pars intermedia adenohypophysis*) and hypophyseal cleft (Fig. 7A). The *pars tuberalis adenohypophysis* in AGR was identified together with pituitary

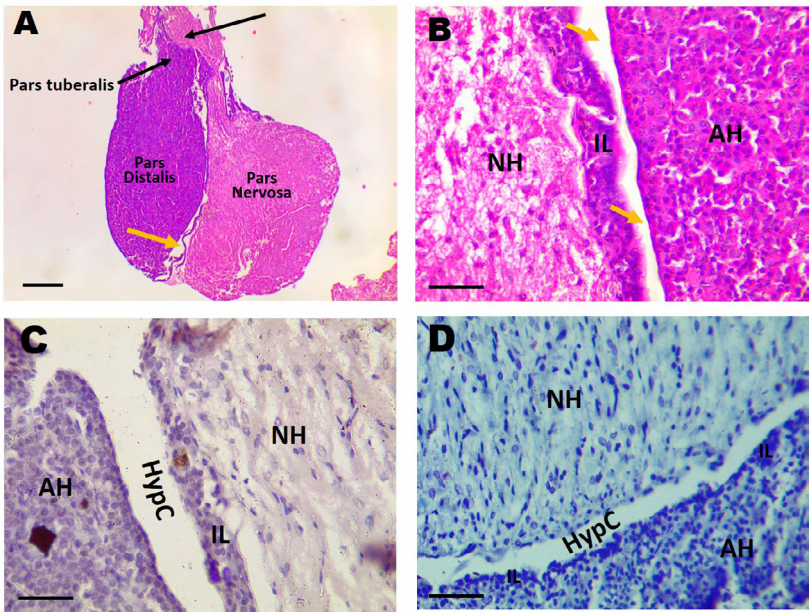

Fig. 7.- The pituitary gland of the AGR showing the adenohypophysis (pars distalis and pars tuberalis), neurohypophysis (pars nervosa), intermediate lobe (IL) showing melanotrophs (blue arrows), pituitary stalk and hypophyseal cleft (yellow arrow). NH: Neurohypophysis, AH: Adenohypophysis. HypC: Hypophyseal cleft. (**A:** H&E 4x, scale bar = 200 µm. **B:** H&E 40x, scale bar = 50 µm. **C:** PAS 40x, scale bar 50 µm. **D:** Cresyl violet 40x, scale bar 50 µm).

stalk (*infundibulum neurohypophysis*) (Fig. 7A), due to the difficulty in lifting the pituitary gland out of its hypophyseal fossa without rupturing the pituitary stalk. The melanotrophs or melanotrophic cells of intermediate lobe of AGR (Fig. 8) are well developed and were easily distinguished.

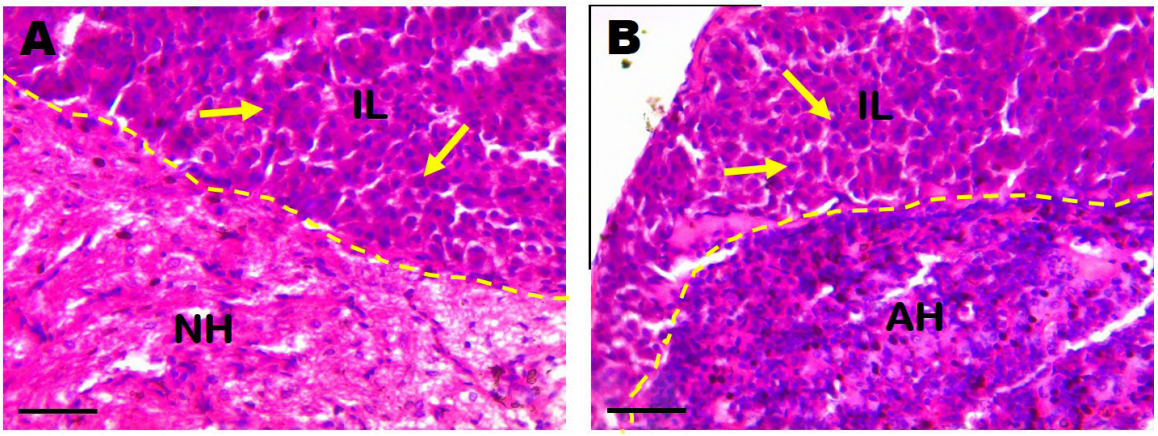

Fig. 8.- Micrographs of the pituitary gland (**A, B**) in the AGR showing the melanotrophs (yellow arrows) in the intermediate lobe (IL). NH: neurohypophysis, AH: adenohypophysis. (H&E 40x, scale bars = 50 µm).

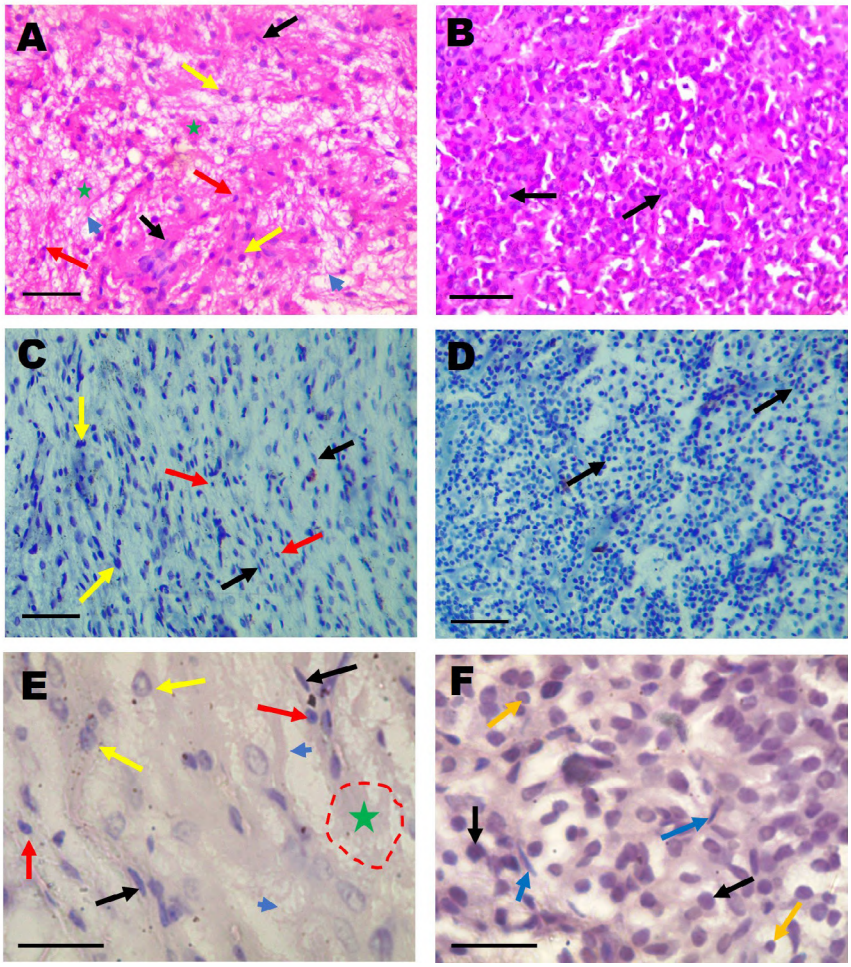

Fig. 9.- The neurohypophysis and adenohypophysis of AGR pituitary gland. **A, C, E:** The neurohypophysis of AGR pituitary gland showing the protoplasmic pituicyte (black arrow), fibrous pituicyte (yellow arrow), Herring bodies (green stars) and unmyelinated nerve fibres (blue arrowheads). In the neurohypophysis, three different pituicyte nuclei were identified: elongated shaped nuclei (black arrow), oval shaped nucleus (yellow arrow) and triangular shaped nucleus (green arrow). **B, D, F:** The adenohypophysis showing the chromophils (blue arrow) with lightly stained cytoplasm by eosin and chromophobes (black arrow) which are the biggest cells in adenohypophysis. (**A, B:** H&E 10x, scale bars = 25 µm. **C, D:** Cresyl violet 100x, scale bars = 50 µm. **E, F:** PAS 100x, scale bars = 25 µm).

Table 3. The mean hypophyseal length and width.

Parameters	Mean Hypophyseal Length (μm)		Mean Hypophyseal Width (μm)	
Group	Mean ± SEM		Mean ± SEM	
	Mean NL	Mean AL	Mean NW	Mean AL
Adult (n = 4	1218.0 ± 163.00	3663.0 ± 211.3	795.0 ± 105.00	1973.0 ± 0.00
Juvenile (n = 4)	403.0 ± 41.60	1621.0 ± 89.20	160.0 ± 17.70	885.0 ± 157.00

SEM = standard error of mean; n = number of experimental AGR used; μm = micrometers; NL = neurohypophyseal length; AL = adenohypophyseal length; NW neurohypophyseal width; AW adenohypophyseal width; Normality test (Shapiro-Wilk test) = mean NL (adult: P<value 0.262; juvenile P<value 0.995), mean NW (adult: P<value 0.957; juvenile P<value 0.850), mean AL (adult: P<value 0.726; juvenile P<value 0.849), mean AL (adult: P<value 0.574; juvenile P<value 0.661).

Chromophils and chromophobes, as the epithelial cells of the adenohypophysis, were identified in the adenohypophysis based on staining properties (Fig. 9). Here the neurohypophysis in AGR is made of nerve fibres and pituicytes, which are supportive astrocytic-like glial cells (Fig. 9). We were able to identify the two types of pituicytes: protoplasmic pituicytes, with elongated nuclei, and fibrous pituicytes, with round nuclei. Furthermore, based on nuclei shape, three kinds of pituicytes were also observed in the neurohypophysis. These are: oval-shaped nucleus, triangle-shaped nucleus and elongated nucleus (Fig. 9). The Herring bodies which are the neurosecretory bodies and non-myelinated nerve fibres extended from the hypothalamus were distinctly visible among the pituicytes in the neurohypophysis (Fig. 9).

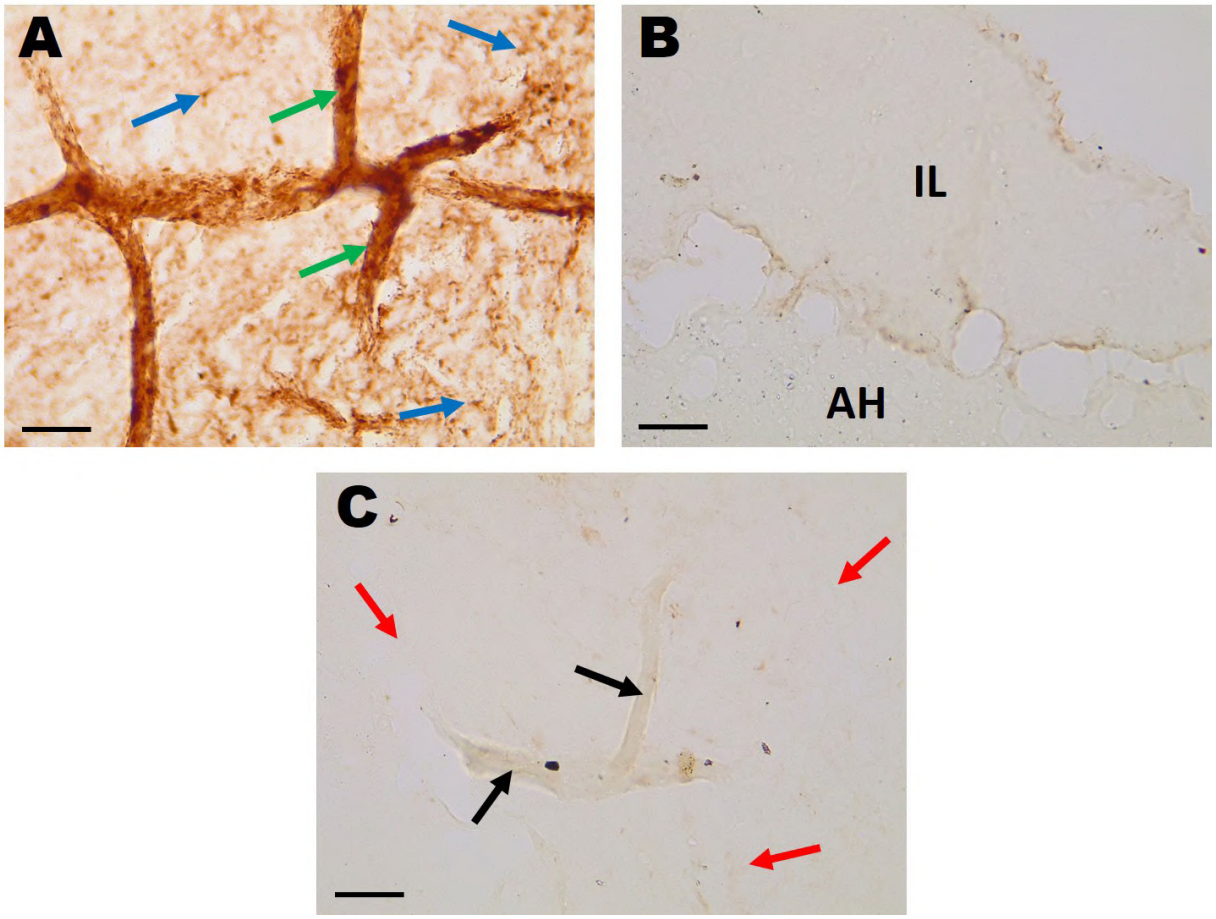

Fig. 10.- Micrographs of the pituitary gland showing GFAP immunohistochemistry in the AGR. **A:** The pituitary gland showing strong immunostaining of pituicytes (blue arrow) in the neurohypophysis. The blood vessels (green arrows) show stronger immunoreactivity to GFAP by the end-feet of the pituicytes. **B:** The gland showing the negative immunoreactivity by parenchyma of both intermediate lobe (IL) and adenohypophysis (AH). **C:** The adenohypophysis showing no immunolabelling to GFAP (red arrow). The black arrow is showing the blood vessels within the its parenchyma. (GFAP 40x, scale bars = 50 μm).

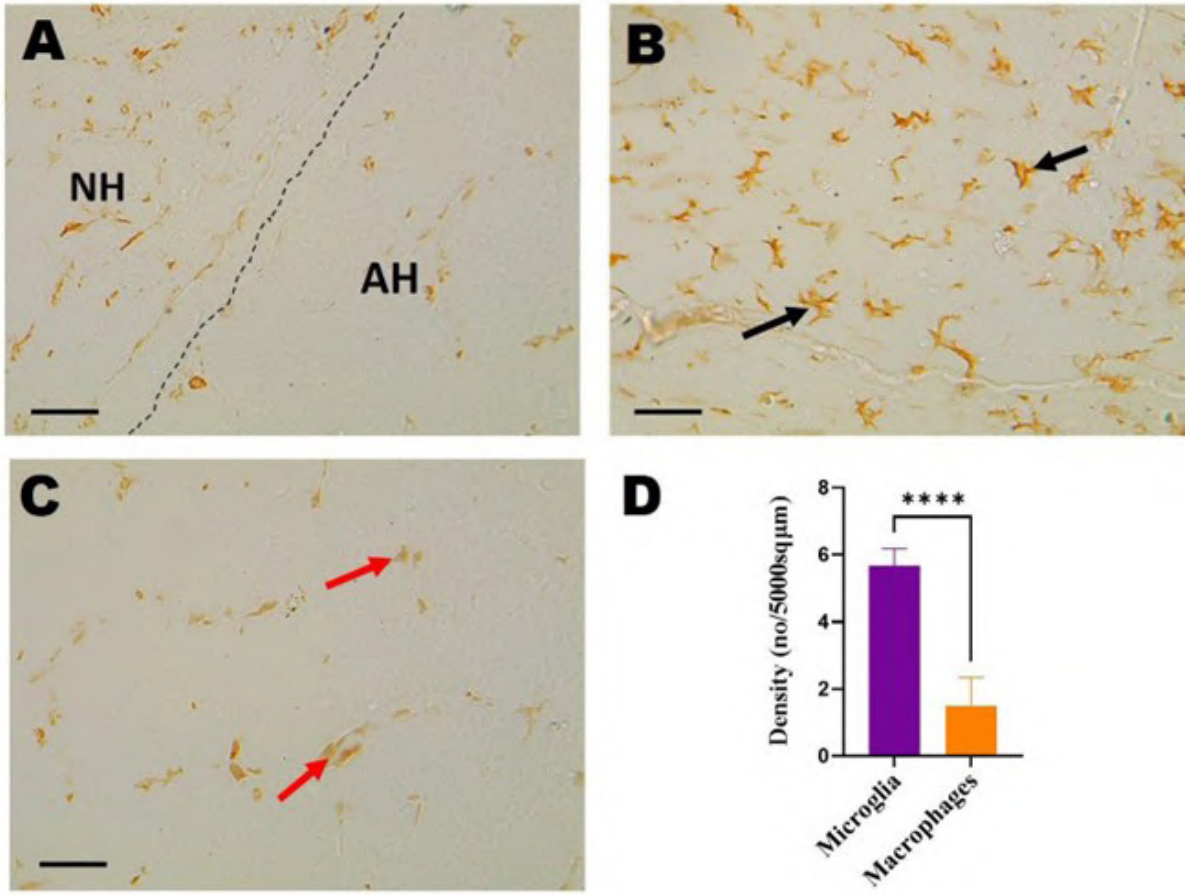

Fig. 11.- Micrographs showing immunohistochemistry of the pituitary gland of AGR to Iba1. **A:** The pituitary gland showing high immunoreactivity of microglia-like cells in the neurohypophysis as compared to adenohypophysis. **B:** The neurohypophysis showing a strong positive immunoreactivity of microglia (black arrow). **C:** Adenohypophysis revealing few macrophages (red arrow) that are immunostained positively to Iba1. **D:** Density of microglia and macrophages in the neurohypophysis and adenohypophysis respectively. Plots are mean ± SEM of microglia/macrophages density. Student's t-test, ****P<0.0001. Statistical significance is indicated for microglia/macrophages density. (Iba1 40x, Scale bars = 50 μm).

Histometric analysis of the pituitary gland

Mean adenohypophyseal length (Mean AL) in juvenile (1621±89.20 μm) and adult (3663.0 ± 211.3 μm) male AGR was noticeably longer than that of neurohypophysis (Mean NL) in juvenile (403.0 ± 41.60) and adult (1218±163.00 μm). Similarly, the mean adenohypophyseal width (Mean AW) in both juvenile (885±157.00 μm) and adult (1973±00.00 μm) was wider than the neurohypophyseal width (Mean NW) in juvenile (160.00 ± 17.70 μm) and adult (795.00 ±105.00 μm) (Table 3).

Immunohistochemical assessment

In AGR pituitary glands, the pituicytes showed strong immunostaining with GFAP antibody in the neurohypophysis, whereas in the adenohypophysis and intermediate lobe there was no immunochemical expression of the same (Fig. 10).

The pituitary gland expressed a stronger positive immunoreactivity to microglia in the neurohypophysis as compared to macrophages in the adenohypophysis. The adenohypophysis revealed the expression of few macrophages that were positively immunolabeled with Iba1 antibody (Fig. 11). The density ratio of microglia present in the neurohypophysis of the AGR pituitary gland was significantly higher than macrophages in the adenohypophysis.

DISCUSSION

Our findings showed that pituitary glands in AGR varies with age which agrees with the reports of Maskey et al. (2021), they reported that the pituitary gland size differs with age and gender. Mixer and Turner (1942) have also reported increased in pituitary weight with corresponding increase

in body weight among male growing albino rats. The late age increase in pituitary length and width was mainly attributed to the increment of gonadotropic hormones due to loss of feedback mechanism of gonadal steroids. However, Luay (2016) reported figures in the guinea pig that appear to be too high when compared to AGR, which is also a large rodent like guinea pig.

Grossly, the pituitary gland of the AGR was located at the base of the brain, on the sphenoid bone, as described for domestic mammals (Dyce et al., 2010). The gland was in an ill-defined depression of the sphenoid bone called *sella turcica*. Our results corroborated those of Mahmood (2014), who described the anatomical and histological features of the pituitary gland in rats and found that, for most investigated species, there was no true *sella turcica*, but rather, a shallow depression in the sphenoid bone. The gland is saddled in shape, contrary to the reports of Mahmood (2014) in rats and Gilbert et al. (2020) in greater cane rats, who both reported a disc shape. The pituitary gland was also seen between the two roots of the trigeminal nerve of AGR as reported by Cao et al. (2017) in mice and Gilbert et al. (2020) in greater cane rats.

Histologically, the neurohypophysis is also considerably smaller than the adenohypophysis, which confirmed previously published data by Mahmood (2014) in rats and Gilbert et al. (2020) in greater cane rats. In this study we also found that the adenohypophysis and the neurohypophysis were in contact and joined through the intermediate lobe, as reported by Mahmood (2014) in rats. This intermediate lobe is absent in the avian species, as reported in turkey by Jahangirfard et al. (2019). Dyce et al. (2010) reported that the intermediate lobe is poorly developed in the primates. Furthermore, Perez-Castro et al. (2012) described that the pituitary gland of humans lacks the intermediate lobe and the hypophyseal cleft.

Our study revealed two types of parenchymal cells in the adenohypophysis. These are: chromophils and chromophobes. This agrees with the reports of Gilbert et al. (2020), where they identified chromophilic acidophils, chromophilic basophils and chromophobes in the pituitary glands of the greater cane rats. These cells in adenohypophysis were seen to be arranged in cords, as reported by Mahmood (2014). Using H&E, the neurohypophysis revealed two types of pituicytes: fibrous and protoplasmic pituicytes, as described by Ye et al. (2018) in camels. Furthermore, three types of pituicyte nuclei were identified in the AGR neurohypophysis: oval-shaped nucleus, triangle-shaped nucleus and elongated nucleus. These types of pituicyte nuclei shapes were also described by Mahmood (2014) and Gilbert et al. (2020).

The strong expression of pituicytes with GFAP antibody in the AGR neurohypophysis was possible because pituicytes are the astrocyte-like cells present in the neurohypophysis. Gilbert et al. (2020) also demonstrated pituicytes immuno-labelled by GFAP antibody in the greater cane rats (GCR). There was positive immunoreactivity of microglia and macrophages to Iba1 antibody in the neurohypophysis and adenohypophysis respectively. This has been corroborated by reports of Mander and Morris (1996), where they demonstrated the presence of neurohypophyseal microglia and adenohypophyseal macrophages in rats. This is contrary to the reports of Gilbert et al. (2020), in which a negative immunostaining to Iba1 antibody both in the neurohypophysis and adenohypophysis of the greater cane rat (GCR) was reported (Gilbert et al., 2020). This may be attributed to species specificity. The density of microglia in the AGR was seen to be higher than macrophages in the adenohypophysis. Mander and Morris (1996) reported that microglia in the neurohypophysis constituted 20% of the non-endothelial cells with the other 80% of cells being pituicytes. Mander and Morris (1996) reported macrophages to be only 1% of the total cells in the adenohypophysis. This current study only considered male AGR, which invariably introduce gender bias – a limitation of this research. We plan to investigate the architecture of the pituitary gland in female AGR for comparative study with regard to sexual dimorphism.

In conclusion, the weight, length and width of the pituitary glands in AGRs increases with age. The gross and histological characteristics of pituitary glands of the AGR are found to be similar to other rodents and mammals in general. We recommend further study to compare morphometrical parameters between males and females of this model.

FUNDING

This work was partially funded by Humboldt Research Hub for Zoonotic Arboviral Diseases (HRH-ZAD), Ibadan. We are grateful to them for granting us access to their experimental animals and infrastructural facilities for the execution of this experiment.

REFERENCES

ACOSTA M, MOHAMED F (2013) Immunohistochemical and morphometric study of pituitary pars distalis folliculostellate cells of nonpregnant and pregnant viscachas. *Biotechnic Histochem*, 88(3-4): 161-169.

AJAYI SS (1974) The biology and domestication of African giant rat (*Cricetomys gambianus*, Waterhouse), Ph.D. Thesis. University of Ibadan, Nigeria.

ANGELA N, VIAENE AN, LEE EB, ROSENBAUM JN, NASRALLAH IM, NASRALLAH MP (2019) Histologic, immunohistochemical, and molecular features of pituicytomas and atypical pituicytomas. *Acta Neuropath Comms*, 7: 6.

ACOSTA M, MOHAMED F (2009) Pituitary pars intermedia of male viscacha (*Lagostomus maximus maximus*): a morphometric study of seasonal and age-related changes in immunohistochemistry. *Cells Tissues Organs*, 190: 219-229.

AMAR AP, WEISS MH (2003) Pituitary anatomy and physiology. *Neurosurg Clin N Am*, 14: 11-23.

AMAT P (1970) Thyrotroph subtypes in the guinea-pig's pituitary after partial and total thyroidectomy. *Cells Tissues Organs*, 76(1): 112-122.

BOTERMANN DS, BRANDES N, FROMMHOLD A, HEß I, WOLFF A, ZIBAT A, HAHN H, BUSLEI R, UHMANN A (2021) Hedgehog signaling in endocrine and folliculo-stellate cells of the adult pituitary. *J Endocr*, 248: 303-316.

CARDIN J, CARBAJAL ME, VITALE ML (2000) Biochemical and morphological diversity among folliculo-stellate cells of the mink (*Mustela vison*) anterior pituitary. *Gen Comp Endocrinol*, 120: 75-87.

CÓNSOLE GM, JURADO SB, OYHENART E, FERESE C, PUCCIARELLI H, GÓMEZ DUMM CLA (2001) Morphometric and ultrastructural analysis of different pituitary cell populations in undernourished monkeys. *Braz J Med Biol Res*, 34(1).

CAO D, MA X, ZHANG WJ, XIE Z (2017) Dissection and coronal slice preparation of developing mouse pituitary gland. *JOVE*, 129: e56356.

DYCE KM, SACK WO, WENSING CJG (2010) Textbook of veterinary anatomy, 4th edition. Saunders. An Imprint of Elsevier Inc, St Louis, Missouri, pp 268-290.

EMERALD M (2016) Pituitary Gland: Pituitary Hormones. *Encycl Food Heal*, pp 392-400.

FREEMAN AR, OPHIR AG, SHEEHAN MJ (2020) The giant pouched rat (*Cricetomys ansorgei*) olfactory receptor repertoire. *PloS One*, 15(4): e0221981.

GILBERT TT, OLOPADE FE, MUSTAPHA OA, FOLARIN OR, OLOPADE JO (2020) Histological and immunohistochemical study of pineal and pituitary glands of the greater cane rat (*Thryonomys swinderianus*, Temminck 1827). *Arch Bas App Med*, 8: 137-142.

JAHANGIRFARD R, SHALIZAR-JALALI A, SHAHROOZ R, NAJAFI G, MINAS N (2019) Anatomical and cytohistological study of the pituitary gland in adult turkey. *Vet Res For*, 10(2): 159-163.

JU K, BAE H, PARK H, CHANG J, CHOI KS, SIM K (2010) Morphometric study of the Korean adult pituitary glands and the diaphragma sellae. *J Korean Neurosurg Soc*, 47: 42-47.

KAUFMAN M, NIKITIN AY, SUNDBERG JP (eds.) (2009) *Histologic basis of mouse endocrine system development: a comparative analysis.* CRC Press, Boca Raton.

KONDOH D, NAKAMURA KG, ONO YS, YUHARA K, BANDO G, WATANABE K, HORIUCHI N, KOBAYASHI Y, SASAKI M, KITAMURA N (2017) Histological features of the vomeronasal organ in the giraffe, *Giraffa cameloparadalis. Microsc Res Tech*, 80(6): 652-656.

LAMICHHANE TR, PANGENI S, PAUDEL S, LAMICHHANE HP (2015) Age and gender related variations of pituitary gland size of healthy Nepalese people using magnetic resonance imaging. *Am J Biomed Engineer*, 5(4): 130-135.

LUAY OH (2016) Some macroscopic and microscopic observation on the pituitary gland of guinea-pig *Cavia culteri. Bas J Vet Res*, 15(4).

MANDER TH, MORRIS JF (1996) Development of microglia and macrophages in the postnatal rat pituitary. *Cell Tissue Res*, 286: 347-355.

MCKLVEEN TL, JONES JC, SPONENBERG DP, KENT S, WARD DL, AARDEMA CH (2003) Assessment of the accuracy of computed tomography for measurement of normal equine pituitary glands. *Am J Vet Res*, 64(11): 1387-1394.

MASKEY S, MANSUR DI, KARKI S, SHRESTHA P, SHRESTHA S, MUKTA SINGH BHANDARI MS (2021) Morphometric study of pituitary gland with correlation of age and gender using Magnetic Resonance Imaging. *BJHS*, 6(2): 1476-1480.

MAHMOOD HB (2014) Anatomical and histological study of pituitary gland of the rats in Iraq. *J Kerb Uni*, 12: 221-228.

MUSTAPHA OA, OLUDE MA, TAIWO B, OLOPADE JO (2019) Cytoarchitecture of the hippocampal formation in the African giant rat (*Cricetomys gambianus*, Waterhouse). *Nigerian J Physiol Sci*, 34(1): 55-62.

MONTEMURRO DG (1964) Weight and histology of the pituitary gland in castrated male rats with hypothalamic lesions. *J Endocr*, 30(1): 57-67.

MIXNER JP, TURNER CW (1942) Pituitary weight of growing male albino rat related to body weight. *Endocrinology*, 31(2): 261-263.

NZALAK JO, AYO JO, NEILS JS, OKPARA JO, ONYEANUSI BI, GHAJI A, OJO SA, ADEBAYO IA (2005) Morphometric studies of the cerebellum and forebrain of the African giant rat (AGR) (*Cricetomys Gambianus*, Waterhouse). *Trop Vet*, 23(3-4): 87-92.

OLOPADE F, FEMI-AKINLOSOTU OM, ADEKANMBI AJ, IGHOGBOJA OO, SHOKUNBI MT (2021) Chronic caffeine ingestion improves memory and learning and increases neuronal population and dendritic length in the hippocampus of adult mice. *Nigerian J Physiol Sci*, 36(2): 165-172.

OLOPADE JO, FATOLA IO, OLOPADE FE (2011) Vertical administration of vanadium through lactation induces behavioural and neuromorphological changes: protective role of vitamin E. *Nigerian J Physiol Sci*, 26(1): 55-60.

OLUDE MA, OGUNBUNMI TK, OLOPADE JO, IHUNWO AO (2014) The olfactory bulb structure of African giant rat (*Cricetomys gambianus*, Waterhouse 1840) I: cytoarchitecture. *Anat Sci Int*, 89(4): 224-231.

OLUDE MA, MUSTAPHA OA, OLOPADE JO (2016) Morphological characterization of the African giant rat (*Cricetomys gambianus*, Waterhouse) brain across age groups: gross features of cortices. *Nigerian J Physiol Sci*, 31: 133-138.

PEREZ-CASTRO C, RENNER U, HAEDO MR, STALLA GK, ARZT E (2012) Cellular and molecular specificity of pituitary gland physiology. *Physiol Rev*, 92: 1-38.

POPOOLA SO, SAKPA CL (2018) Hormones of pituitary-gonadal axis and histology of pituitary gland following oral treatment of male Wistar rats with glyphosate. *J Biomed Res Clin Pract*, 1(2).

RADHIAH NA, AZHAR LJ (2020) Effect of evisect on organo-somatic index and pathohistological changes of some vital organs in white mice. *Sys Rev Pharm*, 11(11): 1910-1914.

RAHMAN M, ARA S, AFROZ H, HAHAR N, SULTANA AA, FATEMA K (2011) Morphometric study of the human pituitary gland. *Bangladesh J Anat*, 9(2): 79-83.

SCHREIBMAN MP, LEATHERLAND JF, MCKEOWN BA (1973) Functional morphology of the teleost pituitary gland. *Amer Zool*, 13: 719-722.

SCHOEMAKER NJ, VAN DER HAGE MH, FLIK G, LUMEIJ JT, RIJNBERK A (2004) Morphology of the pituitary gland in ferrets (*Mustela putorius furo*) with hyperadrenocorticism. *J Comp Path*, 130: 255-265.

TREIER M, O'CONNELL S, GLEIBERMAN A, PRICE J, SZETO DP, BURGESS R, CHUANG PT, MCMAHON AP, ROSENFELD MG (2001) Hedgehog signaling is required for pituitary gland development. *Development*, 128: 377-386.

VIONNA K, KATHERINE Q, ROUX L, ALEXANDRE B (2020) Mensuration of the rabbit pituitary gland from computed tomography. *Vet Radiol Ultrasound*, 61(3): 322-328.

WEMAN B (1974) Fine structure of the pars distalis of the pituitary gland in the female mink, *Mustela vison*. *Acta Zoologica*, 55(2): 119-136.

WEMAN B, NOBIN A (1973) The pars intermedia of the mink, *Mustela vison*. *Z Zellforsch*, 143(3): 313-327.

WITTKOWSKI W (1998) Tanycytes and pituicytes: morphological and functional aspects of neuroglial interaction. *Microsc Res Tech*, 41: 29-42.

YE W, WANG H, WANG F, WANG J (2018) Morphology and ultrastructure of the hypophysis in Bactrian Camels (Camelus bactrianus). *Int J Morphol*, 36(4): 1316-1323.

Position of the mandibular foramen in relation to the occlusal plane in children with skeletal class malocclusion

Arif Keskin[1], Aynur Emine Çiçekcibaşi[2], Gülay Açar[2], Güldane Mağat[3]

[1] Giresun University, Faculty of Medicine, Department of Anatomy, 28200 Turkey

[2] Necmettin Erbakan University, Faculty of Medicine, Department of Anatomy, 42090 Turkey

[3] Necmettin Erbakan University, Faculty of Dentistry, Department of Oral, Dental and Maxillofacial Radiology, 42090 Turkey

SUMMARY

Frequently, practitioners use the inferior alveolar nerve block in the procedures desired on the teeth in the mandible and the surrounding tissues. This study aimed to reveal the position of the mandibular foramen (MF) according to the malocclusion types on panoramic radiographs of children aged 9-18 years living with malocclusion in Turkey. Panoramic and cephalometric radiographs of 330 patients between 9 and 18 years old were analyzed retrospectively. We grouped the skeletal malocclusion types as Class 1, 2, and Class 3 based on lateral cephalometric radiographs and evaluated the location of MF in malocclusion types according to age and gender. We observed that the distances to the occlusal plane, posterior edge, and gonion point increased with age while the distance to the anterior edge decreased. There was a significant difference according to age and gender in all malocclusion types ($p<0.05$). We determined that the MF was positioned upward parallel to the increase in age and approached the midpoint of the ramus of the mandible from the posterior. The fact that MF is placed higher than the occlusal plane in Class 3 malocclusions compared to other types and differs by gender will guide clinicians in providing effective and safe inferior alveolar nerve block in pediatric malocclusions.

Key words: Inferior alveolar nerve block – Malocclusion – Mandibular foramen – Occlusal plane – Panoramic radiograph

ABBREVIATIONS

IANB: Inferior alveolar nerve block

MF: Mandibular foramen

PR: Panoramic radiographs

OP: Occlusal plane

AP: Anteroposterior

mm: Millimeter

GO: Gonion point

Corresponding author:
Arif Keskin, PhD. Giresun University, Faculty of Medicine, Department of Anatomy, 28200 Turkey. Phone: +905337375707. E-mail: arif.keskin@giresun.edu.tr

Submitted: July 30, 2023. **Accepted:** September 25, 2023

https://doi.org/10.52083/UACI5716

INTRODUCTION

One of the critical anatomical points in the ramus of the mandible is the mandibular foramen (MF). Passing vessels and nerves in the mandibular canal through MF is essential in dentistry and anatomy. Generally, clinicians prefer using inferior alveolar nerve block (IANB) for procedures they desire to perform on the teeth in the mandible and surrounding tissues. (Tüloğlu et al., 2010). For adequate anesthesia, the anesthetic solution should be injected around the MF (Moore et al., 2007). The failure of the IANB is due to the absence of intraoral bone markers indicating the injection site (Paryab et al., 2015). If the injection is administered more forward than MF, it cannot provide anesthesia; if administered too far back, introducing the needle into the parotid gland may cause temporary paralysis of the branches of the facial nerve unilaterally (Moore et al., 2007).

The repetition of the injection occurs due to unsuccessful anesthesia application. Repeated injection attempts cause fear and anxiety, especially in children, negatively affecting treatment (Tüloğlu et al., 2010). The occlusal plane (OP) and the anteroposterior (AP) position of the ramus of the mandible are referenced in determining the needle insertion site in IANB. In studies conducted in different races in the literature, it was reported that MF in children with deciduous teeth is at the OP level, slightly above OP during the mixed dentition period, and is displaced upward with increasing age (Afsar et al., 1998; Hwang et al., 1990; Movahhed et al., 2011). In addition, studies show a difference in the OP and AP position of MF compared to adults and children (Benham, 1976; Hwang et al., 1990; Kang et al., 2013).

In a retrognathic position relative to the maxilla in newborns, the mandible shows rapid growth and development, ensuring harmony between the maxilla. This is achieved by the combination of morphological and functional variables such as the eruption of teeth, enlargement of the tongue, lips, and cheeks, the movement and strength of the muscles attached to the mandible, swallowing and feeding habits, as well as the volumetric changes seen in the ramus and body of the mandible (Gill et al., 2013).

Malocclusion, defined as the disruption of normal occlusion during the growth and development period, causes the teeth, jaw, facial bones, and soft tissues to be affected. It leads to developmental problems or functional disorders such as chewing (Öz et al., 2019). There are nutritional habits, genetic and environmental factors in the etiology of malocclusion.

During the development of the mandible, changes are observed in the vertical and horizontal height of the ramus of the mandible (Gill et al., 2013). In the study conducted by Paryab and Ahmadyar (2019), it was reported that there was a difference in MF position due to age in patients with malocclusion. In addition, it has been found that the OP and AP positions of MF show differences between the classes of malocclusion in adult individuals with malocclusion (Park et al., 2015).

In the literature review, there are very few studies about MF positions in pediatric patients with malocclusion (Park et al., 2015; Paryab et al., 2015). As far as we know, the study investigating the position of MF in pediatric patients with malocclusion in Turkey could not be detected. This study aimed to reveal the position of the MF according to the malocclusion classes on panoramic radiographs (PR) of children with malocclusion aged 9-18 living in Turkey.

MATERIALS AND METHODS

In this study, panoramic and cephalometric radiographs of a total of 330 patients between 9-18 years old registered in the archives of the Department of Oral, Dental and Maxillofacial Radiology of the Faculty of Dentistry of Necmettin Erbakan University (Konya-TURKEY) were examined.

A single cephalometric and panoramic radiography (Morita Veraviewepocs 2D R100-P; J MoritaMFG, Kyoto, Japan) device was used to obtain the images in the study. The device is set to 70 kVp, 10 mA, and 10 seconds. The images were obtained by a single technician and according to the reference points specified by the manufacturer. The images were then exported as TIFF files. After the recorded images were set to 2836x1500 pixels with Photoshop CS6 Portable (Adobe Systems Onc. San Jose, CA, ABD), millimetric (mm) measurements were made.

Approval was obtained from Necmettin Erbakan University, Meram Faculty of Medicine, Non-Pharmaceutical and Medical Device Research Ethics Committee (Number: 14567952-050/673, decision number 2020/2497). Individuals between the ages of 9 and 18 with both panoramic and cephalometric radiographs were included in the study. The study did not include those with a previous history of trauma, those who had undergone surgery, individuals with facial and neck anomalies, and images that did not show clear bone boundaries due to poor image quality or images containing radiological artifacts.

The skeletal malocclusion types were grouped as Class 1, Class 2, and Class 3 according to Steiner's ANB angle based on lateral cephalometric radiographs (Point A: the deepest anterior point on the buccal face of the body of maxilla, Point N: Nasion, Point B: the deepest anterior point on the buccal face of the body of mandible, ANB angle: the angle formed by the NA and NB planes), (Fernandez et al., 2018), (Class 1: ANB° = 0° to 4°; Class 2: ANB°> 4°; Class 3: ANB°<0°).

The patients were divided into 9-13 years old and 14-18 years old groups according to their chronological age. The anterosuperior fossa of the posterior lingula of the mandible was determined as MF, 8 points were determined by reference to the study conducted by Movahhed et al. (2011) (Fig. 1) and by creating three planes, distance measurements of the MF to the surrounding anatomical points were performed.

Point 1. The most anterosuperior point of the lingula of the mandible.

Point 2. The most prominent point on the canine tooth crown.

Point 3. The uppermost tubercle crest of the erupted most posterior molar tooth in the mandible.

Point 4. The deepest point of the margo anterior of the ramus of the mandible.

Point 5. The most protruding point of the coronoid process.

Point 6. The most prominent posterior point on the condylar process.

Point 7. The most prominent point on the margo posterior, close to the angle of the mandible.

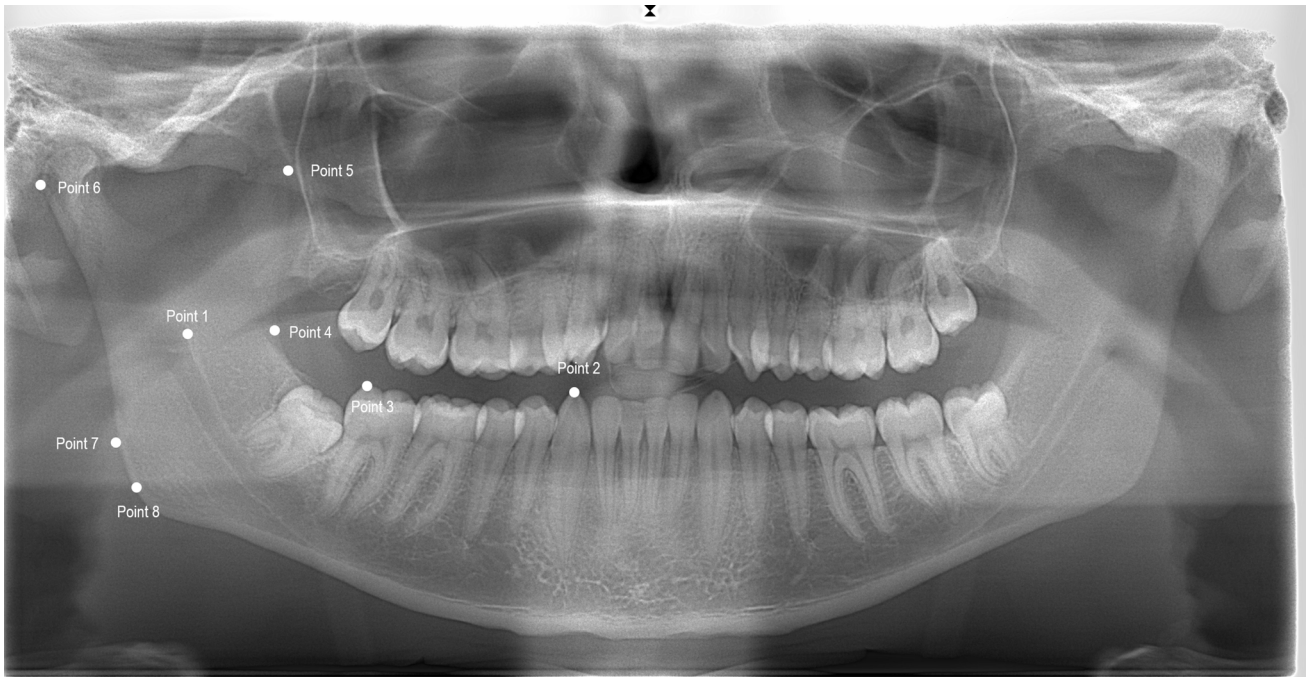

Fig. 1.- Example display of determined points on the panoramic radiographic image (Point 1: The most anterosuperior point of the lingula of the mandible. Point 2: The most prominent point on the canine tooth crown. Point 3: The uppermost tubercle crest of the erupted most posterior molar tooth in the mandible. Point 4: The deepest point of the margo anterior of the ramus of the mandible. Point 5: The most protruding point of the coronoid process. Point 6: The most prominent posterior point on the condylar process. Point 7: The most prominent point on the margo posterior, close to the angle of the mandible. Point 8: The angle at the intersection of the tangents drawn from the body of the mandible and the ramus of the mandible to the angle of the mandible, the location of the bisector of the angle of the mandible).

Point 8. Gonion point (GO). The angle at the intersection of the tangents drawn from the body of the mandible and the ramus of the mandible to the angle of the mandible, the location of the bisector of the angle of the mandible (Movahhed et al., 2011).

Plane 1: The plane connecting points 2 and 3 (OP).

Plane 2: The plane connecting points 4 and 5.

Plane 3: The plane connecting points 6 and 7.

U1: The line length is drawn perpendicular from Point 1 to Plane 1.

U2: The line length is drawn perpendicular from Point 1 to Plane 2.

U3: The line length is drawn perpendicular from Point 1 to Plane 3.

U4: The length of point 1 to GO.

To determine the position of MF on each image, we performed our measurements by using the defined points on the right and left sides of the mandible (Fig. 2).

The data were analyzed with IBM SPSS v23 software (NY, USA). The Shapiro-Wilk test checked normality distributions of quantitative data, and the Levene test checked homogeneity. Parametric evaluations were performed for those who had n>30 parametric conditions. The comparison of the data showing normal distribution was performed with the independent sample t-test. The comparison of more than two groups was performed by One Way ANOVA. In the intergroup evaluations, Post-Hoc was evaluated by multiple comparisons. The correction was made by the Bonferroni test in multiple group comparisons. In the study, the presence and direction of the relationship between MF parameters and the relationship between the parameters and age were determined decisively by Pearson correlation.

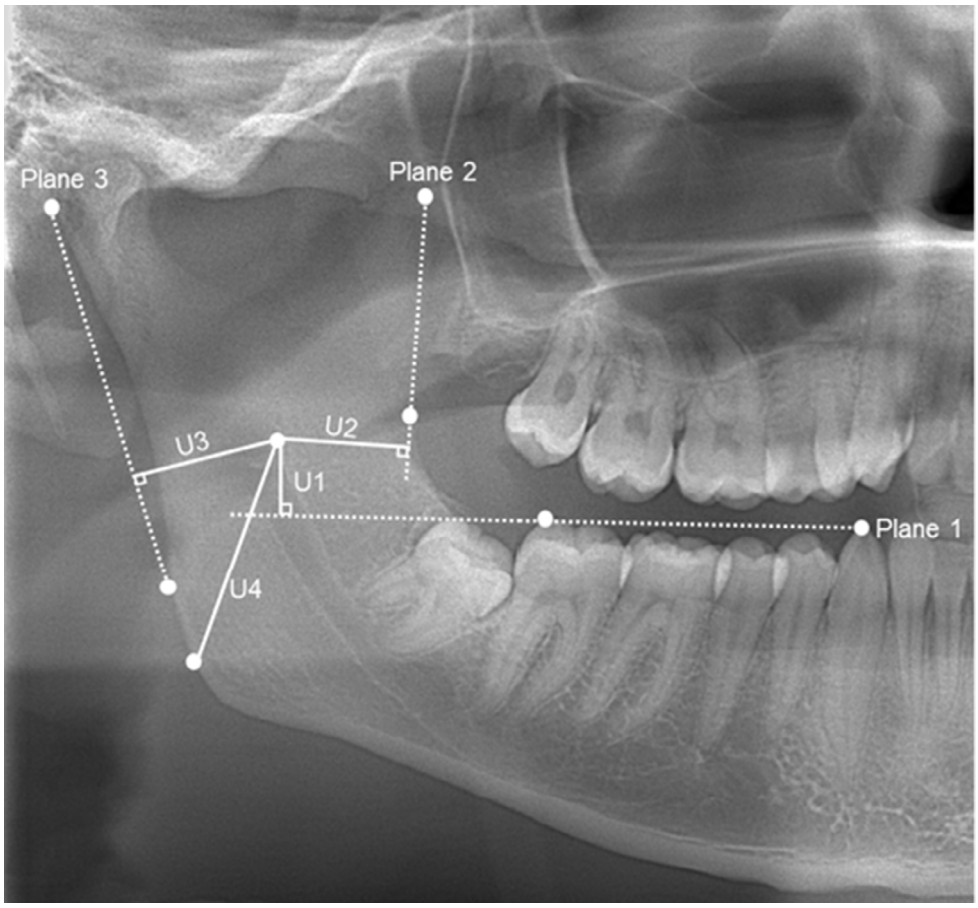

Fig. 2.- Example representation of U1, U2, U3, and U4 distance measurements on the panoramic radiographic image (U1: Length of the line drawn perpendicular to Point 1 to Plane 1. U2: Length of the line drawn perpendicular to Point 1 to Plane 2. U3: Length of the line drawn perpendicular to Point 1 to Plane 3. U4: Point 1 length of to GO).

Table 1. Gender distribution by malocclusion classes.

	Girl	Boy	Total
Malocclusion	**Number (%)**	**Number (%)**	**Number (%)**
Class 1	76 (23.03)	60 (18.18)	136 (41.21)
Class 2	74 (22.42)	35 (10.61)	109 (33.03)
Class 3	52 (15.76)	33 (10.00)	85 (25.76)
Total	202 (61.21)	128 (38.79)	330 (100)

The data were shown in the form of mean ± standard deviation. The significance level was accepted as $p<0.05$ for all statistical tests in the study.

RESULTS

A total of 330 children (202 girls and 128 boys) were included in our study. The gender distribution in malocclusion classes is shown in Table 1.

According to lateralization, the distance of MF to the anterior edge on the right side was significantly higher in Class 1 and Class 2 malocclusion, and the distance to GO on the left side was significantly higher in Class 2 malocclusion. There was no significant difference between the right and left measurement values in Class 3 malocclusion ($p>0.05$).

Regarding gender, men had significantly greater distances from MF to GO in Class 1 and Class 2 malocclusion and from MF to the anterior edge, posterior edge, and GO in Class 3 malocclusion. ($p<0.05$).

Based on the age groups, the distances from MF to OP, posterior edge, and GO in Class 1 and Class 2 malocclusion and from MF to the posterior edge and GO in Class 3 malocclusion were notably higher in the 14-18 age group. ($p<0.05$) (Table 2).

Although we highly measured the MF distances to the anterior edge in the 9-13 age group in all malocclusion classes, they were not statistically significant ($p>0.05$). Measurements of the distance of MF to OP, posterior edge, and GO showed a positive directional correlation with age, and the distance of MF to the anterior edge showed a negative directional correlation (Table 3).

There was a significant difference between the malocclusion classes in the distance of the MF to the OP and the anterior edge ($p<0.05$). The OP to the distance of MF was measured to be the highest in the Class 3 malocclusion group and the lowest in the Class 2 malocclusion group. The distance of MF to the anterior edge was the highest in Class 2 malocclusion and the lowest in Class 1 malocclusion (Table 4).

Table 2. Difference between malocclusion classification of parameters according to age groups (U1: The line length is drawn perpendicular from Point 1 to Plane 1. U2: The line length is drawn perpendicular from Point 1 to Plane 2. U3: The line length is drawn perpendicular from Point 1 to Plane 3. U4: The length of point 1 to GO. * $p<0.05$).

	Class1			Class2			Class3		
	9-13	**14-18**	**p**	**9-13**	**14-18**	**p**	**9-13**	**14-18**	**p**
U1	3.58±2.19	5.23±2.54	**<0.001***	3.63±2.59	4.37±2.44	**0.026***	5.03±2.87	5.78±2.7	0.122
U2	13.73±2.14	13.46±1.84	0.491	14.51±2.24	13.93±2.12	0.071	14.15±2.07	13.84±2.07	0.109
U3	12.89±1.28	13.59±1.47	**<0.001***	13.03±1.27	13.61±1.70	**0.033***	12.62±1.18	13.68±1.63	**<0.001***
U4	23.66±2.30	26.26±3.24	**<0.001***	23.86±2.26	25.20±3.27	**<0.001***	22.65±2.75	26.25±2.86	**<0.001***

Table 3. Correlation of parameters with age (U1: The line length is drawn perpendicular from Point 1 to Plane 1. U2: The line length is drawn perpendicular from Point 1 to Plane 2. U3: The line length is drawn perpendicular from Point 1 to Plane 3. U4: The length of point 1 to GO. * $p<0.05$).

		U1	U2	U3	U4
Age	**r**	0.196	-0.086	0.298	0.407
	p	**<0.001***	**0.027***	**<0.001***	**<0.001***

Table 4. Difference of parameters according to malocclusion classes (U1: The line length is drawn perpendicular from Point 1 to Plane 1. U2: The line length is drawn perpendicular from Point 1 to Plane 2. U3: The line length is drawn perpendicular from Point 1 to Plane 3. U4: The length of point 1 to GO. * p<0.05).

PARAMETERS	Class1	Class2	Class3	*p*
U1	4.55±2.53	4.10±2.51	5.43±2.81	<0.001*
U2	13.57±1.97	14.14±2.17	13.98±2.07	0.005*
U3	13.30±1.43	13.40±1.58	13.19±1.53	0.370
U4	25.19±3.16	24.72±3.01	24.60±3.33	0.281

Table 5. Correlation table of the mandibular foramen (U1: The line length is drawn perpendicular from Point 1 to Plane 1. U2: The line length is drawn perpendicular from Point 1 to Plane 2. U3: The line length is drawn perpendicular from Point 1 to Plane 3. U4: The length of point 1 to GO. * p<0.05).

		U1	U2	U3	U4
U2	r	0.060	1		
	p	0.126	-		
U3	r	-0.077	0.039	1	
	p	**0.048***	0.318	-	
U4	r	0.289	0.143	0.319	1
	p	**<0.001***	**<0.001***	**<0.001***	-

In addition, a negative directional correlation was found between the distance of MF to OP and the posterior edge (p<0.048; r=-0.077). The correlation between the measurement values of MF is shown in Table 5.

DISCUSSION

In dentistry, IANB is used before routine or surgical procedures are planned on the mandible. 15-20% failure is observed in this frequently used anesthesia method. It is aimed to inject the anesthetic into the MF around to increase its success (Moore et al., 2007). Due to the diversity in the facial anatomies of the populations living in the world, there are many differences in the mandible and related structures (Gill et al., 2013). Since the mandible shows rapid growth and development until puberty, the position of MF changes in children aged 8-18 years (Paryab et al., 2015; Apaydın, 2020). Therefore, to obtain adequate and safe anesthesia in the mandible, it is necessary to know well the location of the MF according to race and age.

Very few studies reveal MF's position on pediatric and adult patients with malocclusion (Park et al., 2015; Paryab et al., 2015). Although there have been studies on the location of MF in children belonging to Turkish people (Apaydın, 2020), there have not been any studies in pediatric patients with malocclusion. Therefore, in this study, the position of the MF according to the classification of malocclusion in the PR of children divided into different age groups of developmental age was evaluated.

The panoramic radiography technique allows the mandible and surrounding anatomical structures to be visible on a single film with a low radiation dose. This imaging method is often preferred in dentistry for diagnosing the disease and post-treatment evaluation (Corbet et al., 2009). According to the PR, computed tomography, which provides three-dimensional imaging and realistic measurement results, has a high radiation dose, so its use in pediatric patients is limited. Therefore, in the methodology of our study, PR was used, which is the most frequently used in practice and has a low radiation rate.

It has been reported that there is symmetry between right and left MF in patients who do not have malocclusions (Tsai, 2004; Shukla et al., 2018). On the contrary, some studies report asymmetry (Krishnamurthy et al., 2017; Açıkgöz, 2020). It was reported that there was a significant difference in the distance of the MF to the anteri-

or edge of the ramus of the mandible compared to lateralization in computed tomography images of patients aged 9-18 and 19-71 years belonging to the Turkish population. Still, no difference was detected in other data (Fındık et al., 2014). In this study, a significant difference was observed in the anterior edge of the ramus of the mandible in patients with Class 1 and Class 2 malocclusion, and the distance measurements between the GO compared to lateralization ($p<0.05$). In Class 3 malocclusion, there was no difference decisively between right and left ($p<0.05$). Since the difference between the right and left in the Class 1 and 2 malocclusion group was less than 0.35 mm, it was assumed that it would not cause failure of IANB in patients.

The literature has reported that the values measured in boys are higher than in girls (Açıkgöz, 2020). In children of developmental age, on the other hand, higher values were found in girls because girls enter puberty earlier than boys (Movahhed et al., 2011). In addition, some studies report no difference according to gender (Shukla et al., 2018; Feuerstein et al., 2020; Apaydın, 2020; Akman et al., 2021). In the conical beam computed tomography (CBCT) image of 100 patients aged 18-31 years with skeletal Class I, II, and III malocclusions, there is no significant difference in Class 1 and Class 2 malocclusion in patients according to gender. Still, it was found that the distance of MF to the anterior edge of the ramus of the mandible was significantly higher in male patients with Class 3 malocclusion compared to girls (Park et al., 2015). In our study, similar to the results of Park et al. (2015), there was no difference in Class 1 and Class 2 malocclusion according to gender, while all measurements except the distance to the OP in boys with Class 3 malocclusion were higher than in girls and showed a significant difference ($p<0.05$). We believe detecting MF higher than OP in girls with Class 3 malocclusion than in boys is an important finding that should be considered in increasing the success of anesthesia.

One of the essential anatomical signs used to determine the needle insertion location in IANB is OP. OP is used in the injection made for IANB in the clinic (Movahhed et al., 2011). In the study conducted in adults, a significant difference was found between the skeletal class malocclusion classes and the distance of MF to the OP. MF was higher in the Class 3 malocclusion group than in other groups (Park et al., 2015). In this study, MF was detected above all age groups and malocclusion classes, and a significant difference was observed between malocclusion classes consistent with existing literature ($p<0.05$). The distance between MF and OP was found to be the lowest in the Class 2 malocclusion group and the highest in the Class 3 malocclusion group. We believe that the position of MF relative to OP in children with Class 3 malocclusion is higher than in other classes due to the excessive development of the mandible or the more advanced position of the mandible or since the molar teeth do not keep up with growth and development and remain stable, the OP remains low.

The distance to the OP showed a significant difference between the age groups in all malocclusion classes ($p<0.05$). MF was found to be 4.01 ± 2.59 mm above OP in the 9-13 age group and 5.05 ± 2.60 mm above OP in the 14-18 age group without distinction of malocclusion class. There was a difference of 0.75 mm between the age groups in Class 2 and 3 malocclusions and 1.65 mm in Class 1 malocclusion. Increasing the distance of MF to OP with increasing age indicates an increase in the size of the ramus of the mandible in the upward direction. In many studies, it has been reported that MF changes in the upward course with increasing age, similar to our study (Hwang et al., 1990; Movahhed et al., 2011; Paryab et al., 2015; Shukla et al., 2018). In light of our results, similar to the literature studies, determining the injection site in IANB by taking into account the malocclusion classes and the ages of the patients will help provide adequate anesthesia. Although MF was detected above OP at a rate of 95.45% in our study, it was observed at the OP level at 2.88% and below OP at 1.67%. This difference we detected was thought to be because pediatric patients with mixed dentition periods had canine and molar tooth eruptions at different times.

Studies evaluating the AP position of MF in children reported that the distance to the anterior increased with age, and MF shifted to the poste-

rior (Tsai, 2004; Pereira et al., 2013; Temür et al., 2022). In addition to the studies that report that MF is at the midpoint of the ramus, there are no changes in its age-related position. A study says that MF is in the inferoanterior in children (Hwang et al., 1990). The results are different because the study method, race, and age groups differ. In this study, it was found that the distance of MF to the posterior showed a positive correlation ($p<0.001$; r: +0.298) with age, and the distance of MF to the anterior showed a negative correlation ($p<0.02$; r: -0.086). A significant difference was found between the distance of the MF to the posterior edge and the age groups in all malocclusion classes. Besides, with the increase in age, it was seen that MF approached the middle point from the posterior edge. As a result of the age-related growth and development of the mandible, the distance between GO and MF increases due to MF's change of direction in the upward route (Shukla et al., 2018; Apaydın, 2020). In our study, the MF and GO distance significantly differed between age groups in malocclusion classes ($p<0.05$). We think that the distance between MF and GO shows a positive correlation with age due to the growth of the ramus of the mandible in the vertical direction and the increase in bone in the base of the mandible.

The study was conducted on a limited number of people who applied to the hospital for various reasons. In addition, the change in the OP due to the difference in eruption times of the canine and molar teeth, which form the OP, shows the limitation of this study. Therefore, further clinical studies with larger samples have to be conducted to determine the MF's location.

The position of the MF showed statistically significant differences in malocclusion classes and between age groups. It was seen that the MF was positioned in the upward direction parallel to the age increase and approached the midpoint of the ramus of the mandible from the posterior.

We detected MF 4.55 mm above the OP in Class 1 malocclusion, 4.10 mm in Class 2 malocclusion and 5.43 mm in Class 3 malocclusion. We believe that MF, especially in Class 3 malocclusion, being positioned higher than OP compared to other classes and showing a gender difference, will be a guideline for clinicians to minimize mistakes in providing effective and safe IANB in pediatric patients with malocclusion.

ACKNOWLEDGEMENTS

I would like to thank Prof. Dr. Aynur Emine Çiçekcibaşı for help in designing this article. Also, I would like to thank Research Assistant Betül Digilli for reviewing the text and Associate Professor Mehmet Alkanat for helping with statistical tests.

Ethical Approval

This study was approved by the Necmettin Erbakan University, Faculty of Medicine, Non-Pharmaceutical and Medical Device Research Ethics Committee (Number: 14567952-050/673, decision number 2020/2497).

Authors contributions

Keskin A and Çiçekcibaşı AE designed the study, Keskin A and Mağat G performed the literature search and analysis, Keskin A wrote the manuscript in consultation with Çiçekcibaşı AE and Açar G.

REFERENCES

AÇIKGOZ GS (2020) Farklı yaş grubu çocuklarda mandibular foramen konumunun panoramik radyografiler kullanılarak dijital yöntemle değerlendirilmesi. [Research Thesis, Gazi University] *https://avesis.gazi.edu.tr/yonetilen-tez/b3285e84-344f-4b84-b4b5- 1f99a850ddd1/farkli yas grubu cocuklarda mandibular foramen konumunun panoramik radyografiler kullanilarak dijital yontemledegerlendirilmesi*

AFSAR A, HAAS DA, ROSSOUW PE, WOOD RE (1998) Radiographic localization of mandibular anesthesia landmarks. *Oral Surg Oral Med Oral Pathol Oral Radiol Endodontol*, 86(2): 234-241.

AKMAN H, SURME K (2021) Locating mandibular foramen in children of different age groups using panoramic radiography. *J Stomatol*, 74(1).

APAYDIN BK (2020) Çocuklarda mandibular foramenlerin panoramik radyograflardaki konumu ve okluzal düzlemle ilişkisi. *Selcuk Dental J*, 7(1): 54-58.

BENHAM N (1976) The cephalometric position of the mandibular foramen with age. *ASDC J Dentistry Children*, 43(4): 233-237.

CORBET EF, HO DK, LAI SM (2009) Radiographs in periodontal disease diagnosis and management. *Aust Dent J*, 54 (Suppl 1): S27-43.

FERNANDEZ CCA, PEREIRA CVCA, LUIZ RR, VIEIRA AR, COSTA MC (2018) Dental anomalies in different growth and skeletal mal-occlusion patterns. *Angle Orthod*, 88: 195-201.

FEUERSTEIN D, COSTA-MENDES L, ESCLASSAN R, MARTY M, VAYSSE F, NOIRRIT E (2020) The mandibular plane: a stable reference to localize the mandibular foramen, even during growth. *Oral Radiol*, 36(1): 69-79.

FINDIK Y, YILDIRIM D, BAYKUL T (2014). Three-dimensional anatomic analysis of the lingula and mandibular foramen: A cone beam computed tomography study. *J Craniofacial Surg*, 25(2): 607-610.

GILL DS, NAINI FB (2013) Ortodontide prensipler ve pratik. *Medya yayın grubu*. İstanbul, Türkiye, pp 29-35.

HWANG TJ, HSU SC, HUANG QF, GUO MK (1990) Age changes in location of mandibular foramen. *Zhonghua Ya Yi Xue Hui Za Zhi*, 9(3): 98-103.

KANG SH, BYUN IY, KIM JH, PARK HK, KIM MK (2013) Three-dimensional anatomic analysis of mandibular foramen with mandibular anatomic landmarks for

inferior alveolar nerve block anesthesia. *Oral Surg Oral Med Oral Pathol Oral Radiol*, 115(6): e17-e23.

KRISHNAMURTHY NH, UNNIKRISHNAN S, RAMACHANDRA JA, ARALI V (2017) Evaluation of relative position of mandibular foramen in children as a reference for inferior alveolar nerve block using orthopantamograph. *JCDR*, 11(3): ZC71.

MOORE KL, DALLEY AF (2007) Kliniğe yönelik anatomi. *Nobel Tıp Kitabevleri*, İstanbul, Türkiye.

MOVAHHED T, MAKAREM A, IMANIMOGHADDAM M, ANBIAEE N, SARRAFSHIRAZI A, SHAKERI MT (2011) Locating the mandibular foramen relative to the occlusal plane using panoramic radiography. *J Appl Sci*, 11(3): 573-578.

ÖZ E, KÜÇÜKEŞMEN Ç (2019) Çocuklarda maloklüzyon ve ortodontik tedavi ihtiyacı. *Turkiye Klinikleri Dishekimligi Bilimleri Dergisi*, 25(2): 193-200.

PARK HS, LEE JH (2015) A comparative study on the location of the mandibular foramen in CBCT of normal occlusion and skeletal class II and III malocclusion. *Maxillofac Plastic Reconstr Surg*, 37(1): 9-25.

PARYAB M, AHMADYAR M (2015) Locating mandibular foramen in children with mandibular retrognathism in mixed dentition. *J Dent Res Dent Clin Dent Prospects*, 9(2): 66-71.

PEREIRA PNP, FERNANDES A, GUGISCH MC, ZARONI FM, FRANCO A, REBELLATO NLB (2013) Radiographic assessment of the mandibular foramen in children: Focus on anesthetic procedures. *Arch Oral Res*, 9(3).

SHUKLA RH, TIKU A (2018) Correlation of mandibular foramen to occlusal plane as a clinical guide for inferior alveolar nerve block in children: A digital panoramic radiographic study. *Contemp Clin Dentist*, 9(3): 372.

TEMUR KT, SOGUKPINAR OA (2022) Investigating permanent first molars of a Turkish pediatric sample in the Eastern Mediterranean region: A radiographic study. *J Exp Clin Med*, 39: 611-615.

TSAI HH (2004) Panoramic radiographic findings of the mandibular foramen from deciduous to early permanent dentition. *J Clin Pediat Dentist*, 28(3): 215-220.

TULOGLU DN, BAYRAK Ş (2010) Çocuk diş hekimliğinde kullanılan lokal anestezi teknikleri ve güncel yaklaşımlar. *Atatürk Üniversitesi Diş Hekimliği Fakültesi Dergisi*, (1): 53-61.

Possible therapeutic effect of combined platelet-rich plasma and stem cells on induced knee osteoarthritis in adult male albino rat: histological and immunohistochemical study

Nabila Y.A. Haleem, Mogeda M. Nasralla, Mohammed M. Abd El-Moaty, Eman F. Farid, Doaa M. Shuaib

Department of Anatomy and Embryology, Faculty of Medicine, Cairo University, Egypt

SUMMARY

Osteoarthritis (OA) is a degenerative joint disease that results from breakdown of joint cartilage and underlying bone. It is the most common form of arthritis among elderly individuals. The present study aimed to investigate the effect of intra-articular injection of platelet-rich plasma (PRP) and bone marrow mesenchymal stem cells (BMSCs), both in combination and separately in the treatment of monoiodoacetate (MIA) induced OA in rats. Seventy adult male albino rats were randomly divided into seven groups, 10 rats in each (control, sham control, OA-induced, PRP, BMSCs, PRP+BMSCs and recovery). Histological examination was done using haematoxylin and eosin, alcian blue and Masson's trichrome stains. Immunohistochemical staining for collagen type II antigen and proliferating cell nuclear antigen (PCNA) was carried out. Measurements of serum interleukin 6 (IL-6) was performed using ELISA. Expression of ACAN gene was done using real-time polymerase chain reaction (PCR) and histomorphometric measurements were analyzed. Radiographs were acquired from the knee joint. Light microscopic examination of articular cartilage (AC) from OA-induced group showed disorganization of chondrocytes, loss of zonation, pyknotic nuclei, empty lacunae and absent tidemark. There was a significant decrease in AC thickness, chondrocytes count, optical density of collagen and proteoglycan content, area percent of collagen II in the matrix in OA group compared to control and sham groups. These degenerative histomorphological alterations were associated with significant increase in serum IL-6 and decrease in ACAN gene expression. Radiographs showed narrowing of joint space and subchondral sclerosis. Intraarticular injection of PRP, BMSCs and PRP+BMSCs improved the previously mentioned alterations. Concomitant administration of PRP+BMSCs showed better effect than using PRP and BMSCs alone. In conclusion, PRP potentiated the effects of BMSCs on the repair of MIA-induced AC damage in rats. Injection of combination of

Corresponding author:
Doaa Mahmoud Shuaib. Faculty of Medicine, Cairo University, Department of Anatomy and Embryology, Kasr Al-Ainy Street, Faculty of Medicine, 11562 Cairo, Egypt. Phone: 00201005859263. E- mail: doaa.shuaib@kasralainy.edu.eg

Submitted: July 31, 2023. **Accepted:** September 25, 2023

https://doi.org/10.52083/LOAY6925

PRP with BMSCs could be considered as a promising therapy for OA in patients.

Key words: Osteoarthritis – Chondrocytes – Monoiodoacetate – Platelet rich plasma – Bone marrow mesenchymal stem cells

INTRODUCTION

Osteoarthritis (OA) is the most prevalent degenerative joint disease, which mostly impairs mobility and subsequent quality of life in elder individuals (Mehranfar et al., 2019). It affects both large and small joints of the body including the hand, feet, back, but the most commonly affected joints are hip and knee joints leading to disability (Samsonraj et al., 2017). Monoiodoacetate (MIA) is an inhibitor of glyceraldehyde-3-phosphate dehydrogenase activity and an inhibitor of glycolysis shown to induce chondrocyte death in vitro. Intra-articular injection of MIA induces chondrocyte death in the articular cartilage (AC) of rodent and non-rodent species (Pei et al., 2019).

Intra-articular injection of platelet rich plasma (PRP) is one of the current options for treatment of OA. The regenerative capacity of PRP is attributed to its high content of growth factors, which influence cartilage healing and regeneration. They include platelet-derived growth factor, transforming growth factor-, vascular endothelial growth factor, epidermal growth factor and insulin growth factor (Nabavizadeh et al., 2022). The use of mesenchymal stem cells is another propitious therapy of OA. The therapeutic use of MSCs is related to their anti-inflammatory activity and their capacity to differentiate into mesodermal lineages like fat, bone and cartilage (Bastos et al., 2020). Bone marrow mesenchymal stem cells (BMSCs) are the most studied and used cells in regenerative medicine (Samsonraj et al., 2017). While cell-based therapy has been shown to be hopeful for regeneration, there is a consideration that BMSCs perform better in the presence of PRP (Ahmad et al., 2020).

Although the effect of PRP and BMSCs on damaged cartilage separately is well known in the reviewed literature, studies considering the effect of their combined treatment were limited. Therefore, the aim of the current study was to assess the histological, histomorphometric and biochemical changes in osteoarthritic cartilage of knee joint and the possible ameliorative role of PRP, BMSCs and combined PRP and BMSCs.

MATERIAL AND METHODS

Animals

Seventy adult male albino rats of 170-200gram body weight with apparently healthy knee joints (no swelling or limitation of movement) were obtained from the Animal and Experimental House, Faculty of Medicine, Cairo University following the guidelines for the care and use of laboratory animals (approval NO. CU-III-F-74-19). The animals were housed in groups five per cage measuring 41×28×19 cm and allowed to standardized laboratory diet and water ad libitum throughout the experiment.

Chemicals

Mono-iodoacetate: It was purchased from Sigma-Aldrich Chemie GmbH (Sigma, St. Louis, MO, USA; cat #I2512) in the form of powder. A total amount of 30 mg of MIA powder was dissolved in 15 ml phosphate buffered saline solution (Guzman et al., 2003).

Phosphate buffered saline (PBS): It is a water-based salt solution containing disodium hydrogen, phosphate, sodium chloride, potassium chloride and potassium dihydrogen phosphate. It helps to maintain a constant PH.

Platelet rich plasma: An autologous PRP was freshly prepared and was injected within one hour after preparation in the form of 30µl of PRP dissolved in 20µl PBS intra-articular in the right knee joints of rats (Mifune et al., 2013). They were obtained from the Biochemistry Department, Faculty of Medicine, Cairo University.

Bone–marrow derived Mesenchymal stem cells: Isolation, culture and labeling of BMSCs were performed in Molecular Biology Unit, Biochemistry Department, Faculty of Medicine, Cairo University. According to Institutional Animal Care and Use Committee guidelines, 12 weeks old rats were sacrificed under chloroform anesthesia. The fe-

mur and tibia were removed under aseptic conditions and cancellous bone was removed and washed with PBS 4 or 5 times. Bone marrows were cleaned out using Dulbecco's Modified Eagle's media (DMEM) and media were changed every 3 to 4 days (Smajilagić et al., 2013). When huge colonies formed, cultures were rinsed twice with PBS and trypsin was added to cells (0.25% trypsin in 1ml Ethylene Diamine Tetra Acetate (EDTA)) for 5 minutes at 37°C. After centrifugation, cell pellets were resuspended with serum-supplemented medium and incubated in 25 cm3 culture flasks (Alhadlaq and Mao, 2004). The BMSCs in the culture were identified by their plastic adhesiveness and fusiform shape (Aziz et al., 2007). To track the migration and homing of BMSCs at the site of intraarticular injection, cultured cells were labeled with fluorescent cell tracker PKH26 (Sigma, USA, MINI26) according to manufacturer's instructions (Kyriak ou et al., 2008).

Experimental design

The animals were randomly divided into seven groups (ten rats in each) according to lottery randomization method (Singh and Masuku, 2014). Seven cards were prepared with labels representing the different groups. The cards were placed in a container and shuffled thoroughly. Each card was drawn one by one blindly from the container and each rat was assigned to the corresponding group based on the label on the card. This process was repeated until all rats had been assigned to the groups.

Group I (Control group): The rats were housed without any manipulation or medications. They were then subdivided into two subgroups:

Subgroup Ia: Consisted of five rats. They were sacrificed after two weeks from the onset of the experiment.

Subgroup Ib: Consisted of five rats. They were sacrificed after six weeks from the onset of the experiment.

Group II (Sham control group): The animals were injected intra-articular with a single dose of 0.5 ml of PBS through infrapatellar ligament of the right knee joint. They were then subdivided into two subgroups:

Subgroup IIa: Five rats were sacrificed after two weeks from the onset of the experiment.

Subgroup IIb: Five rats were sacrificed after six weeks from the onset of the experiment.

Group III (OA-induced group): The rats received a single intra-articular injection of 1 mg of MIA dissolved in 0.5 ml of PBS through infrapatellar ligament of the right knee joint and sacrificed two weeks after the injection (Guzman et al., 2003).

Group IV (PRP- treated group): They received single intra-articular injection of 30µl of PRP dissolved in 20µl PBS through infrapatellar ligament of the right knee joint two weeks after injection of MIA. The animals were sacrificed four weeks later (Mifune et al., 2013).

Group V (BMSCs- treated group): They received single intra-articular injection of 5.0X105 BMSCs resuspended in 50µl PBS through infrapatellar ligament of the right knee joint two weeks after injection of MIA, then were sacrificed four weeks later (Mifune et al., 2013).

Group VI (PRP+BMSCs-treated group): The rats received a single intra-articular injection of a combination of 30µl PRP dissolved in 20µl PBS and 5.0 X105 BMSCs through infrapatellar ligament of the right knee joint two weeks after injection of MIA. They were sacrificed after four weeks (Mifune et al., 2013).

Group VII (Recovery group): The rats received a single intra-articular of 1 mg of MIA dissolved in 0.5 ml of PBS through infrapatellar ligament of the right knee joint and were sacrificed six weeks after the injection (Matsumoto et al., 2009).

The animals subjected for intra-articular injection underwent general anesthesia by ether inhalation. The area surrounding the knee joint was trimmed and wiped with alcohol. The patellar ligament was seen as white line below patella. The knee joint was kept in a bent position and the drug was injected in the gap below the patella at a 90° angle using insulin syringe (Pitcher et al., 2016).

All animals were anesthetized by mild ether inhalation at the allocated time of each group, then sacrificed by intraperitoneal injection of phenobarbitone sodium (80µg/g). The femoral condyles of the right knee joint were dissected and fixed in

10% buffered formalin solution. The specimens were decalcified using EDTA. After changing the solution daily for six weeks, the specimens were subjected to the following:

Histological study

The specimens were dehydrated in ascending grades of alcohol, cleared in xylene, embedded in paraffin and sagittal sections of 5 µm thickness were cut and stained by:

- *Haematoxylin and eosin (H&E):* For routine histological examination (Kiernan, 2001).
- *Alcian blue:* For detection of proteoglycan in chondrocytes (Bancroft and Gamble, 2008).
- *Masson's trichrome:* For detection of collagen content in the matrix (Bancroft & Gamble, 2008).
- *Immunohistochemical staining for collagen type II antigen* (Bancroft & Gamble, 2008): Primary antibody: Collagen II Ab-3 (Clone 6B3): It is a mouse monoclonal antibody (thermoscientifice, CA 94538, USA, catalogue number MS-306-R7) at dilution 1:200 for detection of type II collagen.
- *Immunohistochemical staining for Proliferating Cell Nuclear antigen (PCNA):* Primary antibody: The PC10 monoclonal antibody (clone PC10, M0879): It is a mouse monoclonal antibody (Dako company, Cairo, Egypt, Catalog No.IMG.144A) at a dilution 1:100 was used for detection of cell proliferation.

Histomorphometric study

Five non-overlapping high power fields (x400) from five sections (from each rat) of 10 rats per group were randomly chosen. The measurements were obtained using "Leica Qwin 500 C*"* image analyzer computer system Ltd. (Cambridge, England).

The following parameters were measured:

- Articular cartilage thickness in H&E-stained sections (µm). Four measures were taken and the average was calculated for each slide.
- Optical density of proteoglycan content of chondrocytes in alcian blue stained sections.
- Optical density of collagen content of cartilage matrix in Masson's trichrome stained sections.
- Area percent of collagen II immunopositive matrix in collagen II-stained sections. Optical density of proteoglycan content of chondrocytes, collagen content of the matrix and area percent of collagen II immunopositive matrix were done by transforming the colored images into grey images then masking the positive areas by a red binary color using image analyzer software.
- Chondrocytes count in PCNA stained-sections. It was done by using counting cells tool in image analysis software.

Biochemical study

ELISA: Three ml blood was obtained from the rat's tail and collected in heparinized tubes for biochemical determination of serum level of IL-6 by an ELISA kit as described in manufacturer's instructions (R&D Systems, Inc., Minneapolis, MN).

Quantitative analysis of ACAN gene by real time polymerase chain reaction (RT- PCR):

Total RNA extraction: Articular cartilage was harvested and grounded by a mortar and pestle in liquid nitrogen. Extraction of RNA was done by homogenization in TRIzol reagent (Invitrogen, Life Technologies, USA) according to the instructions of the manufacturer. The RNA concentrations and purity were measured with an ultraviolet spectrophotometer.

Complementary DNA (cDNA) synthesis: The cDNA was synthesized from 1 ug RNA using Superscript III First-Strand Synthesis; a system described in the manufacturer's protocol (Invitrogen, Life Technologies). One ug of total RNA was mixed with 50 µM oligo (DT) 20, 50 ng/µL random primers, and 10 mM dNTP mix in a total volume of 10 µL. The mixture was incubated at 56 °C for five minutes. and then placed on ice for three minutes. The reverse transcriptase master mix containing 2 µL of 10× RT buffer, 4 µL of 25 mM MgCl2, 2 µL of 0.1 M DTT, and 1 µL of SuperScript III RT (200 U/µL) was added to the mixture and was incubated at 25 °C for ten minutes followed by 50 minutes at 50 °C.

Real time quantitative PCR: The relative abundance of mRNA species was assessed using the SYBR Green method on an ABI prism 7500 se-

quence detector system (Applied Biosystems, Foster City, CA). Primers were designed with Gene Runner Software (Hasting Software, Inc., Hasting, NY) from RNA sequences from Gene Bank. Quantitative RT-PCR was performed in a 25-µl reaction volume consisting of 2X SYBR Green PCR. Master Mix (Applied Biosystems), 900 nM of each primer and 2-3 µl of cDNA. Amplification conditions were 2 min. at 50°, 10 min. at 95° and 40 cycles of denaturation for 15 seconds and annealing/extension at 60° for 10 min. Data from real-time assays were calculated using the v1·7 Sequence Detection Software from PE Biosystems (Foster City, CA). Relative expression of studied gene mRNA was calculated using the comparative Ct method. All values were normalized to the beta actin gene and reported as fold change.

The primer sequence of the ACAN was:

F: 5′- AGATGGCACCCTCCGATACC -3′ R: 3′- GACACACCTCGGAAGCAGAA -5′

Radiographic evaluation

The procedure was performed at Faculty of Veterinary Medicine, Cairo University. It was carried out immediately after euthanasia before rigor mortis. A dental radiography periapical film unit was used. Radiographs were made in dorsoplantar position at full extension. The images were analyzed by a radiologist without knowledge of groups of animals evaluated (Morais et al., 2016).

Statistical analysis

The quantitative data were tabulated and subjected to statistical analysis using SPSS (statistical package for social science) version 21. The numerical data was described as mean ± standard deviation (SD). The statistical significance of the difference between all the obtained mean values will be assessed using one way ANOVA test. The Bonferroni post hoc test was applied to compare different groups. The probability level (p-value) ≥ 0.05 was considered significant.

RESULTS

Histological and histomorphometric results

Histological examination of AC sections from control group (subgroup Ia and Ib) and sham group (subgroup IIa and IIb) showed similar findings, therefore, they were discussed together.

Haematoxylin and eosin-stained sections: Examination of H&E-stained sections from control group (subgroup Ia and Ib) and sham group (subgroup IIa and IIb) showed normal morphological architecture with regular histological zones of AC. The superficial zone exhibited flat chondrocytes and the transitional zone was formed of rounded chondrocytes with rounded nuclei inside lacuna arranged in cell nests (composed of 2-4 chondrocytes). In the deep zone, chondrocytes were arranged in columns perpendicular to the surface of the cartilage. The tidemark appeared as a basophilic line separating the deep zone from underling calcified zone (Fig. 1a). On the other hand, degenerative histomorphological alterations were observed in OA-induced group in the form of loss of zonation, faint or absent tidemark, disorientation of chondrocytes and presence of ghost cells. Empty lacune with pyknotic nuclei were observed. The articular surface showed exfoliation of superficial zone (Fig. 1b).

Histomorphological improvement was observed in PRP-treated group. Regular articular surface, flat chondrocytes and cell nests were seen in the superficial zone and transitional zones respectively. However, cell columns could not be detected in the deep zone and tidemark was absent (Fig.1c). In BMSCs-treated group, zonal organization was detected apart from absent columns in the deep zone. In addition to obvious tidemark (Fig. 1d). In group VI, concomitant administration of PRP+BMSCs significantly alleviated MIA-induced AC alterations as evidenced by better zonal organization with reappearance of columns in the deep zone. However, the tidemark was faint (Fig. 1e). Moreover, there was no further improvement in recovery group, which showed loss of zonation, disorientation of chondrocytes, absent tidemark. In addition to the presence of clefts and pyknotic nuclei (Fig. 1f).

Statistically significant decrease in the mean AC thickness was observed in OA- induced group compared to control ($p<.001^*$) and sham groups ($p<.001^*$). Meanwhile, PRP, MSCs and concomitant PRP+MSCs groups showed a significant increase in the mean AC thickness compared to

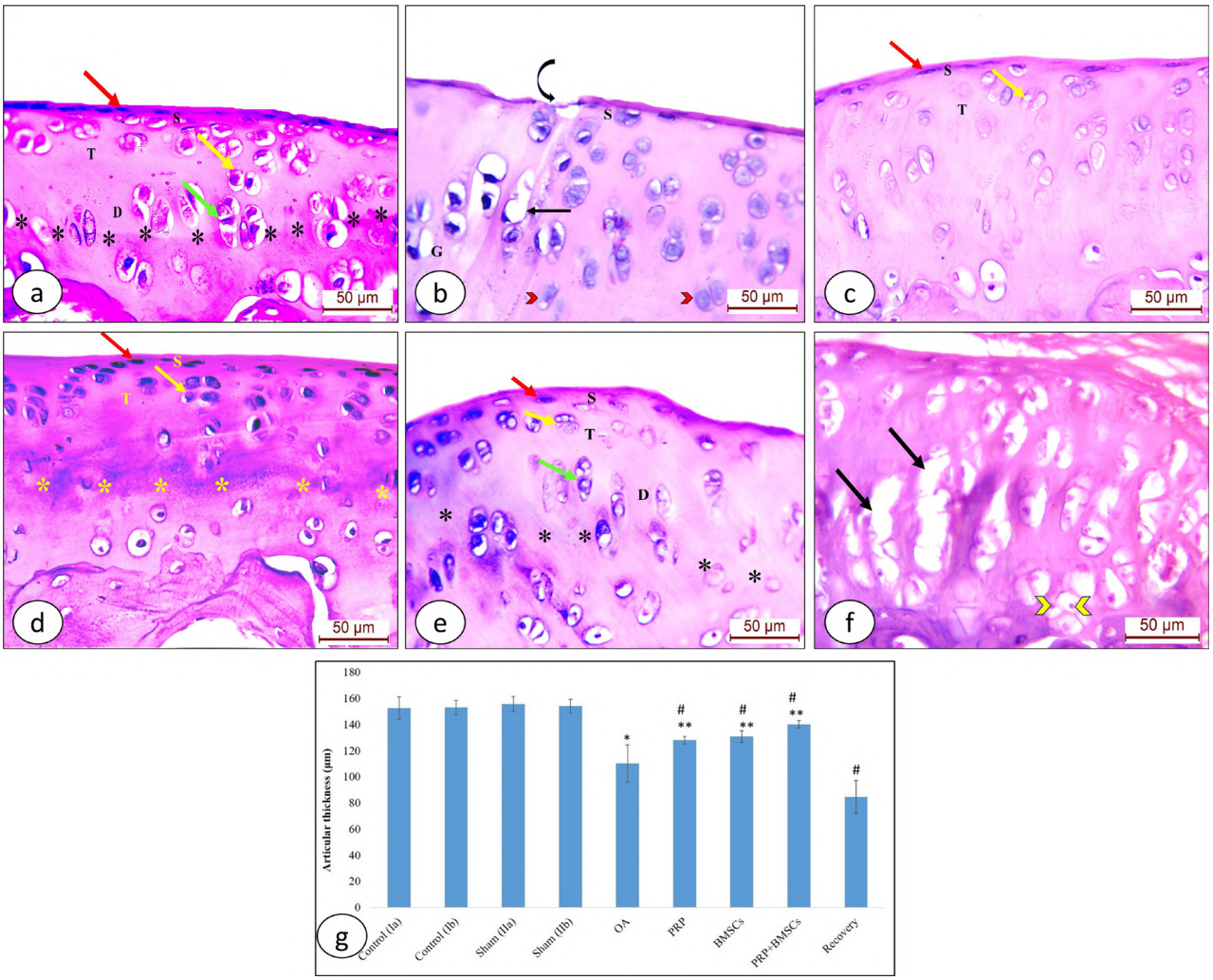

Fig. 1.- H&E-stained sections from rat AC of different groups (x400): **(a)** Sham control group shows normal architecture, elongated flat chondrocytes (red arrow) are shown in the superficial zone (S). The transitional zone (T) reveals rounded chondrocytes in cell nests (yellow arrow). The deep zone (D) displays chondrocytes arranged in columns (green arrow). The tidemark (*) is illustrated. **(b)** Section from OA-induced group demonstrates degenerative histomorphological alterations with loss of zonation, abnormal distribution of cells (arrowheads), exfoliation (curved arrow) in the superficial zone (S) and absent tidemark. Note presence of ghost cell (G). Empty lacuna with pyknotic eccentric nucleus is illustrated (arrow). **(c)** In PRP-treated group, flat chondrocytes (red arrow) and cell nests (yellow arrow) are shown in the superficial (S) and transitional (T) zones respectively. Cell columns and tidemark are absent. **(d)** BMSCs-treated group displays flat chondrocytes (red arrow) in the superficial zone (S) and cell nests (yellow arrow) in the transitional zone (T). Cell columns are absent. The tidemark (*) is shown. **(e)** In group VI, concomitant administration of PRP+BMSCs demonstrates regular articular surface. Flat chondrocytes (red arrow), cell nests (yellow arrow) and cell columns (green arrow) are illustrated in the superficial (S), transitional (T) and deep (D) zones respectivly.5 Faint tidemark (*) is shown. **(f)** Loss of zonation, disorientation of chondrocytes, clefts (arrows) and pyknotic nuclei (arrowheads) are illustrated in recovery group. The tidemark is absent. **(g)** Mean AC thickness in different groups: * (p<.05) vs control group, # (p< .05) vs OA, ** (p< .05) vs recovery. Scale bars: 50 µm.

OA-induced group (p=.041*, .008* and <.001* respectively). However, the difference in the mean AC thickness between PRP, MSCs and concomitant PRP+MSCs groups was statistically non-significant. Regarding recovery group, a statistically significant decrease in AC thickness was found compared to OA (p<.001*), PRP (p=.041*), MSCs (p<.001*) and concomitant PRP+MSCs (p<.001*) treated groups (Fig. 1g) (Table 1).

Alcian blue-stained sections: In alcian blue-stained sections, chondrocytes were deeply stained in control group (subgroup Ia and Ib) and sham group (subgroup IIa and IIb) (Fig. 2a). However, most of chondrocytes exhibited faint alcian blue staining in OA-induced group (Fig. 2b). Improvement was detected in PRP, BMSCs, as well as PRP+BMSCs-treated groups as most of chondrocytes were moderately stained by alcian blue (Figs. 2c, d, E). Faint alcian blue staining was observed in AC sections from recovery group (Fig. 2f).

Regarding the mean optical density of proteoglycan content in alcian blue-stained sections, there

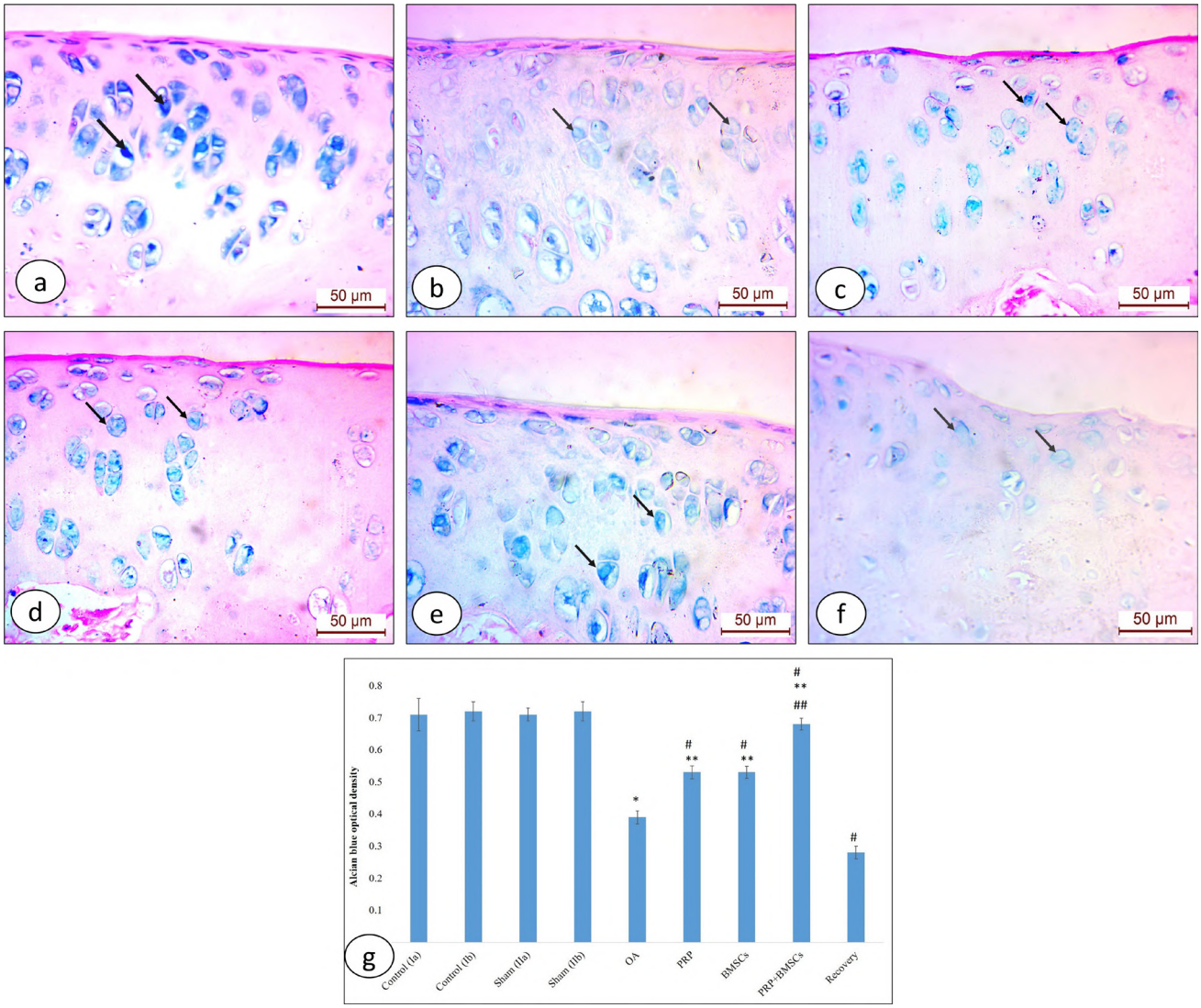

Fig. 2.- Alcian blue-stained sections from rat AC of different groups (x400): **(a)** Deep blue stained chondrocytes are shown in sham group (arrows). **(b)** OA-induced group reveals light blue stained chondrocytes (arrows). **(c, d, e)** Moderately stained chondrocytes are illustrated in PRP, BMSCs and concomitant PRP+BMSCs treated groups (arrows). **(f)** In recovery group, light blue stained chondrocytes are demonstrated (arrows). **(g)** Mean optical density of proteoglycan content of chondrocytes in AC in different groups: *(p<.05) vs control group, # (p< .05) vs OA, ** (p< .05) vs recovery, ## (p< .05) vs PRP group and BMSCs group. Scale bars: 50 µm.

was significant decrease in OA-induced group compared to control (p<.001*) and sham groups (p<.001*). A statistically significant increase in the mean optical density in PRP (p<.001*), MSCs (p<.001*) and concomitant PRP+MSCs (p<.001*) groups was found compared to OA-induced group. Moreover, there was significant increase in the optical density in concomitant PRP+MSCs group compared to PRP (p<.001*) and MSCs (p<.001*) groups indicating better response. Regarding recovery group, the mean optical density showed a significant decrease compared to OA (p<.001*), PRP (p<.001*), MSCs (p<.001*) and concomitant PRP+MSCs (p<.001*) groups (Fig. 2g) (Table 1).

Masson's trichrome-stained sections: Regarding control group (subgroup Ia and Ib) and sham group (subgroup IIa and IIb), examination of Masson's trichrome-stained sections exhibited deeply stained basophilic matrix by large amount of collagen (Fig. 3a). Decreased collagen was observed in OA-induced group in the form of areas of mild to moderate basophilic staining (Fig. 3b). In PRP-treated group, the matrix showed moderate basophilic staining (Fig. 3c), while in BMSCs-treated group, moderate to deep basophilic staining of matrix was detected (Fig. d). Combined PRP+BMSCs treated group exhibited deeply stained basophilic matrix indicating increased collagen (Fig. e). Examination of sections

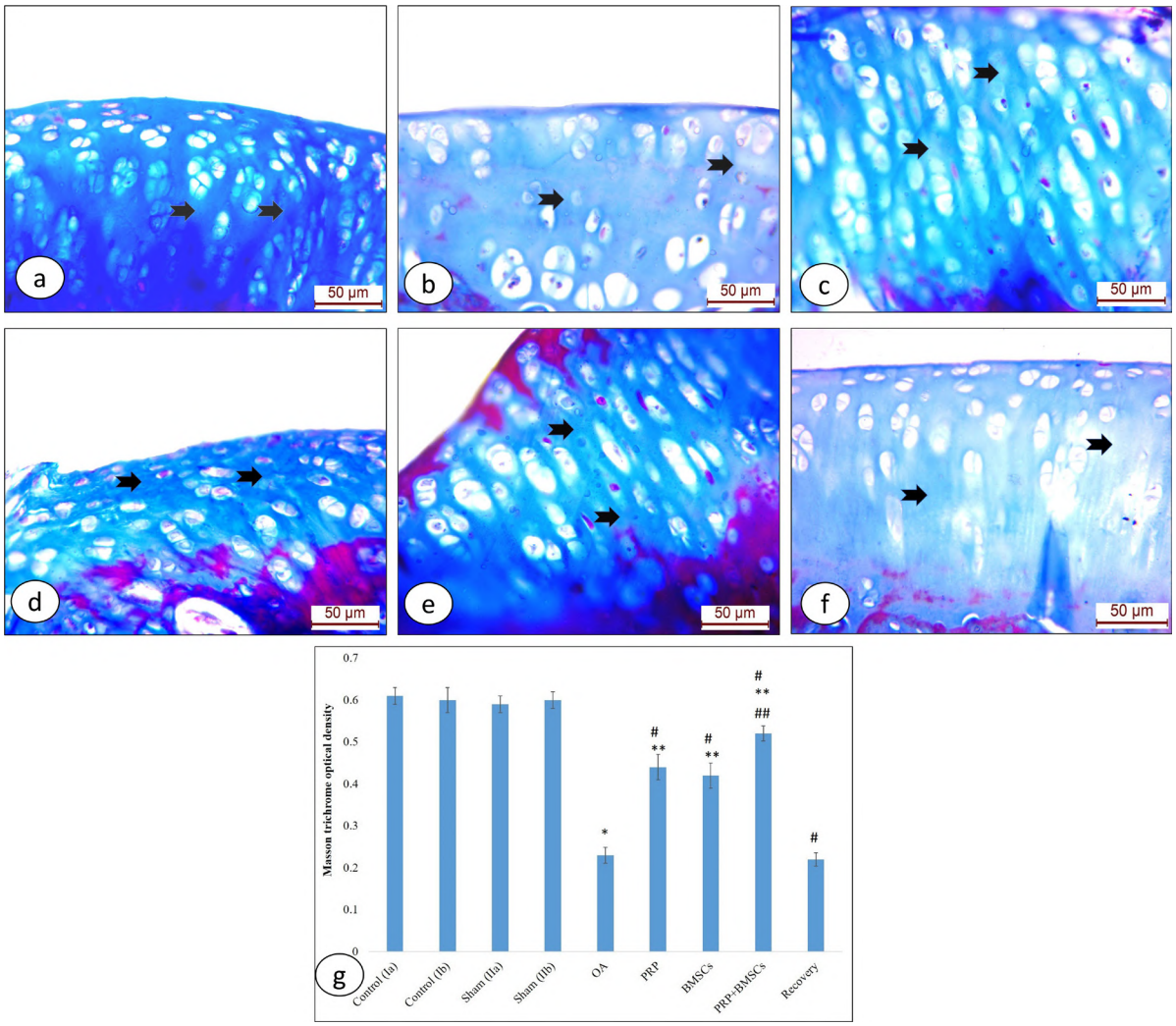

Fig. 3.- Masson's trichrome-stained sections from rat AC of different groups (x400): **(a)** Sham control group shows deeply stained basophilic matrix between chondrocytes. (arrows). **(b)** Mild to moderate basophilic staining of matrix is demonstrated in OA-induced group (arrows). **(c)** Matrix shows moderate basophilic staining in PRP-treated group (arrows). **(d)** In BMSCs-treated group, moderate to deep basophilic staining of matrix is illustrated (arrows). **(e)** PRP+BMSCs cotreatment group displays deeply stained basophilic matrix (arrows). **(f)** Mildly stained basophilic matrix is shown in recovery group (arrows). **(g)** Mean optical density of collagen content in the matrix of AC in different groups: * (<.05) vs control group, # (p< .05) vs OA, ** (p< .05) vs recovery, ## (p< .05) vs PRP group and BMSCs group. Scale bars: 50 µm.

Table 1. Mean values of AC thickness, optical density of proteoglycan content, optical density of collagen content, area percent of collagen II and chondrocytes count in all rat groups.

Groups	Articular cartilage thickness (µm) (Mean± SD)	Optical density of proteoglycan content (Mean± SD)	Optical density of collagen content (Mean± SD)	Area percent of collagen II (Mean± SD)	Chondrocytes count (Mean± SD)
Ia (Control group)	152.7 ± 8.6	0.71 ± .05	0.61 ± .02	58.6± 2.3	50.2± 1.9
Ib (Control group)	153.1 ± 5.4	0.72 ± .03	0.60 ± .03	57.5 ± 1.9	50.6 ± 3
IIa (Sham control group)	155.7 ± 5.7	0.71 ± .02	0.59 ± .02	56.4 ± 1.2	47.8 ± 1.4
IIb (Sham control group)	154.2 ± 5.2	0.72 ± .03	0.60 ± .02	56.9 ± 1.4	49.6 ± 2.7
III (OA-induced group)	110.2 ± 14.2	0.39 ± .02	0.23 ± .019	28.1 ± 1.8	23 ± 2.7
IV (PRP-treated group)	128.1 ± 2.9	0.53 ± .02	0.44 ± .03	34.8 ± 1.0	36.2 ± 3.3
V (MSCs-Treated group)	130.9 ± 4.5	0.53 ± .019	0.42 ± .03	41.02 ± 0.9	38 ± 1.8
VI (PRP+BMSCs-treated group)	140.2 ± 2.7	0.68 ± .018	0.52 ± .018	48.6 ± 2.6	44.2 ± 1.9
VII (Recovery group)	84.6 ± 12.6	0.28 ± .02	0.22 ± .016	18 ± 0.8	13.2 ± 1.6

SD: Standard deviation, OA: Osteoarthritis, PRP: Platelet rich plasma, BMSCs: Bone marrow mesenchymal stem cells

from recovery group revealed mild staining of matrix reflecting decreased collagen (Fig. 3f).

The mean optical density of collagen content in the matrix of AC in OA-induced group showed significant decrease compared to control (p<.001*) and sham groups (p<.001*). Regarding PRP, MSCs and PRP+BMSCs treated groups, a statistically significant increase of the optical density was recognized compared to OA-induced group (p<.001* in the three groups). Further improvement was found in PRP+BMSCs treated group as evident by the significant increase in the optical density compared to PRP (p<.001*) and MSCs (p<.001*) treated groups (Fig. 3g). Furthermore, a statistically significant decrease in the optical density was detected in recovery group compared to OA (p<.001*), PRP (p<.001*), MSCs (p<.001*) and PRP+BMSCs (p<.001*) treated groups (Fig. 3g) (Table 1).

Collagen II immune-stained sections: Examination of collagen II-stained sections of control group (subgroup Ia and Ib) and sham group (subgroup IIa and IIb) showed strong extracellular immunoreactivity in the superficial zone, moderate immunoreactivity in the transitional zone and mild to moderate immunoreactivity of the deep zone. Collagen bundles were seen (Fig. 4a). In OA-induced group, weak extracellular immunoreactivity with patchy appearance was observed (Fig. 4b). Examination of sections from PRP and BMSCs treated groups exhibited strong immunostaining in the superficial zone and moderate staining in the transitional zone. Patches of collagen fibers were detected in the deep zone (Figs. 4c, d). In group VI (PRP+BMSCs concomitant administration), there was an increase in collagen II immunoreactivity with strong immunostaining in the superficial zone, moderate staining in the transitional zone and mild staining of deep zone. Moreover, collagen bundles were observed in this group (Fig. 4e). Sections of group VII (recovery group) revealed weak extracellular immunoreactivity of collagen II (Fig. 4f).

The mean area percent of collagen II revealed a significant decrease in OA-induced group in comparison to control (p<.001*) and sham groups (p<.001*) (Fig. 4g). In PRP, MSCS and PRP+BMSCs treated groups, a statistically significant increase in the mean area percent was found compared to OA-induced group (p<.001* in the three groups) (Fig. 4g). Also, concomitant PRP+BMSCs administration showed a significant increase in the mean area percent compared to PRP (p<.001*) and MSCs (p<.001*) groups (Fig. 4g). When comparing recovery group to OA, PRP, MSCs and PRP+BMSCs treated groups, a significant decrease in the mean area percent was found (p<.001* in the four groups) (Fig. 4g) (Table 1).

PCNA-immunostained sections: Abundant proliferating chondrocytes were detected in PCNA-stained sections from control group (subgroup Ia and Ib) as well as sham group (subgroup IIa and IIb) (Fig. 5a). On the other hand, few chondrocytes were detected in OA- induced group (Fig. 5b). Abundant proliferating chondrocytes were detected in PRP, BMSCs and concomitant PRP+BMSCs treated groups (Figs. 5c, d, e). Sections of AC from recovery group showed few chondrocytes (Fig. 5f).

Regarding chondrocytes count, there was a significant decrease in OA-induced group compared to control (p<.001*) and sham (p<.001*) groups. While in PRP, MSCS and PRP+BMSCs treated groups, a statistically significant increase was found compared to the OA-induced group (p<.001*in the three groups). Moreover, there was a statistically significant increase in the chondrocyte count in PRP+BMSCs treated group compared to PRP and MSCs groups (p<.001*, <.008* respectively) indicating further improvement. When comparing recovery group to OA, PRP, MSCs and PRP+BMSCs treated groups, a statistically significant decrease in chondrocytes count was observed (p<.001* in the four groups) (Fig. 5g) (Table 1).

Biochemical results

Determination of serum level of IL-6: The level of the proinflammatory cytokine interleukin IL-6 was measured in the serum of rats from different groups. A significant increase in the mean serum IL6 level was found in OA-induced group in comparison to control (p<.001*) and sham (p<.001*) groups. Treatment with PRP, MSCs as well as PRP and BMSCs concomitantly resulted in a significant reduction in IL-6 levels compared to OA- induced

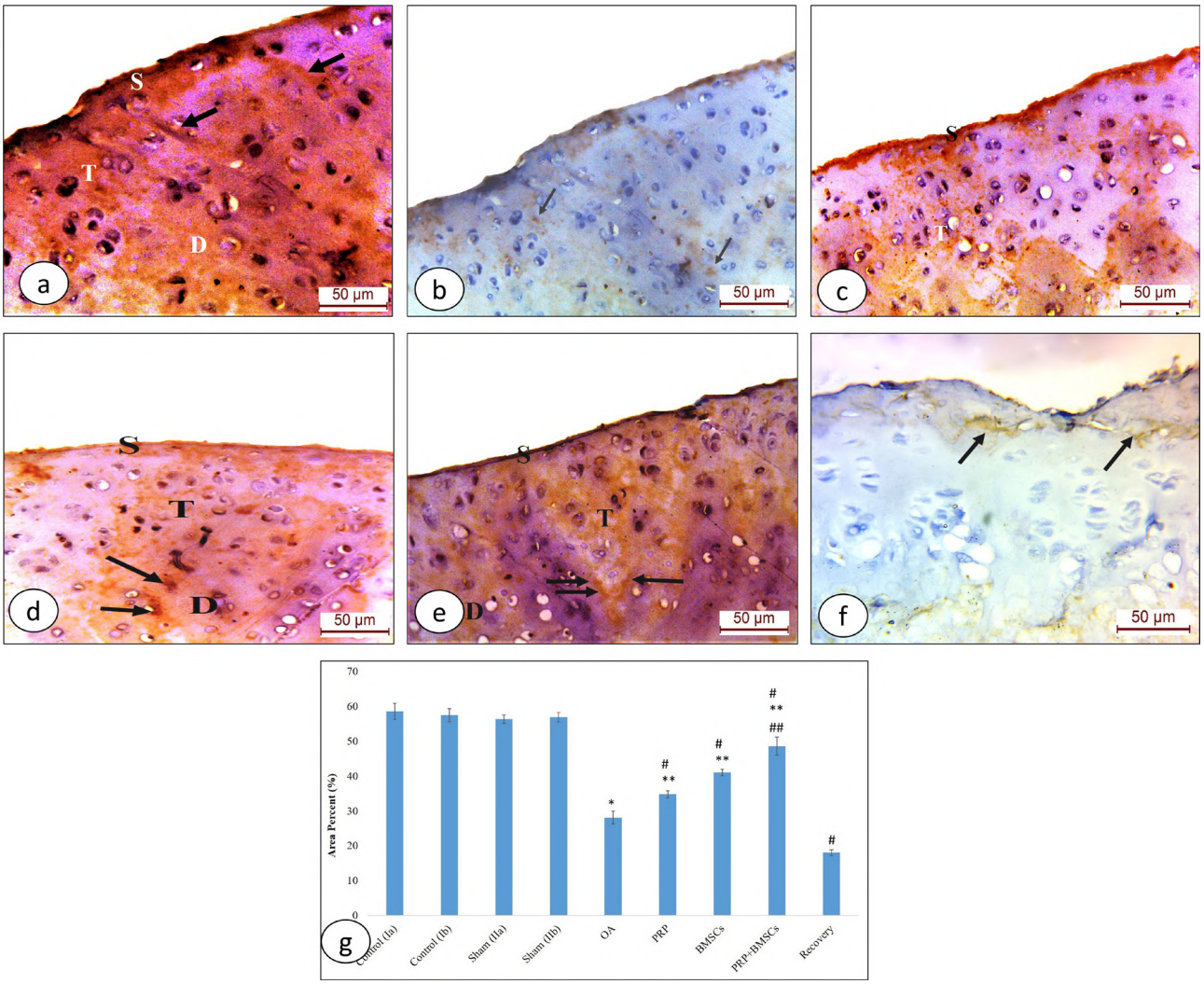

Fig. 4.- Anti collagen II immunostained sections from rat AC of different groups (x400): **(a)** Sham control group shows strong extracellular immunoreactivity in the superficial zone (S), moderate immunoreactivity in the transitional zone (T) and mild to moderate immunoreactivity in deep zone (D). Collagen bundles (arrows) are shown. **(b)** Weak extracellular immunoreactivity of collagen II with patchy appearance is detected in OA-induced group (arrows). **(c)** Strong immunoreactivity in the superficial zone (S) and moderate staining of the transitional zone (T) are demonstrated in PRP-treated group. **(d)** BMSCs-treated group exhibits strong immunoreactivity in the superficial zone (S) and moderate staining in the transitional zone (T). Patches of collagen fibers (arrows) are shown in the deep zone (D). **(e)** Concomitant administration of PRP+BMSCs in group VI displays strong immunoreactivity in the superficial zone (S), moderate staining in the transitional zone (T) and mild staining in the deep zone (D). Collagen bundles are shown (arrows). **(f)** In recovery group, weak extracellular immunoreactivity of collagen II is demonstrated (arrows). **(g)** Mean area percent of collagen II content of cartilage matrix in different groups: * (<.05) vs control group, # (p< .05) vs OA, ** (p< .05) vs recovery, ## (p< .05) vs PRP group and BMSCs group. Scale bars: 50 µm.

group (p<.001* in the three groups). Moreover, better therapeutic effect was found with PRP and BMSCs coadministration as a significant decrease in IL6 level was found in this group compared to PRP (p<.001*) and MSCs groups (p<.001*). Considering recovery group, a significant increase in the level of IL6 was observed in comparison with OA (p<.001*), PRP (p<.001*), MSCs (p<.001*) and PRP+BMSCs (p<.001*) treated groups (Fig. 6) (Table 2).

Expression of ACAN gene in the AC: When compared with control and sham groups, MIA administration in OA-induced group resulted in a significant decrease in ACAN gene expression (p<.001*). In PRP, MSCs and PRP+BMSCs treated groups, there was a statistically significant increase in ACAN gene expression compared to OA-induced group (p<.001* in the three groups). Concomitant administration of PRP and BMSCs in group VI resulted in a considerable upregulation in the expression of ACAN gene when compared to PRP (p<.001*) and MSCs (p<.001*) groups. Recovery from MIA resulted in a statistical drop in the expression of ACAN gene when compared to OA (p<.001*), PRP (p<.001*), MSCs (p<.001*) and PRP+BMSCs (p<.001*) treated groups (Fig. 7) (Table 2).

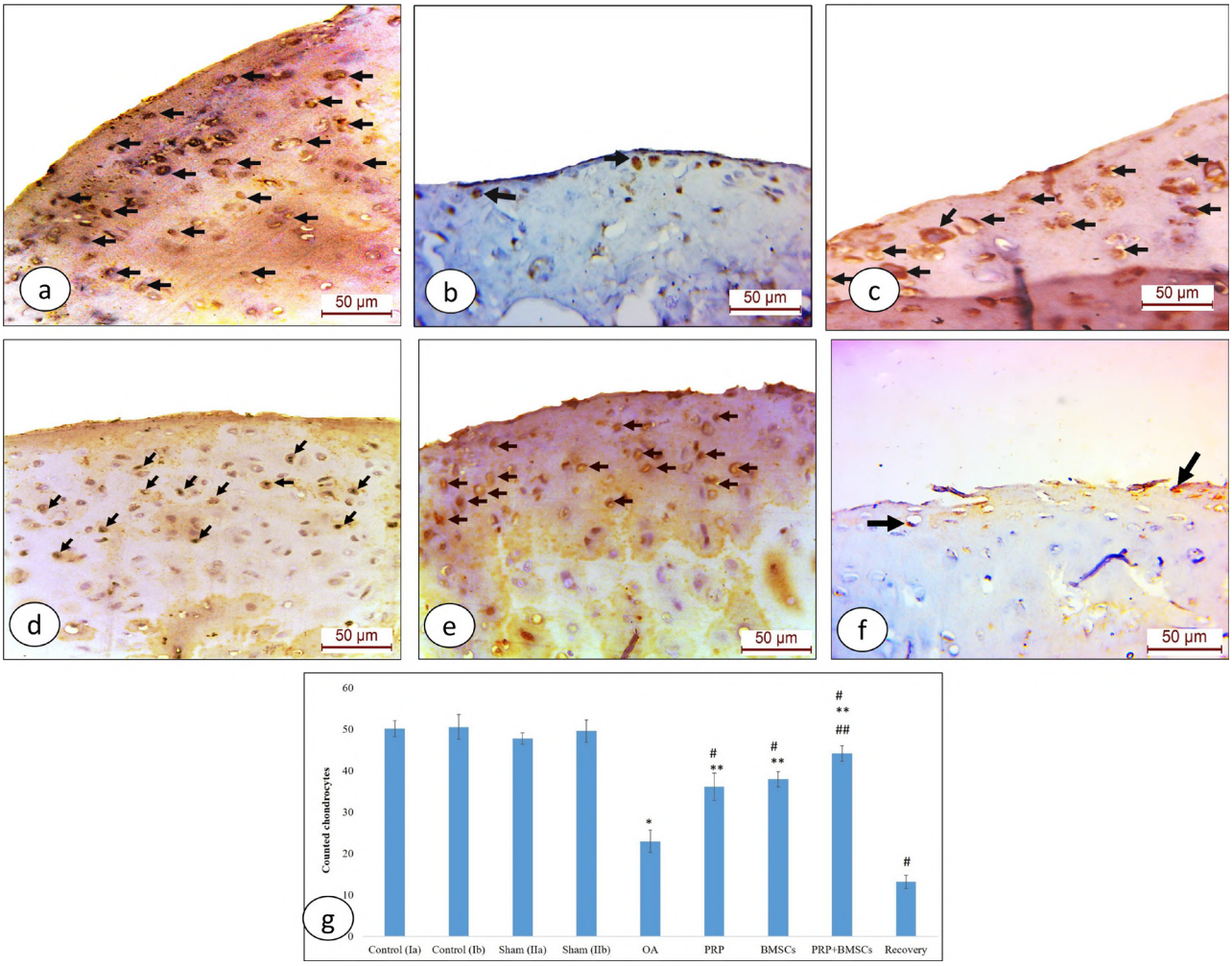

Fig. 5.- PCNA immunostained sections from rat AC of different groups (x400): **(a)** Abundant proliferating chondrocytes are illustrated in control group (arrows). **(b)** OA-induced group exhibits few proliferating chondrocytes (arrows). **(c, d, e)** Abundant chondrocytes are demonstrated in PRP, BMSCs and concomitant PRP+BMSCs treated groups (arrows). **(f)** Recovery group shows few chondrocytes (arrows). **(g)** Mean chondrocytes count in AC in all groups: * (p<.05) vs control group, # (p< .05) vs OA, ** (p< .05) vs recovery, ## (p< .05) vs PRP group and BMSCs group. Scale bars: 50 µm.

Table 2. Mean values of inflammatory marker IL-6 (pg/ml) in serum and ACAN gene expression articular cartilage tissue in all rat groups.

Groups	IL6 (pg/ml) (Mean± SD)	ACAN gene expression (Mean± SD)
Ia (Control group)	33.6 ± 1.3	1.05 ± .03
Ib (Control group)	33.3 ± 1.2	1.06 ± .02
IIa (Sham control group)	33.1 ± 2.2	1.08 ± .06
IIb (Sham control group)	33.5 ± 2.6	1.06 ± .08
III (OA-induced group)	96.2 ± 1.5	.3 ± .04
IV (PRP-treated group)	71.9 ± 3.5	.7 ± .03
V (MSCs-Treated group)	50.7 ± 1.6	.7 ± .03
VI (PRP+BMSCs-treated group)	41.6 ± 1.6	.9 ± .02
VII (Recovery group)	124.5 ± 4.5	.2 ± .04

SD: Standard deviation, OA: Osteoarthritis, PRP: Platelet rich plasma, BMSCs: Bone marrow mesenchymal stem cells

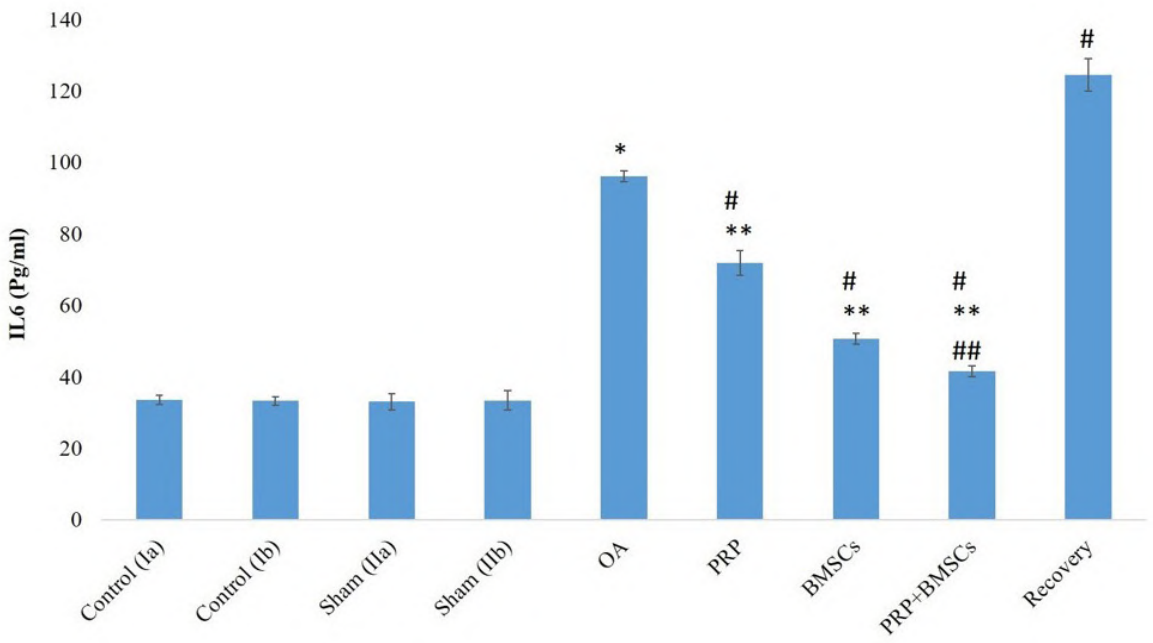

Fig. 6.- Mean level of serum IL-6 in different groups: * (<.05) vs control group, # (p< .05) vs OA, ** (p< .05) vs recovery, ## (p< .05) vs PRP group and BMSCs group.

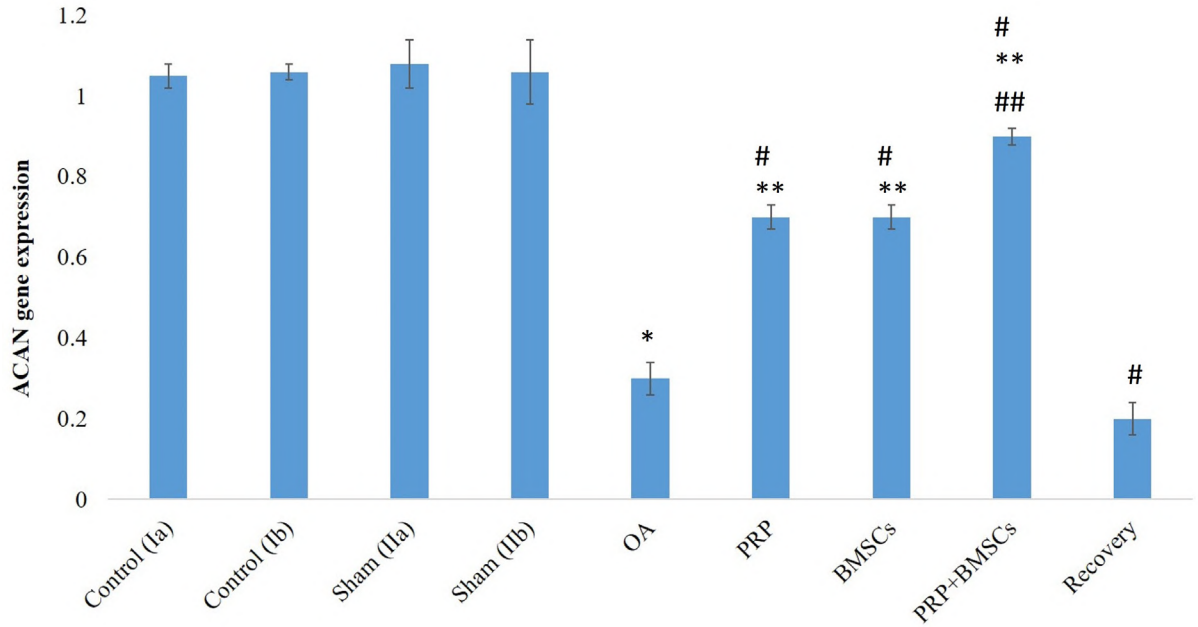

Fig. 7.- Mean level of ACAN gene expression in different groups: * (p<.05) vs control group, # (p< .05) vs OA, ** (p< .05) vs recovery, ## (p< .05) vs PRP group and BMSCs group.

Radiographic results

Radiographs of the knee joint from control and sham groups demonstrated a regular articular surface with normal tibiofibular joint space. No osteophytes were detected (Fig. 8a). On the other hand, X-rays of the knee joint from OA-induced groups showed narrowed tibiofibular joint space compartment, irregular tibial articular surface, subchondral sclerosis and minute marginal osteophytes (Fig. 8b). Improvement of joint space was observed in radiographs from PRP, BMSCs and concomitant treatment groups with no mar-

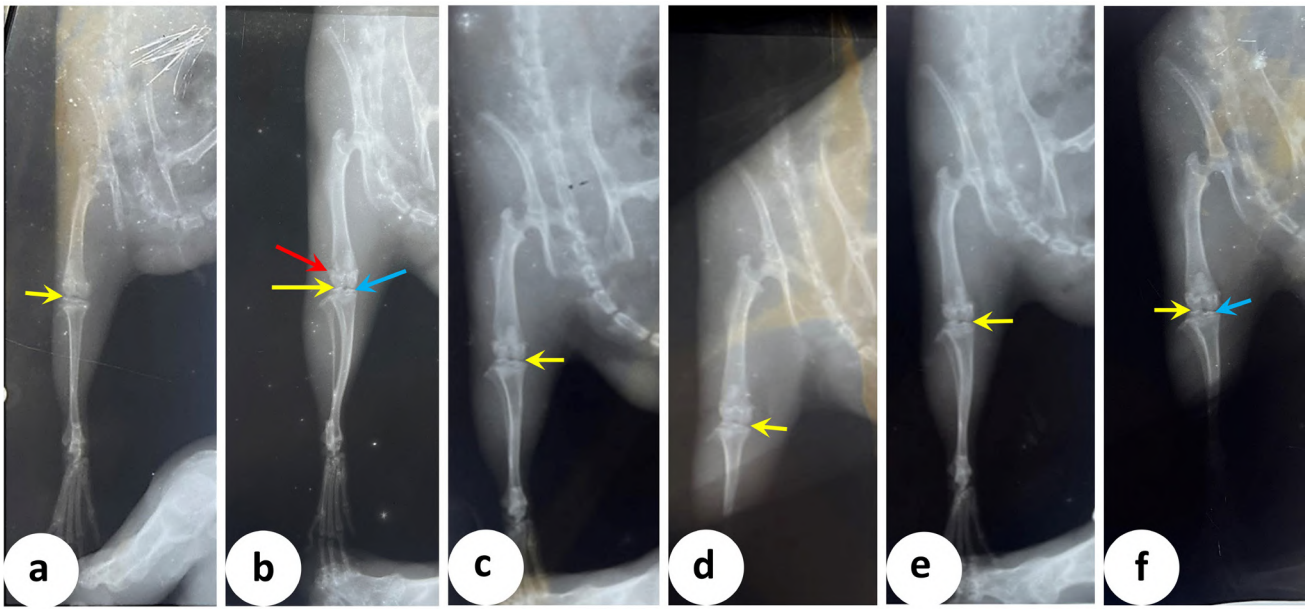

Fig. 8.- Radiographs of the rat right knee joint from different groups: **(a)** Control group shows normal tibiofibular joint space (yellow arrow). **(b)** Joint space narrowing (yellow arrow), minute marginal osteophytes (red arrow), irregular tibial articular surface and subchondral sclerosis (blue arrow) are illustrated in OA-induced group. **(c, d, e)** In PRP, BMSCs and concomitant PRP+BMSCs treated groups, there is apparent improvement of joint space (blue arrows) with absence of marginal osteophytes. **(f)** Recovery from MIA reveals narrowing of joint space (yellow arrow), irregular tibial articular surface and subchondral sclerosis (blue arrow).

ginal osteophytes (Figs. 8c, d, e). Recovery from MIA revealed narrowing of the joint space, irregular tibial articular surface and subchondral sclerosis (Fig. 8f).

DISCUSSION

Osteoarthritis is the most common form of arthritis and one of the leading causes of disability. The knee joint is the most affected joint (Mora et al., 2018). The present study aimed to determine whether PRP can improve the beneficial effect produced by BMSCs for AC repair after OA induction by comparing the therapeutic effect of combined BMSCs and PRP treatment with the PRP and BMSCs alone.

In the current study, examination of rat AC from OA-induced group showed disorganization of chondrocytes, loss of zonation, pyknotic nuclei and empty lacunae. There was a significant decrease in AC thickness compared to control and sham groups. These findings were consistent with Gamal et al. (2019), who induced OA surgically through cartilaginous defect in the rat knee joint. The decrease in AC thickness could be attributed to chondrocyte death and loss of matrix, as suggested by Guzman et al. (2003). Another pathological alteration in the AC from OA-induced group was the significant decrease in chondrocytes count with subsequent diminution of proteoglycan production. This was confirmed by the significant decrease in the optical density of proteoglycan content compared to control and sham groups. Similar findings were reported by Zare et al. (2020), who studied the proteoglycan content in chondrocytes using toluidine blue stain after induction of OA by intraarticular injection of collagenase type II.

The significant decrease in chondrocytes count and proteoglycan in OA-treated group in the current work was associated with downregulation in ACAN gene expression. In agreement with this result, Dranitsina et al. (2019) reported that ACAN gene expression level decreased two times against control after intra-articular injection of MIA. It was reported that ACAN gene provides instructions for making aggrecan, which is a type of proteoglycan that binds collagen II fibrils and retains water, providing osmosis necessary for the normal function of cartilage (Stöve et al., 2001). Largo et al. (2010) suggested that in OA, oxidative stress leads to chondrocytes death with subsequent decrease in ACAN gene expression and proteoglycan.

The matrix of AC in OA-induced group in the present work showed mild to moderate basophilic staining by Masson's trichrome indicating decreased collagen. This result was consistent with Marino-Martínez et al. (2019), who suggested that necrosis of cartilage cells by OA leads to collagen decrease from the matrix. Furthermore, a significant decrease in the mean area percent of collagen II was found in OA-induced group in this study compared to control and sham groups. A similar finding was mentioned by Zhou et al. (2019) in their study on surgically induced rat knee OA.

Recent research by Ahmad et al. (2020) has shown the important role of inflammation in the pathogenesis of OA. The authors hypothesized that IL-6 is a crucial inflammatory mediator that modulates metalloproteinase activity with subsequent destruction of cartilage in OA. In the present work, degenerative changes in OA-induced group were associated with a significant increase in serum IL-6 level compared to control and sham groups. Similar results were reported by Bastos et al. (2020), who found an increase in the level of IL-6 in the serum of patients with OA.

In the present work, histomorphological improvement was observed in AC from PRP-treated group, apart from disorganization of chondrocytes in the deep zone and absent tidemark. In contrast, Gamal et al. (2019) reported complete zonal organization with clearly seen tidemark. The improvement found in PRP-treated group in this study was associated with a significant increase in chondrocytes count and cartilage height. This was in accordance with Asjid et al. (2019), who proposed that the increase in chondrocyte count was due to the inhibitory effect of PRP on chondrocytes apoptosis.

In addition, a significant increase in the mean optical density of proteoglycan content with increase in ACAN gene expression was observed after PRP administration in the present work compared to OA-induced group. Similarly, Gamal et al. (2019), examined proteoglycan content using toluidine blue stain and found significant increase after adding PRP to osteoarthritic rat knee joint.

It was reported that PRP has anti-inflammatory properties, as it decreases inflammation and accelerates the healing process (Ameer et al., 2018). This was evident in the current study by the significant decrease in serum IL-6 level in PRP-treated group compared to OA-induced group. Similarly, Moussa et al. (2017) used human osteoarthritic chondrocytes, which were co-cultured with an increasing concentration of PRP, and reported significant decrease in IL-6 expression in PRP-treated chondrocytes in a dose dependent manner. The potential therapeutic effect of PRP was also attributed to its ability to inhibit the catabolic effect of MIA or stimulate the anabolic response of the damaged cartilage (Dhillon et al., 2014).

Regarding BMSCs-treated group in the current study, well organized chondrocytes with clearly demarcated tidemark were observed, aside from absent columns in the deep zone of AC. A significant increase in AC thickness was found compared to OA-treated group. In agreement with these findings, Zhou et al. (2019) reported that AC thickness increased significantly, and cartilage degradation apparently decreased after MSCs administration in surgically induced rat knee OA. Moreover, the proteoglycan content and ACAN gene expression level in BMSCs-treated group in the present work increased significantly compared to OA-treated group, which agreed with Latief et al. (2016) and Chen et al. (2019). Those authors used Safranin O stain to detect proteoglycan content of chondrocytes in their studies on animal models of OA. Compared to OA-induced group, treatment by BMSCs in the present study showed a significant increase in the mean optical density of collagen and collagen II in Masson's trichrome and collagen II-stained sections respectively. Similar observations were reported by Zhou et al. (2019) and Kim et al. (2021).

Bastos et al. (2020) attributed the therapeutic effect of MSCs to both their anti- inflammatory activity and the multilineage differentiation. This was confirmed in the present study by the significant decrease in IL-6 in the serum of rats in BMSCs-treated group compared to OA-induced group. In agreement to these findings, a significant decrease in IL-6 after treatment of OA model by MSCs was reported by Zhou et al. (2019).

It was reported that combinational therapy in OA is becoming a popular method for cartilage

repair (Ahmad et al., 2020). In the present work, concomitant PRP+BMSCs administration showed better AC surface continuity and integrity with well-organized three zones of AC. A significant increase in chondrocytes count and proteoglycan content was found in this group compared to either PRP or BMSCs treated group alone. Similar findings were observed by Nabavizadeh et al. (2022), who hypothesized that PRP reinforces the beneficial impacts of MSCs. The significant increase in proteoglycan content in combined group in this study was accompanied by upregulation in ACAN gene level compared to PRP and BMSCs treated groups, which agreed with Ahmad et al. (2020). It was suggested that adding PRP to MSCs decreases cartilage degradation and accelerates OA repair through the release of pro-angiogenic factors, which mobilize the circulation and improve the subchondral bone vasculature (Fahy et al., 2018). In addition, Li et al. (2016) reported that PRP forms a gel, which acts as a scaffold to hold stem cells and helps in the sustained release of growth factors.

The collagen content of the matrix in combined PRP+ BMSCS treated group in the current work showed a significant increase in the optical density of Masson trichrome stained and collagen II-stained sections in comparison to PRP and BMSCs groups. Similar results were reported by Ahmad et al. (2020), who used PRP and adipose-derived MSCs, both in combination and separately in the treatment of surgically induced OA in rats. Another study by Nabavizadeh et al. (2022) revealed a significant increase in collagen II after adding PRP to the used MSCs. Mifune et al. (2013) found a significant increase in collagen II immunostaining in MSCs+PRP compared to PRP treated groups. However, the difference between MSCs+PRP and MSCs groups was non-significant. This might be attributed to the type of stem cells they used in their research (mesenchymal stem cells), although they used the same dose and duration as the present study.

Chen et al. (2014) proposed that adding PRP to MSCs induces chondrogenesis by inhibition of inflammation. The current study revealed that concomitant PRP+BMSCs administration was superior to either PRP or BMSCs treatment alone in reducing IL-6 level indicating better anti-inflammatory effect of combined therapy. These results were in accordance with Ahmad et al. (2020). In a contradicting study, Bastos et al. (2020) reported a non-significant difference in human IL-6 level between MSCs, MSCs+PRP and corticosteroid-treated groups. The authors attributed the lack of statistical significance to small sample size and heterogeneity in cytokine levels among donors.

In the present study, worsening of osteoarthritic changes was observed in MIA- recovery group after longer duration without treatment as irregular eroded surface, degenerated chondrocytes and several clefts. Similar results were found by Al-Saffar et al. (2009*),* who reported that the effect of MIA was a time and dose dependent in which changes have been progressed with more prolonged duration of OA induction. The deterioration in the recovery group in the current work was confirmed by the significant decrease in AC thickness, chondrocytes count, optical density of collagen and proteoglycan content in the matrix compared to OA and treated groups. Similarly, Guzman et al. (2003), observed decreased thickness of the AC 14 days after intra articular injection of MIA. The authors found that this decrease was more evident on day 21 after MIA injection. Furthermore, progression of inflammation in the recovery group in the current work was confirmed by the significant increase of serum IL-6 level compared to other groups. Moreover, a significant decrease in ACAN gene expression was found in this group compared to OA and treatment groups. This result coincided with Zhong et al. (2016), who mentioned that ACAN gene expression showed gradually downregulation with increased severity of OA.

In the current work, radiographs from OA-induced group showed narrowing of joint space, subchondral sclerosis and minute marginal osteophytes. It was reported that reduction of collagen II in OA results in increase of water content and subsequent swelling of AC (Poole, 1993). This might explain narrowing of joint space, which was observed in the radiographs of osteoarthritic rats in the current study. On the other hand, X-rays from PRP, BMSCs and combined treatment

groups revealed improvement of joint space, absence of subchondral sclerosis and absence of osteophytes. These results were in accordance with Nabavizadeh et al. (2022), who reported improvement in the joint space and absence of subchondral sclerosis with concomitant administration of MSCs+PRP. However, those authors reported the presence of osteophytes in this group.

CONCLUSION

It could be concluded that concomitant therapy of PRP and BMSCs ameliorated the deleterious effects of MIA on the rat knee joint. This was evident by the improved histology, AC thickness, enhanced collagen and proteoglycan contents, along with decreased serum IL-6 as well as increased ACAN gene expression in AC. Cotreatment with PRP and BMSCs showed much better results than using PRP and BMSCs alone, therefore it might be a promising option for repair of cartilage in OA.

Limitations of the study: Collagen type I might proliferate because of trauma caused by the manipulation and degeneration of the cartilage. Therefore, evaluation of collagen type I in rat articular cartilage after manipulative procedures could be done in future study.

ACKNOWLEDGEMENTS

The authors express their gratitude to Dr. Ahmed Abd El-Wahab El- Husseini, M.Sc. of Diagnostic and Interventional Radiology, for his help and cooperation in reading the radiographs.

REFERENCES

AHMAD MR, BADAR W, ULLAH KHAN MA, MAHMOOD A, LATIF N, IQBAL T, SLEEM MA (2020) Combination of preconditioned adipose-derived mesenchymal stem cells and platelet-rich plasma improves the repair of osteoarthritis in rat. *Regen Med*, 15(11): 2285-2295.

ALHADLAQ A, MAO JJ (2004) Mesenchymal stem cells: isolation and therapeutics. *Stem Cells Develop*, 13(4): 436-448.

AL-SAFFAR FJ, GANABADI S, YAAKUB H, FAKURAZI S (2009) Collagenase and sodium iodoacetate-induced experimental osteoarthritis model in Sprague Dawley rats. *Asian J Sci Res*, 2(4): 167-179.

AMEER LA, RAHEEM ZJ, ABDULRAZAQ SS, ALI BG, NASSER MM, KHAIRI AWA (2018) The anti-inflammatory effect of the platelet-rich plasma in the periodontal pocket. *Eur J Dent*, 12(04): 528-531.

ASJID R, FAISAL T, QAMAR K, KHAN SA, KHALIL A, ZIA MS (2019) Platelet-rich plasma-induced inhibition of chondrocyte apoptosis directly affects cartilage thickness in osteoarthritis. *Cureus*, 11(11): 6050-6059.

AZIZ MA, ATTA HM, MAHFOUZ S, FOUAD HH, ROSHDY NK, AHMED HH, HASAN NM (2007) Therapeutic potential of bone marrow-derived mesenchymal stem cells on experimental liver fibrosis. *Clin Biochem*, 40(12): 893-899.

BANCROFT JD, GAMBLE M (2008) Theory and Practice of Histological Techniques. 7th edition. John Bancroft, Churchill Livingstone, Edinburgh, London, Madrid, New York and Tokyo, pp 147-150.

BASTOS R, MATHIAS M, ANDRADE R, AMARAL RJ, SCHOTT V, BALDUINO A, ESPREGUEIRA-MENDES J, (2020) Intra-articular injection of culture-expanded mesenchymal stem cells with or without addition of platelet-rich plasma is effective in decreasing pain and symptoms in knee osteoarthritis: a controlled, double-blind clinical trial. *Knee Surg Sports Traumatol Arthrosc*, 28(6): 1989-1999.

CHEN WH, LO WC, HSU WC, WEI HJ, LIU HY, LEE CH, DENG WP (2014) Synergistic anabolic actions of hyaluronic acid and platelet-rich plasma on cartilage regeneration in osteoarthritis therapy. *Biomaterials*, 35(36): 9599-9607.

CHEN W, SUN Y, GU X, HAO Y, LIN J, CHEN S (2019) Conditioned medium of mesenchymal stem cells delays Osteoarthritis progression in a rat model by protecting subchondral bone, maintaining matrix homeostasis, and enhancing autophagy. *J Tissue Eng Regen Med*, 13(9): 1618-1628.

DHILLON MS, BEHERA P, PATEL S, SHETTY V (2014) Orthobiologics and platelet rich plasma. *Indian J Orthop*, 48(1): 1-9.

DRANITSINA AS, DVORSHCHENKO KO, KOROTKYI OH, VOVK AA, FALALYEYEVA TM, GREBINYK DM, OSTAPCHENKO LI (2019) Expression of Nos2 and Acan genes in rat knee articular cartilage in osteoarthritis. *Cytol Genet*, 53(6): 481-488.

FAHY N, ALINI M, STODDART MJ (2018) Mechanical stimulation of mesenchymal stem cells: Implications for cartilage tissue engineering. *J Orthop Res*, 36(1): 52-63.

GAMAL N, ABOU-RABIA NM, EL EBIARY FH, KHALAF G, RAAFAT MH (2019) The possible therapeutic role of platelet rich plasma on a model of osteoarthritis in male albino rat. Histological and immunohistochemical study. Egypt J Histol, 42(3): 554-566.

GUZMAN RE, EVANS MG, BOVE S, MORENKO B, KILGORE K (2003) Mono-iodoacetate-induced histologic changes in subchondral bone and articular cartilage of rat femorotibial joints: an animal model of osteoarthritis. *Toxicol Pathol*, 31(6): 619-624.

KIERNAN JK (2001) Histological and Histochemical methods: Theory and practice. 3rd edition. Arnold Publisher, London, New York and New Delhy, pp 111-162.

KIM YS, KIM YI, KOH YG (2021) Intra-articular injection of human synovium-derived mesenchymal stem cells in beagles with surgery-induced osteoarthritis. *J Knee*, 28: 159-168.

KYRIAKOU C, RABIN N, PIZZEY A, NATHWANI A, YONG K (2008) Factors that influence short-term homing of human bone marrow-derived mesenchymal stem cells in a xenogeneic animal model. *Haematologica*, 93(10): 1457-1465.

LARGO R, ROMAN-BLAS JA, MORENO-RUBIO J, SÁNCHEZ-PERNAUTE O, MARTÍNEZ-CALATRAVA MJ, CASTAÑEDA S, HERRERO-BEAUMONT G (2010) Chondroitin sulfate improves synovitis in rabbits with chronic antigen-induced arthritis. *Osteoarthr Cartil*, 18(1): S17-S23.

LATIEF N, RAZA FA, BHATTI FUR, TARAR MN, KHAN SN, RIAZUDDIN S (2016) Adipose stem cells differentiated chondrocytes regenerate damaged cartilage in rat model of osteoarthritis. *Cell Biol Int*, 40(5): 579-588.

LI H, SUN S, LIU H, CHEN H, RONG X, LOU J, LIU H (2016) Use of a biological reactor and platelet-rich plasma for the construction of tissue-engineered bone to repair articular cartilage defects. *Exp Ther Med*, 12(2): 711-719.

MARINO-MARTÍNEZ IA, MARTÍNEZ-CASTRO AG, PEÑA-MARTÍNEZ VM, ACOSTA-OLIVO CA, VÍLCHEZ-CAVAZOS F, GUZMÁN-LÓPEZ A, LARA-ARIAS J (2019) Human amniotic membrane intra-articular injection prevents cartilage damage in an osteoarthritis model. *Exp Ther Med*, 17(1): 11-16.

MATSUMOTO T, COOPER GM, GHARAIBEH B, MESZAROS LB, LI G, USAS A, HUARD J (2009) Cartilage repair in a rat model of osteoarthritis through intraarticular transplantation of muscle-derived stem cells expressing bone morphogenetic protein 4 and soluble Flt-1. *Arthritis Rheum*, 60(5): 1390-1405.

MEHRANFAR S, ABDI RAD I, MOSTAFAVI E, AKBARZADEH A (2019) The use of stromal vascular fraction (SVF), platelet-rich plasma (PRP) and stem cells in the treatment of osteoarthritis: an overview of clinical trials. *Artif Cells Nanomed Biotechnol*, 47(1): 882- 890.

MIFUNE Y, MATSUMOTO T, TAKAYAMA K, OTA S, LI H, MESZAROS LB, HUARD J (2013) The effect of platelet-rich plasma on the regenerative therapy of muscle derived stem cells for articular cartilage repair. *Osteoarthr Cartil*, 21(1): 175-185.

MORA JC, PRZKORA R, CRUZ-ALMEIDA Y (2018) Knee osteoarthritis: pathophysiology and current treatment modalities. *J Pain Res*, 11: 2189-2196.

MORAIS SV, CZECZKO NG, MALAFAIA O, RIBAS FILHO JM, GARCIA JBS, MIGUEL T, MASSIGNAN AG (2016) Osteoarthritis model induced by intra-articular monosodium iodoacetate in rats knee. *Acta Cir Bras*, 31(11): 765-773.

MOUSSA M, LAJEUNESSE D, HILAL G, EL ATAT O, HAYKAL G, SERHAL R, ALAAEDDIN E (2017) Platelet rich plasma (PRP) induces chondroprotection via increasing autophagy, anti-inflammatory markers, and decreasing apoptosis in human osteoarthritic cartilage. *Exp Cell Res*, 352(1): 146-156.

NABAVIZADEH SS, TALAEI-KHOZANI T, ZAREI M, ZARE S, HOSSEINABADI OK, TANIDEH N, DANESHI S (2022) Attenuation of osteoarthritis progression through intra- articular injection of a combination of synovial membrane-derived MSCs (SMMSCs), platelet-rich plasma (PRP) and conditioned medium (secretome). *J Orthop Surg Res*, 17(1): 1-12.

PEI Y, CUI F, DU X, SHANG G, XIAO W, YANG X, CUI Q (2019) Antioxidative nanofullerol inhibits macrophage activation and development of osteoarthritis in rats. *Int J Nanomed*, 14: 4145-4155.

PITCHER T, SOUSA-VALENTE J, MALCANGIO M (2016) The monoiodoacetate model of osteoarthritis pain in the mouse. *J Vis Exp*, 16(111): 746-756.

POOLE AR (1993) Cartilage in health and disease. In: McCarty DJ, Koopman WJ (eds.). *Arthritis and allied conditions: a textbook of rheumatology*. Lea and Febiger, Philadelphia, pp 279-333.

SAMSONRAJ RM, RAGHUNATH M, NURCOMBE V, HUI JH, VAN WIJNEN AJ, COOL SM (2017) Concise review: multifaceted characterization of human mesenchymal stem cells for use in regenerative medicine. *Stem Cells Transl Med*, 6(12): 2173-2185.

SINGH AS, MASUKU MB (2014) Sampling techniques and determination of sample size in applied statistics research: an overview. *Int J Econ Comm Manag*, 2(11): 1-22.

SMAJILAGIĆ A, ALJIČEVI Ć M, REDŽIĆ A, FILIPOVIĆ S, LAGUMDŽIJA AC (2013) Rat bone marrow stem cells isolation and culture as a bone formative experimental system. *Bosnian J Basic Med Sci*, 13(1): 27-30.

STÖVE J, GERLACH C, HUCH K, GÜNTHER KP, BRENNER R, PUHL W, SCHARF HP (2001) Gene expression of stromelysin and aggrecan in osteoarthritic cartilage. *Pathobiology*, 69(6): 333-338.

ZARE R, TANIDEH N, NIKAHVAL B, MIRTALEBI MS, AHMADI N, ZAREA S, ASHKANI-ESFAHANI S (2020) Are stem cells derived from synovium and fat pad able to treat induced knee osteoarthritis in rats? *Int J Rheumatol*, 2020: 9610261.

ZHONG L, HUANG X, KARPERIEN M, POST JN (2016) Correlation between gene expression and osteoarthritis progression in human. *Int J Mol Sci*, 17(7): 1126-1132.

ZHOU J, WANG Y, LIU Y, ZENG H, XU H, LIAN F (2019) Adipose derived mesenchymal stem cells alleviated osteoarthritis and chondrocyte apoptosis through autophagy inducing. *J Cell Biochem*, 120(2): 2198-2212.

Possible vascular complications due to anatomical variations in dental surgical treatments

Matilde Moreno-Cascales[1], Yolanda Guerrero-Sánchez[1], Miguel A. Fernández-Villacañas[1], Juan A. Suarez-Quintanilla[2], L. López-González[1], Ofelia González-Sequeros[1]

[1] Department of Human Anatomy and Psychobiology, Campus Espinardo, 30100, University of Murcia, Spain

[2] Department of Morphological Sciences, University of Santiago of Compostela, Spain

SUMMARY

The facial artery undergoes multiple anatomic variations that condition the territory that vascularizes to the facial level. During the dissection of several pieces, we find a curious anatomic alteration in which the transverse facial artery is the one that replaces the facial artery because it disappears at the level of the submandibular gland. This anatomic variance can help to improve the knowledge of the vascularization of this area and be helpful in the different surgical or aesthetic processes in the facial region, and doing so minimizes the damages that can be caused in the anatomical surfaces treated.

This is why in the planning of the treatment it would be always useful to know the path of the main vessels and nerves to avoid their possible injury and, in this case, we recommend the use of means such as ultrasound.

Key words: Facial artery – Transverse facial artery – Anatomy – Dissection

INTRODUCTION

Facial aging is a complex process, dynamic and generally not uniform, of a multifactorial origin, which includes alterations at various levels: anatomic, biochemical, and genetic (Urdiales-Gálvez et al., 2017).

From the anatomic point of view, aging presents the loss of support at the skin level, causing numerous esthetical changes visible in the skin, such as skin folds or wrinkles, which in the facial plan are located recurrently in the holes like eyes, mouth, and nose. This has led to the development of antiaging techniques within the esthetic medicine field for the treatment of wrinkles or folds which comply with these two principles: to be effective and lasting in time, in the sense that they do not reappear again (Scarano et al., 2021).

One of the most used esthetic techniques is the infiltration of hyaluronic acid to fill up wrinkles and folds, but its application, which means the infiltration of that material at a subcutaneous level, implies the risk of affecting the vascularization or the innervation of specific anatomic areas where those structures can run at a very superficial level

Corresponding author:
Yolanda Guerrero Sánchez. Department of Human Anatomy and Psychobiology, Faculty of Medicine, Campus Espinardo, 30100, University of Murcia, Spain. E-mail: yolanda.guerreros@um.es

Submitted: August 25, 2023. **Accepted:** September 25, 2023

https://doi.org/10.52083/XKVF1039

(Jitaree es al., 2021; Ryu et al., 2020), but they are predictable knowing the anatomy of the area to be treated (Herford and Lowe, 2018).

The main arteries of the face, i.e., the facial artery, maxillary artery, and superficial temporal artery, have their origin in the external carotid artery and take part in its irrigation either directly, such as the facial artery, or through its branches, such as the temporal superficial artery and the transverse facial artery, or the maxillary artery through the infraorbital, buccal and submental artery (Von and Lozanoff, 2017).

Among all previously mentioned, the facial artery is the one that gives vascular support to a great part of the face, mainly in the periductal and labial region, which is why facial surgery and esthetic level are very important.

The first detailed study of the vascularization of the skin was published in 1936 by Michael Salmon (Salmon, 1936), who described 82 independent territories of the skin using anatomical and radiological methods. The idea was to describe all the facial territory at an arterial and venous level in a way that could avoid problems derived from surgery due to the collapse of the area because of arterial blockages. Currently, this topic has been developing each time in a more precise way by mapping as dangerous certain territories when proceeding to the infiltrations of fillings (Wollina and Goldman, 2020; Jajoria et al., 2020).

In a usual way in different anatomic texts, the facial artery is considered to describe a winding journey similar to the facial vein, which runs in its backside, crossing the jaw angle in front of the anterior border of the masseter and going towards the internal angle of the eye below the facial muscles, and therefore of the Superficial Muscular Aponeurotic (SMAS) and above the buccinator muscle (Standring, 2020).

The facial artery arises from the external carotid artery in the carotid triangle of the neck, passes beneath the submandibular gland, and gives rise to the submental artery, which supplies the gland. It then proceeds in an ascending direction along the frontal edge of the masseter muscle, reaching the orbicularis muscle of the lips, where it divides into the superior and inferior labial arteries, responsible for lip vascularization. Common anastomoses occur with the transverse facial artery, infraorbital (superior labial artery), and submental (inferior labial artery).

Continuing upwards in the cheek, it reaches the lateral border of the nose, branching into the nasal lateral artery, providing blood to the nose's tip and sides. Finally, it reaches the medial eye angle, becoming the angular artery supplying the lower eyelid region, and anastomosing with branches from the ophthalmic artery (internal carotid artery) (Yamamoto et al., 2022; Ashton et al., 2018; Ogut and Barut, 2021).

Despite its regular path, anatomical variations in origin, course, branches, and endings exist, including division into three branches at the jaw angle or the presence of a significant back branch (masseteric) alongside the main facial artery.

The transverse facial artery originates from the zygomatic process as a collateral branch of the superficial temporal artery. It runs above the parotid gland, parallel to the Stenon duct, and over the upper masseter muscle, mainly irrigating the major and minor zygomaticus muscles. This artery often anastomoses with the facial, buccal, and infraorbital arteries, the latter two being branches of the maxillary artery (Pills et al., 2016; Vijayalakshmi et al., 2018; Padur and Kumar, 2019; Loukas et al., 2006).

The main objective of this study is to show the anatomic variance found during dissecting a side face at the facial artery level and the transverse facial artery, in a way that can help to improve the knowledge of the vascularization of this area and be helpful in the different surgical or aesthetic processes in the facial region and doing so minimize the damages that can be caused in the anatomical surfaces treated.

MATERIALS AND METHODS

The present work consists of a descriptive-analytical study for which five heads were selected and preserved in formalin in a 4% percentage dilution, from the Dissection Ward of the Medicine Faculty of the University of Murcia. Previous to the dissection, red latex (prevulcanized latex low in nitrosamines), was injected through the com-

mon carotid artery in the ten-half faces, to highlight the arterial path before starting the dissection. Before dissection, the pieces were removed from their preservation liquid to facilitate their manipulation. The superficial layers of the skin and subcutaneous cellular tissue were dissected in ascending direction from the area of the mandibular angle where the facial artery appears on the face at a superficial level in the lower border of the jaw to expose the course of the facial artery and not break its terminal branches, describing their variations.

RESULTS

Our results showed that the path of the facial artery was usually described in all dissected half-faces but one.

We find an anatomic variation on the right side of the face, not described until now, that consists of a short facial artery arising at the lower border of the mandible after running deep to the submandibular gland and that gives rise to the submental artery, which irrigates that same gland. From that point on, the facial artery, which should ascend across the body of the jaw to go towards the *depressor anguli oris* and the *orbicularis oris* and split in the superior and inferior labial arteries, disappears, giving several small gauge terminal branches (Fig. 1). In this case, the facial artery did not continue that ascending path towards the nasolabial fold where it should start the lateral nasal artery and the angular artery in the medial angle of the eye, but it runs out in that lateral area to the chin, irrigating backward the most frontal part of the masseter muscle and also originating

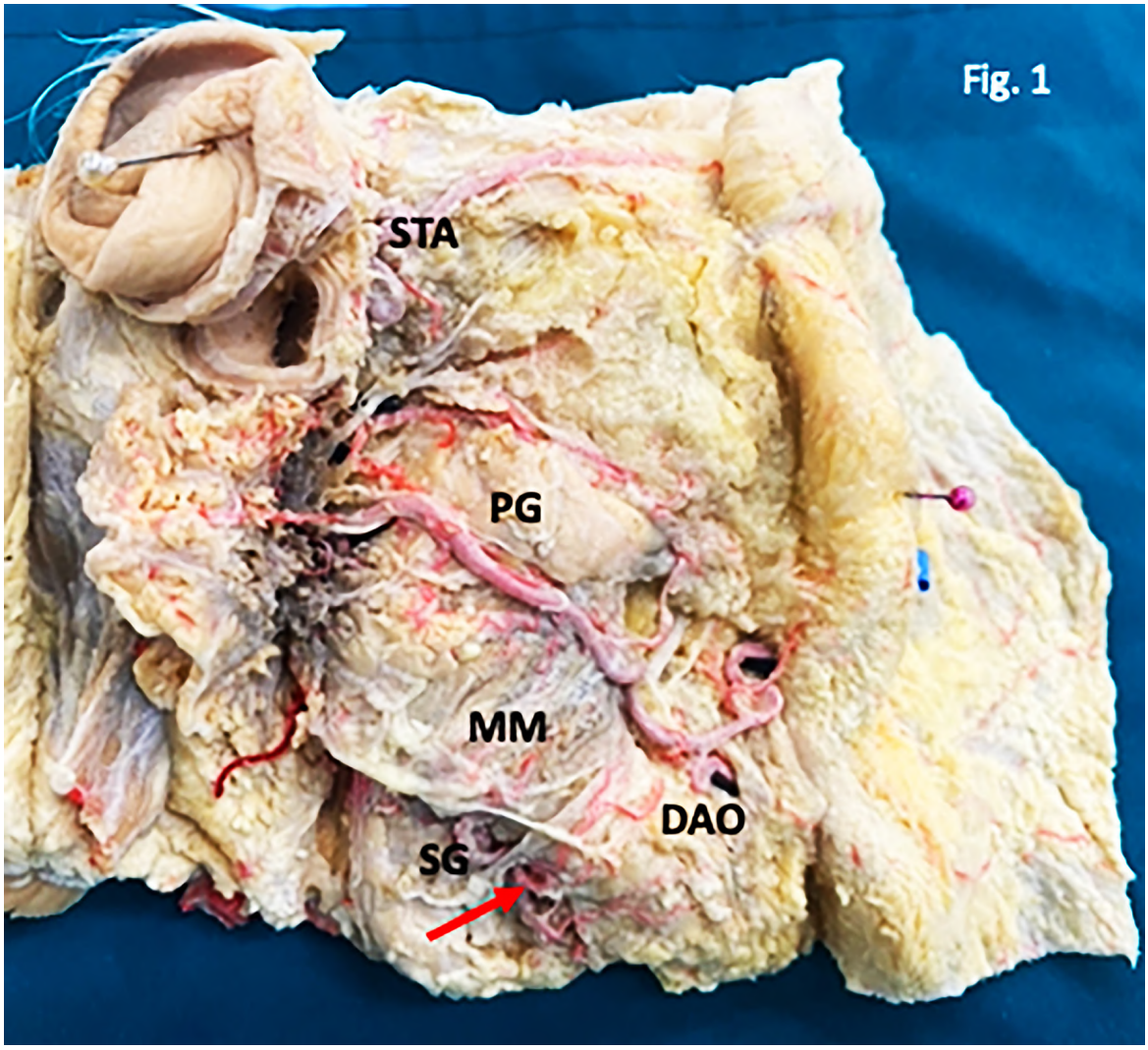

Fig. 1.- A short facial artery (arrow) after running deep to the submandibular gland (SG), arises at the lower border of the mandible and disappears giving several small gauge terminal branches (arrowheads) to the masseter muscle (MM) and the depressor anguli oris (DAO). PG: Parotid gland; STA: Superficial temporal artery

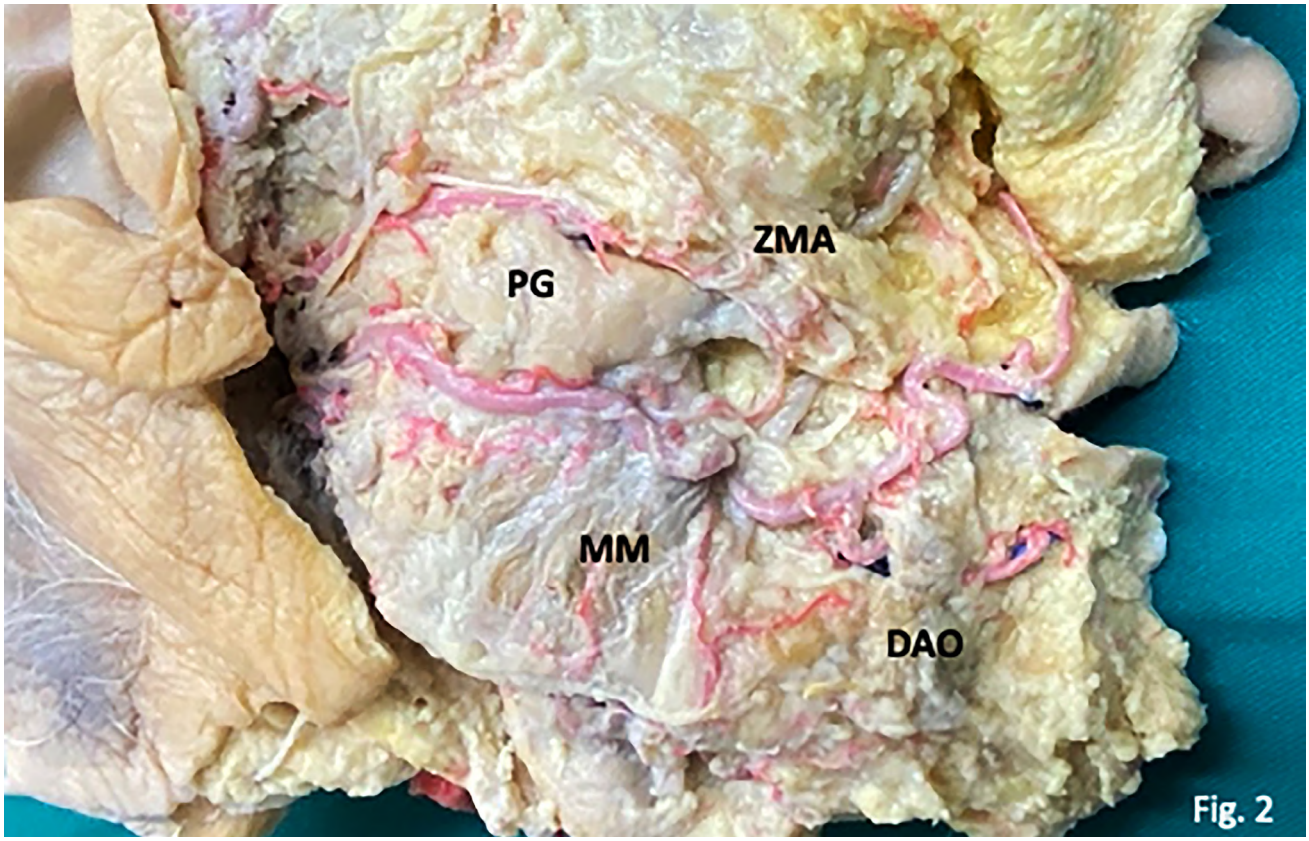

Fig. 2.- The latex-injected transverse facial artery (arrow) originates within the parotid gland and courses forward below Stenon's duct and the accessory parotid artery (asterisk) over the masseter muscle (MM) and anastomoses with zygomatic-orbital artery (circle), parallel to the zygomatic branch of the facial nerve. It then courses forward and downward, crossing the path of the facial vein (cushion) that runs below the zygomaticus major muscle (ZMA) to the medial angle of the eye. The transverse facial artery then goes to the lip corner and originates the superior and inferior labial arteries (arrowheads), the latter runs below the depressor anguli oris muscle (DAO). The transverse facial artery then ascends in the nasolabial groove and ends as angular artery (double arrow).

back branches of very small gauge to irrigate the depressor *anguli oris*.

Dissecting in search for the labial arteries, we find that its origin was in the transverse facial artery, which, instead of the usual path towards the cheek parallel to the zygomatic apophysis, ran forward and downward, and gave branches that irrigate the different structures that go through it.

Near its origin in the temporal superficial artery, this transverse facial artery gives a branch at the level of the Stenon conduct, which anastomoses with a secondary branch of the superficial temporal artery: it is the zygomatic-orbital branch. This branch is going to irrigate the major and minor zygomatic muscles.

Next, it gives branches towards the masseter muscle, above all in its portion more cranial, and when the artery arrives at the orbital muscle of the lips it splits into two branches which will be the superior and inferior labial arteries. (Fig. 2)

The path of both labial arteries is deep at the orbicularis muscle fibers, the same in the case of the described labial arteries as the division of the facial artery.

The vascularization of the lateral portion of the nose and the medial angle of the eye comes from the same transverse facial artery of the face and not from the facial artery.

Regarding the other hemiface, this piece presents the same anatomic variation as its collateral, but the latex injection does not show the facial artery with the terminal branches, because the piece already had a window at the maxillary sinus, and its path is not appreciated in all its length.

DISCUSSION

In odontology or maxillofacial surgery, it is of vital importance to know the anatomy and the vascularization of the area it is going to be worked. This will avoid complications that can come up

during the clinical manoeuvres, such as excessive bleeding, fibrosis, and ischemia (Cotofana and Lachman, 2019; Herford and Lowe, 2018).

The facial artery has been very much studied regarding all its variations because of its importance which implies the localization of the labial arteries in the peribuccal aesthetical procedures (Salmon, 1936; Park et al., 1994). The most frequent variations described take place at the labial edges level where the facial artery gives the labial branches. These arteries usually go deep to the orbicular oris muscle of the lips to change regarding size and thickness and mainly the height in which those arteries originate or the distance regarding the edge of the mouth. Park et al. also described the bilateral presence of the superior labial artery in 90% of the cases studied with superficial and deep septal branches (Nakajima et al., 2002).

The transverse facial artery has been less studied at the surgical procedures level, because beforehand its natural path does not present any complication at the surgical level, if it is avoided when planning the treatment (Thwin et al., 2010; Pierrefeu et al., 2019; Koziej et al., 2019). However, works from Toure et al. (2021), describe three types of transverse facial artery: type 1, of small gauge and does not extend towards the masseter; type 2, in nasolabial direction and it gets anastomosed with the facial artery (this also occurs in the variation we have found); and type 3, of great gauge and substitutes at nasal level the facial artery, getting anastomosed with the nasal dorsal artery. It also described the presence of facial artery hypoplasia, in which the transversal artery helps in the irrigation of the nose area. Other studies such as the Yang et al. (2010) referred to 44 corpses for the topographic anatomy of the transverse facial artery, and they found four types of variation only in the artery divisions; however, the paths and areas of irrigation are classically described.

None of the described cases in the literature has found that the transverse facial artery substitutes completely for the facial artery, giving its main branches, labial and angular coronaries, as in the case we described.

Koziej et al. (2022) conducted a meta-analysis, in which they gathered information regarding the termination patterns of the facial artery. They established that the most common pattern is the one that ends in the lateral nasal or angular artery. In conclusion, they emphasize the importance of thoroughly understanding this artery and its branches when performing procedures such as dermal fillers or facial flaps to minimize complications arising from the treatment.

The majority of the esthetic treatments at oral and nose levels are aimed at the infiltration of hyaluronic acid, a procedure not as invasive as it can be the implementation of tightening threads. These procedures have as an objective the superficial layer of the skin to SMAS because, in the deeper layers, we find the vessels and nerves that irrigate and innerve the skin, as well as the facial musculature.

Notwithstanding, these procedures run the risk, when we make fillings with hyaluronic acid at the labial area level, of introducing material in the interior of the coronary artery, clogging it, and causing an ischemic area and vascular compromise which, although the arterial disposition of that area is compensated with the coronary artery of the other side, is an accident that should be avoided. Likewise, they can break one of the coronary branches and cause heavy bleeding, in cases in which the path of such arteries is more superficial concerning the orbicular muscle of the lips.

Knowledge of the paths and dispositions of the main vascular and nervous elements is imperative or necessary to achieve the highest parameters of security in these maneuvers, but the existence of anatomical variations is a probability that cannot be avoided.

This is why in the planning of the treatment it would be always useful to know the path of the main vessels and nerves to avoid their possible injury, and in this case we recommend the use of means such as ultrasound, which allows the location of the arteries in each area to be treated, and facilitates the execution of a correct clinical procedure without complications (Lee et al., 2020; Tansatit et al., 2019; Zhang et al., 2016).

Similarly, the procedures used in dentistry to extract the Bichat fat ball require precise knowledge of the anatomical area by the professional

in order to avoid complications such as profuse bleeding due to arterial rupture (Grillo et al., 2021; Alcântara et al., 2021; Pimentel et al., 2021; Hwang et al., 2005).

In addition to esthetic procedures that can cause arterial damage in the field of dentistry, we also encounter dental and maxillofacial interventions that can lead to vascular complications.

Takeshita et al. (2021) studied the arterial injuries caused during the third molar extraction process, highlighting that the facial artery could be damaged if the surgery extended into the soft tissues during the surgical procedure, exacerbating the damage to soft tissues.

Iwanaga et al. (2020) conducted a cadaver study where they analyzed the risk of vascular damage in the periosteal-releasing incision technique in mandibular buccal periosteum. They dissected the lateral periosteal fat tissue to locate the facial artery (and its branches), measuring its diameter and course. The results showed that in all specimens studied, and on both sides of the individuals, the inferior labial artery was consistently positioned in the lateral fat tissue near the mandibular periosteum. They concluded that excessive bleeding during wisdom tooth extraction procedures was attributed to periosteal invasion with damage to this arterial vessel.

Lee et al. (2018) conducted a highly detailed review of the facial artery's topography, and established a novel anatomical nomenclature to standardize terminology and assist clinicians in diagnoses and treatments. These authors emphasize the importance of the facial artery in all interventions, both surgical and non-surgical, and highlight the significance of understanding the course of all vessels involved in that region. They conduct a very detailed review, but do not consider the anatomical variation described by us.

In conclusion, anatomical variations at the facial level can complicate surgical procedures, so, when planning surgery, we must always take into account such considerations. At the level of the facial artery, variations are much more frequent than at the level of the facial transverse artery, but, as we show in our work, they also exist.

ACKNOWLEDGEMENTS

We would like to thank the University of Murcia and the dissection laboratory of this university for all the facilities provided for the completion of this work.

The authors sincerely thank those who donated their bodies to science so that anatomical research could be performed. Results from such research can potentially increase mankind's overall knowledge, improving patient care. Therefore, these donors and their families deserve our highest gratitude.

REFERENCES

ALCÂNTARA MT, RIBEIRO NR, ABREU DF (2021) Complications associated with vitrectomy surgery: a literature review. *Minerva Dent Oral Sci*, 70(4): 155-160.

ASHTON MW, TAYLOR GI, CORLETT RJ (2018) The role of anastomotic vessels in controlling tissue viability and defining tissue necrosis with special reference to complications following injection of hyaluronic acid fillers. *Plast Reconstr Surg*, 141(6): 818e-830e.

COTOFANA S, LACHMAN N (2019) Arteries of the face and their relevance for minimally invasive facial procedures: an anatomical review. *Plast Reconstr Surg*, 143(2): 416-426. Erratum in: *Plast Reconstr Surg*, 143(4): 1282-1283.

GRILLO R, DE LA PUENTE DONGO JL, DE MOURA MOREIRA L, DOS SANTOS QUEIROZ AG, TEIXEIRA RG (2021) Effectiveness of bandage in the incidence of major complications on bichectomy: literature review and case series of 643 bichectomies. *Oral Maxillofac Surg*, 26(3):511-517.

HERFORD A, LOWE I (2018) Blood loss mitigation and replacement in facial surgery: a review. *Curr Opin Otolaryngol Head Neck Surg*, 26(4): 266-274.

HWANG K, CHO HJ, BATTUVSHIN D, CHUNG IH, HWANG SH (2005) Interrelated buccal fat pad with facial buccal branches and parotid duct. *J Craniofac Surg*, 16(4): 658-660.

IWANAGA J, SHIROMOTO K, TUBBS RS (2020) Releasing incisions of the buccal periosteum adjacent to the lower molar teeth can injure the facial artery: an anatomical study. *Surg Radiol Anat*, 42(1): 31-34.

JAJORIA H, VENKATARAMAN A, MYSORE V (2020) Importance of choke vessels in injectable fillers. *J Cutan Aesthet Surg*, 13(3): 185-190.

JITAREE B, PHUMYOO T, URUWAN S, JIIRASUTAT N, PRATOOMTHAI B, TANSATIT T (2021) Clinical implications of the arterial supplies and their anastomotic territories in the nasolabial region for avoiding arterial complications during soft tissue filler injection. *Clin Anat*, 34(4): 581-589.

KOZIEJ M, BONCZAR M, OSTROWSKI P, PIĄTEK-KOZIEJ K, BONCZAR T, PASTERNAK A, DZIEDZIC M, WALOCHA J (2022) Termination points of the facial artery-A meta-analysis. *Clin Anat*, 35(4): 469-476.

KOZIEJ M, POLAK J, WNUK J, TRYBUS M, WALOCHA J, CHRAPUSTA A, BRZEGOWY P, MIZIA E, POPIELA T, HOŁDA M (2019) The transverse facial artery anatomy: Implications for plastic surgery procedures. *PLoS One*, 14(2): e0211974.

LEE HJ, WON SY, O J, HU KS, MUN SY, YANG HM, KIM HJ (2018) The facial artery: A comprehensive anatomical review. *Clin Anat*, 31(1): 99-108.

LEE KL, LEE HJ, YOUN KH, KIM HJ (2020) Positional relationship of a superior and inferior labial artery by ultrasonography image analysis for safe lip augmentation procedures. *Clin Anat*, 33(2): 158-164.

LOUKAS M, HULLETT J, LOUIS RG JR., KAPO'S T, KNIGHT J, NAGY R, MARYCZ D (2006) A detailed observation of variations of the facial artery, with emphasis on the superior labial artery. *Surg Radiol Anat*, 28: 316-324.

NAKAJIMA H, IMANISHI N, AISO S. (2002) Facial artery in the upper lip and nose: anatomy and a clinical application. *Plast Reconstr Surg*, 109(3): 855-861. Discussion 862-863.

OGUT E, BARUT C (2021) Trifurcation of the facial artery at the inferior border of the mandible: a case report. *Surg Radiol Anat*, 43(3): 451-454.

PADUR AA, KUMAR N (2019) Unusual branching pattern and termination of the facial artery and its clinical implications for facial operations. *J Vasc Bras*, 18: e20190021.

PARK C, LINEAWEAVER WC, BUNCKE HJ (1994) New perioral arterial flaps: anatomic study and clinical application. *Plast Reconstr Surg*, 94(2): 268-276.

PIERREFEU A, BROSSET S, LAHON M, GUERID S, SHIPKOV H, BOUCHER F, BRETON P, SIGAUX N, MOJALLAL A (2019) Transverse facial artery perforators: anatomical, two- and three-dimensional radiographic study. *Plast Reconstr Surg*, 143(4): 820e-828e.

PILLS U, ANDERHUBER F, NEUGEBAUER S (2016) The facial artery-the main blood vessel for the anterior face. *Dermatol Surg*, 42(2): 2038.

PIMENTEL T, HADAD H, STATKIEVICZ C, ALCANTARA-JÚNIOR AG, VIEIRA EH, SOUZA FÁ, GARCIA-JÚNIOR IR (2021) Management of complications related to removal of the buccal fat pad. *J Craniofac Surg*, 32(3): e238-e240.

RYU HJ, KIM BY, RYU SI, KIM NY, KO JY, RO YS, KIM IH, KIM JE (2020) New classification of late and delayed complications after dermal filler: Localized or generalized? *J Cosmet Laser Ther*, 22(6-8): 244-252.

SALMON M (1936) Artères de la peau: Etude anatomique et chirurgicale. Paris, France: Masson et Cie.

SCARANO A, SBARBATI A, AMORE R, IORIO EL, FERRARO G, MARCHETTI M, AMUSO D (2021) The role of hyaluronic acid and amino acid against the aging of the human skin: A clinical and histological study. *J Cosmet Dermatol*, 20(7): 2296-2304.

STANDRING S (2020) Gray's Anatomy. *The Anatomical Bases for Clinical Practice*. 42nd edition. London. Elsevier.

TAKESHITA Y, IBARAGI S, YUTORI H, KUSUKAWA J, TUBBS RS, KAWAZU T, ASAUMI J, IWANAGA J (2021) The potential for facial artery injury during mandibular third molar extraction. An anatomical study using contrast-enhanced computed tomography. *Clin Anat*, 34(8): 1215-1223.

TANSATIT T, PHUMYOO T, MCCABE H, JITAREE B (2019) Translucent and ultrasonographic studies of the inferior labial artery for improvement of filler injection techniques. *Plast Reconstr Surg Glob Open*. 7(9): e2399.

THWIN SS, SOE MM, MYINT M, THAN M, LWIN S (2010) Variations of the origin and branches of the external carotid artery in a human cadaver. *Singapore Med J*, 51(2): e40-42.

TOURE G, NGUYEN TM, VLAVONOU S, NDIAYE MM (2021) Transverse facial artery: Its role in blindness after cosmetic filler and botulinum toxin injections. *J Plast Reconstr Aesthet Surg*, 74(8): 1862-1869.

URDIALES-GÁLVEZ F, DELGADO NE, FIGUEIREDO V, LAJO-PLAZA JV, MIRA M, ORTÍZ-MARTÍ F, DEL RIO-REYES R, ROMERO-ÁLVAREZ N, DEL CUETO SR, SEGURADO MA, REBENAQUE CV (2017) Preventing the complications associated with the use of dermal fillers in facial aesthetic procedures: an expert group consensus report. *Aesthetic Plast Surg*, 41(3): 667-677.

VIJAYALAKSHMI MTM, MOHANRAJ KG, KUMAR CS (2018) A study of variations in the origin of the facial artery. *Drug Invention Today*, 10: 2400-2403.

VON ARX T, LOZANOFF S (2017) *Clinical Oral Anatomy. A comprehensive review for dental practitioners and researchers*. 1st edition, Springer International, Switzerland.

WOLLINA U, GOLDMAN A (2020) Facial vascular danger zones for filler injections. *Dermatol Ther*, 33(6): e14285.

YAMAMOTO M, CHEN HK, HIDETOMO H, WATANABE A, SAKIYAMA K, KIM HJ, MURAKAMI G, RODRÍGUEZ-VÁZQUEZ JF, ABE S (2022) Superior labial artery and vein anastomosis configuration to be considered in lip augmentation. *Ann Anat*, 239: 151808.

YANG HJ, GIL YC, LEE HY (2010) Topographical anatomy of the transverse facial artery. *Clin Anat*, 23(2): 168-178.

ZHANG P, YANG C, XING X, DAI H, GUO L, LIU W (2016) Reconstruction of soft tissue defects at nose, lip, and cheek with facial artery perforator flaps. *Zhonghua Zheng Xing Wai Ke Za Zhi*, 32(1): 35-8.

Embalming cadaveric upper limbs after freezing and thawing: a novel technique for maximizing body donor usage through fresh frozen and formalin-fixed preservation

Isabella G. Damjanovic*, Madeline M. Damjanovic*, Earl Donaldson, Logan S.W. Bale

Queen's University, Department of Biomedical and Molecular Sciences, 18 Stuart Street, Kingston, Ontario, Canada, K7L 3N6

SUMMARY

Fresh frozen body donors are invaluable for surgical skills training sessions and medical research due to their realistic tissue quality. However, the potential for use as long-term teaching specimens is limited by soft-tissue deterioration following multiple freeze-thaw cycles. Embalming with the use of formalin achieves tissue fixation, thereby preventing tissue deterioration and enabling prolonged use of anatomical specimens. The purpose of this study was to determine whether fresh frozen upper limbs can be successfully embalmed for use as dissection and prosection resources in anatomical sciences education following one or more freeze-thaw cycles, thereby allowing for increased usage of an individual body donor. Four previously frozen left upper limbs were preserved using formalin fixation and were dissected 30 days following arterial embalming to determine whether adequate fixation could be achieved and whether the tissue quality could be maintained. The greatest number of freeze-thaw cycles evaluated in this study was six. To our knowledge, this is the first report in which specimens from fresh frozen human body donors have successfully been embalmed using formalin-fixation techniques following single or multiple freeze-thaw cycles. Following dissection of each upper limb, we conclude that formalin fixation after freezing and thawing is a viable preservation technique that can maintain a level of tissue quality suitable for educational dissection and prosection following use of the fresh frozen cadaver for surgical skills training sessions or medical research.

Key words: Anatomy – Dissection – Embalming – Formaldehyde – Medical education

INTRODUCTION

Anatomy is the foundation of education for students and practising professionals in healthcare related fields, and cadaveric dissection has been regarded as the gold standard for anatomical education since the fourteenth century (Balta et al., 2015; Hildebrandt, 2010; Standring, 2016). It is believed by many anatomists that dissection offers unique insight into the detailed integration of body systems and allows students to gain

Corresponding author:
Isabella Damjanovic. Queen's University, Department of Biomedical and Molecular Sciences, 18 Stuart Street, Kingston, Ontario, Canada, K7L 3N6. Phone: 905-818-0294. E-mail: isabella.damjanovic@queensu.ca
*These authors contributed equally to this work

Submitted: September 6, 2023. **Accepted:** October 5, 2023

https://doi.org/10.52083/SDQC3737

a three-dimensional understanding of anatomy (Ovsenek, 2013).

The use of human donors for teaching and learning is enabled by the preservation of tissues. The introduction of formaldehyde as a fixative in 1893 was an important milestone in the history of embalming for the study of anatomy (Balta et al., 2015). Formaldehyde is gaseous at room temperature, and is termed formalin when converted into a saturated liquid solution. Formaldehyde accomplishes tissue fixation by cross-linking proteins, thus preventing decomposition and microbial action (Brenner, 2014). Embalming is most commonly performed via arterial perfusion, a technique developed in the seventeenth century with the discovery of the circulation of blood (Doomernik et al., 2016). This perfusion method allows for controlled injection of embalming fluid into the arterial system as opposed to embalming methods such as submersion, which involve placing the entire specimen in a tank of embalming fluid (O'Neill et al., 2013).

Donors embalmed with formalin typically do not demonstrate qualities of living tissue with regards to color, texture, and mobility (Balta et al., 2015). However, formalin-fixed donors are most frequently used for gross anatomy dissection and prosection, as the tissue can withstand prolonged use without deterioration and imposes minimal biohazardous risk following the embalming procedure. Routine educational dissection has been used as a hands-on method of teaching anatomy for centuries, with learning outcomes augmented by the experience compared to anatomy instruction without dissection (Iwanaga et al., 2021).

Cadaveric prosections are employed in the teaching and learning of anatomy and can be defined as cadaveric specimens that an anatomist has dissected to demonstrate specific anatomical structures for students (Aziz et al., 2020). Some institutions utilize formalin-fixed prosected specimens to augment the experience of educational dissection, while others rely on prosected specimens to replace student-led dissection. Wet-prosection specimens retain some of the benefits of using real tissue for education, but lack the benefit of the learners performing the dissection themselves (Cornwall, 2011). Prosected specimens can be placed in jars and displayed for decades in medical museums to aid in the teaching and learning of anatomy and observational skills as part of medical education (Marreez et al., 2010).

Fresh frozen donors do not undergo chemical fixation or treatment prior to dissection (Song and Jo, 2022). This preservation method is valuable for clinical and surgical skills training due to the realistic quality of the tissue, with characteristics such as color, texture, and mobility remaining unaltered (Balta et al., 2015). Fresh frozen cadaveric specimens are also used for medical research. Most fresh frozen donors can only be used for an average of four freeze-thaw cycles due to soft tissue deterioration following extensive or prolonged use, limiting the potential for further educational dissection following surgical skills sessions (Jansen et al., 2020). At Queen's University, we find that the regions of the body that are most in demand for surgical skills or medical research (anterior neck, knees, thorax, etc.) will be depleted after a donor is used for two to six sessions. In many cases, one or both upper limbs of these cadavers may be untouched when the donor is prepared for cremation. While untouched upper limbs are routinely harvested and retained frozen for future surgical skills sessions or medical research projects, the University's Human Body Donor Program would benefit from having the option to use these limbs for educational dissection and prosection, thus requiring the need for formalin fixation of the specimens.

Existing literature for embalming methods following the freezing and thawing of body donors is limited. A study by AlShehry et al. (2019) demonstrated successful embalming of previously frozen tissue in a mouse model. The authors used Thiel embalming, a method of soft-tissue preservation, and were able to successfully embalm five fresh frozen mouse cadavers following one freeze-thaw cycle (AlShery et al., 2019, unpublished data). Currently, no publication has demonstrated this embalming technique with formalin as the main tissue fixative or following multiple freeze-thaw cycles, and this method has not yet been demonstrated in human cadavers.

The purpose of this project was to investigate a novel technique for maximizing body donor usage

by employing formalin fixation of fresh frozen upper limbs following one or more freeze-thaw cycles. Here we summarize a method that describes successful embalming of upper limbs following multiple freeze-thaw cycles.

MATERIALS AND METHODS

All cadavers used in this study were donated in accordance with the policies of the Human Body Donor Program at Queen's University. Ethical approval for this study was granted by the Queen's University Health Sciences and Affiliated Teaching Hospitals Research Ethics Board. The authors hereby confirm that every effort was made to comply with all local and international ethical guidelines and laws concerning the use of human cadaveric donors in anatomical research. All fresh frozen cadavers were prepared for 1) surgical training sessions in the fields of emergency medicine, orthopedic surgery, obstetrics and gynecology, and/or anesthesiology, or 2) medical research projects, before undergoing fixation procedures for this study. Photographs were obtained throughout the embalming and dissection procedures using an iPhone XR and exported as JPEG files and stored on Microsoft OneDrive.

Cadaver Information and Arterial Embalming Procedure

The left upper limbs of four fresh frozen cadavers (see Table 1) were embalmed following one or more freeze-thaw cycles. Arterial embalming via the axillary artery was performed using a batch solution containing formalin (see Table 2).

Table 2. List of embalming solution batch ingredients and corresponding volumes. Each upper limb was embalmed with 1.5 L of the batch solution.

Ingredient	Volume
Potassium Acetate	150 mL
Phenol	1 L
Formalin (37% formaldehyde)	1 L
Dettol	600 mL
Glycerol	1 L
Ethanol (95%)	20 L

For the embalming procedure, donors were placed in a supine position and a vertical skin incision was made at the midpoint of the clavicle with an 11-blade scalpel. A small segment of the clavicle, approximately five centimeters in length, was removed using a RIDGID battery-operated saw to provide adequate visualization of the subclavian/axillary artery and vein. Using a probe and forceps, the axillary artery and vein were accessed and isolated using blunt dissection. Two pieces of string were threaded under the axillary artery, and positioned to create a small gap between the strings. The axillary artery was tied off at the proximal end. A small incision in the axillary artery was made parallel to its course, and an embalming trocar was inserted and secured distally with the previously placed string (Fig. 1a). To

Table 1. Characteristics of the four cadavers.

Specimen #	Sex	Age	Cause of Death	# of Freeze-Thaw Cycles	Previous Uses for Surgical Skills and Medical Research
1	Female	92	Congestive heart failure, electrolyte imbalance, dehydration	1	*Emergency Medicine*: surgical airway, chest tubes, thoracotomy *Medical Research:* knees
2	Female	57	Myelodysplastic syndrome and necrotizing pneumonia	2	*Orthopedic Surgery*: feet and ankles *Emergency Medicine*: surgical airway, chest tubes, thoracotomy *Medical Research:* knees
3	Female	106	Advanced dementia, cerebrovascular disease, atrial fibrillation	4	*Emergency Medicine/Anesthesiology*: surgical airway, chest tubes, thoracotomy *Medical Research*: deep back, knees
4	Female	83	Metastatic esophageal cancer	6	*Orthopedic Surgery*: feet and ankles, spine *Emergency Medicine/Anesthesiology*: surgical airway, chest tubes, thoracotomy *Obstetrics and Gynecology*: laparoscopic hysterectomy *Medical research*: knees

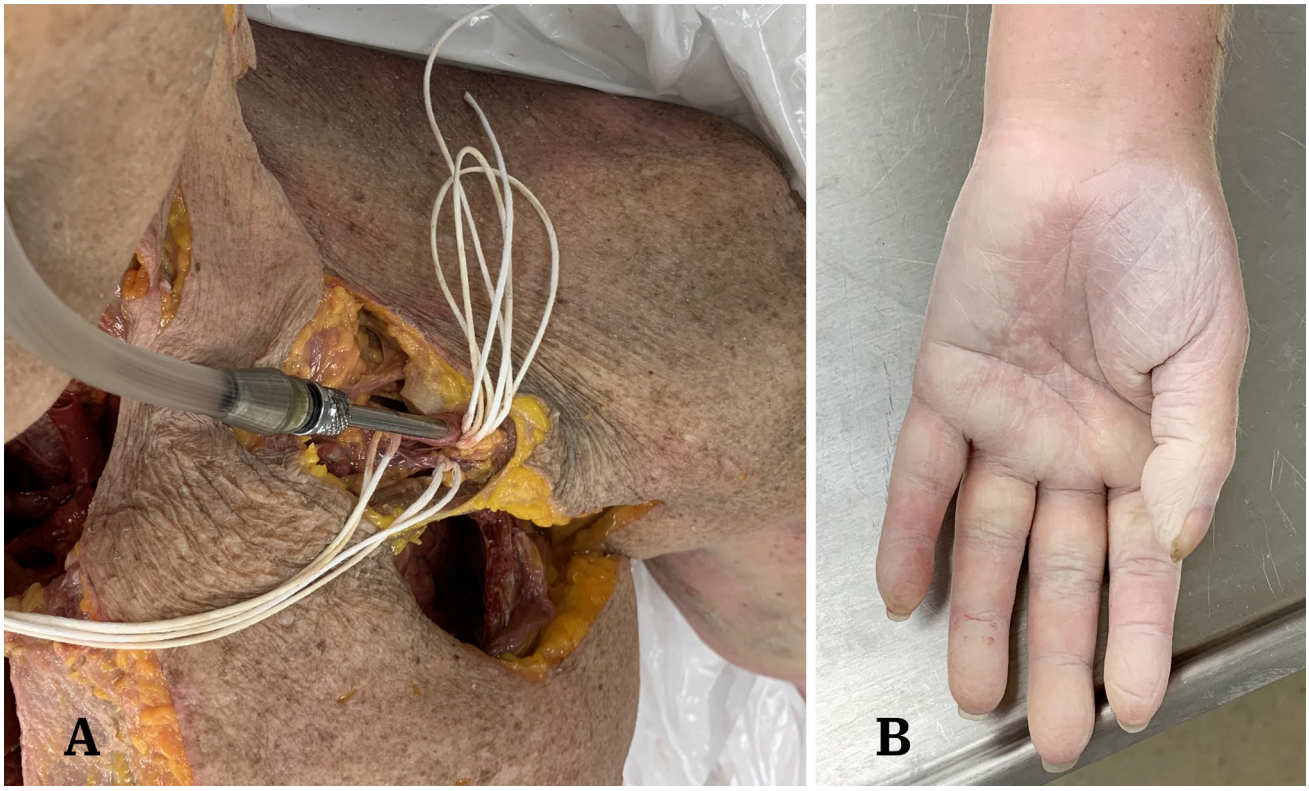

Fig. 1a.- Superior view of left axilla and proximal upper limb with cadaver in supine position to show the embalming site prior to injection of fluid. **1b:** The upper limb was monitored throughout the procedure for signs of tissue perfusion, such as skin mottling (skin appears white in some areas).

increase pressure and minimize retrograde flow of embalming fluid into the axilla and thorax, the axillary vein was tied off at the same level as the axillary artery. One and a half liters of embalming fluid were pumped into each limb at a minimal pressure of 6-7 pounds per square inch, and any small blood vessels that continued to leak fluid under pressure were clamped using hemostats. The embalming fluid was pumped to perfuse each upper limb using a PORTI-BOY Mark V embalming machine. Throughout the embalming procedure, the upper limb was monitored for signs of tissue perfusion, such as skin mottling (Fig. 1b). The embalming line was disconnected when the procedure was complete. The trocar was left in the axillary artery and all hemostats remained clamped. The donor cadavers were placed in a refrigerator at four degrees Celsius for 24 hours following embalming.

Disarticulation and Storage Procedures

Following the 24-hour period, each donor was removed from the refrigerator and an incision was made along the cut end of the clavicle and through the axilla using a 22-blade scalpel. The incision was extended posteriorly along the external surface of the ribs to facilitate the removal of the upper limb from the body at the scapulothoracic joint. The disarticulated limb was placed in a polyethylene bag that measured 20 x 30 inches and 6 mil in thickness. The elbow joint was bent at approximately 90 degrees so that the proximal part of the limb could be submerged in the embalming fluid that drained from the limb during storage (Fig. 2a). Each bag was labelled with the donor's identification number and sealed with a zip tie. The bagged upper limbs were positioned in metal trays to maintain an upright position and the trays were placed in a refrigerator at four degrees Celsius. Three days after disarticulation, a wooden block (7.5 cm x 7.5 cm x 6 cm tall) was placed under each elbow to elevate the limb, assisting in draining excess fluid towards the exposed shoulder region (Fig. 2b). Seven days following elevation of the elbow (ten days after initial disarticulation of the limb) the blocks were removed and the limbs were stored in a flat position in the refrigerator. All upper limbs were allowed to undergo fixation for a total of 30 days following the arterial embalming procedure.

Dissection Procedure

Following storage for 30 days to allow for fixation, limbs were dissected to evaluate the degree of fixation and the quality of the tissue to determine the potential for use as an educational resource. Each limb was photographed prior to the dissection process for documentation. Excess embalming fluid that was pooled in the bottom of the polyethylene bags was disposed according to standard procedures. The upper limbs were dissected by three of the contributing authors, all of whom have considerable experience dissecting formalin-fixed specimens. Standard dissection procedures, as outlined in Appendix A, were followed for the shoulder, arm, forearm, and hand. Each limb was dissected over a two-day period, with two days of storage between the first and second dissection sessions. The upper limbs were wrapped in linen saturated with moistening solution (Table 3) after the first dissection day, and stored in a refrigerator at four degrees Celsius in the original polyethylene bag that corresponded to each specimen. Photos were taken of the completed specimens.

Table 3. List of moistening solution batch ingredients and corresponding volumes.

Ingredient	Volume
Potassium Acetate	150 mL
Ethanol (95%)	250 mL
Dettol	750 mL
Glycerol	1500 mL

RESULTS

All four upper limbs demonstrated adequate tissue fixation 30 days following the arterial embalming procedure. The fixation methods provided suitable conditions for educational dissection and the preparation of prosected specimens. Local areas of unfixed tissue were not identified.

Within each upper limb specimen there were slight differences in texture, such that certain areas of the limb were softer and more edematous compared to other areas, which were firmer. Minimal skin slippage was observed on the wrists and hands prior to dissection of the upper limbs. Additionally, the anterior arm of some specimens had tissue integrity that was delicate, and therefore careful handling was required to avoid unwanted tearing of structures.

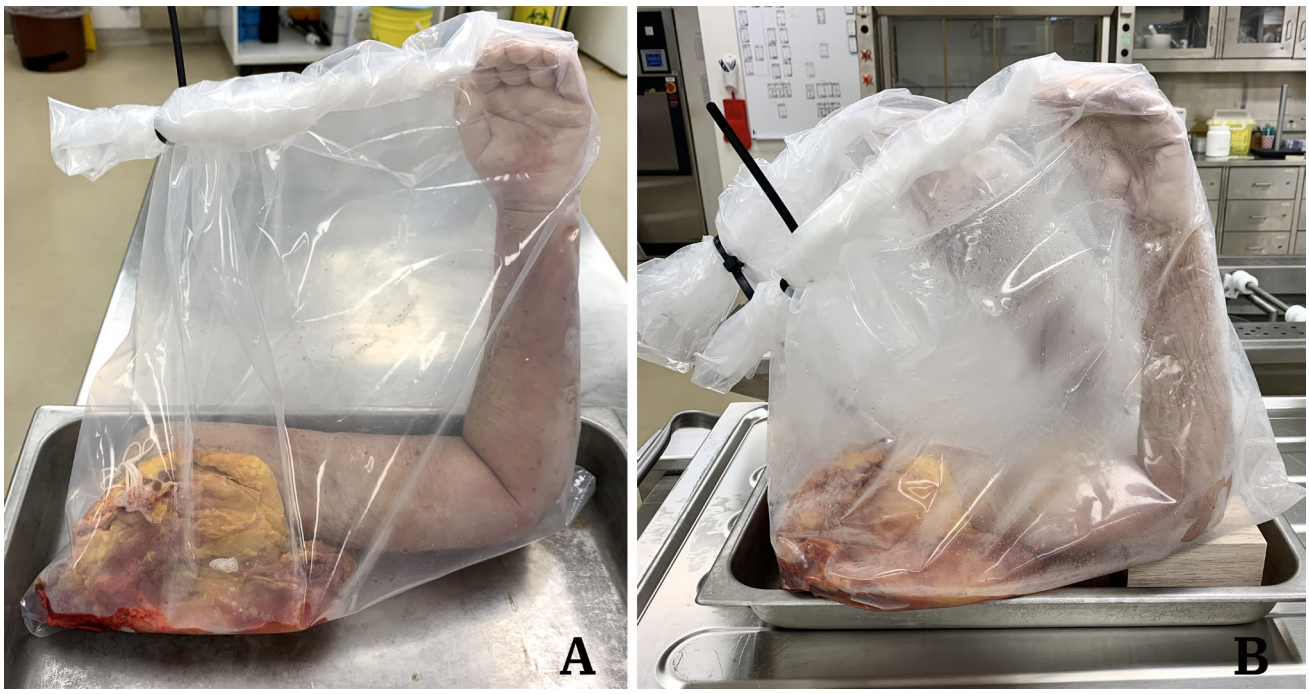

Fig. 2a.- Image of a left upper limb in a polyethylene bag for storage following disarticulation. The upper limb was positioned with the elbow bent at a 90-degree angle to aid in the drainage of additional embalming fluid for partial immersion. **2b:** The elbow was positioned on a wooden block three days following disarticulation to gather fluid at the exposed shoulder region.

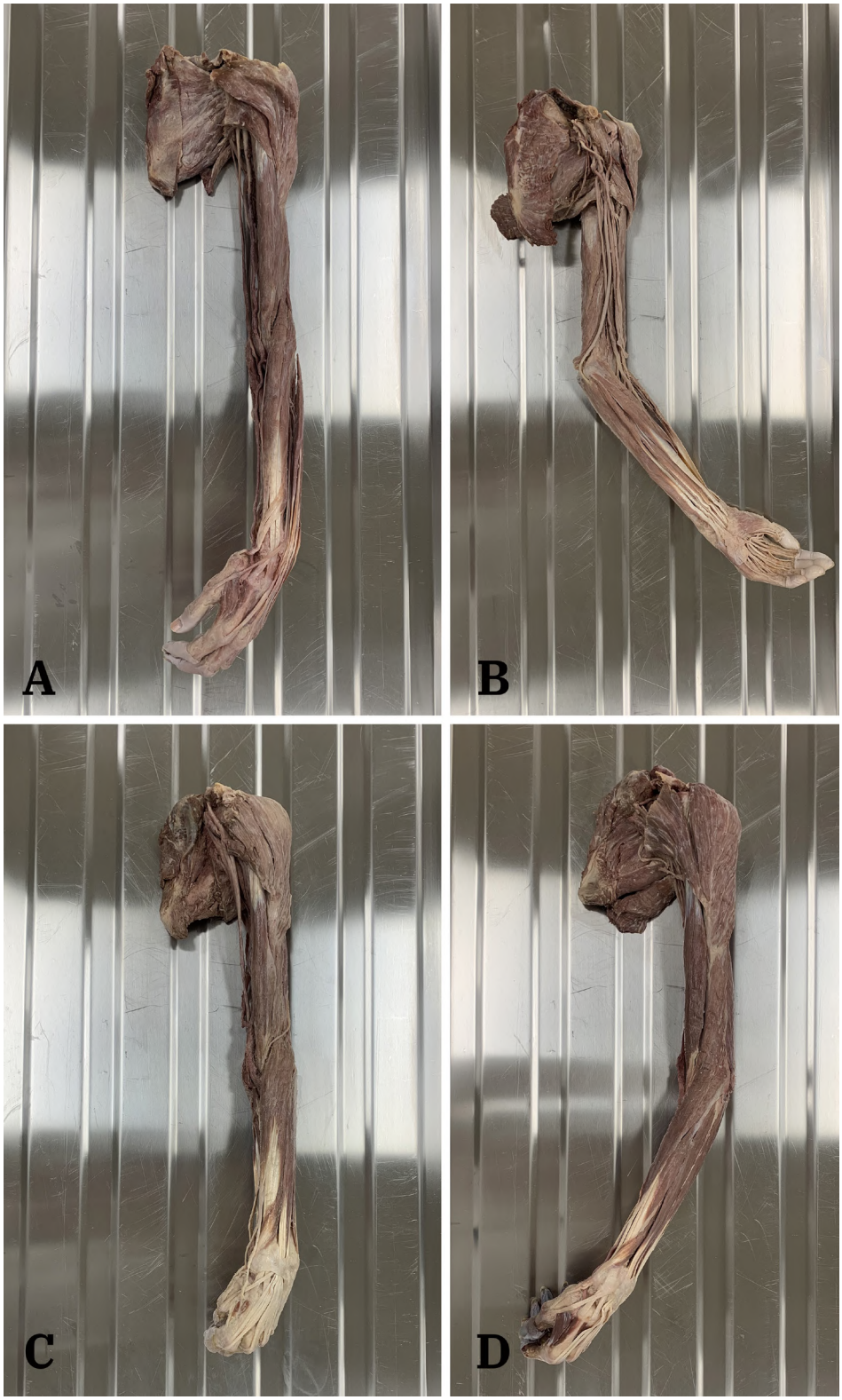

Fig. 3.- Images of four dissected left upper limbs in order of number of freeze-thaw cycles. **3a:** One freeze-thaw cycle. **3b:** Two freeze-thaw cycles. **3c:** Four freeze-thaw cycles. **3d:** Six freeze-thaw cycles.

Despite these observations, all four limbs were deemed to be valuable for use during educational dissection and for prosection purposes. The variety of educational resources that can be created and utilized from formalin-fixed tissue that has previously been frozen and thawed allows for maximal use of body donors for surgical skills training, medical research, and anatomical sciences education.

Educational Dissection

The tissue demonstrated acceptable quality for use as an educational dissection resource, re-

Fig. 4.- Images representing muscle reflections to demonstrate deep structures of the arm and forearm. **4a:** Reflection of extensor digitorum. **4b:** Reflection of deltoid.

gardless of the number of freeze-thaw cycles. The soft tissues were flexible and easy to manipulate, while still maintaining proper form. A superficial dissection demonstrated good muscle integrity, allowing for the definition and mobilization of muscle borders and isolation of neurovascular structures (Fig. 3). A deep dissection following reflection of deltoid, pronator teres, palmaris longus, and extensor digitorum demonstrated adequate tissue integrity, even to the deepest layers of muscle (Fig. 4). The tissue quality allowed for detailed dissection of delicate neurovascular structures, such as the common and proper palmar digital arteries, arising from the superficial palmar arch, and the common and proper palmar digital nerves, arising from the median and ulnar nerves, in the palmar hand (Fig. 5).

Prosection

Two upper limbs from this project were added to the collection of wet prosected specimens at Queen's University, which are used to facilitate the teaching and learning of gross anatomy of the upper limb during laboratory sessions without requiring the time-consuming dissection process.

Additionally, two upper limbs were processed further and added to the collection of specimens displayed in glass jars in the upper limb section of the Anatomy Museum at Queen's University (Fig. 6). The prosections that were produced during this project will be maintained for long-term preservation, and will be beneficial for learners from a wide range of degree programs and educational levels.

DISCUSSION

In this study, four fresh frozen left upper limbs were successfully embalmed using formalin-fixation methods following one or more freeze-thaw cycles. The fixation was deemed to provide sufficient conditions for specimen preparation through educational dissection and prosection, the latter including both wet specimens that can be handled, and specimens preserved in glass jars for long term display. The upper limbs maintained adequate form and tissue integrity while still allowing for the mobilization of muscular and neurovascular structures during dissection. The highest number of freeze-thaw cycles evaluated in this study was six. This limb demonstrat-

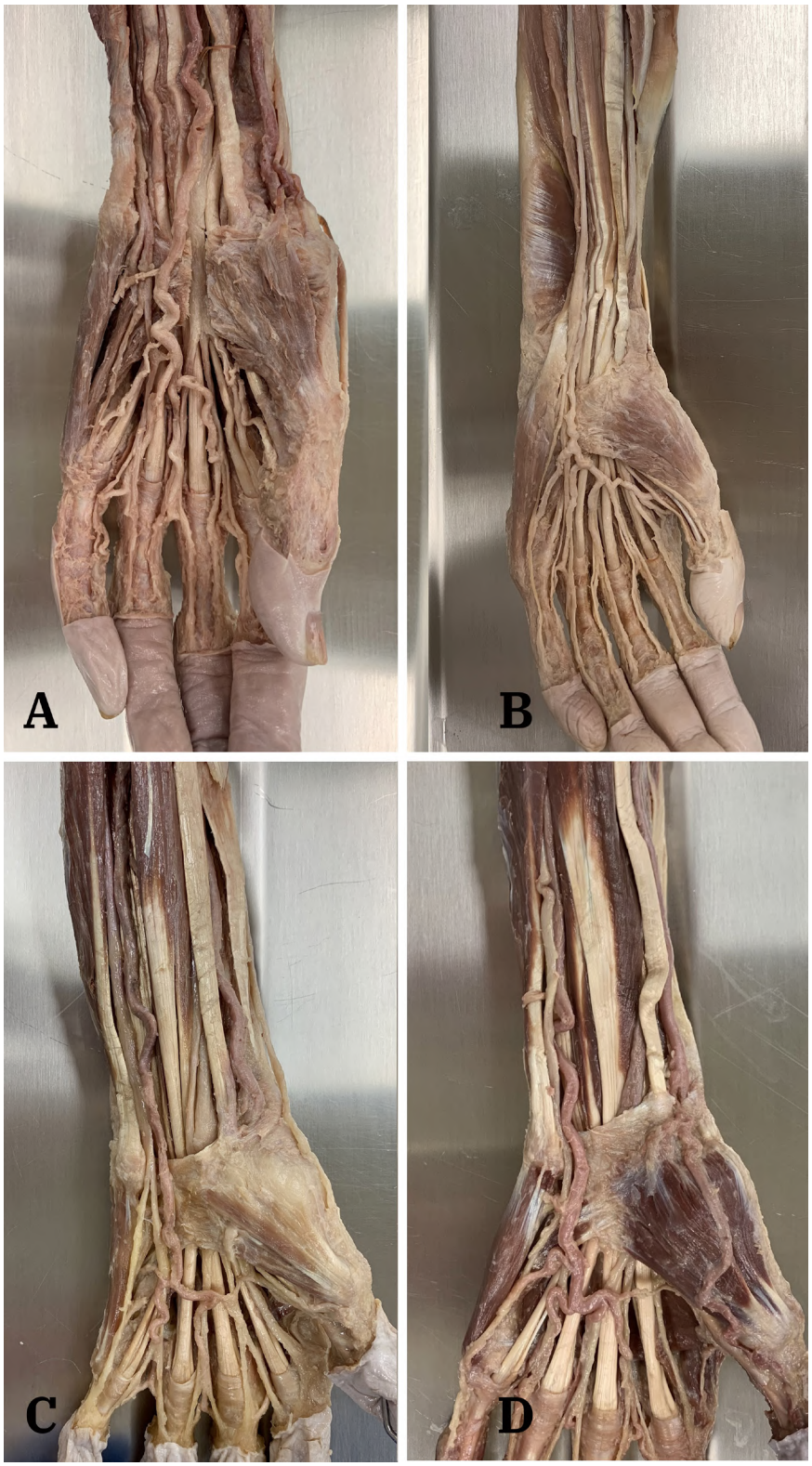

Fig. 5.- Images of the distal anterior forearms and palmar hands of four dissected upper limbs in order of number of freeze-thaw cycles. **5a:** One freeze-thaw cycle. **5b:** Two freeze-thaw cycles. **5c:** Four freeze-thaw cycles. **5d:** Six freeze-thaw cycles.

ed similar tissue characteristics compared to the other three limbs included in the study and was suitable for use as a museum specimen.

Although all four upper limbs were successfully embalmed and demonstrated adequate tissue fixation and tissue quality, some observations that were noted by the dissectors during specimen preparation include: local areas that varied in texture (softer, firmer, edematous, etc.), skin slippage on the wrists and hands, and delicate tissue integrity within the anterior arm of some of the limbs. These factors were not considered to be major impediments with respect to the overall tissue quality

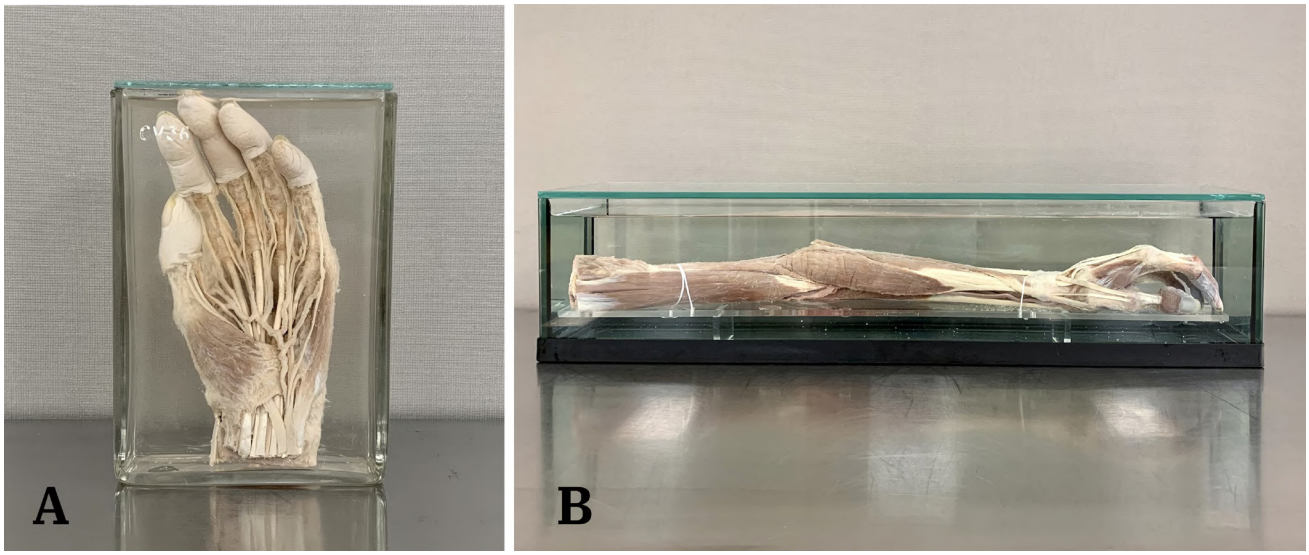

Fig. 6.- Image of two jarred specimens. **6a:** Two freeze-thaw cycles. **6b:** Six freeze-thaw cycles.

of the specimens and the potential use of the specimens for educational dissection and prosection.

Arterial perfusion embalming was selected for the work reported here because body donors designated for formalin-fixation are embalmed using arterial perfusion at Queen's University. Arterial perfusion was considered advantageous compared to simply submerging the upper limbs in fixative. While most often discussed as a component of Thiel embalming (Thiel, 1992), submersion was not considered a viable fixation method for the upper limb specimens. Submersion was predicted to require a greater amount of embalming fluid and fixation time compared to arterial perfusion, and would have complicated storage during the fixation process because of the need for vessels large enough to submerge the specimens for an extended period. The storage procedures for the method described in this work were simple, whereby each specimen was bagged and the limb positioned so that the exposed shoulder was in contact with the excess embalming fluid that pooled in the bag. Fixation of the shoulder region was expected to require partial immersion for two reasons: firstly, the cut end of the specimen was not fully covered by skin and therefore would not retain fluid well after embalming; and secondly, the site the embalming trocar was placed into the axillary artery was distal to the proximal end of the specimen, and therefore it was difficult to predict how well the embalming fluid would travel to the blood vessels in the shoulder region.

Anatomical education with the use of cadaveric dissection as a learning resource is dependent on the ability of body donation programs to maintain a sustainable supply of body donors, a process which requires balancing the number of donations with requests for use (McCumber et al., 2021). Fresh frozen donors are typically reserved for use in surgical skills training sessions or medical research projects, and are prone to tissue deterioration over time, thus limiting their potential use for educational dissection and prosection following the initial sessions. This study has demonstrated a novel approach to maximize body donor usage through formalin fixation of previously frozen and thawed upper limbs. This method allows for the use of fresh frozen donors for surgical skills training sessions and medical research, as well as educational dissection, prosection, and long-term preservation following the formalin-fixation embalming procedure.

We recognize that our study has limitations, such as the small sample size of four left upper limbs and the lack of an objective assessment tool for evaluating the quality of the specimens after fixation is complete. Future methodology may consider assessing the tissue fixation and tissue quality by surveying the users of the specimens. This approach has been used to evaluate the quality of cadavers used in surgical skills training, and could be applied to formalin-fixed specimens (Wang, et al. 2023).

It is likely that untouched lower limbs could be preserved using the method described here by perfusing the femoral artery after a donor has completed fresh frozen usage. Likewise, we believe that formalin-fixed head and neck specimens could be produced by perfusing the common carotid artery, although the brain would not likely be viable, as significant deterioration is expected as a result of freezing and thawing.

As adequate fixation was achieved 30 days following the embalming procedure, we predict that a shorter fixation window could be feasible in achieving adequate results using this technique. However, in estimating the number of days required for fixation it is predicated that the size of the upper limb is an important consideration, as a large upper limb from an overweight donor would likely require a greater number of days for fixation compared to a small upper limb from an emaciated donor.

In conclusion, formalin fixation of four upper limbs following freezing and thawing resulted in tissue fixation and tissue quality suitable for use as educational resources, maximizing the potential usage of human body donors for education and research in anatomical sciences.

ACKNOWLEDGEMENTS

The authors sincerely thank those who donated their bodies to science so that anatomical research and teaching could be performed. Results from such research can potentially increase scientific knowledge and can improve patient care. Therefore, these donors and their families deserve our highest respect. We also thank Dr. William Borman and the Department of Basic Sciences at University of Western States for providing use of the dissection instructions.

REFERENCES

ALSHEHRY M, KANDIL M, ALZAHRANI R, SOAMES R (2019) Thiel embalming pre-frozen cadavers: a mouse model. *BioRxiv*, 523514.

AZIZ M, KERNICK ET, BECK DALLAGHAN GL, GILLILAND KO (2020) Dissection versus prosection: A comparison of laboratory practical examinations. *Med Sci Educ*, 30(1): 47-51.

BALTA JY, CRONIN M, CRYAN JF, O'MAHONY SM (2015) Human preservation techniques in anatomy: A 21st century medical education perspective. *Clin Anat*, 28(6): 725- 734.

BRENNER E (2014) Human body preservation - old and new techniques. *J Anat*, 224(3): 316-344.

CORNWALL J (2011) The diverse utility of wet prosections and plastinated specimens in teaching gross anatomy in New Zealand. *Anat Sci Educ*, 4(5): 269-274.

DOOMERNIK DE, KRUSE RR, REIJNEN MMPJ, KOZICZ TL, KOOLOOS JGM (2016) A comparative study of vascular injection fluids in fresh-frozen and embalmed human cadaver forearms. *J Anat*, 229(4): 582-590.

HILDEBRANDT S (2010) Lessons to be learned from the history of anatomical teaching in the United States: The example of the University of Michigan. *Anat Sci Educ*, 3(4): 202-212.

IWANAGA J, LOUKAS M, DUMONT AS, TUBBS RS (2021) A review of anatomy education during and after the COVID-19 pandemic: Revisiting traditional and modern methods to achieve future innovation. *Clin Anat*, 34(1): 108-114.

JANSEN MM, HAZENBERG CE, DE RUITER QM, VAN HAMERSVELT RW, BLEYS RL, VAN HERWAARDEN JA (2020) Feasibility of fresh frozen human cadavers as a research and training model for endovascular image guided interventions. *PLoS One*, 15(11): e0242596.

MARREEZ YMAH, WILLEMS LN, WELLS MR (2010) The role of medical museums in contemporary medical education. *Anat Sci Educ*, 3(5): 249-253.

MCCUMBER TL, LATACHA KS, LOMNETH CS (2021) The state of anatomical donation programs amidst the SARS-CoV-2 (Covid-19) pandemic. *Clin Anat*, 34(6): 961-965.

O'NEILL J, O'NEILL MDA, ANDRADE F, PAIS D (2013) Improvement of the embalming perfusion method: the innovation and the results by light and scanning electron microscopy. *Acta Med*, 26(3): 188-194.

OVSENEK N (2013) College of medicine gross anatomy report. *University of Saskatchewan*, 51.

SONG YK, JO DH (2022) Current and potential use of fresh frozen cadaver in surgical training and anatomical education. *Anat Sci Educ*, 15(5): 957-969.

STANDRING S (2016) A brief history of topographical anatomy. *J Anat*, 229(1): 32-62.

THIEL W (1992) The preservation of the whole corpse with natural color. *Ann Anat*, 174(3): 185-195.

WANG A, DE SA D, DARIE S, ZHANG B, ROCKARTS J, PALOMBELLA A, NGUYEN L, DOWNER N, WAINMAN B, MONTEIRO S. (2023) Development of the McMaster Embalming Scale (MES) to assess embalming solutions for surgical skills training. *Clin Anat*, 36(5): 754-763.

APPENDIX A. DISSECTION INSTRUCTIONS

Modified from Gross Anatomy I Dissector, University of Western States Original author Dr. William Borman

Initial Dissection

Remove all skin from the shoulder to the middle phalanges. It is not necessary to preserve superficial neurovascular structures. Veins, particularly large and obstructive veins, should be removed to facilitate an efficient dissection.

Posterior Shoulder

1. **Find, clean, and reflect the deltoid muscle**
   Remove the deep fascia from the deltoid muscle so the directionality and borders of the muscle fibers are clearly visible.
   Reflect the posterior fibers of the deltoid muscle from the scapular spine and acromion process.
   Locate and identify the axillary nerve and posterior humeral circumflex artery passing through the quadrangular space.
2. **Locate and identify the posterior scapular muscles**
   Remove the infraspinous deep fascia and supraspinous deep fascia to reveal the infraspinatus and supraspinatus muscles.
   Locate the slender teres minor muscle and larger teres major muscle.
   Follow and clean the tendon of latissimus dorsi muscle to its insertion.
3. **Locate and identify two of the heads of the triceps brachii muscle**
   Clean and isolate the long head and lateral head of the triceps brachii muscle.

Anterior Shoulder & Arm

1. **Reflect the rest of the deltoid muscle and identify the anterior arm muscles**
   Remove the deep fascia from the deltoid muscle so the directionality of the muscle fibers and its borders are clearly visible.
   Reflect the anterior fibers of the deltoid muscle from the clavicle and acromion process.
   When completed, the deltoid muscle will only be attached to the humerus.
   Confirm that pectoralis minor, coracobrachialis, and short head of biceps brachii each attach to the coracoid process of the scapula.
2. **Locate and identify the subscapularis muscle insertion**
   Locate the insertion of the subscapularis muscle on the lesser tubercle of the humerus.
3. **Trace the terminal branches of the brachial plexus through the arm**
   Musculocutaneous nerve (terminates as lateral antebrachial cutaneous nerve)
   Median nerve
   Ulnar nerve
   Medial antebrachial cutaneous nerve
   Radial nerve
   Axillary nerve
4. **Trace the vascular elements through the anterior arm**
   Brachial artery
   Brachial veins
   Profunda brachii artery is an early branch of the brachial artery that passes with the radial nerve toward the triangular interval to the posterior arm.
   Several muscular arteries branch from the brachial artery to supply the anterior arm muscles.

Cubital Fossa & Anterior Forearm

1. **Reflect the bicipital aponeurosis**
   Identify and incise the bicipital aponeurosis to expose the brachial artery and median nerve in the cubital fossa.
2. **Identify the muscular elements of the cubital fossa and reflect pronator teres**
   Brachioradialis muscle forms the lateral border of the cubital fossa.
   Pronator teres muscle (with its deep and superficial heads) forms the medial border of the cubital fossa.
   Brachialis muscle forms the floor of the cubital fossa medially.
   Locate the median nerve and trace it between the superficial and deep heads of the pronator teres muscle.
   Reflect the pronator teres muscle from its distal attachment on the radius.
3. **Identify the forearm flexor muscles**
   Identify and remove the deep fascia from the anterior forearm.
   Identify the three remaining superficial forearm flexor muscles: flexor carpi ulnaris, flexor carpi radialis, and palmaris longus.
   Identify the ulnar nerve and artery as they run deep to the flexor carpi ulnaris muscle and become superficial at the wrist.
   Flexor digitorum superficialis muscle is the large muscle in the intermediate layer.
   Flex the hand at the wrist and move the tendons of flexor digitorum superficialis to the side to expose the flexor digitorum profundus muscle in the deep layer.
   Locate and identify the flexor pollicis longus muscle in the deep layer, lateral to the flexor digitorum profundus muscle.
   Pronator quadratus muscle is located deep to the tendons of flexor digitorum profundus.
4. **Locate and identify the radial nerve and its two branches**
   Locate the radial nerve deep in the tissue plane between the brachioradialis muscle and the brachialis muscle.
   Identify the bifurcation of the radial nerve into the superficial radial nerve and deep radial nerve.

5. **Locate the radial and ulnar arteries in the cubital fossa**
   Brachial artery bifurcates in the cubital fossa to form the radial artery (laterally) and ulnar artery (medially)

Posterior Forearm & Dorsum Hand

1. **Identify the superficial forearm extensor muscles**
   Identify and remove the deep fascia from the posterior forearm.
   Brachioradialis muscle forms the lateral border of the cubital fossa.
   Identify the extensor carpi radialis longus muscle on the lateral aspect of the forearm and trace it to its attachment on the base of the 2nd metacarpal.
   Identify the extensor carpi radialis brevis muscle on the lateral aspect of the forearm and trace it to its attachment on the base of the 3rd metacarpal.
   Extensor digitorum muscle is the centrally located multicaudal muscle. Note the expansion of these tendons on the dorsum of the digits.
   Extensor digiti minimi muscle is often blended with the medial aspect of the extensor digitorum muscle.
   Extensor carpi ulnaris muscle is located on the medial aspect of the forearm.
   Locate and identify the extensor retinaculum.

2. **Identify the deep and outcropping forearm extensor muscles**
   Extending the hand at the wrist will facilitate separating and identifying these muscles.
   Three outcropping muscles act on the thumb: abductor pollicis longus, extensor pollicis brevis, and extensor pollicis longus.
   One of the deep muscles acts on the index finger: extensor indicis.
   Expose the supinator muscle and the outcropping muscles more fully by reflecting the extensor digitorum muscle from its proximal attachment.

3. **Identify the neurovascular elements of the posterior forearm**
   Locate and identify the deep radial nerve in the anterolateral elbow.
   Locate and identify the posterior interosseous nerve as it emerges from the supinator muscle.
   Observe the tendinous borders of the anatomical snuffbox: abductor pollicis longus tendon and extensor pollicis brevis tendon laterally and the extensor pollicis longus tendon medially.
   Identify the radial artery in the anatomical snuffbox

Palmar Hand

1. **Carefully reflect the skin from the palmar surface of the hand and digits**
   Palmaris brevis muscle will be in the superficial palmar fascia near the proximal region of the hypothenar eminence.

2. **Find, clean, and reflect the palmar aponeurosis**
   Expose the palmar aponeurosis and note it is a relatively thick, tough sheet of dense fascia with fibrous cords extending longitudinally to the digits and deep to the metacarpal bones.
   Carefully reflect the palmar aponeurosis from its distal attachments and its metacarpal attachments leaving it connected only to the palmaris longus tendon and palmaris brevis muscle.
   The palmar carpal ligament is under the palmaris longus tendon.

3. **Follow the ulnar artery into the palm**
   Trace the ulnar artery superficial to the flexor retinaculum to its bifurcation into the deep and superficial branches.
   The deep branch of the ulnar artery contributes to the formation of the deep palmar arterial arch.
   The superficial branch of the ulnar artery is the predominant contributor to the superficial palmar arterial arch.
   Common palmar digital arteries branch from the superficial palmar arterial arch and subsequently bifurcate into proper palmar digital arteries.

4. **Follow the ulnar nerve and median nerve into the hand**
   Trace the ulnar nerve superficial to the flexor retinaculum.
   Deep ulnar nerve enters the hypothenar eminence and continues to several deep muscles in the palm.
   Superficial ulnar nerve branches to form common palmar digital nerves which subsequently branch to form proper palmar digital nerves to the medial 1 ½ digits.
   Just distal to the flexor retinaculum, identify the recurrent branch of the median nerve entering the thenar eminence.
   Identify the common palmar digital nerves as they arise from the median nerve and subsequently branch to form proper palmar digital nerves to the lateral 3 ½ digits.

5. **Separate and identify muscles of the palm**
   Blunt dissect and separate the three muscles of the thenar eminence: abductor pollicis brevis, flexor pollicis brevis, and opponens pollicis.
   Blunt dissect and separate the three muscles of the hypothenar eminence: abductor digiti minimi, flexor digiti minimi brevis, and opponens digiti minimi
   Separate and identify the four lumbrical muscles.
   Clean and identify the fibrous digital sheaths surrounding the tendons of the flexor digitorum superficialis muscle and flexor digitorum profundus muscle.

The anatomical location of the great saphenous vein at the thigh and ankle: a neonatal cadaver study

Daniël J. van Tonder[1,2], Ahmad Kathrada[1], Adnan Lokhandwala[1], Martin L. van Niekerk[3], Albert van Schoor[2]

[1] Department of Anatomy and Cellular Biology, College of Medicine and Health Sciences, Khalifa University, Abu Dhabi, United Arab Emirates

[2] Department of Anatomy, Basic Medical Sciences Building, Prinshof Campus, Faculty of Health Sciences, University of Pretoria, South Africa

[3] Department of Paediatric Surgery, Faculty of Health Sciences, University of Pretoria, South Africa

SUMMARY

Providing critically ill neonatal patients with parenteral nutrition, medication, fluids, and access to blood sampling is essential in intensive care units. One option for blood sampling is the great saphenous vein within the proximal thigh, and near the medial malleolus in neonates via 'conventional' landmark and ultrasound techniques. Practitioners in many countries still use the traditional landmark approach to locate the great saphenous vein in neonates, regardless of access to ultrasound. We aim to provide measurements that accurately describe the anatomy of the great saphenous vein in neonates to aid in cannulation success.

The great saphenous vein was exposed in the proximal thigh and near the medial malleolus by reflecting the skin in 31 and 30 formalin-fixed neonate cadavers, respectively. Pins were placed at essential bony landmarks and soft tissue structures. The termination of the great saphenous vein within the proximal thigh can be located 6.8 ± 1.5 mm inferior to the inguinal ligament. The average shortest distance from the medial malleolus to the great saphenous vein was 4.3 mm, 2.0 mm anterior, and 3.1 mm superiorly. The diameter of the great saphenous vein in the proximal thigh and at the medial malleolus ranged between 1.4 mm and 1.6 mm, and 0.9 mm and 1.1 mm, respectively with a 95% confidence level. Our results provide a more accurate description to gain venous access through the great saphenous vein. However, if available, ultrasound should be used to locate and confirm the diameter of the great saphenous vein in the lower limb.

Key words: Parenteral nutrition – Cannulation – Formalin-fixed – Ultrasound – Vascular access – Catheterization

Corresponding author:
Daniël J. van Tonder. Department of Anatomy and Cellular Biology, College of Medicine and Health Sciences, Khalifa University, PO Box 127788, Abu Dhabi, United Arab Emirates. Phone: +971 2 312 4721. E-mail: daniel.tonder@ku.ac.ae - ORCID: 0000-0001-8246-915X

Submitted: July 12, 2023. **Accepted:** October 23, 2023

https://doi.org/10.52083/GDNI1668

INTRODUCTION

Obtaining peripheral venous access can be difficult, but is essential in critically ill neonatal populations. Acquiring venous access in neonatal patients will allow for parenteral nutrition, medication, fluids administration, and will also provide access for blood sampling (Detaille et al., 2010; Rocha et al., 2017). Successfully cannulating venous structures on the first attempt within neonates is vital, as multiple attempts to penetrate the venous structure could result in associated pain with atypical sensitivity and behavioral changes (Ponnusamy et al., 2014). Most peripheral veins in neonates are especially small in diameter, which complicates visualization and cannulation (Ponnusamy et al., 2014). Historically, venous access was obtained using only anatomical landmarks. With the introduction of ultrasound guidance, venous cannulation is now much safer, particularly in neonates. A high-frequency linear array transducer can be used to give the best resolution without the need for significant tissue penetration (Brass et al., 2015; Bruzoni et al., 2013; Sigaut et al., 2009). However, ultrasound-guided venous cannulation is not advantageous when users have limited ultrasound training (Bair et al., 2008): this is especially true if the user does not have a good understanding of the anatomy visualized on the screen.

The great saphenous vein "*Vena saphena magna*" is the longest vein in the human body, originating at the medial foot and receiving deep pedal tributaries from the dorsal venous arch of the foot "*arcus venosus dorsalis pedis*" and the dorsal digital veins of the big toe "*venae digitalis dorsalis pedis primae*" as it courses to the medial malleolus (Caggiati et al., 2002; Kachlik et al., 2011). The great saphenous vein courses anteriorly to the medial malleolus as it moves superiorly over the posteromedial aspect of the knee joint before continuing to the saphenous opening overlying the femoral triangle, on the anterior aspect of the proximal thigh, where it terminates at the saphenofemoral junction and drains into the common femoral vein (Kachlik et al., 2011; Standring, 2020). The great saphenous vein is a suitable and safe alternative for venous access, particularly in small infants (Aria et al., 2014). Gaining vascular access through the great saphenous vein within the proximal thigh can be attempted with an open surgical technique inferior to the inguinal crease and medial to the femoral artery, or through a cutaneous landmark approach (Chokshi et al., 2010). The great saphenous vein near the medial malleolus is a commonly used venous access point in neonates due to its sufficient diameter and its position to the skin (Ponnusamy et al., 2014). In addition, the great saphenous vein near the medial malleolus provides sufficient stabilization while aiding in easy cannulation into the inferior vena cava (Uygun, 2016).

Cannulation of the great saphenous vein in neonates is rarely investigated in medical literature due to its concealed nature and poor direct visibility under high-frequency ultrasounds (Bian et al., 2021). Nonetheless, it is important to note that while a limited number of studies have used the great saphenous vein as a route for central venous access in neonates and infants, there are multiple locations to puncture the great saphenous vein, including: near the medial malleolus (Bian et al., 2021), medial to the popliteal fossa (Tu et al., 2021), and within the proximal thigh below the femoral pulse (Pramod et al., 2022). Access through the great saphenous vein coincides with the logical progression of attempting peripheral venous access first, and moving to more central venous structures, minimizing complications such as thrombosis, arterial injury, or complete occlusion to central veins (Aria et al., 2014). The recommended choice for the site of peripherally inserted central catheters to minimize catheter-related blood stream infection is the great saphenous vein in relation to the medial malleolus (Sarmento Diniz et al., 2022). This would optimize the first attempt success rate, reducing the duration of the procedure and limiting the complications of stress and pain in neonates (D'Andrea et al., 2022). In instances where the great saphenous vein is occluded, the risks associated with gaining venous access decrease (Aria et al., 2014). Furthermore, the diameter of the great saphenous vein is an important variable with respect to the success rate of cannulation. Hanada et al. (2017) and Schnadower et al. (2007) reported that the diameter of the vein has an association with the success rate of the first puncture. As such, there

is a need to provide accurate anatomical measurements of the great saphenous vein within the proximal thigh and near the medial malleolus in neonates for successful localization and venous cannulation.

This study aims to provide the location of the great saphenous vein in relation to the inguinal ligament within the proximal thigh, and to determine the shortest distance between the most prominent point of the medial malleolus and the great saphenous vein at the ankle. Moreover, we determine the diameter of the great saphenous vein in the proximal thigh and near the medial malleolus. Furthermore, we identify the necessary locations and compare literature for making incisions to guide successful location and venous cannulation in neonatal patients.

MATERIALS AND METHODS

Materials

A sample of 31 and 30 formalin-fixed neonate cadavers was used in this study to investigate the great saphenous vein near the proximal thigh and at the medial malleolus, respectively. All cadavers had been donated to the Department of Anatomy, University of Pretoria under the rules and regulations of the South African National Health Act, 61 of 2003 for research and teaching purposes. Ethical clearance to conduct this study was obtained from the University of Pretoria's Faculty of Health Sciences Research Ethics Committee (ethics clearance number: 447/2018). At the time of death, all the cadavers were younger than six weeks. Cadavers were obtained and stored according to the standards set out in the South African National Health Act (61 of 2003), as well as the 1964 Declaration of Helsinki. All sample demographics are presented in Table 1 and 2. We excluded cadavers with any developmental abnormalities in the lower limb region or where previous dissections had disrupted the normal anatomy of the region.

A Vernier mechanical dial caliper (accuracy of 0.01mm) manufactured by Beta (Beta©, 2023, Beta Utensili S.P.A., Sovico, Italy) was used to make all the measurements.

Methods

Within the proximal thigh, two lateral incisions were made: one at the trans-tubercular line — the imaginary line connecting the two iliac tubercles (located on the iliac crests) — and the second approximately at the mid-thigh, from the medial surface extending anteriorly across to the lateral

Table 1. Demographic information concerning the neonatal cadavers used to measure the great saphenous vein near the proximal thigh. (n = number of individuals).

	n	Range	Minimum	Maximum	Mean	Std. Deviation
Age (days)	31	16	0	16	1.10	3.13
Height (m)	31	0.24	0.29	0.53	0.38	0.06
Weight (kg)	31	2.00	0.60	2.60	1.25	0.58
BMI	31	10.47	5.00	15.47	8.34	2.95
Male	17	-	-	-	-	-
Female	14	-	-	-	-	-

Table 2. Demographic information concerning the neonatal cadavers used to measure the great saphenous vein at the medial malleolus. (n = number of individuals).

	n	Range	Minimum	Maximum	Mean	Std. Deviation
Age (days)	30	27	0	27	2.53	5.67
Height (m)	30	0.27	0.29	0.56	0.38	0.06
Weight (kg)	30	2.40	0.60	3.00	1.27	0.64
BMI	30	10.47	5.00	15.47	8.52	2.83
Male	17	-	-	-	-	-
Female	13	-	-	-	-	-

surface. Another midline incision was made extending from the trans-tubercular line to the incision made at the thigh. The skin of the proximal thigh and the inguinal region was then reflected laterally to expose the underlying subcutaneous fat and fascia. The subcutaneous fat together with the saphenous fascia surrounding the great saphenous vein and the fascia lata superficial to the common femoral vein (Caggiati, 1999) were carefully separated to clearly see the course of the vessels. The sartorius muscle and the inguinal ligament were cleaned, so that the medial border of the sartorius and the inferior border of the inguinal ligament were clearly visible (Fig. 1a). The neonatal cadaver was then positioned and clamped supine with the thigh rotated externally. This was to simulate as much as possible the surgical position that a neonate would be placed in when attempting to insert a catheter into the great saphenous vein in the proximal thigh. Pins were then placed on the anterior superior iliac spines, pubic tubercle, and other soft tissue structures such as the saphenofemoral junction and great saphenous vein.

The distance between the anterior superior iliac spine and the pubic tubercle was used to determine the inguinal ligament length. The midpoint termination of the great saphenous vein into the common femoral vein was projected superiorly perpendicularly to the inguinal ligament and was used to determine where the great saphenous vein terminates in relation to the inguinal ligament. The distance from the translocated point on the inguinal ligament to the termination of the great saphenous vein was measured.

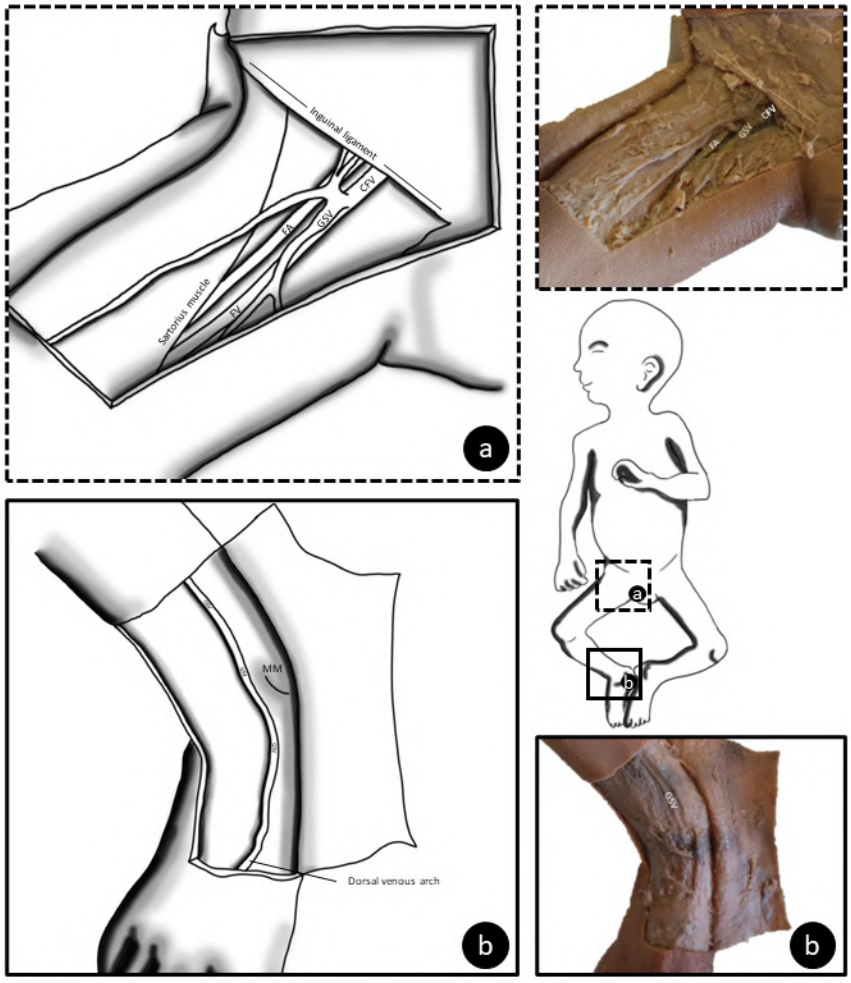

Fig. 1.- Schematic representation of the great saphenous vein within the proximal thigh and near the medial malleolus. **a)** Anterior view of the proximal thigh illustrating cleaned superficial and deep vascular structures. **b)** Medial aspect of the ankle, illustrating the course of the great saphenous vein as it courses from the dorsal venous arch of the foot superiorly. (CFV = Common femoral vein; FA = Femoral artery; FV = Femoral vein; GSV = Great saphenous vein; MM = Medial malleolus).

To expose the great saphenous vein near the medial malleolus, the skin covering the medial malleolus was reflected by making three skin incisions. The first, superior to the medial malleolus, extended horizontally from the anterior aspect of the ankle to the superior aspect of the medial malleolus. The second was inferior to the medial malleolus, extending from the anterior surface of the dorsum of the foot to the inferior aspect of the medial malleolus. Finally, the third incision was made, connecting both the anterior incisions from the anterior aspect of the ankle to the dorsum of the foot (Fig. 1b). The most prominent point on the anterior margin of the medial malleolus was identified and pinned, as well as the great saphenous vein closest to the medial malleolus. Care was taken not to disturb the course of the great saphenous vein while the vein was being exposed.

To determine the location of the great saphenous vein near the medial malleolus at the distal end of the lower limb, the measurement between the most prominent point on the anterior margin of the medial malleolus and the great saphenous vein was measured. In addition, two planes were established: the first parallel to the plantar surface of the foot — the horizontal plane — and the second perpendicular to the plantar surface of the foot — the vertical plane. The distances between the most prominent aspect of the medial malleolus and the great saphenous vein in the horizontal planes, as well as the distance in the vertical plane, will allow the location of the great saphenous vein to be described in quantitative values.

In addition, the outer diameter of the great saphenous vein within the proximal thigh and near the medial malleolus was measured as close to the point of interest as possible. Care was taken not to compress the vein when the diameter was measured.

Statistical analysis

Statistical analysis was conducted on IBM SPSS Statistics version 27.0.1.0 (2023©, IBM®, SPSS Inc, New York USA) and summarized using descriptive statistics, including mean, median, standard deviation and 95% confidence intervals. We compared measurements from the left and right sides using a paired t-test or Wilcoxon Signed Rank test, depending on the distribution of the data determined by a Shapiro-Wilk test for normality, and after outliers were removed via standardized values. We used an inter- and intra-observer error analysis to test for repeatability and accuracy, following Bland and Altman (2010) on 25% of the sample.

RESULTS

Quantitative data

After both left and right distribution were determined to be normal with a Shapiro-Wilk test for normality, the paired t-test revealed no significant difference (p-value > 0.05) between the left and right measurements. This was followed by combining the left and right sides and producing a descriptive statistical analysis together with a 95% confidence interval.

The descriptive statistical analysis of the great saphenous vein within the proximal thigh is outlined in Table 3. The average length of the inguinal ligament in the sample was 25.5 ± 3.4 mm (mean

Table 3. Descriptive statistical analysis and 95% confidence interval in mm, after combining applicable left and right sides of the great saphenous vein in the proximal thigh. (n= number of individuals; Min= Minimum; Max= Maximum; SD= Standard deviation; GSV = great saphenous vein; IL = Inguinal ligament; PT = Pubic tubercle).

	n	Range	Minimum	Maximum	Mean		SD	95% Confidence interval for mean	
					Statistic	Std. Error		Lower	Upper
IL length	58*	14.10	19.45	33.55	25.51	0.45	3.40	24.41	26.45
GSV-IL	60	5.91	0.89	6.80	3.90	0.19	1.50	3.38	4.24
IL-PT	59*	11.71	3.09	14.80	8.17	0.33	2.50	7.57	8.97
GSV diameter	49*	1.58	0.71	2.29	1.49	0.05	0.36	1.38	1.60

*Removal of outliers reduced number of individuals

Table 4. Descriptive statistical analysis and 95% confidence interval in mm, after combining applicable left and right sides of the great saphenous vein near the medial malleolus. (n= number of individuals; SD= Standard deviation; MM = medial malleolus; GSV = great saphenous vein).

	n	Range	Minimum	Maximum	Mean		SD	95% Confidence interval for mean	
					Statistic	Std. Error		Lower	Upper
MM-GSV	55*	5.40	1.58	6.98	4.25	0.18	1.33	3.85	4.58
Horizontal plane	56*	5.03	0.05	5.08	2.03	0.14	1.05	1.69	2.23
Vertical plane	57*	5.42	0.39	5.81	3.12	0.19	1.42	2.74	3.52
GSV diameter	55*	1.24	0.49	1.73	1.04	0.04	0.29	0.94	1.10

*Removal of outliers reduced number of individuals

± standard deviation), while the distance from the termination of the great saphenous vein to the inguinal ligament averaged 3.9 ± 1.5 mm. The average distance from the termination of the great saphenous vein's perpendicular projected point on the inguinal ligament to the pubic tubercle had a mean distance of 8.2 ± 2.5 mm. The great saphenous vein's diameter ranged between 1.4 mm and 1.6 mm, with a confidence level of 95%.

The descriptive statistical analysis of the great saphenous vein near the medial malleolus is outlined in Table 4. The average shortest distance between the medial malleolus and the great saphenous vein was 4.3 ± 1.3 mm. In the horizontal plane, the average distance to the great saphenous vein from the medial malleolus was 2.0 ± 1.1 mm anteriorly. While in the vertical plane, the mean distance to the great saphenous vein was 3.1 ± 1.4 mm superiorly. With a confidence level of 95%, the average diameter of the vein ranged between 0.9 mm and 1.1 mm.

Interobserver and intra-observer error analysis

No clinically significant difference and bias for the interobserver and intra-observer measurements could be identified when Bland and Altman (2010) method was used. The results of this study were therefore considered to be repeatable and accurate.

DISCUSSION

Peripheral intravenous cannulation in neonates can present with symptoms such as extravasation, phlebitis, leakage, spontaneous dislodgment, and catheter-associated blood stream infections (Garland et al., 1992; Unbeck et al., 2015). As a result, ultrasound-guided venipuncture in all ages is more attractive as it provides 'real-time' imagery, while cannulation of venous structures is attempted. The ultrasound-guided technique for cannulation of the great saphenous vein has been shown to reduce the number of attempts needed when compared to the anatomical approaches (Joshi et al., 2010). More specifically with reference to neonates, ultrasound-guided techniques have been demonstrated in terms of success rates, comfort, improved localization, and decreased total procedural times (Bian et al., 2021; Pramod et al., 2022; Tu et al., 2021). However, it has been also indicated that ultrasound-guided cannulation techniques have limited capabilities in terms of safety and quality, especially with those practitioners that have limited ultrasound training (Bair et al., 2008; Brass et al., 2015; Otani et al., 2018). Ultrasound effectiveness is significantly dependent on the training, skill, and experience of the health professional, as indicated by Schoenfeld *et al.*(2011). Further evidence shows that it takes as many as nine attempts after training to achieve a 70% probability of success in pediatric patients (Anderson et al., 2021). As such, other than the ultrasound-guided methods, the landmark approach is still commonly used for the localization of the great saphenous vein in neonates (Pramod et al., 2022; Tu et al., 2021).

Chokshi et al. (2010) state that the saphenofemoral junction is a reliable and easy route to gain central venous access. Access is achieved by making a small incision inferior to the inguinal crease and medial to the femoral artery, and the vein will be found within the subcutaneous tissue (Chokshi

et al., 2010). Dronen and Lanter (1999) located the proximal great saphenous vein in adults by making an incision 50 mm inferior to the junction between the middle and medial one-third of the imaginary line running from the pubic tubercle to the anterior superior iliac spine. In this neonatal cadaver sample, the great saphenous vein and its termination as the saphenofemoral junction was found 6.8 ± 1.5 mm inferior to the inguinal ligament. The termination of the great saphenous vein at the saphenofemoral junction perpendicularly projected to the inguinal ligament was on average 8.2 mm inferior to the inguinal ligament. The distance between the pubic tubercle and the anterior superior iliac spine, or the inguinal ligament length, was 25.5 ± 3.4 mm. The ratio between the distance from the pubic tubercle to the projected point, the great saphenous vein's termination perpendicular to the inguinal ligament and the inguinal ligament's length in this neonatal sample is one-third the distance (Fig. 2a). The diameter of the proximal great saphenous vein ranged between 1.4 mm and 1.6 mm with a confidence interval of 95%.

The great saphenous vein originates from the dorsal venous arch of the foot and courses superiorly anterior to the medial malleolus, and then runs just behind the medial aspect of the knee and is often visible on the posteromedial aspect of the knee where it curves round the top of the tibia (Kachlik et al., 2010; Lockhart et al., 2019). The site near the popliteal fossa is a good site for central venous catheter insertion. Tu et al. (2021) reported the vein diameter near the popliteal fossa of neonates to be 0.8 mm and 0.7 mm in the

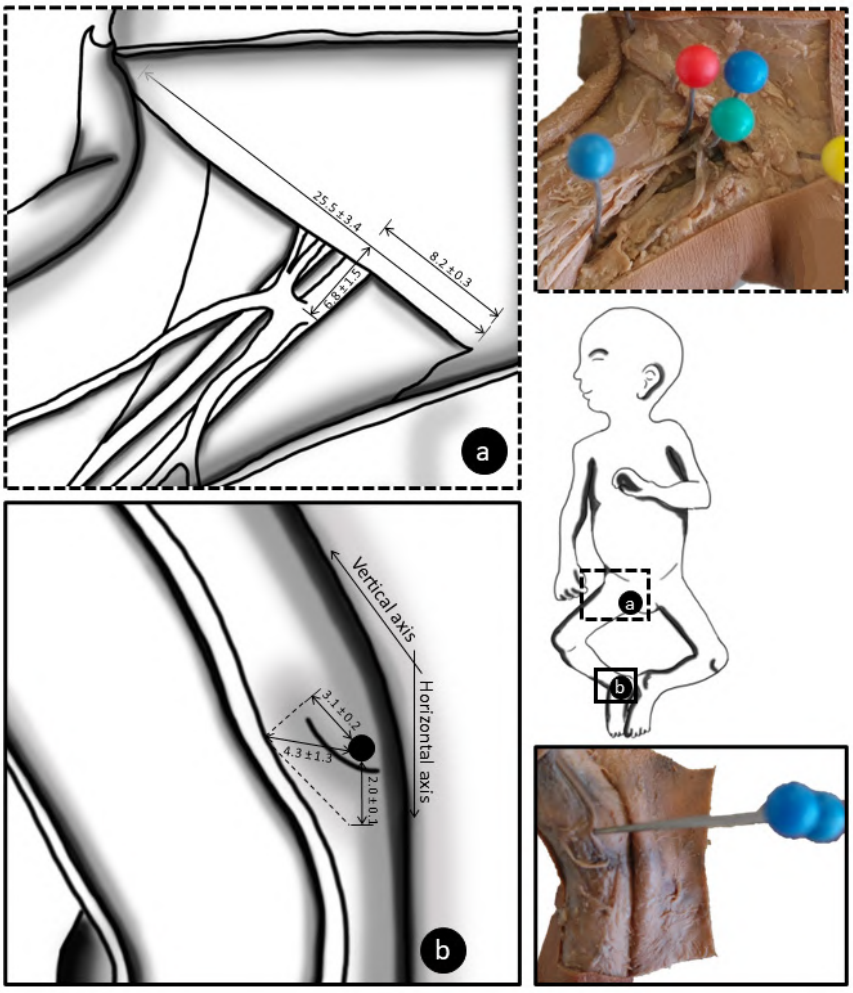

Fig. 2.- Schematic representation of the location of the great saphenous vein within the proximal thigh and near the medial malleolus. **a)** Anterior view of the proximal thigh indicating the length of the inguinal ligament the distance from the great saphenous vein to the inguinal ligament. **b)** Medial aspect of the ankle, showing the shortest distance from the most prominent point of the medial malleolus to the great saphenous vein and the distances in a vertical and horizontal axis.

ultrasound group and control group, respectively. Another variable measured in this study is termed the venous depth, which refers to the distance between the skin and the near edge of the vein.

Bian et al. (2021) conducted a randomized clinical trial, in which they explored the great saphenous vein's anatomy at the medial malleolus in 144 infants between the ages of four and nine months with congenital heart disease, using both ultrasound and conventional anatomical landmark techniques. They reported the diameter and depth of the great saphenous vein measured via both techniques were not significantly different. The depth was 3.62 ± 1.41 mm and 3.61 ± 1.42 mm for ultrasound-assisted group and 'traditional' anatomical landmark group, respectively. Additionally, the diameter of the great saphenous vein was found to be 1.49 ± 0.32 mm and 1.54 ± 0.40 mm for the ultrasound-assisted group and the 'traditional' anatomical landmark group, respectively. In addition, Triffterer et al. (2012) investigated the measurements of the great saphenous vein at the level of the medial malleolus via ultrasound-guided technique in 65 infants (less than six months of age) and neonates for venous cannulation. They reported the median diameter of neonates and infants' right lower limb's great saphenous vein as 1.5 mm (1.1 mm to 2.99 mm). Additionally, the median depth of the great saphenous vein at the site of the right leg's medial malleolus to be 4.4 mm (1.5 mm to 9.5 mm). In this study, the measured diameter of the great saphenous vein near the medial malleolus ranged between 0.9 mm and 1.1 mm, with a confidence level of 95%. Table 5 compares the different findings from the studies conducted by Bian et al. (2021), Tu et al. (2021) and Triffterer et al. (2012). Furthermore, Triffterer et al. (2012) indicated that agenesis may be explored in the case of the great saphenous vein not being visible under high resolution ultrasound. When gaining venous access at the great saphenous vein near the medial malleolus, Puntis (1987) used a silastic feeding line with an external diameter of 0.6 mm. The silastic feeding line used by Puntis (1987) would have been appropriate for this sample population. Church and Jarboe (2017) suggest using imaging technology like ultrasound and fluoroscopy to accurately determine the diameter of the vein before venous access is gained — this would greatly increase the safety and ease of the procedure.

Triffterer et al. (2012) inferred that there is a high degree of variability of the great saphenous vein's anatomy in neonates. Wald et al. (2019) suggested finding the great saphenous vein at the medial malleolus in infants and children by using one-half to one finger width in the anterior quadrant. Chokshi et al. (2010) found that the ideal location to expose the great saphenous vein is through a small transverse incision superior and anterior to the medial malleolus. This study found the great saphenous vein superior to the medial malleolus 4.3 ± 1.3 mm in the superior anterior quadrant, and, unlike Wald et al. (2019), this would translate to a quarter of a finger's breadth. Using numeric values to determine the location will be more advantageous, as there is no standard measurement for a "finger's breadth". In this neonatal sample, the great saphenous vein can be found approximately 2.0 mm anterior and 3.1 mm superior to the most palpable part of the medial malleolus (Fig. 2b).

Table 5. Anatomical characteristics of the great saphenous vein by latest studies (2021-2022).

Study	Tu et al. (2021)	Bian et al. (2021)	Triffterer et al. (2021)	Current study
Samples	Neonates	Infants	Infants	Neonates
Vein depth (ultrasound) (mm)	2.0(0.2)	3.6(1.4)	4.4(1.5-9.5)	-
Vein depth (landmark) (mm)	2.0(0.2)	3.6(1.4)	-	-
Vein diameter (ultrasound) (mm)	0.8(0.1)	1.4(0.3)	1.5(1.1-2.99)	-
Vein diameter (landmark) (mm)	0.7(0.1)	1.5(0.3)	-	1.04(0.04)
Location of GSV measurement	Popliteal fossa	Medial malleolus	Medial malleolus	Medial malleolus

Note: Measurements unless stated are represented means (standard deviation). Triffeterer et al. (2021) reported their measurements in Median (range).

There were no "strong" correlations seen when comparing any measurement of the great saphenous vein within the proximal thigh or near the medial malleolus with the weight, height, or BMI of the sample.

In conclusion, the great saphenous vein within the proximal thigh can be located 6.8 ± 1.5 mm inferior to the inguinal ligament, and medial to the pulse of the femoral artery, and the diameter of the vein will range between 1.4 mm and 1.6 mm, with a confidence interval of 95%. The great saphenous vein near the medial malleolus in this sample can be located by making an incision 4.3 ± 1.3 mm anterosuperior to the medial malleolus in the anterosuperior quadrant. This implies that the great saphenous vein could be located if an incision was made 2.0 mm anterior and 3.1 mm superior to the most prominent palpable part of the medial malleolus. A silastic feeding tube with an external diameter of 0.6 mm could be ideally cannulated into the great saphenous vein at the medial malleolus. These anatomical guidelines provide a more accurate description in the pursuit of gaining venous access in the great saphenous vein at two anatomical locations. However, if available, and using the anatomical information that was presented in this study, ultrasound guidance should be used in order to locate the great saphenous vein prior to attempting venous access.

Limitations

This study has several limitations. As with any dissection of formalin-embalmed cadavers, we encountered tissue stiffness. In addition, tissue shrinkage could be present within the embalmed neonatal cadavers. Measuring the diameter of the great saphenous vein on a living population of neonates using ultrasound should be considered a more accurate measurement. Although we took great care not to disrupt the vein when measuring the diameter of the great saphenous vein, the fact that it was done on a cadaveric sample should be taken into account.

DECLARATIONS

Ethics approval and consent to participate

The studies involving human participants were reviewed and approved (Ethics clearance number: 447/2018) by the Health Sciences Research Ethics Committee at the University of Pretoria, South Africa. All methods and observations were carried out in accordance with the relevant requirements, guidelines, and regulations stipulated in the South African National Health Act (61 of 2003), as well as the 1964 Declaration of Helsinki.

Acknowledging donor cadavers

The authors sincerely thank those who donated their bodies to science so that anatomical research could be performed. Results from such research can potentially increase mankind's overall knowledge that can then improve patient care. Therefore, these donors and their families deserve our highest gratitude.

Authors' contributions

DJ van Tonder: Protocol development, Data collection, Data analysis, Manuscript writing, Literature research, Critical review

A Kathrada: Manuscript writing, Literature research, Critical review

A Lokhandwala: Manuscript writing, Literature research, Critical review

ML van Niekerk: Protocol development, Manuscript editing, Critical review

A van Schoor: Protocol development, Data collection, Data analysis, Manuscript writing, Literature research, Critical review

REFERENCES

ANDERSON AP, TAROC AM, WANG X, BEARDSLEY E, SOLARI P, KLEIN EJ (2021) Ultrasound guided peripheral IV placement: An observational study of the learning curve in pediatric patients. *J Vasc Access*, 23: 250-256.

ARIA DJ, VATSKY S, KAYE R, SCHAEFER C, TOWBIN R (2014) Greater saphenous venous access as an alternative in children. *Pediatr Radiol*, 44: 187-192.

BAIR AE, ROSE JS, VANCE CW, ANDRADA-BROWN E, KUPPERMANN N (2008) Ultrasound-assisted peripheral venous access in young children: a randomized controlled trial and pilot feasibility study. *Western J Emerg Med*, 9: 219.

BIAN Y, HUANG Y, BAI J, ZHENG J, HUANG Y (2021) A randomized controlled trial of ultrasound-assisted technique versus conventional puncture method for saphenous venous cannulations in children with congenital heart disease. *BMC Anesthesiol*, 21. https://doi.org/10.1186/s12871-021-01349-y

BLAND JM, ALTMAN DG (2010) Statistical methods for assessing agreement between two methods of clinical measurement. *Int J Nurs Stud*, 47: 931-936.

BRASS P, HELLMICH M, KOLODZIEJ L, SCHICK G, SMITH AF (2015) Ultrasound guidance versus anatomical landmarks for subclavian or femoral vein catheterization. *Cochrane Database Syst Rev*, 1(1): CD011447.

BRUZONI M, SLATER BJ, WALL J, ST PETER SD, DUTTA S (2013) A prospective randomized trial of ultrasound- vs landmark-guided central venous access in the pediatric population. *J Am Coll Surg*, 216: 939-943.

CAGGIATI A (1999) Fascial relationships of the long saphenous vein. *Circulation*, 100: 2547-2549.

CAGGIATI A, BERGAN JJ, GLOVICZKI P, JANTET G, WENDELL-SMITH CP, PARTSCH H (2002) Nomenclature of the veins of the lower limbs: An international interdisciplinary consensus statement. *J Vasc Surg*, 36: 416-422.

CHOKSHI NK, NGUYEN N, CINAT M (2010) Access in the neonatal and pediatric patient. In: *Vascular Access: Principles and Practice*. Lippincott Williams & Wilkins, Philadelphia, pp 137-149.

CHURCH JT, JARBOE MD (2017) Vascular access in the pediatric population. *Surg Clin North Am*, 97: 113-128. https://doi.org/10.1016/j.suc.2016.08.007

D'ANDREA V, PRONTERA G, PEZZA L, BARONE G, VENTO G, PITTIRUTI M (2022) Rapid superficial vein assessment (RaSuVA): A pre-procedural systematic evaluation of superficial veins to optimize venous catheterization in neonates. *J Vasc Access*, 20: 11297298221098481.

DETAILLE T, PIROTTE T, VEYCKEMANS F (2010) Vascular access in the neonate. *Best Pract Res Clin Anaesthesiol*, 24: 403-418.

DRONEN S, LANTER P (1999) Venous cutdown. In: Robert J, Hedges J (Eds.). *Clinical Procedures in Emergency Medicine*. W.B. Saunders Co., Philadelphia, pp 341-351.

GARLAND JS, DUNNE WM, HAVENS P, HINTERMEYER M, BOZZETTE MA, WINCEK J, BROMBERGER T, SEAVERS M (1992) Peripheral intravenous catheter complications in critically ill children: a prospective study. *Pediatrics*, 89: 1145-1150.

HANADA S, VAN WINKLE MT, SUBRAMANI S, UEDA K (2017) Dynamic ultrasound-guided short-axis needle tip navigation technique vs. landmark technique for difficult saphenous vein access in children: a randomised study. *Anaesthesia*, 72: 1508-1515.

JOSHI M, WILSON G, ENGELHARDT T (2010) Comparison of landmark technique and ultrasound guidance for localisation of long saphenous vein in infants and children. *Emerg Med J*, 27: 443-445.

KACHLIK D, PECHACEK V, BACA V, MUSIL V (2010) The superficial venous system of the lower extremity: new nomenclature. *Phlebology*, 25: 113-123.

KACHLIK D, PECHACEK V, MUSIL V, BACA V (2011) The deep venous system of the lower extremity: new nomenclature. *Phlebology*, 27: 48-58.

LOCKHART ME, DEURDULIAN C, BHATT S, LYSHCHIK A (2019) Diagnostic ultrasound, Vascular. Elsevier, Philadelphia.

OTANI T, MORIKAWA Y, HAYAKAWA I, ATSUMI Y, TOMARI K, TOMOBE Y, UDA K, FUNAKOSHI Y, SAKAGUCHI C, NISHIMOTO S, HATAYA H (2018) Ultrasound-guided peripheral intravenous access placement for children in the emergency department. *Eur J Pediatr*, 177: 1443-1449.

PONNUSAMY V, VENKATESH V, CLARKE P (2014) Skin antisepsis in the neonate: What should we use? *Curr Opin Infect Dis*, 27: 244-250.

PRAMOD S, TEJASHWINI K, SHANTHI M, KUMAR D (2022) Feasibility of long saphenous vein cut down at sapheno-femoral junction for central venous access in neonates: A single centre experience of 3 years. *Eur J Mol Clin Med*, 09.

PUNTIS JWL (1987) Percutaneous insertion of silastic central venous feeding catheters. *Intensive Therapy Clinical Monitoring*, 8: 7-10.

ROCHA G, SOARES P, PISSARRA S, SOARES H, COSTA S, HENRIQUES-COELHO T, GUIMARÃES H (2017) Vascular access in neonates. *Minerva Pediatr*, 69: 72-82.

SARMENTO DINIZ ER, DANTAS DE ARAÚJO SANTOS CAMARGO J, SANTOS DE MEDEIROS K, ROSENDO DA SILVA RA, COBUCCI RN, RONCALLI AG (2022) Risk factors for the development of peripherally inserted central catheter-related bloodstream infection in neonates: Prospective cohort study. *J Neonatal Nursing*, https://doi.org/10.1016/J.JNN.2022.08.006

SCHNADOWER D, LIN S, PERERA P, SMERLING A, DAYAN P (2007) A pilot study of ultrasound analysis before pediatric peripheral vein cannulation attempt. *Acad Emerg Med*, 14: 483-485.

SCHOENFELD E, BONIFACE K, SHOKOOHI H (2011) ED technicians can successfully place ultrasound-guided intravenous catheters in patients with poor vascular access. *Am J Emerg Med*, 29: 496-501.

SIGAUT S, SKHIRI A, STANY I, GOLMAR J, NIVOCHE Y, CONSTANT I, MURAT I, DAHMANI S (2009) Ultrasound guided internal jugular vein access in children and infant: A meta-analysis of published studies. *Pediatric Anesthesia*, 19: 1199-1206.

STANDRING S (2020) The anatomy of the vascular and lymphatic systems. In: Standring S (Ed.). *Gray's Anatomy*. Elsevier Health Sciences, London, pp 1464. e56-1464.e129.

TRIFFTERER L, MARHOFER P, WILLSCHKE H, MACHATA AM, REICHEL G, BENKOE T, KETTNER SC (2012) Ultrasound-guided cannulation of the great saphenous vein at the ankle in infants. *Br J Anaesth*, 108: 290-294.

TU Z, TAN Y, LIU L, XIE J, XU Y, LIU W (2021) Ultrasound-guided cannulation of the great saphenous vein in neonates: a randomized study. *Am J Perinatol*, 40(11): 1217-1222.

UNBECK M, FÖRBERG U, YGGE BM, EHRENBERG A, PETZOLD M (2015) Peripheral venous catheter related complications are common among paediatric and neonatal patients. *Acta Paediatr*, 104: 566-574.

UYGUN I (2016) Peripherally inserted central catheter in neonates: A safe and easy insertion technique. *J Pediatr Surg*, 51: 188-191.

WALD SH, MENDOZA J, MIHM FG, COTÉ CJ (2019) Procedures for vascular access. In: Coté CJ, Lerman J, Anderson BJ (eds.). *A Practice of Anesthesia for Infants and Children*. 6th edit. Elsevier, pp 1129-1145.

An exploration of the enigmatic ponticulus posticus: a cone beam computed tomographic study

Karthikeya Patil, Sanjay CJ, Mahima V. Guledgud, Namrata Suresh, Eswari S, Vidya G. Doddawad

Department of Oral Medicine and Radiology, JSS Dental College and Hospital, JSS Academy of Higher Education and Research, Mysore - 570 015 India

SUMMARY

During embryonic development, the activity of neural crest cells has the potential to induce the ossification of the posterior atlantooccipital ligament, resulting in the formation of an abnormal bony bridge known as "Ponticulus Posticus" (PP). The presence of PP increases the likelihood of vertebral artery obstruction, and patients with this condition frequently exhibit symptoms of vertebrobasilar insufficiency. Furthermore, connections have been depicted between PP and dental agenesis, malocclusions, and cleft lip and palate. This study assessed the prevalence, morphology, and superior articular facet (SAF) dimensions in PP using Cone Beam Computed Tomography (CBCT). In this retrospective study, SPSS 22.0 was used to analyse 202 cervical CBCT images devoid of pathologies. PP, age, and sex relationship were examined using the t-test and chi2 analysis. Pearson correlation examined the relationship between PP and non-PP SAF dimensional differences. P values <0.05 were significant. The prevalence of PP was 8.4%, with 64.7% constituting complete type and 35.2% partial type. The unilateral partial group's anteroposterior (D1) and transverse (D2) dimensions showed a strong positive association and significant difference. Understanding this anomaly and the changes it can cause in depth is essential for a clinician to diagnose orofacial pain. Taking into account the benefits of using CBCT enables a detailed evaluation of the vertebral column in three different planes, allowing us to measure the metrical dimensions of SAF precisely in the present study. It can be considered a gold standard in evaluating PP as a diagnostic tool.

Key words: Arcuate foramen – Cone beam CT – Orofacial pain – Atlas

INTRODUCTION

"Atlas", the first cervical vertebra of the spine (C1), derives its name from Greek mythology, in which "Atlas", the son of Titan, was forced to carry the weight of the sky on his shoulders for eternity. Similarly, the Atlanto-occipital joint is the primary element of "head joints" that bears the weight of the skull. (Patil et al., 2016) An anomaly related to the atlanto-occipital region is the PP, which is a malformed bridge at the posterior segment of the superior articular eminence and the posterolat-

Corresponding author:
Sanjay CJ. Department of Oral Medicine and Radiology, JSS Dental College and Hospital, JSS Academy of Higher Education and Research, Mysore - 570 015 India. Phone: +91 97425 65566. E-mail: drsanjaycj_dch@jssuni.edu.in - ORCID ID: 0000-0003-2830-1481

Submitted: September 4, 2023. **Accepted:** November 6, 2023

https://doi.org/10.52083/XXAS2397

eral part of the superior margin of the posterior arch of the atlas. PP is also known as the arcuate foramen, foramen arcuate atlantis, posterior ponticle, or Kimerle anomaly. (Falah-kooshki et al., 2022) In recent times, such anomalies have been highlighted to have the potential to join the list of those pathophysiologic conditions whose etiologies have confounded diagnosticians.

Significant anatomic structures such as the vertebral artery and the suboccipital nerve are in the vicinity of PP. Any compression of these might cause symptoms such as migraine, vertigo, diplopia, shoulder pain, and neck pain **(**Bayrakdar et al., 2018**)** It was suggested that, due to the attachment PP to the atlanto-occipital membrane and dura mater, the pressure exerted on the dura results in a type of headache seen in migraine. (Sharma et al., 2010) It also causes alterations in the morphometry of SAF, which has an adverse effect on ergonomics. A study conducted by Dhall et al. discovered larger SAF on the PP side compared to the non-PP side of the same individual (unilateral PP), which may have an impact on joint ergonomics (Dhall et al., 1993). Given the limitations of lateral radiographs, such as the inability to observe the extent and completeness, or superimposition of both sides, Computed tomography (CT), and CBCT is the preferred approach. As CBCT offers lower radiation exposure, faster imaging, and better spatial resolution than CT; hence, it is the preferred imaging modality in this scenario. This study was aimed to investigate the prevalence and morphological characteristics of PP and the subsequent difference in dimensions of the SAF using CBCT to understand this atlanto-occipital joint anomaly more precisely.

MATERIALS AND METHODS

A total of 202 CBCT scans of patients with an age range of 20-60 years were included in this retrospective study. The sample size was calculated using quota sampling method and the formula applied was n= (z2) P(1-P)/d2, where n = sample size, z = statistics for the level of confidence, P = expected prevalence, and d = allowable error. The above formula assumed P and d as decimal values, but it would be also correct if they were percentages, with the exception that the term (1-P) in the numerator would become (100-P).

The study received approval from the Institutional Ethical Committee of JSS Dental College & Hospital. (IEC Protocol Number: 09/2023).

Inclusion criteria

1. Superior quality CBCT images depicting the complete face to cervical region.
2. Scans acquired for all oral and maxillofacial diagnostic and treatment purposes excluding any past history of maxillofacial, cervical trauma or anomalies.
3. CBCT scans including all the boundaries of the atlas vertebrae.

Exclusion criteria

1. Subjects with craniofacial osseous abnormalities, or a history of, or evidence of, orthognathic surgery.
2. Subjects with anomalies involving the midface, previous trauma, and surgeries of the midface.

The 202 CBCT scans were taken using the Planmeca Promax 3D Mid CBCT machine with exposure parameters of 94kVp, 14 mA tube current, 27 s scan time, 20*17 cm FOV and 0.4–0.6 µm voxel sizes. Two oral radiologists performed a radiographic examination of the study scans under optimal viewing conditions separately, twice with an interval of two weeks, to rule out any disparity or bias in the interpretation of results.

The axial images were reconstructed to generate multiplanar reformatted coronal and sagittal images. The prevalence and types of PP, i.e., complete or partial, were evaluated bilaterally in sagittal sections. A complete PP was considered as a circumferential bony bridge over the posterior vertebral sulcus of the atlas, (Fig. 1A) and a partial PP was defined when there was a distinct bony spicule downward from the SAF or upward from the posterior arch that did not enclose circumferentially (Fig. 1B). The unilateral or bilateral presence of PP were recorded.

The maximum dimensions of the SAF in the long axis anteroposteriorly (D1) and transversely (D2) were measured by two oral radiologists independently, who were blinded to patient identity and the presence or absence of PP (Fig. 2).

Fig. 1A.- Depicting complete type of Ponticulus posticus.

Fig. 1B.- Depicting partial type of Ponticulus posticus.

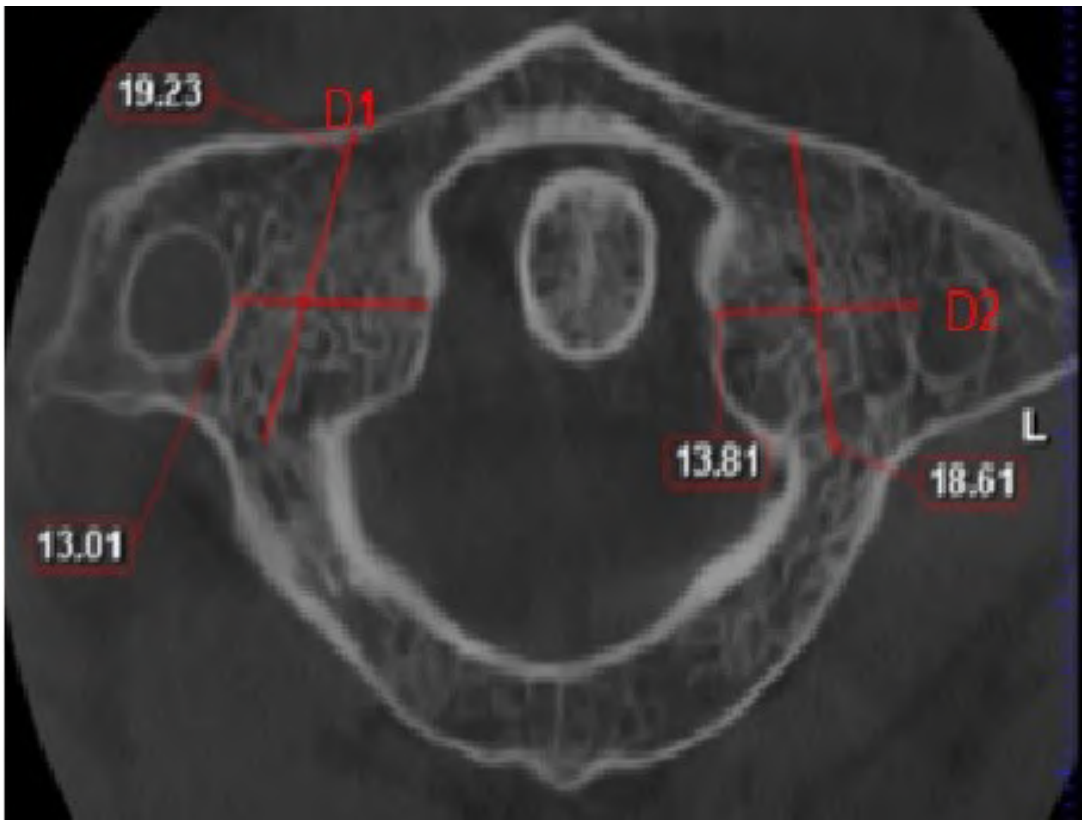

Fig. 2.- Depicting anteroposterior dimension(D1) and transverse dimension (D2) of superior articular facet.

Table 1. Showing prevalence of various types of ponticulus posticus.

Type	Bilateral	Unilateral	
		Right	Left
Partial Ponticulus Posticus (64.7%)	3(50%)	3 (27%)	5(45%)
Complete Ponticulus Posticus (35.2%)	3(50%)	2 (18%)	1(9%)

Statistical analysis

Kolmogorov-Smirnov and Shapiro-Wilk test were done, which revealed that data were normally distributed. Data were analysed using 22.0 version of SPSS software. The relationship among PP, age, and sex was assessed with the t-test and chi^2 analysis, respectively This study used Pearson correlation to evaluate the correlation between the dimension differences of the atlas SAF between PP and non-PP. P values <0.05 were statistically significant.

RESULTS

A total of 202 participants, 101 males and females each, were involved in this retrospective study. The age ranged from 20 to 60 years. Mean age ± std. deviation was 35.16 ± 11.28. When the CBCT scans of 202 patients were evaluated for PP, a prevalence of 8.4% (n=17) was noted, of which 64.7% and 35.2% were of complete and partial type respectively. Within the partial type, 27.2% showed bilateral presentation and 72.7 % were present unilaterally. The complete type, however, was equally distributed unilaterally and bilaterally (Table 1). A two-tailed t-test for independent samples showed that the difference between absence and presence of PP with respect to the dependent variable age was not statistically significant, t (22.95) = 0.7, p = .491, 95% confidence interval (-2.85, 5.77). A Chi^2 test was performed between sex and PP. All expected cell frequencies were greater than 5, thus the assumptions for the Chi^2 test were met. There was no statistically significant relationship between sex and PP χ^2 (1) = 0.06, p = .8, Cramér's V = 0.02.

D1 and D2 results (complete PP side vs non-PP side) (Table 2)

A Pearson correlation was performed to determine if there is a correlation between variables D1(complete pp side) and D1 (complete non-PP side). There was a very high, positive association between D1 and complete pp and non-pp side with r=1. Similarly, there was a very high, positive association between D2(complete PP side) and D2 (complete non PP side) with r=0.92. However, there was no statistically significant correlation (p>0.05).

Table 2. Showing unilateral complete group (n=3).

Dimensions	PP side	Non-PP side	P Value
D1	24.36±2.1	23.99±1.84	>0.05
D2	11.31±0.5	10.7±0.63	>0.05

D1 and D2 results (partial PP side vs partial non-PP side) (Table 3)

A Pearson correlation was performed to determine if there was a correlation between variables D1(partial pp side) and D1 (partial non pp side). There was a very high, positive correlation between variables D1(partial pp side) and D1 (partial non-pp side) with r= 0.87. Similarly, there was a very high, positive association between D2(partial pp side) and D2 (partial non pp side) with r=0.79. A statistically significant correlation was observed between the variables (p<0.05).

Table 3. Showing unilateral partial group (n=8).

Dimensions	PP side	Non-PP side	P Value
D1	22.88 ±1.6	21.29 ±1.64	<0.05
D2	10.6 ±0.52	9.98 ±0.5	<0.05

DISCUSSION

The ponticulus posticus, often known as the "little posterior bridge" because of the ossification and calcification of the posterior atlanto-occipital ligament, is an anomaly often related to neural crest cell activity during foetal development. It has been linked to orofacial pain disorders, mi-

graines, and chronic tension-type headaches. In fact, Putrino et al. in 2018 have stated that in all of these cases, patients' opinions be taken into account, as complications associated with this vertebral defect may necessitate cervical spine surgery. Furthermore, certain variations in the vertebral anatomy such as the presence of the lateral bridge spanning from the lateral mass to the transverse process should essentially be distinguished from the PP (Mann et al., 2016).

The prevalence in the literature has been reported to range from 5.1% to 38.3% (Putrino et al., 2018; Sharma et al., 2010; Falah-kooshki et al., 2022). The prevalence observed in the present study was 8.4%, which aligns with the aforementioned finding (Table 1). The above-referenced prevalence of PP exhibits considerable diversity, mostly influenced by the specific methodology applied in various studies. These methodologies encompass several approaches, such as the examination of fresh or preserved cadaveric tissue, and the employment of radiographic imaging techniques (Hauser and De Stefano, 1989; Pastor et al., 2001). However, the majority of the studies in the literature assessed the prevalence on lateral cephalograms, where it was observed that the prevalence of PP was comparatively lower (Mosavat et al., 2023; Gibelli et al., 2016; Giri et al., 2017; Adisen et al., 2017; Di Venere et al., 2022), as compared to CBCT or CT studies (Bayrakdar et al., 2018; Tripodi et al., 2019; Buyuk et al., 2017; Martiniz et al., 2021; Sekerci et al., 2015). In fact, Kim et al. in 2007 conducted a comparative study between 225 CT scans and 312 LC scans, and found the prevalence of PP to be 26% and 14%, respectively. The observed disparities in the outcomes suggest that the 3D-imaging modality possesses a greater level of sensitivity, potentially leading to a more accurate evaluation of PP. However, Chen et al. in 2015 discovered conflicting outcomes where out of 500 CBCT scans 35 patients (7%) had PP. This result was analogous to the present study (8.4% prevalence). A potential rationale for this observed resemblance may be attributed to ethnic heterogeneity, as stated by Martinez et al. in 2021, who claimed that PP is more prevalent in European and North American populations compared to Asian populations.

The existing body of literature does not provide evidence of a statistically significant difference between males and females (Chen et al., 2015; Bayrakdar et al., 2014). This finding was consistent with the present study (p-value>0.05). However, certain studies showed conflict in gender predilections, where Sharma et al. (2010) presented with female predominance and Martinez et al. (2021) reported male predilection.

This study demonstrated no statistically significant variation in the prevalence of PP in accordance with age (p-value> 0.05). This finding was consistent with the study conducted by Chen et al. (2015), Falah-kooshki et al. (2022) and Hasani et al. (2016). However, Paraskevas et al. (2005) have observed that the gradual mineralization of the PP over time, transitioning from partial to complete ossification, indicates a potential association with the ageing process. Therefore, while ossification may proceed gradually, the presence of PP appears to be a congenital skeletal abnormality of the atlas bone, characterized by various degrees of ossification. The notion could be substantiated by the discoveries of the cartilaginous PP in fetuses and children reported by BG Lamberty et al. (1973).

The SAF establishes an atlantooccipital joint with the occipital condyle, facilitated by the presence of two lateral masses located on the upper surface of the atlas. This joint serves to distribute the weight of the head and enables the movement associated with nodding or shaking the head in a yes or no fashion. The occurrence of dimensional alterations in the articulating surfaces of the atlantooccipital joint results in imbalanced motion within the intervertebral motion segment. Hence, the alterations in ergonomics could potentially be considered as significant contributors to the etiology of migraine, cervical strains, or tension-type headaches (Chen et al., 2015). In the present study, a high positive correlation was noted between D1 and D2 dimensions of SAF of unilateral complete pp side and non pp side, however, the difference was insignificant (p- value >0.05) (Table 2). Whereas, a very high positive correlation and significant difference (p- value<0.05) was noted between D1 and D2 of unilateral partial group (Table 3). This was consistent with the findings of

study conducted by Chen et al. (2015). Although the insignificant difference in unilateral complete group could be attributed to small sample size of the present study.

In addition, a multitude of research in the academic literature have established a correlation between PPs and various dental abnormalities. Chitroda et al. (2013) have reported that the presence of PP is associated to a higher incidence of skeletal Class II malocclusion, characterized by mandibular retrusion and an overjet. In a study conducted by Xu et al. (2022), it was found that the presence of PP was associated with an increased prevalence of skeletal Class III malocclusion, characterized by a protruded jaw. Moreover, a study conducted by Sekerci et al. (2015) revealed that the existence of posterior positioning (PP) was linked to an increased occurrence of malocclusions, including overjet, overbite, and crossbite. Further research is required to ascertain the specific mechanisms through which PP may potentially contribute to alterations in skeletal patterns and the development of malocclusions.

Furthermore, Bayradkar et al. (2017) observed a greater prevalence of PP among individuals with cleft lip and palate compared to those without this defect.

Further investigation is required in order to precisely ascertain the specific correlation between PP and the occurrence of cleft lip and palate.

The results of the present study suggest that presence of PP could ultimately alter ergonomics. To the best of our knowledge, this is the first CBCT study conducted on Indian population assessing the difference in dimensions of SAF on PP side and non-PP side in the same individual, elucidating the influence of PP on the dimensions of the SAF. However, further studies with larger sample size and universally accepted criteria to assess partial PP are required and can be a scope for future research, which can aid clinicians in diagnosing orofacial pain with profound accuracy.

REFERENCES

ADISEN MZ, MISIRLIOGLU M (2017) Prevalence of ponticulus posticus among patients with different dental malocclusions by digital lateral cephalogram: a comparative study. Surg Radiol Anat, 39: 293-297.

BAYRAKDAR IS, MILOGLU O, ALTUN O, GUMUSSOY I, DURNA D, YILMAZ AB (2014) Cone beam computed tomography imaging of ponticulus posticus: prevalence, characteristics, and a review of the literature. Oral Surg Oral Med Oral Pathol Oral Radiol, 118: e210-219.

BAYRAKDAR IŞ, YASA Y, DUMAN ŞB, KARATURGUT UE, OCAK A, GÜNEN YILMAZ S (2018) Cone beam computed tomography evaluation of ponticulus posticus in patients with cleft lip and palate: a retrospective radio-anatomic study. Folia Morphol, 77: 72-78.

BUYUK SK, SEKERCI AE, BENKLI YA, EKIZER A (2017) A survey of ponticulus posticus: Radiological analysis of atlas in an orthodontic population based on cone-beam computed tomography. Niger J Clin Pract, 20: 106-110.

CHEN CH, CHEN YK, WANG CK (2015) Prevalence of ponticuli posticus among patients referred for dental examinations by cone-beam CT. Spine J, 15: 1270-1276.

CHITRODA PK, KATTI G, BABA IA, NAJMUDIN M, GHALI SR, KALMATH B, ET AL. (2013) Ponticulus posticus on the posterior arch of atlas, prevalence analysis in symptomatic and asymptomatic patients of Gulbarga population. J Clin Diagn Res, 7: 3044-3047.

DHALL U, CHHABRA S, DHALL JC (1993) Bilateral asymmetry in bridges and superior articular facets of atlas vertebra. J Anat Soc India, 42: 23-27.

DI VENERE D, LAFORGIA A, AZZOLLINI D, BARILE G, DE GIACOMO A, INCHINGOLO AD, RAPONE B, CAPODIFERRO S, KAZAKOVA R, CORSALINI M (2022) Calcification of the atlanto-occipital ligament (ponticulus posticus) in orthodontic patients: a retrospective study. Healthcare (Basel), 10(7): 1234.

FALAH-KOOSHKI S, NIKKERDAR N, IMANI MM, FARAJI R, GOLSHAH A (2022) Correlation of ponticulus posticus with dentofacial skeletal patterns. Contemp Clin Dentist, 13: 35.

GIBELLI D, CAPPELLA A, CERUTTI E, SPAGNOLI L, DOLCI C, SFORZA C (2016) Prevalence of ponticulus posticus in a Northern Italian orthodontic population: a lateral cephalometric study. Surg Radiol Anat, 38: 309-312.

GIRI J, POKHAREL PR, GYAWALI R (2017) How common is ponticulus posticus on lateral cephalograms? BMC Research Notes, 10: 1-5.

HASANI M, SHAHIDI S, RASHEDI V, HASANI M, HAJIYAN K (2016) Cone beam CT study of ponticulus posticus: Prevalence, characterictics. Biomed Pharmacol J, 9(3): 1067-1072.

HAUSER G, DE STEFANO GF (1989) Epigenetic variants of the human skull. Schweizerbart'sche Verlagsbuchhandlung. Stuttgart, Germany, p 111.

KIM KH, PARK KW, MANH TH, YEOM JS, CHANG BS, LEE CK (2007) Prevalence and morphologic features of ponticulus posticus in Koreans: Analysis of 312 radiographs and 225 three-dimensional CT scans. Asian Spine J, 1: 27-31.

LAMBERTY BG, ZIVANOVIĆ S (1973) The retro-articular vertebral artery ring of the atlas and its significance. Acta Anat (Basel), 85: 113-122.

MANN RW, HUNT DR, LOZANOFF S (2016) Photographic regional atlas of non-metric traits and anatomical variants in the human skeleton. Charles C Thomas, Springfield, USES, pp 568-572.

MARTÍNEZ F, DEL CASTILLO J, HERMOSILLA S, KENNY J, SGARBI N, EMMERICH J (2021) Ponticulus Posticus prevalence in Uruguayan population: dry bone and cervical CT imaging. Eur J Anat, 25: 179-185.

MOSAVAT F, SARMADI S, AMINI A, ASGARI M (2023) Evaluation of dimension and bridging of sella turcica and presence of ponticulus posticus in individuals with and without cleft: a comparative study. Cleft Palate Craniofac J, 60: 695-700.

PARASKEVAS G, PAPAZIOGAS B, TSONIDIS C, KAPETANOS G (2005) Gross morphology of the bridges over the vertebral artery groove on the atlas. Surg Radiol Anat, 27: 129-136.

PASTOR JF, GIL JA, DE PAZ FJ, BARBOSA M (2001) Atlas de variaciones epigenéticas craneales. Valladolid: Universidad de Valladolid, Secretariado de Publicaciones e Intercambio Editorial.

PATIL D, VG D, JOSHY D, CHANDRAN D, PENUMATSA D (2016) The prevalence of ponticulus posticus among patients visiting JSS dental college - A radiographic study. J Med Radiol Pathol Surg, 3: 1-4.

PUTRINO A, LEONARDI RM, BARBATO E, GALLUCCIO G (2018) The association between ponticulus posticus and dental agenesis: a retrospective study. Open Dent J, 12: 510-519.

SEKERCI AE, SOYLU E, ARIKAN MP, AGLARCI OS (2015) Is there a relationship between the presence of ponticulus posticus and elongated styloid process? Clin Imaging, 39: 220-224.

SHARMA V, CHAUDHARY D, MITRA R (2010) Prevalence of ponticulus posticus in Indian orthodontic patients. Dentomaxillofac Radiol, 39: 277-283.

TRIPODI D, TIERI M, DEMARTIS P, PERO G, MARZO G, D'ERCOLE S (2019) Ponticulus posticus: clinical and CBCT analysis in a young Italian population. Eur J Paediat Dent, 20(3): 219-223.

XU X, ZHU Y, DING X, YIN M, MO W, MA J (2022) Research progress of ponticulus posticus: a narrative literature review. Front Surg, 9: 834551.

Anatomical variant of the azygos vein course in a cancer patient and review of the literature

Kevin Doello[1,4], Francisco Quiñonero[2,3,4], Gloria Perazzoli[2,3,4], Jose Prados[2,3,4], Cristina Mesas[3,4]

[1] *Medical Oncology Service, Virgen de las Nieves Hospital, 18014 Granada, Spain*
[2] *Department of Anatomy and Embryology, University of Granada, Granada 18071, Spain*
[3] *Institute of Biopathology and Regenerative Medicine (IBIMER), Biomedical Research Center (CIBM), Granada 18100, Spain*
[4] *Instituto Biosanitario de Granada, (ibs.Granada), SAS-Universidad de Granada, Granada 18012, Spain*

SUMMARY

The azygos vein is responsible for drainage through a staff of venous blood from the chest wall for the most part. Sometimes its course causes the independence of part of the lung parenchyma, which is known as the accessory lobe of the azygos. The present article presents the casual radiological finding of this anatomical variant in a 70-year-old patient undergoing a computed tomography scan for colon cancer. The azygos accessory lobe is a mostly asymptomatic anatomical variation, but it can be a problem in some thoracic surgeries.

Key words: Azygos vein – Lung – Accessory lobe – Radiology

INTRODUCTION

The azygos vein is an important structure that arises from the junction of the right subcostal and ascending lumbar veins, ascending through the posterior mediastinum to drain into the superior vena cava (Fig. 1). The azygos vein is responsible for the drainage of the thoracic and abdominal walls, esophagus, bronchi and trachea, and is able to divert blood to the superior or inferior vena cava in the event of a blockage of one of these large vessels (anastomotic system) (Notsu et al., 2020; Petrenko et al., 1990). Despite the fact that its anatomical variations are not very frequent, in some individuals the azygos vein may present variations in its origin, route, termination or tributaries, which have been described in many articles including classical anatomical literature (Adachi, 1940; Falla et al. 1963; Nathan, 1960; Hatfield et al., 1987; Koutsouflianiotis et al., 2018). In the case of unusual routing, this can lead to the formation of isolated regions of the lung parenchyma that may have important clinical implications. These isolated regions are known as “azygos lung lobes” or “vestigial lung lobes”. It is generally believed that they form as a result of an abnormal division of respiratory structures during embryogenesis, resulting in the formation of additional lung structures that are not connected to the rest of the lung parenchyma (Donohue and Daly, 2023).

Corresponding author:
Dr J. Prados. Department of Anatomy and Embryology, University of Granada, Granada 18071, Spain. Phone: +34-958249322; Fax: +34-958246296. E-mail: jcprados@ugr.es

Submitted: June 24, 2023. **Accepted:** September 11, 2023

https://doi.org/10.52083/JHCE5294

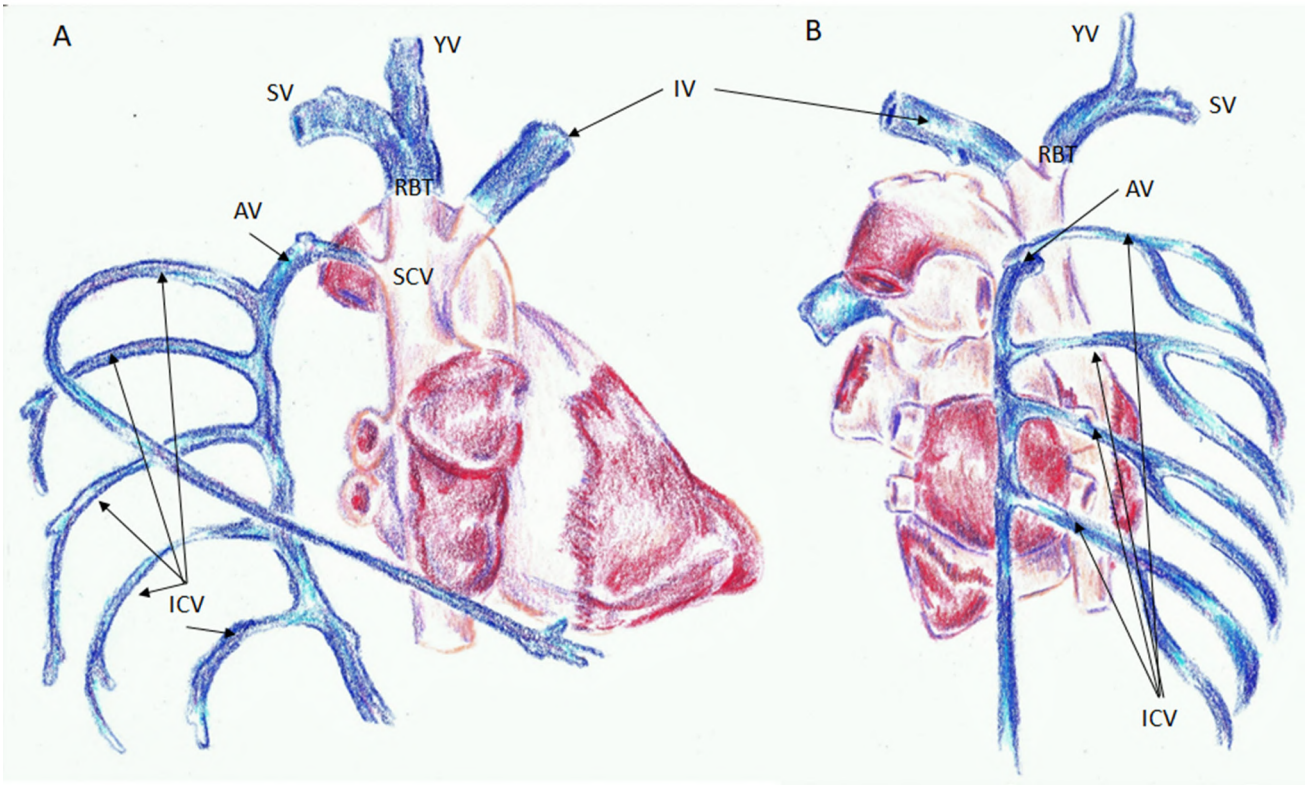

Fig. 1.- Representation of the anatomy of the azygos vein in its normal course, seen from a lateral (**A**) and a posterior view (**B**). AV (azygos vein); ICV (intercostal veins); YV (yugular vein); SV (subclavian vein); RBT (right brachiocephalic trunk); SCV (superior cava vein).

CASE PRESENTATION

A 70-year-old female patient with a personal history of hypercholesterolemia and cataract surgery. In 2016, the patient began with rectal bleeding, for which a lower digestive endoscopy (LDE) was performed, which revealed a rectal mass that was diagnosed as a rectal adenocarcinoma by pathology. In the CT corresponding to the extension study, an anatomical variant (Fig. 2) is observed by chance, consisting of the existence of a region of the medial right lung parenchyma that is isolated from the rest due to the existence of a longer than usual course of the vein azygos as it opens into the superior vena cava. The staging of the

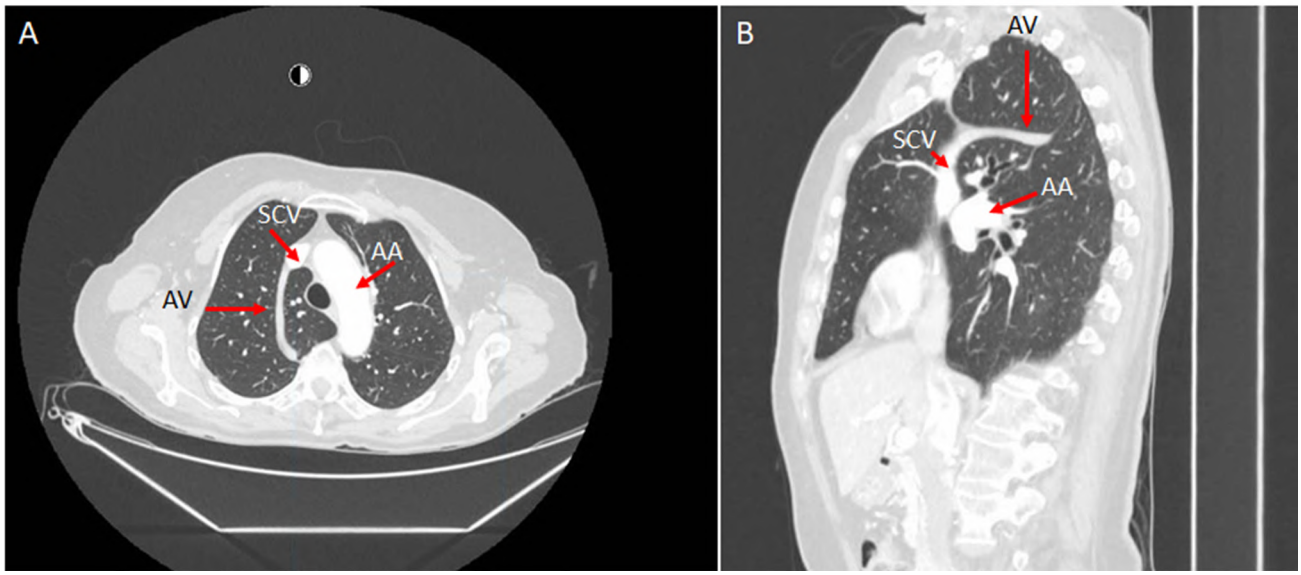

Fig. 2.- Computed tomography scan image showing an accessory azygos lung lobule in **A**) axial view and **B**) sagittal view. AV (azygos vein); AA (aortic arch); SCV (superior cava vein).

rectal tumor was T3N20 after the patient underwent surgery for low anterior rectal resection. The patient was treated with adjuvant chemotherapy with FOLFOX for 12 cycles (6 months). The patient is currently in good general condition and is free of disease.

DISCUSSION

The presence of azygos lung lobes is a relatively rare anatomical variation, and its incidence has been estimated at around 0.05% in the general population detected in 0.4% of medical examinations. Although they are generally considered a benign anatomical variation, their presence may have clinical implications in certain cases. For example, the presence of an azygos lung lobe can make interpretation of radiological images difficult, and can be confused with a lung lesion. In addition, the presence of an azygos lung lobe may increase the risk of complications during certain surgical procedures or radiological interventions (Atari et al., 2017). In the medical literature, several cases of azygos lung lobes have been described in asymptomatic patients, as well as in patients with respiratory or cardiovascular symptoms (Adachi, 1940; Falla et al. 1963; Nathan, 1960). In general, the diagnosis is made by imaging techniques, such as computed tomography or chest X-ray, and treatment depends on the presence of associated symptoms or complications. The presence of this anomaly is usually discovered incidentally in patients with pneumothorax, although some studies report that this anomaly is frequently found in patients who are going to undergo a sympathectomy for hyperhidrosis (Nakata et al., 2016; de Oliveira et al., 2022). There are occasions where, in the operation itself, although it does not cause pathology, the course of the azygos vein is reorganized and it is repositioned in its normal position (Choi et al., 2023). In addition to the formation of azygos lung lobes, other anomalies have been described, such as duplication of the azygos vein, the absence of the azygos vein, or its connection with abnormal structures. Another setting where azygos vein variations are diagnosed is in teaching cadaveric dissections such as rare anatomical variant discovered during dissection classes for medical students. In this case, the azygos vein was located on the left side of the descending thoracic aorta, coursed up the left side of the descending thoracic aorta and crossed the left subclavian artery and left vagus to terminate in the left brachiocephalic vein (Nayak et al., 2020). During dissection, various anatomical variations of the azygos vein have been reported (Badagabettu et al., 2016; Liu et al., 2020) such as a common origin (inferior vena cava) to the azygos venous branch and hemiazygos vein and a shortening of the azygos vein with exclusive drainage of the right intercostal veins (Atari et al., 2017), among others. In terms of embryological development, azygos lobule is made up when a branch from cardinal posterior vein migrates along lung upper lobe instead of the apex, so, this vein drags pleural layers and provokes the independence of this lung region called azygos lobe due to the apparition of the azygos fissure. Cardinal veins involutionate in left side but not in right side, setting up the inferior cava vein and azygos system (Tran et al., 2023). In clinical terms, the presence of azygos vein variations may have implications in surgical and radiological procedures. For example, the presence of an azygos lung lobe can make interpretation of radiological images difficult and can be confused with a lung lesion. In addition, the presence of an abnormal connection between the azygos vein and the superior vena cava may increase the risk of complications during certain surgical procedures or radiological interventions. In this case, this finding is not relevant but it could be a risk factor in this patient if she would have to undergo chest surgery for a metastasectomy.

CONCLUSION

In conclusion, anatomical variation of the azygos vein is a relatively common phenomenon, and it may be associated with pulmonary anomalies and complications in surgical and radiological procedures. Understanding these variations and their relationship to lung anatomy may be important for proper diagnosis and treatment of certain clinical conditions.

ACKNOWLEDGEMENTS

María Dubus Martos for the anatomical diagrams (University of Jaén).

REFERENCES

ADACHI B (1940) Das Venensystem der Japaner. Kenkyusha: Tokio, pp 1-198.

ATARI M, NAKAJIMA Y, FUKUHARA M, IIJIMA Y, KINOSHITA H, MINAMIYA Y, URAMOTO H (2017) An extremely rare case report of surgery of lung cancer with the absence of azygos vein. *Surg Radiol Anat*, 39(1): 103-106.

BADAGABETTU SN, SHETTY P, D'SOUZA MR (2016) A unique variation of azygos system of veins. *J Cardiovasc Echogr*, 26(2): 61-64.

CHOI MS, KIM EJ (2023) Migratory azygos lobe: a case report. *J Chest Surg*, 56(2): 140-142.

DE OLIVEIRA L, AMARAL VH, DE SAE SOUZA CF, SILVA A, DE FARIA D, SILVA JG (2021) Clinical and surgical implications of the pulmonary azygos lobe: a systematic review. *Int J Morphol*, 40(2): 442-448.

DONOHUE JR, DALY DT (2023) Anatomy, thorax, azygos Veins. In: StatPearls [Internet]. Treasure Island (FL): StatPearls Publishing. https://www.ncbi.nlm.nih.gov/books/NBK554430/

FALLA A, PRESTON FW, ANSON BJ (1963) Classification and calibration of the azygos venous system in 100 specimens. *Surg Gynecol Obst*, 116: 405-412.

HATFIELD MK, VYBORNY CJ, MACMAHON H, CHESSARE JW (1987) Congenital absence of the azygos vein: a cause for "aortic nipple" enlargement. *Am J Roentgenol*, 149(2): 273-274.

KOUTSOUFLIANIOTIS K, PARASKEVAS GK, ILIOU K, NOUSSIOS G (2018) A left-sided azygos vein in a cadaver: anatomical and surgical considerations. *Cureus*, 10(5): e2610.

LIU F, RUZE A, AMUTI S, WANG S, CHEN S, YIMING A, XIONG K (2019) A rare variation of the hemiazygos vein draining into the persistent left superior vena cava. *Anat Sci Int*, 94(3): 269-273.

NAKATA S, SATAKE S, OKUMURA Y, HARA S, MIN K, NAKAYAMA K (2016) Primary spontaneous pneumothorax with an azygos lobe. *Kyobu Geka*, 69(12): 1017-1019.

NATHAN H (1960) Anatomical observations on the course of the azygos vein (vena azygos major). *Thorax*, 15(3): 229-232.

NAYAK SB, SOUMYA KV (2020) Transposition and variant termination of azygos and hemiazygos veins: an extremely rare variation. *Surg Radiol Anat*, 42(11): 1303-1306.

NOTSU E, ONO K, HORIE S, MORRIS JF, TOIDA K (2020) Double superior venae cavae with absence of the coronary sinus and anomalies of the azygos venous system. *Anat Sci Int*, 95(3): 420-424.

PETRENKO VM (1990) Development of the ascending lumbar and azygos veins in human embryogenesis. *Arkh Anat Gistol Embriol*, 98(6): 65-70.

TRAN CT, MIAO KH, LUI F (2023) Anatomy, Thorax, Lung Azygos Lobe. In: StatPearls [Internet]. Treasure Island (FL): StatPearls Publishing; https://www.ncbi.nlm.nih.gov/books/NBK518977/

Gallbladder sinistroposition (left-sided) finding in laparoscopic cholecystectomy, a case report

Jesús C. Herrera-Pacheco[1β], Rodrigo Bravo-García[1β], Rodrigo E. Elizondo-Omaña[1], Juan M. Valdivia-Balderas[2], Luis A. Alvarez-Lozada[1*], Alejandro Quiroga-Garza[1,2*]

[1] Universidad Autonoma de Nuevo Leon, School of Medicine, Human Anatomy Department, Clinical-Surgical Research Group (GICQx), Mexico

[2] Instituto Mexicano del Seguro Social, Delegacion de Nuevo Leon, General Surgery Division, Monterrey, Mexico

SUMMARY

A left-sided gallbladder (LSGB), also known as sinistropostition, is a rare anatomical variant with a reported incidence of 0.2-1.1%. It is defined as a gallbladder located on the left side of the falciform ligament, embedded in the third hepatic lobe, without situs inversus viscerum.

A 37-year-old Latino man with a history of bilateral inguinal repair underwent a scheduled laparoscopic cholecystectomy due to multiple gallbladder polyps. Preoperative ultrasound reported a gallbladder of 60x20 mm, wall thickness of 1 mm, with polyps of up to 10 mm. Standard laparoscopic cholecystectomy trocar placement was used. Upon revision of the right hepatic lobe, there was an absence of the GB in the visceral side of segments IV, V, or VI. It was identified to the left of the falciform ligament with adhesions to the anterior and superior portions of the pylorus and lesser curvature. The subxiphoid trocar was adjusted to the left of the falciform ligament, and Calot's triangle dissection was performed to obtain a critical view of safety. No other anatomical variants were identified. The procedure was performed safely with a satisfactory view of critical cholecystectomy steps and anatomy identification. After the procedure, the surgeon complained of right-hand pain and numbness due to a medial position of the subxiphoid trocar for dissection. The surgical approach of a LSGB in laparoscopic surgery should be individualized for each patient. A minimally invasive approach may be realized successfully when critical thinking by the surgeon is applied and always prioritizing the safety of the patient.

Key words: Left-sided gallbladder – Sinistroposition – Laparoscopic cholecystectomy – Anatomy importance – Surgical critical thinking

Corresponding author:
Alejandro Quiroga-Garza, MD, PhD, FACS or Luis Adrian Alvarez-Lozada, MD, MSc. Departamento de Anatomía Humana, Facultad de Medicina, Universidad Autónoma de Nuevo León, Francisco I. Madero y Aguirre Pequeño sin número, Colonia Mitras Centro Monterrey, Nuevo León, México, CP 64460. Phone: +52 81 8329 4171. E-mail: dr.aquirogag@gmail.com / luis.adrian.1a@gmail.com

β Both authors participated equally and are both in the position of the first author.

Submitted: September 13, 2023. **Accepted:** October 5, 2023

https://doi.org/10.52083/QJHL4113

INTRODUCTION

A Left-Sided Gallbladder (LSGB) also known as "sinistroposition" is a rare anatomical variant with a reported incidence of 0.2 to 1.1% (Abongwa et al., 2017). It is defined as a gallbladder (GB) located on the left side of the falciform ligament, embedded in the third hepatic lobe, without situs inversus viscerum (Pereira et al., 2019; Almas et al., 2021). Routine identification of this anatomical variant is uncommon, usually missed by ultrasound (US), as approximately 80% are identified transoperatively (Pereira, 2019). Computed tomography (CT) is the best imaging study alternative, with 85% of LSGB identified this way, but it is not a standard study for GB disease assessment (Jung, 2022). Laparoscopic cholecystectomy continues to be the gold standard for cholecystitis. However, challenges arise in the surgical approach when anatomy is distorted by acute or chronic inflammation, as well as anatomical variants of the GB or biliary tract (Lamah et al., 2001).

Surgeons must consider alternative or complementary surgical strategies to improve the safety view of elemental structures (Abongwa et al., 2017; Lamah et al., 2001). This might include the repositioning or addition of more trocars, to allow for better traction and safer dissection (Nastos, 2014; Pereira, 2019). If the anatomy cannot be fully visualized or the surgeon is doubtful, intraoperative cholangiography (IOC) should be performed. If needed, conversion to an open approach or subtotal cholecystectomy should be considered to avoid biliary tract injury (Pereira, 2019; Jung, 2022). Knowledge of typical anatomy and its variants involved in cholecystectomies has a high impact on the assessment of surgical procedures and their safety. We present the case of a LSGB during laparoscopic surgery, with its management and outcomes. This case has been reported in line with the SCARE criteria, for reporting surgical cases (Agha et al., 2020).

CLINICAL CASE

A 37-year-old Latino man with a history of bilateral inguinal repair, and a body mass index of 27.2, underwent a scheduled laparoscopic cholecystectomy due to multiple gallbladder polyps. Previous 2-year follow-up with gastroenterology with progressive polyp growth, the reason behind indicating surgical procedure. The patient was otherwise asymptomatic to GB symptoms. Preoperative ultrasound reported a GB of 6x2 cm, wall thickness of 1 mm, with polyps of up to 10 mm. There were no other significant findings. Preoperative laboratories were within the normal ranges, except for a slight increase of serum glutamate-pyruvate transaminase (GPT 61.5 U/L) and serum glutamate-oxaloacetate transaminase (GOT 52.5 U/L).

Standard laparoscopic cholecystectomy trocar placement was used with an 11 mm trocar in the umbilicus for 30° 10mm telescope, and under direct visualization, an 11 mm subxiphoid trocar was placed towards the patient's right side of the falciform ligament, and a 5 mm right subcostal trocar for GB traction. Upon revision of the right hepatic lobe, there was an absence of the GB in the visceral side of segments IV, V, and VI (Fig. 1). Upon further examination, it was identified to the left of the falciform ligament with adhesions to the anterior and superior portions of the pylorus and lesser gastric curvature. The subxiphoid trocar was retracted and adjusted through the extraperitoneal space to the left of the falciform ligament. An additional 5 mm left subcostal trocar was considered, however, once adhesions were liberated, the GB could be retracted to the right for adequate Calot's triangle dissection with a critical view of safety. The cystic duct was identified and dissected, placing clips, before continuing with dissection and identifying a posterior angulation. The cystic artery was identified further into the GB bed, towards the posterior of the GB body. No other anatomical variations were identified. IOC was considered but deemed not necessary to avoid additional costs. The cystic duct and artery were cut, and the remaining GB was removed. There was no need for drain placement. Total operative bleeding was quantified as 10 ml. The surgical time was 52 minutes. The postoperative period was uneventful. The patient was discharged the following day. Pathology reported a GB of 7.5x2.6x2.5 cm, 2 mm walls with mucosal cholesterol polyps of up to 8 mm. Lymphocyte inflammatory infiltrates throughout the GB wall, thickened muscle layers, and congested blood vessels were found. Seven-day and 30-day follow-up visits were uneventful.

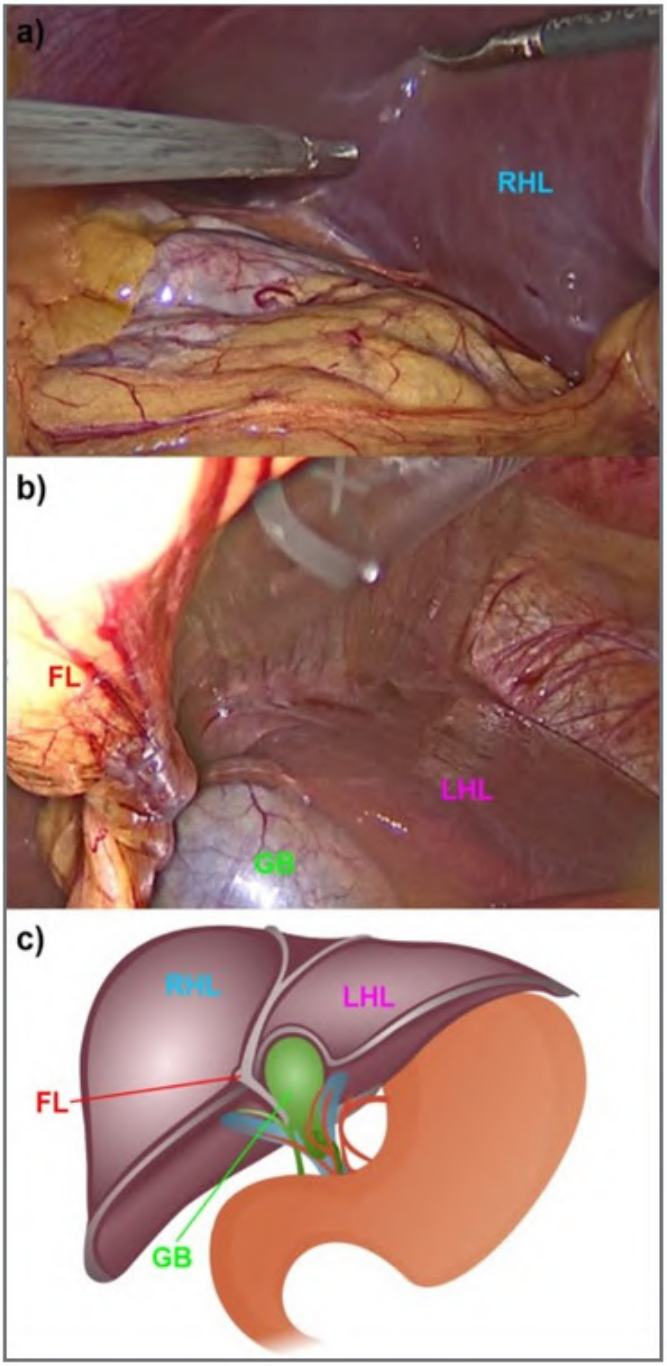

Fig. 1.- Left-sided Gallbladder. **a)** Examination of right hepatic lobe, with abscess of gallbladder. **b)** Gallbladder embedded in left hepatic lobe, segment III. **c)** Schematic drawing of left/sided gallbladder. RHL: right hepatic lobe; LHL: left hepatic lobe; FL: falciform ligament; GB gallbladder.

The procedure was performed safely with a satisfactory view of critical cholecystectomy steps and anatomy identification. The trocar incisions were not relocated by choice of the operating surgeon, only the angulation of the subxiphoid trocar, however, this was contemplated during the surgery due to ergonomy, and not due to safety concerns. After the procedure, the surgeon complained of slight pain and numbness in both hands, primarily the right hand, secondary to uncomfortable right-hand dissection due to a medial position of the subxiphoid trocar. The 5 mm right subcostal trocar was not adjusted and provided adequate GB traction; however, this was further than usual, also creating discomfort and strain, which was alleviated shortly after the surgery with non-steroid anti-inflammatory drugs.

Written consent was acquired by the patient to report the case without any personal information.

DISCUSSION

Awareness of anatomical variants such as a "sinistroposition" of the gallbladder is essential to a well-prepared surgeon. Surgical personnel may frequently be exposed to scenarios of uncertainty and rely on clinical reasoning and use of their anatomical knowledge to solve unforeseen circumstances. Constant exposure to extensive training in different scenarios via simulation will aid in more assertive performance (Quiroga-Garza et al., 2020; Fernández-Reyes et al., 2022). Changing the angle of the subxiphoid trocar for positioning the left of the falciform ligament allows a surgical approach without the need to modify the surgical field. In the present case, due to favorable conditions, no further modification was needed. However, the optimal surgical approach for LSGB has been subject to scrutiny and debate (Nastos, 2014; Pereira, 2019; Abongwa, 2017). Each patient's anatomy will be individual and the approach has to be considered with the intent of visualizing the critical anatomical view needed for safe dissection. Some reported approaches are placement of additional ports, different patient positioning, mirror image setup, retrograde dissection, conversion to open surgery, use of existing ports with manipulation of the falciform ligament, and IOC (Nastos, 2014).

The most frequent presentation of LSGB is when the cystic duct joins the hepatic duct on the right side after a hairpin turn anterior to the common hepatic duct (Pereira, 2019). Other variations have been recorded, such as the union of the cystic duct left of the common hepatic duct, the union on the left hepatic duct, the right hepatic duct, and a branch of the right hepatic duct (Pereira, 2019). Assessment of other anatomical variants should be on the surgeon's mind, as it is frequent to find multiple anatomical variations or malformations in individuals who present one (Jung, 2022).

The risk of complications is a very important consideration when a surgeon plans the approach as the normal anatomy is altered in LSGB cases. The line of dissection has a direct impact on critical anatomical landmarks like Calot's triangle since obstruction of a clear view of biliary and vascular structures has a higher risk of injury (Pereira, 2019). The use of IOC is recommended to evaluate associated anatomical variations and avoid biliary tract lesions (Jung, 2022). In this case, the operating surgeon was satisfied with the critical safety view and continued careful dissection, with a watchful approach for other anatomical variants (Quiroga-Garza et al., 2020; Tapia-Nañez, 2022). Also, to avoid additional costs, as the patient was paying out-of-pocket, although patient safety should always be prioritized.

The LSGB is usually associated with other anatomic variants and is important for the surgeon to be aware of them. A lawsuit analysis reported 10% of *mala praxis* lawsuits were due to surgical errors attributed to "ignorance about anatomical variations" and 13% due to abnormal or difficult anatomy (Cahill and Leonard, 1999; Rogers et al., 2006). Surgeons must constantly review the anatomy of their procedures and consider anatomical variations to reduce the risk of errors and complications (Tapia-Nañez, 2022). Higher exposure via simulation has been proven to increase the comfort of the surgeon in different scenarios enabling faster decision-making and critical thinking when considering the safety of the procedure (Fernández-Reyes et al., 2022).

Take-Away Lessons

The surgical approach for LSGB in laparoscopic surgery must be individualized to each case taking into consideration the anatomy, the expertise of the surgeon, and the frequency of intraoperative incidental findings. The best approach for each case must be developed according to the surgeon's critical thinking and always prioritizing the safety of the patient. If accurate anatomical structure identification is achieved a minimally invasive approach may be the best alternative.

REFERENCES

ABONGWA HK, DE SIMONE B, ALBERICI L, IARIA M, PERRONE G, TARASCONI A, BAIOCCHI G, PORTOLANI N, DI SAVERIO S, SARTELLI M, COCCOLINI F, MANEGOLD JE, ANSALONI L, CATENA F (2017) Implications of left-sided gallbladder in the emergency setting: retrospective review and top tips for safe laparoscopic cholecystectomy. *Surg Laparosc Endosc Percutan Tech*, 27(4): 220-227.

AGHA RA, FRANCHI T, SOHRABI C, MATHEW G, KERWAN A, SCARE Group (2020) The SCARE 2020 Guideline: Updating consensus Surgical CAse REport (SCARE) Guidelines. *Int J Surg (London, England)*, 84: 226-230.

ALMAS T, MURAD MF, MANSOUR E, KHAN MK, ULLAH M, NADEEM F, SHAFI A, KHEDRO T, ALMUHAILEEJ M, ABDULHADI A, ALSHAMLAN A, NAGARAJAN VR, MANSOOR E (2021) Look, but to the left: A rare case of gallbladder sinistroposition and comprehensive literature review. *Ann Med Surg*, 71: 103016.

CAHILL DR, LEONARD RJ (1999) Missteps and masquerade in American Medical Academy: Clinical anatomists call for action. *Clin Anat*, 12(3): 220-222.

FERNANDEZ-REYES BA, FLORES-GONZÁLEZ AK, ALVAREZ-LOZADA LA, GUERRERO-ZERTUCHE JT, ARRAMBIDE-GARZA FJ, QUIROZ-PERALES XG, QUIROGA-GARZA A, ELIZONDO-OMAÑA RE, GUZMÁN-LÓPEZ S (2022) The importance of simulation training in surgical sciences. *Int Surg J*, 9(6): 1289-1293. JUNG YK, CHOI D, LEE KG (2022) Laparoscopic cholecystectomy for left-sided gallbladder. *Langenbeck's Arch Surg*, 407(1): 207-212.

LAMAH M, KARANJIA ND, DICKSON GH (2001) Anatomical variations of the extrahepatic biliary tree: review of the world literature. *Clin Anat*, 14(3): 167-172.

LIN HY, LEE RC (2018) Is right-sided ligamentum teres hepatis always accompanied by left-sided gallbladder? Case reports and literature review. *Insights Imaging*, 9(6): 955-960.

NASTOS C, VEZAKIS A, PAPACONSTANTINOU I, THEODOSOPOULOS T, KOUTOULIDIS V, POLYMENEAS G (2014) Methods of safe laparoscopic cholecystectomy for left-sided (sinistroposition) gallbladder: A report of two cases and a review of safe techniques. *Int J Surg Case Rep*, 5(10): 769-773.

PEREIRA R, SINGH T, AVRAMOVIC J, BAKER S, ESLICK GD, COX MR (2019) Left-sided gallbladder: a systematic review of a rare biliary anomaly. *ANZ J Surg*, 89(11): 1392-1397.

QUIROGA-GARZA A, TERAN-GARZA R, ELIZONDO-OMAÑA RE, GUZMÁN-LÓPEZ S (2020) The use of clinical reasoning skills in the setting of uncertainty: a case of trial femoral head migration. *Anat Sci Educ*, 13(1): 102-106.

ROGERS SO, GAWANDE AA, KWAAN M, PUOPOLO AL, YOON C, BRENNAN TA, STUDDERT DM (2006) Analysis of surgical errors in closed malpractice claims at 4 liability insurers. *Surgery*, 140(1): 25-33.

TAPIA-NAÑEZ M, QUIROGA-GARZA A, GUERRERO-MENDIVIL FD, SALINAS-ALVAREZ Y, JACOBO-BACA G, DE LA FUENTE-VILLARREAL D, GUZMAN-LOPEZ S, ELIZONDO-OMAÑA E (2022) A review of the importance of research in Anatomy, an evidence-based science. *Eur J Anat*, 26(4): 477-486.

Aberrant right subclavian artery: its clinical importance in thoracic surgery

Kenjiro Arisawa, Sén Takeda

Department of Anatomy, Teikyo University School of Medicine

SUMMARY

Anomalies of the aortic arch include various variations. Aberrant right subclavian artery (ARSA) is one of the most common variations in this region, with an incidence of approximately 1% of all population. For this reason, ARSA is accidentally encountered during clinical settings. In 2019, we encountered a case of ARSA during a human cadaver dissection course for medical students at Teikyo University. This cadaver did not have a Kommerell's diverticulum, which is often accompanied in ARSA. While the present case is a vascular anomaly, it has a clinical relevance because of its topographical nature juxtaposed to the trachea and esophagus.

Key words: Anatomy – Cardiovascular system – Blood vessels – Arteries – Subclavian artery

ABBREVIATIONS

6w (6 weeks)

Aberrant right subclavian artery (ARSA)

Aortic arch (AA)

Aortic sac (AS)

Ascending aorta + Aortic arch + Descending aorta (ACA + AA + DCA)

Brachiocephalic artery (BCA)

Bronchi (B)

Common carotid trunk (CCT)

Common carotid artery + External carotid artery + Internal carotid artery (CCA + ECA + ICA)

Dorsal aorta (DA)

Esophagus (E)

Kommerell's diverticulum (KD)

Left and right internal thoracic arteries (LIT and RIT)

Left subclavian artery (LSA)

Non-recurrent laryngeal nerve (NRLN)

Pulmonary artery + Ductus arteriosus (PA + DA)

Right subclavian artery (RSA)

Right and left common carotid arteries (RCCA and LCCA)

Subclavian artery (SCA)

Trachea (T)

INTRODUCTION

The aortic arch and its branches begin to form during the early developmental stages through highly dynamic remodeling of anlages (Sadler, 2023). Therefore, anomalies affecting the aortic arch are well-known and reported relatively frequently (Stojanovska et al., 2012).

Corresponding author:
Kenjiro Arisawa, Sén Takeda. Department of Anatomy, Teikyo University School of Medicine, 2-11-1 Kaga, Itabashi, Tokyo, Japan. E-mail: arisawak@med.teikyo-u.ac.jp / takeda.sen.xm@teikyo-u.ac.jp

Submitted: May 24, 2023. **Accepted:** November 30, 2023

https://doi.org/10.52083/YHNN6249

To date, there are at least 10 major patterns of anomalies in terms of aortic arch branches (Williams et al., 1932). Among them, there are two subtypes showing an aberrant position of the right subclavian artery (ARSA). In ARSA, the right subclavian artery (RSA) is the last branch from the aortic arch, and it runs behind the esophagus to direct towards the right upper extremity. The major difference between the two types lies in the absence (type G) and presence (type H) of the common carotid trunk (CCT).

ARSA occasionally accompanies a unique combined sequela called the Kommerell's diverticulum (KD). It is an aneurysm-like dilatation at the origin of the ARSA, and is assumed to be a persistent dorsal aorta from the embryonic period (Kommerell, 1936). Considering this, KD may become a toehold for delineating the developmental sequence that leads to ARSA. In addition, while it is very rare, ARSA tends to accompany the so-called "non-recurrent laryngeal nerve (NRLN)" compared with normal individuals (Stewart et al., 1972). It will increase the risk of complications during surgery of head and neck.

In this report, we present a case of type H ARSA without KD and discuss its clinical importance in terms of thoracic surgical intervention.

CASE REPORT

During a dissection course for medical students in 2019, we encountered a 95-year-old female cadaver with an ARSA. The patient had died from heart failure. The cadaver was fixed with 3% formalin solution. During the dissection of the thoracic region, an ARSA was found, while the surrounding structures such as the recurrent laryngeal nerves were partially eliminated.

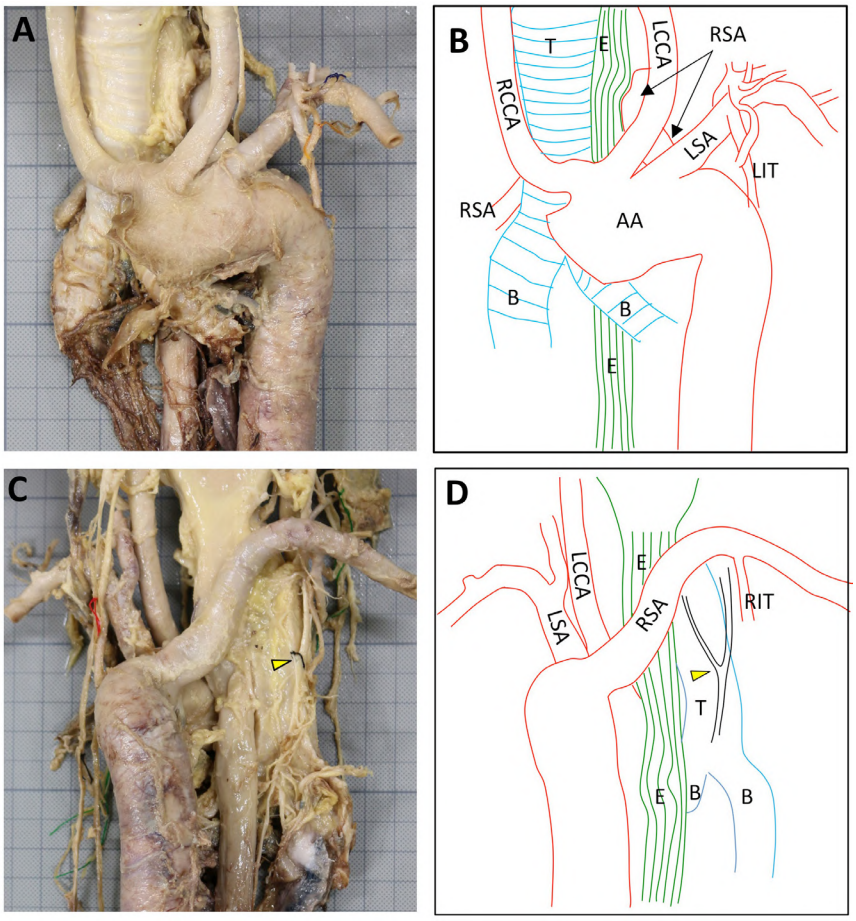

Fig. 1.- Photographs and schematic diagrams of eviscerated arterial system and the trachea and esophagus from the cadaver. **A** and **B**: Ventral views. The common carotid trunk is the first branch of the aortic arch (AA). The common trunk was immediately divided into the right and left common carotid arteries (RCCA and LCCA). The left subclavian artery (LSA) is the second branch. The third branch, which is the right subclavian artery (RSA), is not clearly visible on the ventral side. **C** and **D** show the dorsal views. The RSA runs dorsally to the esophagus (E), trachea (T), and bronchi (B). The left and right internal thoracic arteries (LIT and RIT) originated from the subclavian arteries as usual.

At first glance, the shape and route of the aortic arch appeared normal; however, considerable deviations in branching patterns were noted. The common carotid trunk appeared at the superior edge of the aortic arch, followed by the left subclavian artery. As the last branch, the right subclavian artery passed through the dorsal side of the aortic arch and branched off to the right (Fig. 1A, B). Then, the right subclavian artery ran obliquely between the esophagus and the vertebral column toward the right axilla (Fig. 1C, D). No KD was noted.

The CCT was very short and appeared stunted, with an outer diameter of 18 mm. The CCT gave rise to the left and right common carotid arteries with similar outer diameters, both of which directed the head forward. The outer diameters of the right and left common carotid arteries were respectively 13 mm and 11 mm. The left subclavian artery emerged immediately next to the CCT and was clearly demarcated by a steep incisure. After leaving the aortic arch, it ran obliquely upward towards the left, leaving the vertebral artery. Therefore, this is identified as the left subclavian artery. The peripheral branching pattern of the left subclavian artery was normal. Morphometry on the arterial outer diameter is summarized in Table 1.

Table 1. Morphometry on the diameter of observed arteries.

	Outer diameter(mm)
Ascending aorta	30
Descending aorta	25
Common carotid trunk	18
Right common carotid artery	13
Left common carotid artery	11
Right subclavian artery	14
Left subclavian artery	10

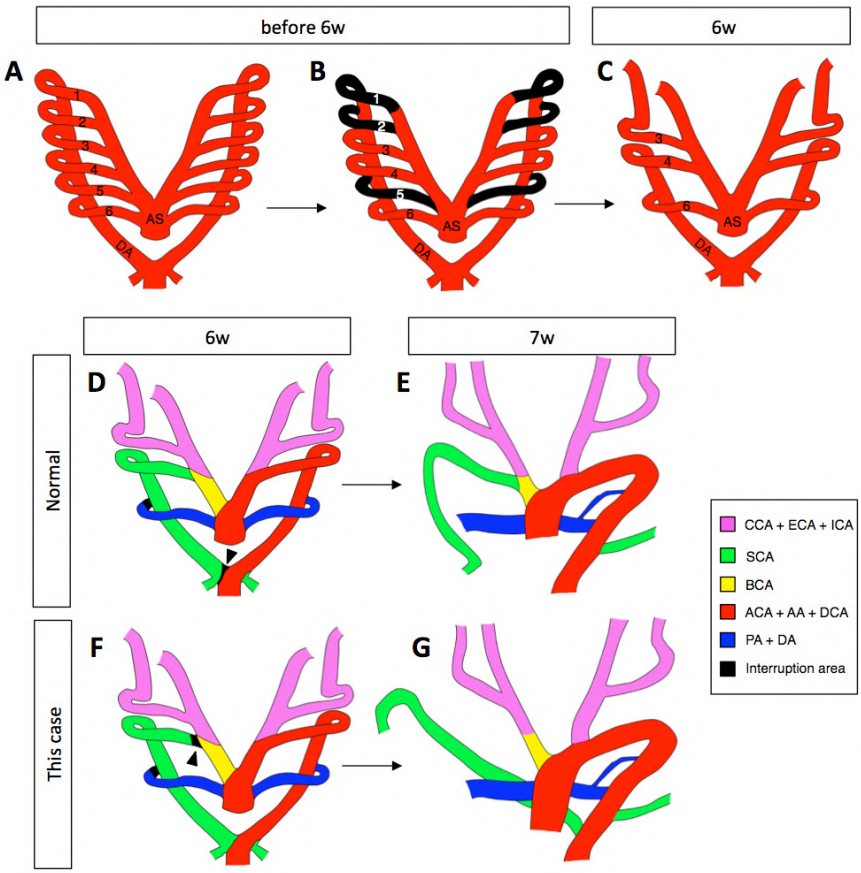

Fig. 2.- Schematic diagram comparing the normal development of the aorta and its branches (A-E) with the present case (F-G). **A)** Six-paired primitive aortic arch before the sixth week of gestation. **B)** The same period as the schematic in **A**, showing future regression of the arterial areas in black areas. **C)** The arterial arch at the sixth week of gestation after regression of the black area in **B**. **D** and **F** show the schematic in **C** with future arterial areas color-coded, and regressing areas were indicated with black areas and arrowheads. **E** and **G** show the separation of the right subclavian artery from the arterial arch, as black areas in **D** and **F** degenerate. The normal right subclavian artery separates from the future descending aorta. However, in the present case, it separates from the future brachiocephalic artery.

There are no apparent branches in the ventral view. Nevertheless, when we examined the dorsal side of the aortic arch, a relatively large artery with an outer diameter of 14 mm arose from the most caudal region of the aortic arch. This large, aberrant right subclavian artery ran towards the right with a slight elevation to the head, followed by a steep turn that formed an S-shape. Finally, the aberrant right subclavian artery directed towards the right axilla and passed behind the esophagus.

With respect to the recurrent laryngeal nerve, the left trunk followed a normal pathway, turning around the aortic arch to climb the trachea. The right trunk, which normally turns around the right subclavian artery, was lost at the time we found the ARSA. However, a branch emerging directly from the right vagal nerve was identified, which ran cranially between the trachea and esophagus and finally innervated the right larynx. Therefore, the present cadaver did not appear to have NRLN. No significant abnormalities were observed in the venous network.

COMMENTS

Developmental sequelae that cause ARSA are relatively well-assumed (Fig. 2), but no direct evidence has been obtained experimentally. Briefly, three of six pairs of primitive aortic arches connect to the AS regress to form an anlage of the definitive aortic arch around the sixth gestational week (Sadler, 2023). Stojanovska et al. (2012) assumed that the fifth dorsal right arterial arch located behind the origin of the right subclavian artery regresses, giving rise to anlages of the brachiocephalic, common carotid, and subclavian arteries. Therefore, the right fourth aortic arch and right dorsal aorta, located behind the esophagus, were forced to remain in contact. The retro-esophageal arch becomes the last branch of the aortic arch, which further differentiates into the right subclavian artery.

In contrast, ARSA adopts different segregation trajectories. In this case, the junction between the AS and fourth right aortic arch regressed, resulting in detachment of the prospective brachiocephalic artery from the definitive aortic arch. To maintain the bloodstream in the right upper limb, the right dorsal aorta does not lose its connection with the dorsal aortic trunk, originally called the AS.

From a clinical standpoint, Polguj (2014) reported that 126 of 141 cases were discovered during routine radiological examinations, whereas only 15 were noticed and recorded during dissection-related activities. While Polguj focused on ARSA in childhood, ARSA is often accidentally discovered in middle age. In such cases, care should be taken in the thoracic part of the digestive system and respiratory system during surgical interventions.

Demographically, 30% of all cases were found in Caucasian population, while Japanese cases account for 6-7%. However, according to Iimura (2017), the incidence of type G and H is estimated to be between 0.2-1.6% in the Japanese population, suggesting that this anomaly is rather frequent in the Japanese population, especially in female.

Although KD is present in 60% of ARSA (Epstein et al. 2002), it was not in our case. Japanese population revealed KD in 38 (59%) of 69 cases, the results is consistent with Epstein's report.

ACKNOWLEDGEMENTS

The authors sincerely thank those who donated their bodies to science so that anatomical research and teaching could be performed. Results from such research can potentially increase scientific knowledge. Therefore, these donors and their families deserve our highest respect. We would like to thank Editage (www.editage.com) for English language editing.

Ethical considerations

This study was conducted in compliance with the principles set forth in the Declaration of Helsinki and the guidelines for research involving cadavers established by the Japanese Association of Anatomists. We collected and preserved self-signed consent forms for body donation in accordance with international and university standards. Consent was obtained from the bereaved family before the dissection.

REFERENCES

EPSTEIN DA, DEBORD JR (2002) Abnormalities associated with aberrant right subclavian arteries: a case report. *Vasc Endovascular Surg*, 36(4): 297-303.

IIMURA A, OGUCHI T, TOU M, MATSUO M (2017) The retroesophageal right subclavian artery -A case report and review. *Okajimas Folia Anat Jpn*, 94(3): 75-80.

KOMMERELL B (1936) Verlagerung des Ösophagus durch eine abnorm verlaufende Arteria subclavia dextra (Arteria lusoria). *Fortschr Gebiet Röntgenstrahlen Nuklearmedizin*, 54: 590-595.

POLGUJ M, CHRZANOWSKI Ł, KASPRZAK JD, STEFANCZYK L, TOPOL M, MAJOS A (2014) The aberrant right subclavian artery (arteria lusoria): the morphological and clinical aspects of one of the most important variations--a systematic study of 141 reports. *Sci World J*, 2014: 292734.

SADLER TW (2010) Cardiovascular System. *Langman's Medical Embryology*. Chapter 12, 11th edition. Wolters Kluwer, USA, pp 165-200.

STEWART GR, MOUNTAIN JC, COLCOCK BP (1972) Non-recurrent laryngeal nerve. *Br J Surg*, 59(5): 379-381.

STOJANOVSKA J, CASCADE PN, CHONG S, QUINT LE, SUNDARAM B (2012) Embryology and imaging review of aortic arch anomalies. *J Thorac Imaging*, 27(2): 73-84.

WILLIAMS GD, AFF HM, SCHMECKEBIER M, EDOMONDS HW, GRAUL EG (1932) Variations in the arrangement of the branches arising from the aortic arch in American whites and negroes. *Anat Rec*, 54(2): 247-251.

Coexistence of bilateral Langer's arm arch and Kaplan's anastomosis: a case report and literature review

Axel O. Colombo[1], Sofia Funes[1], Agustina Medin[1], Tomás Ferré[1], Juan M. De Zan[1], Mariana Bendersky[1,2]

[1] Living Anatomy Laboratory, 3rd Normal Anatomy Department, School of Medicine, University of Buenos Aires, Argentina
[2] ENyS (National Scientific and Technical Research Council - CONICET)

SUMMARY

The axillopectoral muscle [Langer's arm arch (LAA)], is described as a supernumerary musculo-tendino-fascial structure, which connects at least two muscles that make up the walls of the axillary fossa. This anatomical variant is found in around 7% and 15% of the population, usually unilaterally, on the right side and in females. Kaplan described a nervous communication between the dorsal and the terminal superficial branches of the ulnar nerve, both sensory, with an incidence of the 2% to 4%.

A case report is presented of an anatomical preparation, in which Langer's arm arch and Kaplan anastomosis coexisted on both sides. A review of literature of LAA and Kaplan's anastomosis is also presented. The knowledge of these anatomical variations is important as they are involved in a wide variety of vascular, nervous and functional disorders of the upper limb.

Key words: Langer's arm arch – Kaplan's anastomosis – Anatomical variations – Upper limb – Gross anatomy

INTRODUCTION

Alexander Ramsay discovered the LAA in 1795, and in 1812 he made the first publication about it. However, it was Carl Langer that described it more accurately in 1846, and that is the reason why the arch was named after him (Hoogbergen and Kauer, 1992). The Langer's arm arch (LAA) is described as a supernumerary musculo-tendino-fascial structure connecting two or more muscles that make up the boundaries of the axillary fossa, usually from the *latissimus dorsi* muscle to the to the lower fibers of the pectoralis major muscle (Macalister, 1889; Piñero et al., 1975; Ortiz et al., 2009; Hirtler, 2014). This anatomical variation is found in about 7% to 15% of the population, mostly females, and is more frequently unilateral, right sided (Hoogbergen and Kauer, 1992). The utmost importance of studying the LAA lies in the fact that it is involved in several disorders of the upper limb, such as loss of axillary concavity; axillary vein entrapment; numbness, paresthesias, and burning sensation in the upper limb; venous thrombosis of the upper limb; hyperabduction syndrome; shoulder instability; masking of axillary lymph nodes; and compression of axillary nerve elements (Stopford, 1918; Paraskevas et

Corresponding author:
Axel Omar Colombo. Living Anatomy Laboratory, 3rd Normal Anatomy Department, School of Medicine, University of Buenos Aires, Argentina.
E-mail: axelcolombo59@gmail.com

Submitted: August 4, 2023. **Accepted:** November 6, 2023

https://doi.org/10.52083/ETTH6352

al., 2008; Ballesteros-Acuña, Bravo-Pacheco and Forero-Porras, 2019; Bonilla-Sepúlveda, 2021).

In 1963 Kaplan described a nervous communication between the dorsal branch of the ulnar nerve and the terminal superficial branch of the same nerve. This nervous communication is formed on the hypothenar region, being its prevalence between 2% to 4%. Kaplan's anastomosis provides sensory innervation to this region, with variations on the nervous distribution pattern. It accounts for the pain and loss of sensitivity in patients undergoing hand surgery due to damage to the pisiform bone, the flexor carpi ulnaris tendon, or damage to the Guyon canal (Torre et al., 2015). To the best of our knowledge, there have been no reports of the co-occurrence of aforementioned anatomical variations within a singular subject's bilateral upper extremities.

We present a case report of an anatomical preparation in which LAA and Kaplan's anastomosis were found bilaterally during routine dissection. A literature review was made in classical anatomy textbooks, PubMed, Google scholar and Scielo about previous reports of these anatomical variations.

CASE PRESENTATION

A male cadaver of 50 to 55 years old at death, preserved in 10% formalin, was subjected to routine anatomical dissection for research and teaching at the 3rd Normal Anatomy Department of the School of Medicine of the University of Buenos Aires. Both upper limbs were dissected using standard techniques.

Langer's arm arch

Dissection began with removal of the skin and superficial fascia of the arms and torso, and then of the subcutaneous tissue and fascia. The anterior surface of the pectoralis major (PM) was dissected following the direction of its fibers, from proximal to distal. Around its distal portion, a supernumerary muscular fascicule was found, showing different dispositions in each upper limb (Fig. 1). On the right side (Figs. 2, 3), it extended from the ascending distal portion of the latissimus dorsi muscle to the coracoid process, on the joined insertion of the short head of biceps brachii muscle and coracobrachialis muscle (conjoined tendon).

On the left side (Figs. 4, 5), it extended as his right homonymous from the *latissimus dorsi* to the conjoined tendon, but it was also inserted on the distal portion of the PM. Then, the PM was sectioned distally and rebated medially for dissecting and later sectioning the pectoralis minor muscle, in order to display the vascular-nervous elements of the axilla. Both aberrant muscles laid across the neurovascular bundle as they adopted a musculo-tendino-fascial consistency. Their proximal origin was completely muscular, but their distal

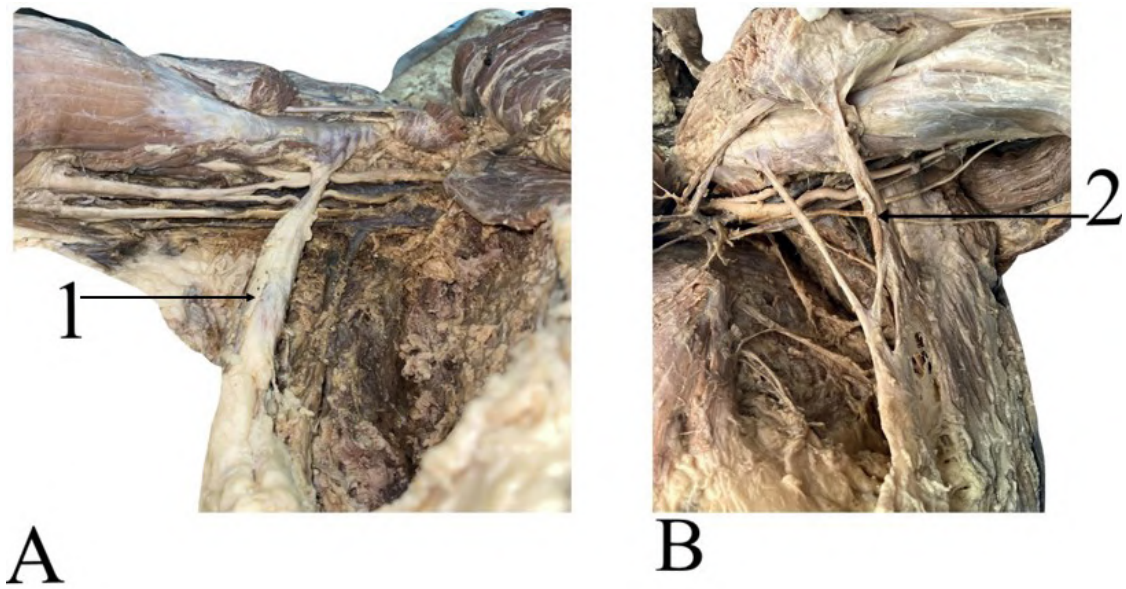

Fig. 1.- A: right axilla. **B:** left axilla. 1: right Langer's arm arch; 2: left Langer's arm arch.

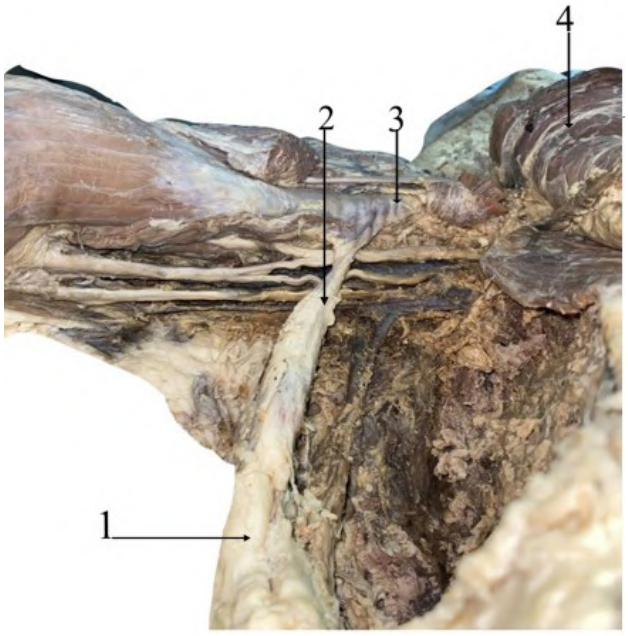

Fig. 2.- Right axilla. 1: latissimus dorsi; 2: Langer's arm arch; 3: conjoined tendon; 4: pectoralis major.

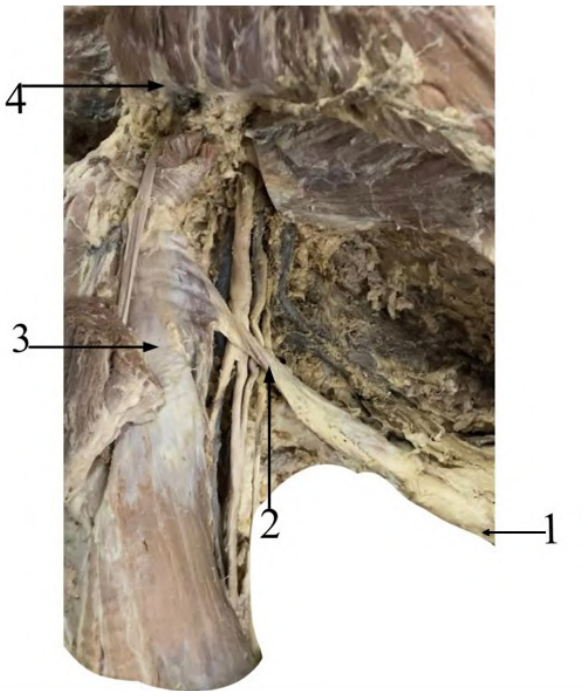

Fig. 3.- Right axilla. 1: latissimus dorsi; 2: Langer's arm arch; 3: conjoined tendon; 4: pectoralis major.

portion was tendino-fascial. A bilateral Langer's arm arch was then identified and classified based on its specific structural origin, relations, and subsequent termination (Piñero et al., 1975).

Kaplan´s anastomosis

Moving on to the dissection of the cadaveric preparation, both upper limbs were dissected. The ulnar nerve was followed to its end.

By doing so, we were able to notice how, on the left side, a nervous branch was born from the medial edge of the superficial terminal branch of the ulnar nerve. This anomalous branch crossed the hypothenar region and the distal portion of the flexor carpi ulnaris muscle, from lateral and proximal to medial and distal, in order to reach the dorsal branch of the ulnar nerve, just before the dorsal branch of the ulnar nerve passed to the posterior

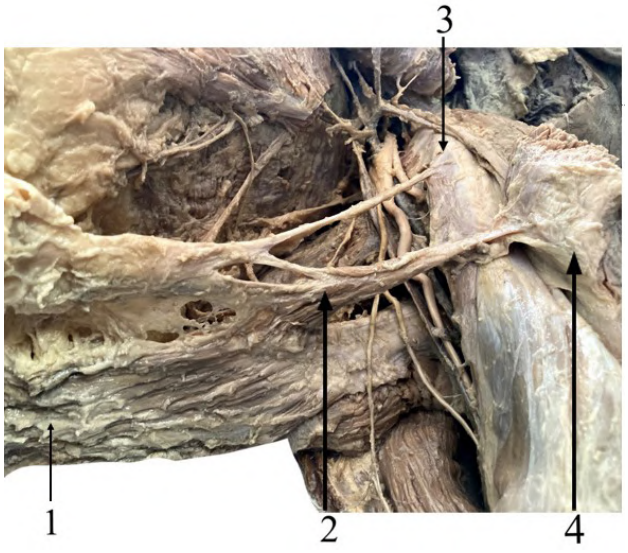

Fig. 4.- Left axilla. 1: latissimus dorsi; 2: Langer's arm arch; 3: conjoined tendon; 4: pectoralis major.

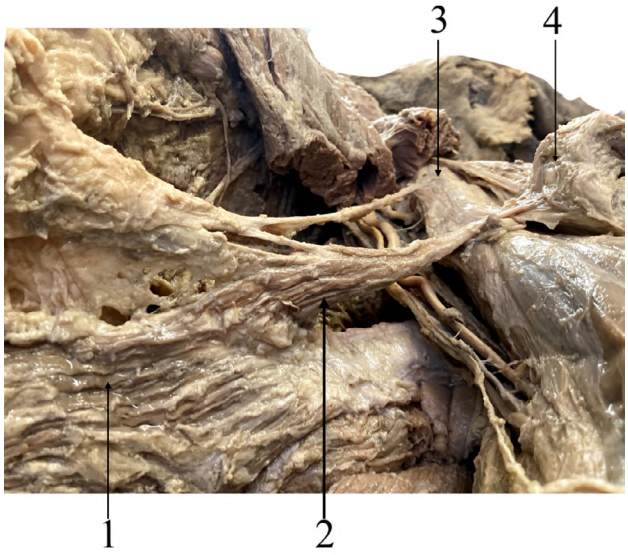

Fig. 5.- Left axilla. 1: latissimus dorsi; 2: Langer's arm arch; 3: conjoined tendon; 4: pectoralis major.

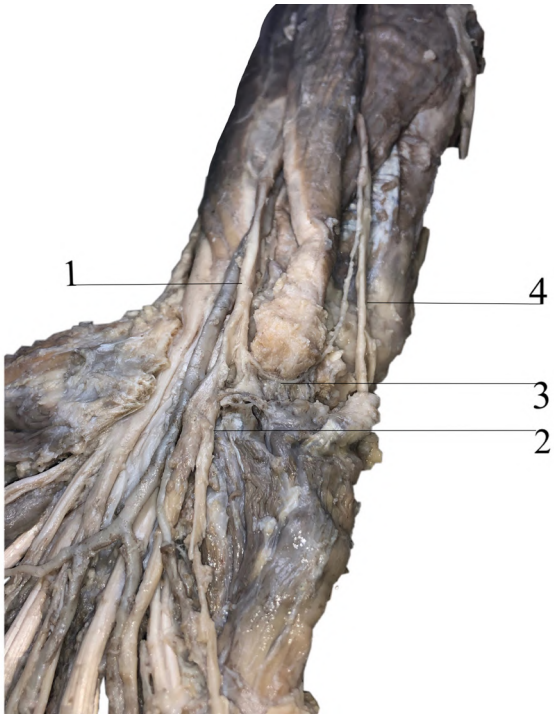

Fig. 6.- Right hand. 1: ulnar nerve; 2: superficial branch of the ulnar nerve; 3: Kaplan's anastomotic branch; 4: dorsal branch of the ulnar nerve.

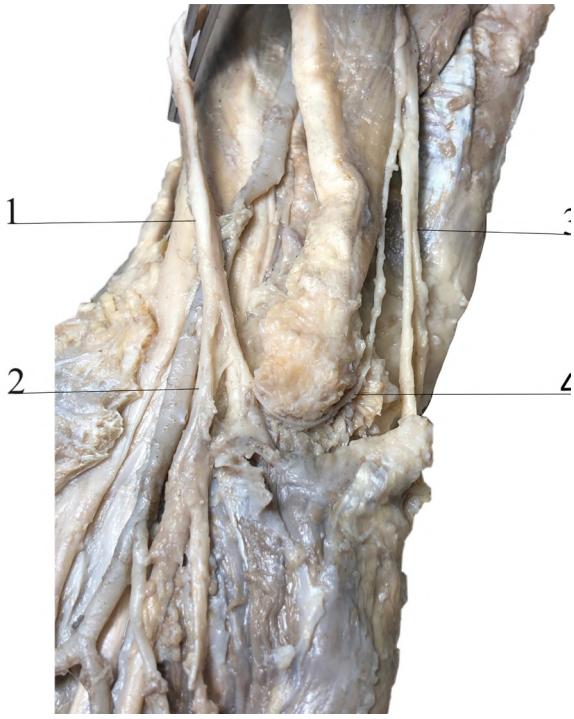

Fig. 7.- Right hand. 1: ulnar nerve; 2: superficial branch of the ulnar nerve; 3: dorsal branch of the ulnar nerve; 4: Kaplan's anastomotic branch.

portion of the wrist, over the ulnar canal [Guyon] (Figs. 8, 9). On the right side this anastomosis was found on a deeper level. On account of this we decided to follow this anastomotic branch from its origin until it reached the dorsal branch of the ulnar nerve, just to discover how in the lower third of the forearm it described a faithful pass around the distal insertion of flexor carpi ulnaris muscle.

Carrying on its way, (from lateral to medial) it outlined the pisiform bone, went deep into the hypothenar muscles and finally reached the ulnar nerve right before this one entered the cubital canal (Figs. 6, 7). On behalf of the anatomical disposition of these supernumerary branches, we were able to assume that they were Kaplan ´s anastomosis (Garibaldi and Nucci, 2000; Torre et al., 2015; Iwanaga et al., 2021).

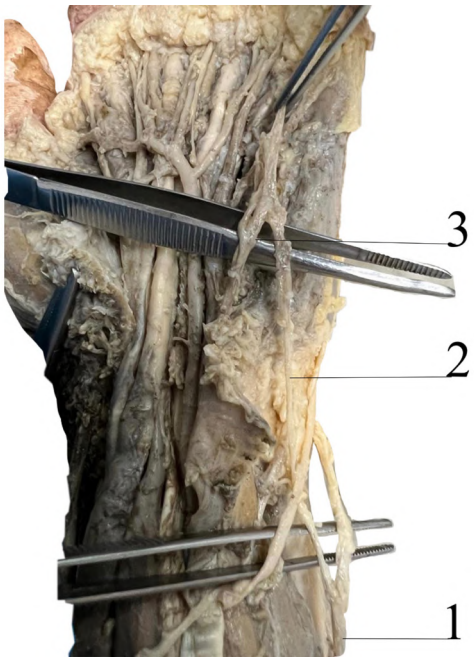

Fig. 8.- Left hand. 1: dorsal branch of the ulnar nerve; 2: Kaplan's anastomotic branch; 3: superficial branch of the ulnar nerve.

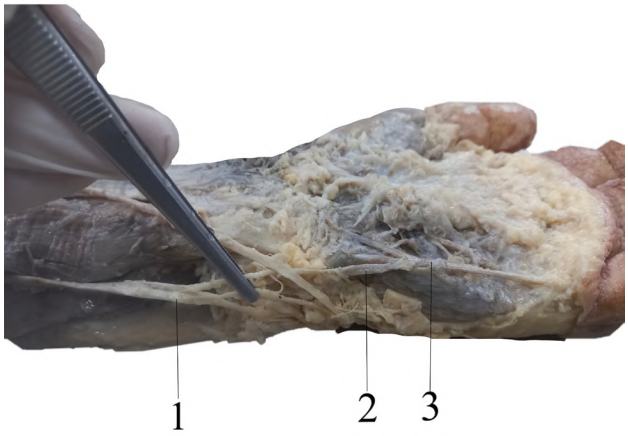

Fig. 9.- Left hand. 1: dorsal branch of the ulnar nerve; 2: Kaplan's anastomotic branch; 3: superficial branch of the ulnar nerve.

DISCUSSION

We present a case report of the coexistence of two different anatomical variations on both upper limbs in the same individual. As far as we know, this is the first description of this co-occurrence.

Langer's arm arch

Langer's arm arch (LAA), also known as axillo-pectoral muscle or pectorodorsal arch (Piñero et al., 1975), is described as a musculo-tendino-fascial structure that extends from the *latissimus dorsi* muscle to the *pectoralis major*, and sometimes it can also have attachments to the short head of the biceps brachii muscle or its fascia, teres major muscle, coracoid process, coracobrachialis muscle or its fascia, and pectoralis minor muscle (Tubbs et al., 2016). This supernumerary muscle is found by dissection, surgery, or by palpating the base of the axillary region while maintaining the upper limb in abduction at 90° (Clarys et al., 1996). The embryological origin of this structure is related to a large extension of muscle associated with the skin called "*panniculus carnosus*", highly developed in mammals in order to improve functional mobility of the arm. Its incidence varies on around 7% to 15% of the population and it has mostly been found unilaterally, on the right side and in females. It has also been found to exist with other slips of muscle arising from the fascia over the fifth digitation of the serratus anterior muscle and the interval between the pectoralis major and latissimus dorsi muscles (Tubbs et al., 2016). Diverse authors had been able to accomplish a common categorization according to these variabilities (Bonilla-Sepúlveda, 2021):

1. *"According to the structure:* Type I (muscular), Type II (tendinous), including four different subtypes depending on their insertion and innervation.
2. *According to the origin:* Category 1, the most usual, arises from the lateral edge of the *latissimus dorsi*, and ends on the distal portion of the *pectoralis major*. Category 2 consists of an incomplete arch which distal insertion, described by Testut in 1884, may vary from the *pectoralis minor* and the axillary fascia, to the *biceps brachii* , the *coracobrachialis*, the coracoid process, and the intertubercular groove (Testut and Latarjet, 1984).
3. *According to the shape:* Type 1, is described as a well-defined muscle born from the lateral edge of the latissimus dorsi. Type 2 consists of a group of fibers that leave the lateral edge of the *latissimus dorsi* in order to reach and cross the axilla. Type 3 is a fan-shaped arch."

According to this classification, we could establish that our case, on the right axilla, regarding its characteristics, can be classified as:

1. *According to the structure:* the proximal portion is type 1, and the distal is type 2.
2. *According to the origin:* category 2, being its distal insertion on the conjoined tendon.
3. *According to the shape:* type 1.

On the left axilla, regarding its characteristics, it can be classified as:

1. A*ccording to the structure:* the proximal portion is type 1, and the distal is type 2.
2. *According to the origin:* category 1 and 2, as its distal insertion is by two fascicles.
3. *According to the shape:* type 3.

In most of the cases, the innervation of the LAA is provided by the *ansa pectoralis*, the medial pectoral nerve or the thoracodorsal nerve, and it receives blood from the lateral pectoral artery (Tubbs et al., 2016). Other studies have concluded that these are deeply connected to the embryological origin of the arch.

The LAA is involved in several vascular, nervous and functional alterations of the upper limb, such as: loss of axillary concavity (Ortiz et al., 2009); axillary vein entrapment (Ballesteros-Acuña et al., 2019); numbness, paresthesias, and burning sensation in the upper limb; venous thrombosis of the upper limb (Tilney et al., 1970); hyperabduction syndrome (Piñero et al., 1975); shoulder instability; masking of axillary lymph nodes; and compression of axillary nerve elements with loss of sensibility and pain. Furthermore, the presence of this arch brings up complications during the resection of lymph nodes during breast cancer surgery (Ballesteros-Acuña et al., 2019).

Kaplan's anastomosis

Nervous anastomoses are frequently found on the upper limb, but most of them are motor fibers, for example Martin Gruber's and Riche-Cannieus anastomosis. Sensory anastomoses are quite rare to find and Kaplan's anastomosis is an example of them, being described as an unusual branch connecting the superficial terminal branch of the ulnar nerve with the dorsal branch of the same one along the hypothenar region. This supernumerary branch was first identified by Kaplan in dissection and has become known as a Kaplan's anomalous branch. In joining the superficial branch, a Kaplan's anomalous branch makes a loop around the pisiform; Kaplan surmised this loop to be a source for persistent pisiform pain (Tubbs et al., 2016). This anastomosis explains why patients that had suffered ulnar nerve injuries around the cubital canal may present with hypesthesia not only on the palm but also on the dorsal region of the hand (something that is usually related to more proximal ulnar injuries) leading to misdiagnosis and uncertain interpretation of neurophysiological studies.

According to this anastomosis characteristics, it can be classified in 6 types:

1. *Hankins & Flemming*, if the anastomosis takes place on the cubital canal [Guyon] between the dorsal branch of the ulnar nerve and the ulnar nerve (Hankins and Flemming, 2005).
2. *Kaplan*, if the anastomosis is done between the dorsal branch of the ulnar nerve and the superficial terminal branch of the ulnar nerve (Hankins and Flemming, 2005).
3. *Hoogbergen & Kauer*, if the anastomosis is done between the dorsal branch of the ulnar nerve and the terminal motor branch of the same nerve (Hankins and Flemming, 2005).
4. *Camper*, if the anastomosis is done between the dorsal branch of the ulnar nerve and the medial palmar digital nerve of the fifth finger (Hankins and Flemming, 2005).
5. *Wulle*, same as Camper, the difference lies in the fact that it forms at the level of the proximal phalanx of the fifth finger (Hankins and Flemming, 2005).
6. *McCarthey & Nalebuff*, there is no nervous communication, but there is an aberrant branch being born from the dorsal branch of the ulnar nerve and ending on the pisiform bone (Hankins and Flemming, 2005).

There are no studies that report the prevalence of these different types of anastomosis, but Kaplan's anastomosis is known to be rare.

According to the aforementioned classification, in our subject, the right hand had a type 1 (Hankins-Flemming) anastomosis, and the left one, a type 2 (Kaplan).

In short, on the same cadaveric preparation where we found LAA bilaterally, we also found two Kaplan's anastomoses, one on each hand.

CONCLUSION

This case report highlights the unusual coexistence of two anatomical variations: Langer's arm arch and Kaplan's anastomosis, and also the bilateral disposition of both of them in a male subject. Anatomical variations generally have no effect on the function of the body under normal circumstances, but their knowledge is important to improve diagnosis and treatment. An unresolved question pertains to whether the detection of multiple anatomical variations within a single individual could serve as an indication for the presence of other associated variations or abnormalities.

ACKNOWLEDGEMENTS

The authors sincerely thank those who donated their bodies to science so that anatomical research and teaching could be performed. Results from such research can potentially increase scientific knowledge and can improve patient care. Therefore, these donors and their families deserve our highest respect (Iwanaga et al., 2021).

REFERENCES

BALLESTEROS-ACUÑA LE, BRAVO-PACHECO FA, FORERO-PORRAS PL (2019) Expresión morfológica del músculo axilopectoral. Un estudio anatómico directo en una muestra de población Colombiana. *Int J Morphol*, 37(4): 1262-1266.

BONILLA-SEPÚLVEDA OA (2021) Arco axilar de Langer: serie de casos y revisión de la literatura. *Revista Colombiana de Cirugía*, 36(2): 268-274.

CLARYS JP, BARBAIX E, VAN ROMPAEY H, CABOOR D, VAN ROY P (1996) The muscular arch of the axilla revisited: its possible role in the thoracic outlet and shoulder instability syndromes. Manual Therapy. Elsevier, 1(3), pp 133-139.

GARIBALDI SG, NUCCI A (2000) Dorsal cutaneous branch of ulnar nerve: an appraisal on the anatomy, injuries and application of conduction velocity studies in diagnosis. *Arquivos Neuro-Psiquiatria*, 58: 637-641.

HANKINS CL, FLEMMING S (2005) A variant of Kaplan's accessory branch of the dorsal cutaneous branch of the ulnar nerve: a case report and review of the literature. *J Hand Surg*, 30(6): 1231-1235.

HIRTLER L (2014) Langer's axillary arch—Case presentation and literature overview. *Austin J Anat*, 1(4): 1020.

HOOGBERGEN MM, KAUER JM (1992) An unusual ulnar nerve-median nerve communicating branch. *J Anat*, 181(Pt 3): 513.

IWANAGA J, SINGH V, OHTSUKA A, HWANG Y, KIM HJ, MORYŚ J, RAVI KS, RIBATTI D, TRAINOR PA, SAÑUDO JR, APAYDIN N, ŞENGÜL G, ALBERTINE KH, WALOCHA JA, LOUKAS M, DUPARC F, PAULSEN F, DEL SOL M, ADDS P, HEGAZY A, TUBBS RS (2021) Acknowledging the use of human cadaveric tissues in research papers: Recommendations from anatomical journal editors. *Clin Anat*, 34(1): 2-4.

MACALISTER A (1889) A Text-book of Human Anatomy. Charles Griffin Co., pp 266.

ORTIZ JI, RAMIREZ F, PETROSINO P, MILANO M, ARENAS A, CASTILLO V (2009) Arco axilar de Langer (músculo axilopectoral): Variante supernumeraria inusual del músculo latísimo del dorso. Reporte de tres casos. *Int J Morphol*, 27(4): 1209-1212.

PARASKEVAS G, GEKAS CH, TZAVEAS A, SPYRIDAKIS I, STOLTIDOU A, TSITSOPOULOS PPH (2008) Kaplan anastomosis of the ulnar nerve: a case report. *J Med Case Rep*, 2: 107.

PIÑERO A, GALINDO PJ, RIQUELME J, ILLANA J, PARRILLA P (1975) El arco axilar de Langer: una variación anatómica con importancia quirúrgica. *Rev Senologia Patol Mam*, 22(2): 75-77.

STOPFORD JSB (1918) The variation in distribution of the cutaneous nerves of the hand and digits. *J Anat*, 53(Pt 1): 14.

TESTUT JL, LATARJET A (1984) Tratado de Anatomía Humana. Tomo primero: osteología-artrología-miología, chapter 9, pp 689-690.

TILNEY NL, GRIFFITHS HJG, EDWARDS EA (1970) Natural history of major venous thrombosis of the upper extremity. *Arch Surg*, 101(6): 792-796.

TORRE F, ERTHAL R, FERNANDES RMP, BABINSKI MA, CISNE R (2015) A communicating branch between the dorsal and superficial ramus of the ulnar nerve (Kaplan's Anastomosis): Clinical and surgery discussion. *Int J Morphol*, 33(03): 865-867.

TUBBS RS, SHOJA MM, LOUKAS M (2016) Bergman's Comprehensive Encyclopedia of Human Anatomic Variation. John Wiley & Sons, pp 266-268; 1093.

Duplicated internal jugular vein: a case report

Ana Villar Píriz[1], Leticia Vázquez Ballefín[1], Sofia Martínez Ventura[1], Eduardo Olivera Pertusso[1], Santiago Cubas Sosa[1-2]

[1] Departamento de Anatomía, Facultad de Medicina, Universidad de la República, Montevideo, Uruguay

[2] Centro Cardiovascular Universitario, Hospital de Clínicas "Dr. Manuel Quintela"

SUMMARY

Anatomical variants of the venous central system are very infrequent; nevertheless, it is useful to be aware of them in order to avoid complications during common procedures. The purpose of the present study is to describe an anatomical variant of the Right Internal Jugular Vein (RIJV), and to investigate the frequency of this variant reported in the current literature.

Authors present an anatomical variant of RIJV, found during the dissection of an adult male cadaver, previously fixed in a formaldehyde-based solution, who was voluntarily donated to the Faculty of Medicine of Universidad de la República in Montevideo, Uruguay. The cadaveric material was used taking into account the Helsinki Declaration regarding prior live donation and informed consent. A photographic record and a bibliographic search in electronic bases were carried out in order to discover the frequency with which this variant occurs. It was described as an isolated duplicated RIJV, which had its origin at the level of the right jugular foramen, and had its division next to the thyroid cartilage after a path of 6.5 cm into two branches (anteromedial and posterolateral) that ended separately, and were 7.2 cm and 5.4 cm in length, respectively. The relations with near structures such as the accessory nerve and the omohyoid muscle were also described and compared with the literature reviewed.

Key words: Internal jugular vein – Duplication – Fenestration – Vein catheterization – Case report

INTRODUCTION

The Internal Jugular Vein (IJV) is classically described as a vessel that originates as a continuation of the sigmoid sinus in the interior of the cranial cavity, and ends behind the sternoclavicular joint when it reaches the subclavian vein to form the brachiocephalic vein.

The anatomical variants of great veins of the body are infrequent when compared to the peripheral veins. A rare variant of the IJV is its duplication, which consists of two divergent branches of the vein that originate after its emergence as a unique vessel, and end up separately (Downie et al., 2007; Hashimoto et al., 2012; Wong et al., 2012; Nayak et al., 2015; Contrera et al., 2016).

Although it is unlikely that variants have any physiological implications, they must be taken into account in regard to avoiding injuries during

Corresponding author:
Ana Villar Píriz. Hector Gutiérrez Ruiz 1296, Montevideo, Uruguay 11100. Phone: +598 92 449 719. E-mail: anaa.villar@hotmail.com

Submitted: January 20, 2023. **Accepted:** December 20, 2023

https://doi.org/10.52083/VWXF7751

the realization of interventional procedures (Downie et al., 2007).

In regard to the etiology of variants, some authors agreed on the existence of three embryological theories: neural, bony and vascular (Prades et al., 2002; Hashimoto et al., 2012; Nayak et al., 2017). Downie et al. (2007) added a fourth theory: the muscular one. However, there is no agreement on which theory is the most plausible.

The Right Internal Jugular Vein (RIJV) is the preferred site for placement of central venous catheters (Downie et al., 2007; Nayak et al., 2015), because it has a more direct path to the heart, in comparison to the contralateral vein. For this reason, it is necessary to know the normal anatomy and its variants.

The aim of this study is to describe the anatomy of this rare case of a variant of RIJV and to compare this finding with the ones published in the current literature in order to determine the frequency of this variant.

CASE REPORT

The present case is an anatomical variant of RIJV that was found during curricular neck dissection of an adult male cadaver, previously fixed in a formaldehyde-based solution, who voluntarily was donated to Facultad de Medicina after signing an ethical consent.

The dissection was carried out at Departamento de Anatomía de Facultad de Medicina, Universidad de la República in Montevideo, Uruguay. The cadaver did not have previous surgical approaches or pathology in thorax or neck.

The skin approach required a longitudinal incision in the middle line of the neck and two complementary ones: a superior one at the level of the lower border of the mandible, and an inferior one parallel to the clavicle. The skin flap, the platysma muscle, the superficial layer of the cervical fascia and the sternocleidomastoid muscle (SCM) were reclined laterally to the posterior border of SCM, in order to dissect the neurovascular bundle of the neck.

To expose the entire course of the RIJV, both portions (clavicular and sternal) of the SCM were desinserted, as well as distal portions of the infrahyoid muscles. The thorax was approached by median sternotomy.

The following variables were registered: vein origin, course, termination, tributaries, level of the division, level relative to the thyroid cartilage, relation with the omohyoid muscle and accessory nerve. The following measures were recorded: diameter and length of the medial and lateral branches. All the measurements were taken by a digital caliper, which was manipulated by the same researcher.

Finally, an exhaustive bibliography research was carried out in electronic bases like Medline and Pubmed, using words like “internal jugular vein”, “anatomical variation”, “duplication”, “bifurcation” in combination with Boolean operators “AND”, “OR”. The collected articles were used for the discussion and analysis of the findings presented in this study, and they are properly cited at the end of this paper.

Regarding the results, it was possible to determine that RIJV corresponds to the duplicated morphology (Fig. 1A).

About the origin, it was found that the vein emerged from the jugular foramen as a unique vessel. At the level of the inferior border of the thyroid cartilage, after a path of 6.5 cm it was divided into two branches of unequal caliber (Fig. 1A).

The anteromedial branch was 1.3 cm in diameter and 7.2 cm in length. The posterolateral branch was 0.6 cm in diameter and 5.4 cm in length.

Regarding the termination, the anteromedial branch was tributary of the left brachiocephalic vein, and the posterolateral branch formed the right brachiocephalic vein with the homolateral subclavian vein (Fig. 1B).

The following were registered as tributaries of the anteromedial branch: the inferior thyroid vein and the thyrolinguofacial trunk. There were no tributaries of the posterolateral branch (Fig. 1B).

Lastly, in reference to the anatomical relations, it has been observed that the accessory nerve passes behind the RIJV in its origin, and goes straight to reach the SCM. In addition, the omohyoid muscle ran anterior to the point of division of the vein.

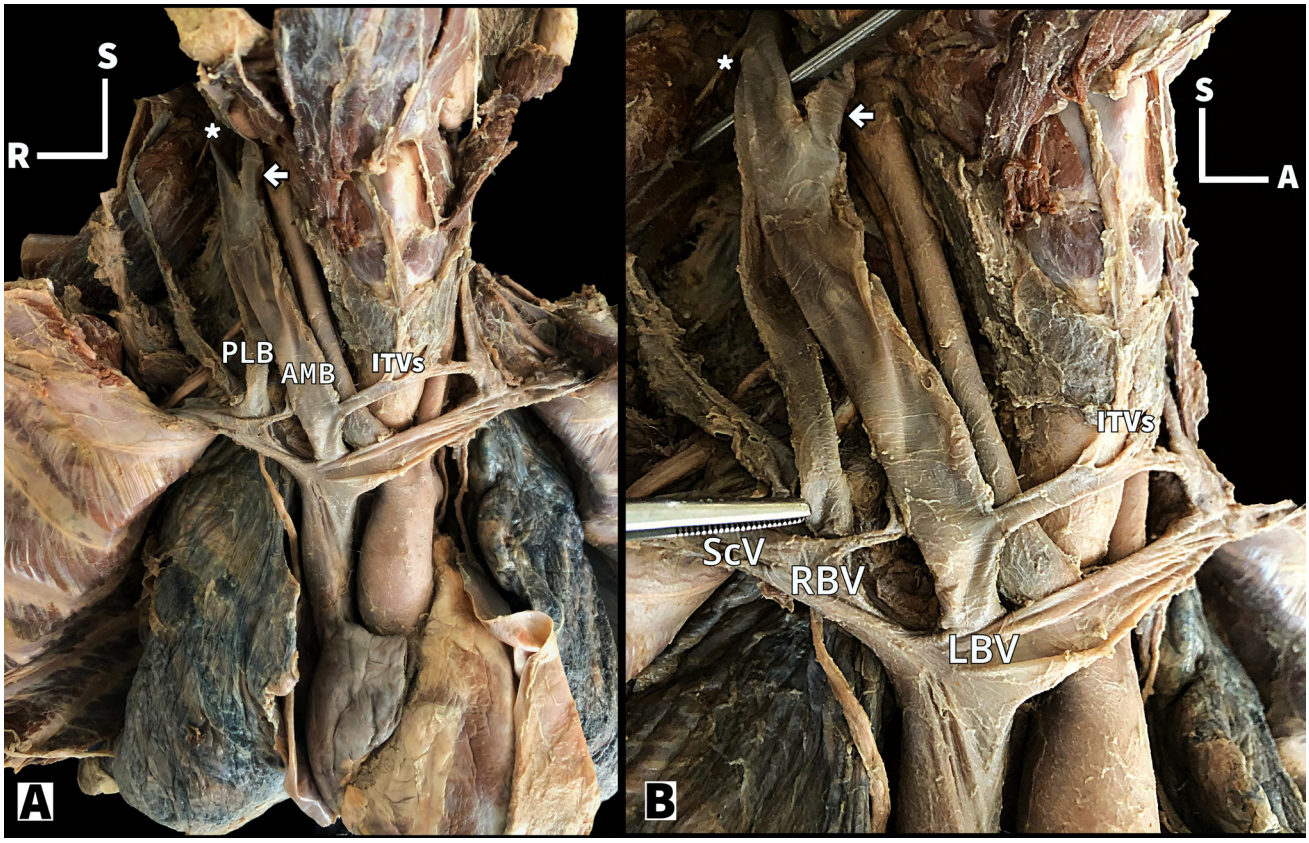

Fig. 1.- A- Anterior view of the neck and thorax. There is a Duplicated RIJV that originates as a unique vessel and ends as two separated branches. AMB: anteromedial branch; PLB: posterolateral branch; **B-** Right sided view of the neck. The totality of RIJV, its two branches, its tributaries and its termination is observed. The anteromedial branch is thicker and it drains in the Left Brachiocephalic vein. The posterolateral one ends up merging with the right subclavian vein to form the right brachiocephalic vein. ScV: Right Subclavian vein; RBV: Right Brachiocephalic vein; LBV: Left Brachiocephalic vein; ITVs: Inferior Thyroid veins; *: Accessory Nerve; arrow: Thyrolinguofacial trunk.

COMMENTS

A few cases of anatomical variants of Internal Jugular Vein (IJV) have been reported, using in an indistinct way the following terms: duplication, bifurcation and fenestration.

Some authors distinguish between the terms duplication and bifurcation, taking into account the level of division of the branches with respect to the omohyoid muscle. They affirm that, if IJV divides inferior to the muscle, the correct term to use is duplication. On the other hand, if it divides superior or at the level of the muscle, the proper term to use is bifurcation. (Mumtaz and Singh, 2019).

Nayak et al. (2017) propose a morphological classification into three types: A, B, C. Type A corresponds to the division of the IJV in two branches up to the level of the posterior belly of the digastric muscle, and the final reunion of the branches at the level of the omohyoid muscle with the accessory nerve passing through both branches. Type B differs from type A in the caudal extension, which continues inferior to the tendon of the omohyoid muscle. Finally, in type C the duplication begins at the level of the hyoid bone. About the termination of types B and C, it is interpreted from the image that follows the text that the branches end independently, although this is not specified in writing.

Other authors like Downie et al. (2007), Hashimoto et al. (2012) and Contrera et al. (2016) refer to duplication when the IJV divides into two independent branches after being originated as a unique vessel, and to fenestration when previous to its end, the two branches are reunited in an only vessel. Having said that, duplication acquires an inverted “Y” shape and fenestration an eyelet one (Downie et al., 2007). In order to avoid confusion in the use of terms, the authors of this manuscript will be using the aforementioned criteria and will reclassify the previous reports to unify terms.

Due to the inconsistency about the proper terminology, the incidence of these variants is still unknown (Downie et al., 2007). Prades et al.

Table 1. Reclassification of the IJV morphology of previous reports, using Downie et al. (2007), Hashimoto et al. (2012), and Contrera et al. (2016) definition of Duplication and Fenestration. R: right; L: left; M: male; F: female.

Author	Cases and Gender (M; F)	Neck side	Proposed Classification	Reclassification
Rossi and Totori-Donati, (2001)	1 F	Bilateral	R Duplication L Partial duplication	R Duplication L Fenestration
Prades et al. (2002)	3 M	2 L 1 R	Duplications	Fenestrations
Turan-Ozdemir et al. (2004)	1 F	R	Duplication	Duplication
Downie et al. (2007)	1 F	Bilateral	Duplication R Duplication L	Duplication R Duplication L
Hashimoto et al. (2012)	4 M	3 L 1 R	Fenestrations	Fenestrations
Contrera et al. (2015)	3 (2 M, 1 F)	2 L 1 R *	Fenestration L Fenestration L Duplication R	Fenestration L Fenestration L Duplication R
Nayak et al. (2017)	1 M	L	Duplication	Fenestration
This paper	1 M	R	Duplication	Duplication

*: Corresponds to the Female case.

(2002) report a prevalence of 0.4%. Hashimoto et al. (2012) report 3.3%, and Contrera et al. (2016) report 1.0%. The authors of the present manuscript have decided to reclassify the obtained data in order to unify the terminology (Table 1).

In reference to the prevalence of this variant, taking into account the neck side and gender, 17 cases were found in the literature. A total of 6 cases of double internal jugular vein have been described in four women, due to the fact that two of them presented bilateral cases. There is a clear predominance of the left side (58.8%) over the right one (41.2%), and there is a male predominance, with 11 cases over the female cases, which are only 4 (Table 1). However, in the literature reviewed a reason for this predominance has not been specified.

The RIJV described in this paper was originated as a unique vessel at the level of the jugular foramen, and so were the veins described by other authors (Prades et al., 2002; Turan-Ozdemir et al., 2004; Downie et al., 2007; Hashimoto et al., 2012; Contrera et al., 2016; Nayak et al., 2017 and Mumtaz et al., 2019).

Prior to RIJV's division into two branches, it had a 6.5 cm distance, in comparison to Downie et al. (2007), which registered a distance of 5.0 cm at that point.

The point of division was at the level of the inferior border of the thyroid cartilage. Other authors used different landmarks to localize this point. Prades et al. (2002) used 2 cm above the hyoid bone; Turan-Ozdemir et al. (2004) used the level of true vocal cord, and Downie et al. (2007) and Contrera et al. (2016) the level of the hyoid bone.

The branches of RIJV had unequal caliber and length. The anteromedial one had 1.3 cm of diameter and 7.2 cm in length. The posterolateral one had 0.6 cm of diameter and 5.4 cm in length. Downie et al. (2007) registered diameters of 1.5 cm for the medial branch, and 2.0 cm for the lateral branch.

In regard to the tributary veins, in the present study the anteromedial branch received the inferior thyroid vein. No tributaries of the posterolateral branch were found. The main trunk of RIJV received the thyrolinguofacial trunk before dividing. Downie et al. (2007) registered as tributaries of the medial branch: the facial, superior and inferior thyroid veins and the thyrolinguofacial trunk, while the lateral branch received the transverse cervical vein.

About the RIJV termination, in the present work the anteromedial branch drained into the left brachiocephalic vein, and the posterolateral branch formed the right brachiocephalic vein along with the homolateral subclavian vein. Some authors reported that the duplication drained into the homolateral subclavian vein (Turan-Ozdemir et al., 2004; Downie et al., 2007; Contrera et al., 2016).

None of them report a contralateral termination like this report does.

In reference to the embryological origin, vessels develop from a capillary plexus that suffers many changes, such as atrophy and development of channels in order to configure their definitive adult pattern. The IJV develops from persistence of the cranial portion of the Anterior Cardinal vein located above the transverse anastomosis at thoracic level. When more than one venous channel persists from the initial capillary plexus in the embryo, a duplicated or fenestrated pattern is seen. This corresponds to the "venous theory" (Prades et al., 2002; Nayak et al., 2017).

However, there exist other well-explained theories about the origin of duplication named "neural theory", "muscular theory" and "bone theory" (Prades et al., 2002; Contrera et al., 2016; Nayak et al., 2017). The neural theory explains the origin of two venous branches when a nerve like the accessory is trapped between venous capillaries during development.

The bone theory proposes that the duplication is due to variations during skull ossification at birth, which may lead to the formation of two separated branches of the vein (Prades et al., 2002; Nayak et al., 2015; Contrera et al., 2016). Finally, the muscular theory argues that the duplicated IJV originates around the posterior belly of the omohyoid muscle (Contrera et al., 2016).

About the relations of duplicated RIJV, some of them may explain this vascular phenomenon as it was explained in the theories, such as those with the accessory nerve and omohyoid muscle. In this report, it was seen that the accessory nerve passes behind the main trunk of RIJV, whereas some authors reported in their fenestration cases the passage of the nerve through the branches of the vein (Prades et al., 2002; Hashimoto et al., 2012; Contrera et al., 2016; Nayak et al., 2017).

In this report, the omohyoid muscle passed in front of the point of division of the vein when compared to Downie et al. (2007), who described on the left side the passage of the muscle between the lateral branch of the duplicated vein and an aberrant one. Nayak et al. (2017) registered the finalization of fenestration at the level of the central tendon of this muscle.

Regarding the clinical importance of these findings, Prades et al. (2002) report that fenestrations are associated with venous ectasia, and Wong et al. (2012) affirm that these variants can be confused with laryngoceles or branchial cysts.

Many authors point out the importance of being aware of the existence of these variants during interventional procedures, such as the cannulation of a duplicated IJV and the neck lymph node dissection (Downie et al., 2007; Wong et al., 2012; Ferreira-Arquez et al., 2016; Nayak et al., 2017). In this context, an injury of anatomical structures adjacent to the vein may occur that may require challenging management, as well as wrong interpretations of the local imagenology. Due to this, Contrera et al. (2016) strongly recommend the documentation of the variants found, and Fernández et al. (2002) concluded that ultrasound-guided punctures can minimize the risk of associated complications when placing a central venous catheter.

CONCLUSIONS

A rare variant of RIJV was analyzed, which corresponds to the term "duplicated", according to the bibliography. The real number of cases of this variant around the world cannot be estimated due to the inconsistency of the use of the terms "duplication" and "fenestration".

The anatomy of the venous central system does not vary frequently. However, it is essential to take into account the existence of the aforementioned variants in order to avoid complications, due to the high frequency of procedures involving these vessels, such as central venous catheterization and those that involve the thyroid gland or its satellite lymph nodes.

ACKNOWLEDGEMENTS

The authors sincerely thank those who donated their bodies to science so that anatomical research and teaching could be performed. Results from such research can potentially increase scientific knowledge and can improve patient care. Therefore, these donors and their families deserve our highest respect.

REFERENCES

CONTRERA K, AYGUN N, WARD B, GOOI Z, RICHMON J (2016) Internal jugular vein duplication and fenestration: Case series and literature review. *Laryngoscope*, 126(7): 1585-1588.

DOWNIE SA, SCHALOP L, MAZUREK JN, SAVITCH G, LELONEK GJ, OLSON TR (2007) Bilateral duplicated internal jugular veins: Case study and literature review. *Clin Anat,* 20(3): 260-266.

FERNÁNDEZ CEAN J, ORIHUELA S, CARBONELL E (2002) Utilidad de la ecografía para la cateterización venosa central en pacientes en hemodiálisis periódica. *Rev Méd Urug,* 18(3): 239-243.

FERREIRA-ARQUEZ H (2016) Variaciones anatómicas en el drenaje venoso del cuello. *Rev CES Med,* 30(2): 238-243.

HASHIMOTO Y, OTSUKI N, MORIMOTO K, SAITO M, NIBU K (2012) Four cases of spinal accessory nerve passing through the fenestrated internal jugular vein. *Surg Radiol Anat,* 34: 373-375.

MUMTAZ S, SINGH M (2019) Surgical review of the anatomical variations of the internal jugular vein: An update for head and neck surgeons. *Ann R Coll Surg Engl,* 101(1): 2-6.

NAYAK SP, ASHRAF M, DAM A, BISWAS J (2017) Internal jugular vein duplication: review and classification. *Indian J Surg Oncol,* 8(2): 222-226.

PRADES JM, TIMOSHENKO A, DUMOLLARD JM, DURAND M, MERZOUGUI N, MARTIN C (2002) High duplication of the internal jugular vein: clinical incidence in the adult and surgical consequences, a report of three clinical cases. *Surg Radiol Anat,* 24: 129-132.

TURAN-OZDEMIR S, COSKUN H, BALBAN M (2004) Phlebectasia of the external jugular vein associated with duplication of the internal jugular vein. *Clin Anat,* 17(6): 522-525.

WONG BY, STRACHAN DR, LONEY EL (2012) Duplication of internal jugular veins: case report. *J Laryngol Otol,* 124: 341-344.

European Journal of Anatomy